



University  
of Glasgow

Vybulkova, Lada (2013) *A study of the wake of an isolated tidal turbine with application to its effects on local sediment transport*. PhD thesis.

<http://theses.gla.ac.uk/4997/>

Copyright and moral rights for this thesis are retained by the author

A copy can be downloaded for personal non-commercial research or study, without prior permission or charge

This thesis cannot be reproduced or quoted extensively from without first obtaining permission in writing from the Author

The content must not be changed in any way or sold commercially in any format or medium without the formal permission of the Author

When referring to this work, full bibliographic details including the author, title, awarding institution and date of the thesis must be given

# A Study of the Wake of an Isolated Tidal Turbine with Application to its Effects on Local Sediment Transport



Lada Vybulkova  
School of Engineering  
University of Glasgow

Submitted in fulfilment of the requirements for the degree of

*Doctor of Philosophy*

October 2013

---

To Jochen

## **Acknowledgements**

First and foremost I would like to thank my supervisors, Professor Richard Brown and Dr Marco Vezza for their valuable advice and support throughout the PhD project. I have learned a lot and the experience has changed me.

I have been very fortunate to get continuous encouragement and support from my family and friends, particularly during the last months of my PhD which ended up being the most difficult.

Special thanks are reserved for the IT support team, namely for Gordon, Mike, Ken, Grant and Walter.

# Declaration

I declare that this thesis is my own work and it has not been submitted for a degree at this or any other university.

Lada Vybulkova

Glasgow, October 2013

# Abstract

Tidal energy conversion devices (TECDs) are in development throughout the world to help reduce the need for fossil fuels. These devices will generally be mounted on the seabed and remain there over a period of years. Most of the previous research on TECDs has focused on their power extraction capability and efficient design. The handful of studies which have focused on the effects of the devices on the marine environment have not considered small-scale three-dimensional phenomena occurring in the flow near the rotor. These phenomena are likely to disturb the marine environment by altering the dynamics of sediment.

The accurate prediction of the rapidly changing flow down-stream of a TECD and its influence on the seabed poses a challenge. The nature of the interactions between such a flow and sediment has not been experimentally established. Predictions of these interactions, as is necessary for an assessment of the effects of the devices on the seabed, need to account for the depth-dependence of the flow velocity and its changes during the tidal cycle. The difference between the typical time-scales of the development of the rotor wake and the tidal cycle represents a difficulty for the computational modelling of the interactions between the device and the tidal flow.

This dissertation presents an inviscid analysis of the flow down-stream of horizontal-axis, vertical-axis and cross-flow TECDs by means of computer modelling. The Vorticity Transport Model, modified to simulate the flow down-stream of a TECD mounted onto the seabed, predicts the shear stress inflicted by the flow on the seabed. The shear stresses on the seabed, generated by small-scale vortical structures in the wake down-stream of the devices, cause sediment to uplift. This process along with the subsequent motion of the sediment is simulated by a sediment model implemented into the Vorticity Transport Model. The critical bed shear stress is known as a threshold for initiation of sediment motion, therefore the relative difference between the stress on the seabed and the critical bed shear stress, called the excess bed shear stress, is chosen here as an indicator of the impact of the TECDs on the seabed.

The evolution of the instantaneous stresses on the seabed is predicted to vary with the configuration of TECD. The results suggest that the average excess bed shear stress inflicted on the seabed by the horizontal-axis device increases with the inflow velocity during the flood part of the representative tidal cycle and that the increase can be expressed by a simple algebraic expression. It is also predicted that the impact of this device on the seabed does not monotonically decrease with increasing separation between the rotor and the seabed. In addition, the relationship between the excess bed shear stress and the position of the rotor is established. Furthermore, the simulations indicate that the wake down-stream of the horizontal-axis device is lifted by the flow away from the seabed, which result in a confinement of its impact to the vicinity of the rotor. In contrast with the horizontal-axis configuration, it is concluded that the vertical-axis and cross-flow configurations of the rotor would promote the erosion of the seabed further away from the device, at a location where the wake approaches the seabed again and that this location depends on the inflow velocity.

The predicted effects of these devices on the marine environment need to be considered in advance of their installation on the seabed.

# Contents

<b>List of Figures</b>	<b>viii</b>
<b>1 Introduction</b>	<b>1</b>
1.1 State of the Art . . . . .	1
1.2 Research Objectives . . . . .	8
1.3 Synopsis . . . . .	10
<b>List of Symbols and Abbreviations</b>	<b>1</b>
<b>2 Hydrodynamic model</b>	<b>11</b>
2.1 Studied Turbine Configurations . . . . .	12
2.2 Wake of a TECD . . . . .	17
2.3 Vorticity Transport Model . . . . .	20
2.3.1 Rotor Model . . . . .	21
2.3.2 Governing Equations . . . . .	25
2.3.3 Velocity Calculation . . . . .	27
2.3.4 Discretization of the Governing Equations . . . . .	28
2.3.5 Advection Scheme . . . . .	30
2.3.6 Adaptive Computational Grid . . . . .	32
2.3.7 Octree Data Storage . . . . .	33
2.3.8 Fast Multipole Method . . . . .	34
2.4 Tidal Flow Model . . . . .	39
2.4.1 Velocity Profiles . . . . .	41
2.4.2 Free Stream Vorticity . . . . .	42
2.4.3 Tide Induced Wake Vorticity . . . . .	43

2.4.4	Fixed Computational Grid . . . . .	46
2.4.5	Boundary Conditions . . . . .	46
2.4.6	Sediment in the VTM . . . . .	50
2.4.7	Turbulent Diffusion Effects . . . . .	51
2.5	Model Validation . . . . .	52
2.6	Summary . . . . .	54
<b>3</b>	<b>Sediment Model</b>	<b>56</b>
3.1	Sediment Characteristics at Potential Tidal Sites . . . . .	58
3.2	Initiation of Sediment Motion . . . . .	59
3.3	Erosion and Sediment Load . . . . .	63
3.4	Sediment Transport . . . . .	65
3.4.1	Settling Velocity . . . . .	66
3.5	Turbulence and Sediment Diffusivity . . . . .	66
3.6	Summary . . . . .	68
<b>4</b>	<b>TECD in Uniform Flow</b>	<b>69</b>
4.1	Specifications of the TECD . . . . .	71
4.2	Structure of the Wake . . . . .	72
4.3	Relative Erosion Flux . . . . .	79
4.4	Motivation for Tidal Flow Simulations . . . . .	85
4.5	Summary . . . . .	86
<b>5</b>	<b>TECD in Tidal Flow</b>	<b>88</b>
5.1	Structure of the Wake . . . . .	93
5.2	Excess Bed Shear Stress . . . . .	96
5.3	Tidal Cycle . . . . .	99
5.4	Effect of the Distance from the Seabed on the EXSS . . . . .	111
5.4.1	TECD close to the seabed . . . . .	124
5.5	Sediment Concentration . . . . .	133
5.5.1	Sediment Size . . . . .	141
5.6	Summary . . . . .	143

<b>6</b>	<b>Influence of Rotor Configuration on Sediment Motion</b>	<b>145</b>
6.1	Vertical Axis TECD . . . . .	146
6.2	Cross-Flow TECD . . . . .	159
6.3	Summary . . . . .	180
 <b>7</b>	 <b>Conclusions and Future Work</b>	 <b>183</b>
7.1	Research Outcomes . . . . .	185
7.1.1	What does the wake of a TECD look like? . . . . .	185
7.1.2	How does the wake affect the flow velocity close to the seabed? 187	187
7.1.3	What effects do the devices have on the sediment? . . . . .	187
7.1.4	Can the change of these effects over time be approximated by an algebraic expression? . . . . .	188
7.1.5	Does the expression apply for all configurations of a TECD? 189	189
7.1.6	Which are the key factors influencing the effects of the de- vices on the seabed? . . . . .	189
7.1.7	What could be the long term consequences of the presence of the TECDs on the seabed? . . . . .	191
7.1.8	How could the marine environment change due to the pres- ence of the TECD? . . . . .	191
7.2	Future Work . . . . .	192
 <b>Appendix A</b>	 	 <b>195</b>
 <b>Appendix B</b>	 	 <b>196</b>
 <b>References</b>	 	 <b>197</b>

# List of Figures

2.1	Position of the blades of the HATT in the coordinate system. . . .	14
2.2	Position of the blades of the VATT in the coordinate system. . . .	16
2.3	Position of the blades of the CF TT in the coordinate system. . . .	16
2.4	Scale comparison of the studied devices. . . . .	17
2.5	Schematic representation of the wake of a horizontal axis turbine in uniform flow . . . . .	18
2.6	Schematic representation of the wake of a horizontal axis turbine for a non-uniform inflow model, where the inflow velocity increases with the height above the seabed . . . . .	18
2.7	Computational domain with marked boundaries - 1) inlet; 2) right wall (from down-stream direction); 3) outlet; 4) left wall; 5) top. . .	19
2.8	An iso-surface of rotor vorticity in the computational domain. . .	20
2.9	A section of rotor vorticity in the computational domain. . . . .	20
2.10	Schematic representation of the inner model . . . . .	22
2.11	Schematic representation of the intercell vorticity fluxes, figure taken from [1] . . . . .	30
2.12	Schematic representation of an octree grid structure, figure taken from [1] . . . . .	33
2.13	Decomposition of the vorticity field in to the far field (white), in- termediate field (dark grey), near field (light grey) of cluster $i$ , figure taken from [1] . . . . .	37
2.14	Illustration of a velocity profile as an inflow condition . . . . .	41
2.15	Illustration of the implemented seabed boundary condition and a possible free-surface representation. . . . .	49

**LIST OF FIGURES**

---

2.16	Illustration of the influence of the mirror vortex on the flow. The dark grey arrow represents the wake induced velocity vector without an influence of free surface, the light grey arrow represents the velocity induced by the mirror vortex and the black arrow indicates the wake induced velocity vector affected by the simple free-surface model. . . . .	50
2.17	Comparison between the variation in VTM-predicted aerodynamic loading and experimental measurements made by Strickland et al. [2] for $TSR = 5$ , left: normal force, right: tangential force. Image taken from Scheurich [3]. . . . .	52
2.18	Smoke flow visualisation of the wake produced by a two bladed rotor in ground effect. Image taken from Lee et al. [4] . . . . .	53
2.19	Vorticity distribution from a two bladed rotor in proximity to the ground plane as calculated using the VTM. Image taken from Phillips [5]. (The rotor was hovering one radius above the ground)	53
4.1	Position of the blades of the horizontal-axis TECD in the coordinate system. . . . .	71
4.2	Dependence of the power coefficient of the TECD on TSR. . . . .	72
4.3	Three-dimensional representation of the rotor vorticity field evolving in time, the black lines denote the position of the seabed ( $z = 0$ ). . . . .	74
4.4	The iso-surface of the vorticity field, equal to 10% of the maximal magnitude of the vorticity for $TSR = 4$ , of the fully developed wake; from top to bottom: $TSR = 4, 4.5, 5, 5.56, 6, 6.67, 7$ . . . . .	76
4.5	The near-bed velocity induced by the fully developed wake, from top to bottom: $TSR = 4, 4.5, 5, 5.56, 6, 6.67, 7$ . The value of the free-stream velocity is depicted by black colour, the regions where the near-bed velocity exceeds the free-stream value are red. . . . .	78
4.6	Illustration of the abrupt changes in the near-bed velocity, $TSR = 4$ , from top to bottom: $25.6 T_{rr}, 26.7 T_{rr}, 34.5 T_{rr}, 36.8 T_{rr}$ , where $T_{rr}$ denotes the time of one rotor revolution. . . . .	80
4.7	REEF for $TSR = 4$ , left: $z_{hub} = 1.5R$ , right: $z_{hub} = 1.2R$ . . . . .	81
4.8	REEF for $TSR = 4.5$ , left: $z_{hub} = 1.5R$ , right: $z_{hub} = 1.2R$ . . . . .	82

## LIST OF FIGURES

---

4.9	REEF for $TSR = 5$ , left: $z_{hub} = 1.5R$ , right: $z_{hub} = 1.2R$ . . . . .	82
4.10	REEF for $TSR = 5.56$ , left: $z_{hub} = 1.5R$ , right: $z_{hub} = 1.2R$ . . . . .	82
4.11	REEF for $TSR = 6$ , left: $z_{hub} = 1.5R$ , right: $z_{hub} = 1.2R$ . . . . .	83
4.12	REEF for $TSR = 6.67$ , left: $z_{hub} = 1.5R$ , right: $z_{hub} = 1.2R$ . . . . .	83
4.13	REEF for $TSR = 7$ , left: $z_{hub} = 1.5R$ , right: $z_{hub} = 1.2R$ . . . . .	83
4.14	The mean value of REEF of the fully developed wake, left: $z_{hub} = 1.5R$ , right: $z_{hub} = 1.2R$ . . . . .	85
5.1	The velocity of the flow at the rotor plane ( $x = 0$ ), $v_{hub}/v_{tip} = 0.2$ , $z_{hub} = 1.5R$ , $R = 5$ m. . . . .	89
5.2	Boundary layer flow for $v_{hub} = 1.25$ m/s. . . . .	90
5.3	Free-stream vorticity for $v_{hub} = 1.25$ m/s. . . . .	91
5.4	Comparison of the rotor vorticity field for the two inflow models, top: uniform inflow velocity, $V_{uniform} = 1.25$ m/s, bottom: the velocity profile, $v_{hub} = 1.25$ m/s. . . . .	93
5.5	Illustration of the evolution of the rotor vorticity field, calculated by the modified VTМ. . . . .	94
5.6	The rotor vorticity field of the fully developed wake, $v_{hub} = 1$ m/s and $z_{hub} = 1.5R$ . . . . .	95
5.7	The tide induced wake vorticity of the fully developed wake, planar section perpendicular to the seabed and the rotor plane, $v_{hub} = 1$ m/s and $z_{hub} = 1.5R$ . . . . .	95
5.8	The near-bed velocity, $v_{hub} = 1$ m/s and $z_{hub} = 1.5R$ , from top to bottom: $t = 20.2 T_{rr}$ , $27.9 T_{rr}$ , $32.3 T_{rr}$ , $36.8 T_{rr}$ , where $T_{rr}$ denotes the time of one rotor revolution. . . . .	96
5.9	The excess bed shear stress, $v_{hub} = 1$ m/s and $z_{hub} = 1.5R$ , from top to bottom: $t = 20.2 T_{rr}$ , $27.9 T_{rr}$ , $32.3 T_{rr}$ , $36.8 T_{rr}$ . . . . .	97
5.10	The averaged excess bed shear stress, $v_{hub} = 1$ m/s and $z_{hub} = 1.5R$ . . . . .	98
5.11	Set of velocity profiles used to represent subsequent stages of the tidal cycle, $z_{hub} = 1.5R$ , $R = 5$ m. . . . .	99
5.12	The power extracted by the HATT with respect to the power available in an uniform flow of speed $v_{hub}$ . . . . .	100
5.13	The difference of the inflow velocity across the HATT. . . . .	101

## LIST OF FIGURES

---

5.14	The rotor vorticity field of the fully developed wake, from top to bottom: $v_{tip}/v_{hub} = 4, 4.5, 5, 5.56, 6, 6.67, 7$ . . . . .	102
5.15	Y-slice of the rotor vorticity field of the fully developed wake, from top to bottom: $v_{tip}/v_{hub} = 4, 4.5, 5, 5.56, 6, 6.67, 7$ . . . . .	103
5.16	Y-slice of the tide induced vorticity field of the fully developed wake, from top to bottom: $v_{tip}/v_{hub} = 4, 4.5, 5, 5.56, 6, 6.67, 7$ . . .	104
5.17	The near-bed velocity of the fully developed wake, from top to bottom: $v_{tip}/v_{hub} = 4, 4.5, 5, 5.56, 6, 6.67, 7$ . . . . .	106
5.18	The excess bed shear stress once the wake is fully developed, from top to bottom: $v_{tip}/v_{hub} = 4, 4.5, 5, 5.56, 6, 6.67, 7$ . . . . .	107
5.19	The AEXSS evolution for the HATT for the inflow conditions listed in Table 5.1. . . . .	108
5.20	The dependence of the MAEXSS on the inflow velocity for the HATT under two threshold conditions described in section 3.2, left: $\theta \geq \theta_{cr}$ , right: $ \mathbf{v}  \geq v_t$ . . . . .	109
5.21	The dependence of the MAEXSS for the HATT on the inflow velocity, comparison of the VTM's simulations with the algebraic expression Eq. 5.10. . . . .	110
5.22	Velocity at the rotor plane, from left to right: $z_{hub} = 1.4R, 1.7R, 2R$ . . . . .	111
5.23	The investigated velocity profile, $V_{in} = 2$ m/s at 40 m above the seabed. . . . .	112
5.24	The difference of the inflow velocity across the rotor for the investigated positions of the HATT above the seabed, listed in Tables 5.3 and 5.4. . . . .	113
5.25	The rotor vorticity field of the fully developed wake, from top to bottom: $z_{hub} = 1.3R, 1.4R, 1.5R, 1.6R, 1.7R, 1.8R, 1.9R, 2R$ . . .	114
5.26	The rotor vorticity field of the fully developed wake, $v_{tip}/v_{hub} = 5.56$ , $z_{hub} = 1.5R$ , top: $v_{hub} = 0.90$ m/s, bottom: $v_{hub} = 1.42$ m/s. . .	115
5.27	Y-slice of the rotor vorticity field of the fully developed wake, from top to bottom: $z_{hub} = 1.3R, 1.4R, 1.5R, 1.6R, 1.7R, 1.8R, 1.9R, 2R$ . . .	116

**LIST OF FIGURES**

---

5.28	Y-slice of the tide induced wake vorticity of the fully developed wake, from top to bottom: $z_{hub} = 1.3R, 1.4R, 1.5R, 1.6R, 1.7R, 1.8R, 1.9R, 2R$ . . . . .	118
5.29	The near-bed velocity induced by the fully developed wake, from top to bottom: $z_{hub} = 1.3R, 1.4R, 1.5R, 1.6R, 1.7R, 1.8R, 1.9R, 2R$ .	119
5.30	The excess bed shear stress once the wake is fully developed, from top to bottom: $z_{hub} = 1.3R, 1.4R, 1.5R, 1.6R, 1.7R, 1.8R, 1.9R, 2R$ .	120
5.31	Variation of the AEXSS evolution with the position of the HATT above the seabed, $z_{hub} \geq 1.3R$ . . . . .	121
5.32	Dependence of the MAEXSS on the position of the HATT above the seabed. . . . .	122
5.33	Dependence of the MAEXSS on the position of the HATT above the seabed, comparison with Eq. 5.14, where $\xi_{-2}^z = 16.5$ . . . . .	123
5.34	Velocity at the rotor plane, left: $z_{hub} = 1.05R$ , right: $1.3R$ . . . . .	124
5.35	The rotor vorticity field of the fully developed wake, from top to bottom: $z_{hub} = 1.05R, 1.1R, 1.15R, 1.2R, 1.25R$ . . . . .	125
5.36	Y-slice of the rotor vorticity field of the fully developed wake, from top to bottom: $z_{hub} = 1.05R, 1.1R, 1.15R, 1.2R, 1.25R$ . . . . .	126
5.37	Z-slice of the rotor vorticity field of the fully developed wake, detailed behaviour of the wake close to the seabed. . . . .	127
5.38	X-slice of the rotor vorticity field of the fully developed wake, comparison between cases $z_{hub} = 1.05R$ and $z_{hub} = 1.3R$ . . . . .	127
5.39	Y-slice of the tide induced wake vorticity of the fully developed wake, from top to bottom: $z_{hub} = 1.05R, 1.1R, 1.15R, 1.2R, 1.25R$ .	128
5.40	The near-bed velocity induced by the fully developed wake, from top to bottom: $z_{hub} = 1.05R, 1.1R, 1.15R, 1.2R, 1.25R$ . . . . .	129
5.41	The excess bed shear stress once the wake is fully developed, from top to bottom: $z_{hub} = 1.05R, 1.1R, 1.15R, 1.2R, 1.25R$ , showing the asymmetry of the exposed area of the seabed for small $z_{hub}$ , caused by the local deformation of the rotor vorticity. . . . .	130
5.42	Variation of the AEXSS evolution with the position of the HATT above the seabed, $z_{hub} \leq 1.3R$ . . . . .	131

## LIST OF FIGURES

---

5.43 Dependence of the temporal mean of the AEXSS on the position of the HATT above the seabed. . . . .	132
5.44 The rotor vorticity field of the fully developed wake. . . . .	133
5.45 Y-slice of the rotor vorticity field of the fully developed wake. . .	134
5.46 The near-bed velocity induced by the fully developed wake. . . . .	134
5.47 Y-slice of the sediment concentration $c$ , from top to bottom: $\eta = 0.001, 0.002, 0.003, 0.004, 0.005$ and $0.006 \text{ m}^2/\text{s}$ . . . . .	135
5.48 Y-slice of the sediment concentration $c$ , from top to bottom: $\eta = 0.007, 0.008, 0.009, 0.010$ and $0.050 \text{ m}^2/\text{s}$ . . . . .	136
5.49 Z-slice of the sediment concentration $c$ at height 1 m, from top to bottom: $\eta = 0.001, 0.002, 0.003, 0.004, 0.005$ and $0.006 \text{ m}^2/\text{s}$ . . . . .	137
5.50 Z-slice of the sediment concentration $c$ at height 1 m, from top to bottom: $\eta = 0.007, 0.008, 0.009, 0.010$ and $0.050 \text{ m}^2/\text{s}$ . . . . .	138
5.51 Y-slice of the magnitude of sediment concentration gradient $ \nabla c $ , from top to bottom: $\eta = 0.001, 0.002, 0.003, 0.004, 0.005$ and $0.006 \text{ m}^2/\text{s}$ . . . . .	139
5.52 Y-slice of the magnitude of sediment concentration gradient $ \nabla c $ , from top to bottom: $\eta = 0.007, 0.008, 0.009, 0.010$ and $0.050 \text{ m}^2/\text{s}$ . . . . .	140
5.53 EXSS once the wake is fully developed, from top to bottom: Sediment size $d = 0.25 \text{ mm}, 0.50 \text{ mm}$ and $0.75 \text{ mm}$ . . . . .	141
5.54 The evolution of the AEXSS for the three sediment sizes, $d = 0.25 \text{ mm}, 0.50 \text{ mm}$ and $0.75 \text{ mm}$ . . . . .	142
6.1 Position of the blades of the VATT in the coordinate system. . . . .	146
6.2 Power coefficient of the VATT. . . . .	147
6.3 Position of the blades of the VATT above the seabed. . . . .	148
6.4 Illustration of the evolution of the rotor vorticity field for the VATT, simulated by the modified VTM. . . . .	148
6.5 The rotor vorticity field of the fully developed wake down-stream of the VATT. . . . .	149
6.6 Set of velocity profiles used to represent a part of the tidal cycle. . .	150
6.7 The difference of the inflow velocity across the VATT. . . . .	150

## LIST OF FIGURES

---

6.8	The rotor vorticity field of the fully developed wake, from top to bottom: $v_{tip}/v_{R/2} = 4, 4.5, 5, 5.56, 6, 6.67, 7$ . . . . .	151
6.9	Y-slice of the rotor vorticity field of the fully developed wake, from top to bottom: $v_{tip}/v_{R/2} = 4, 4.5, 5, 5.56, 6, 6.67, 7$ . . . . .	152
6.10	Y-slice of the tide induced wake vorticity field of the fully developed wake, from top to bottom: $v_{tip}/v_{R/2} = 4, 4.5, 5, 5.56, 6, 6.67, 7$ . . . . .	153
6.11	Composition of the induced vorticity $\omega_I = \omega^* + \omega_w$ of the fully developed wake, $\max  \omega^* $ vs. $\max  \omega_w $ . . . . .	155
6.12	The excess bed shear stress induced by the fully developed wake, from top to bottom: $v_{tip}/v_{R/2} = 4, 4.5, 5, 5.56, 6, 6.67, 7$ . . . . .	157
6.13	The AEXSS evolution for the VATT. . . . .	158
6.14	Clock-wise sense of rotation of the CFATT. . . . .	159
6.15	Power coefficient of the CFATT and the VATT. . . . .	160
6.16	Illustration of the evolution of the rotor vorticity field for the CFATT, simulated by the modified VTM. . . . .	160
6.17	The rotor vorticity field of the fully developed wake down-stream of the CFATT. . . . .	161
6.18	Illustration of the evolution of the rotor vorticity field for the CFATT, simulated by the modified VTM. . . . .	161
6.19	Set of velocity profiles used to represent a part of the tidal cycle. . . . .	162
6.20	The difference of the inflow velocity across the CFATT. . . . .	163
6.21	The rotor vorticity field down-stream of the CFATT of the fully developed wake, from top to bottom: $v_{tip}/v_{hub} = 4, 4.5, 5, 5.56, 6, 6.67, 7$ . . . . .	164
6.22	The rotor vorticity field down-stream of the CFATT of the fully developed wake, from top to bottom: $v_{tip}/v_{hub} = 4, 4.5, 5, 5.56, 6, 6.67, 7$ . . . . .	165
6.23	Y-slice of the rotor vorticity field of the fully developed wake, top: the CFATT, bottom: the CFATT, $v_{tip}/v_{hub} = 4$ . . . . .	166
6.24	Y-slice of the rotor vorticity field of the fully developed wake, top: the CFATT, bottom: the CFATT, $v_{tip}/v_{hub} = 4.5$ . . . . .	166
6.25	Y-slice of the rotor vorticity field of the fully developed wake, top: the CFATT, bottom: the CFATT, $v_{tip}/v_{hub} = 5$ . . . . .	167

## LIST OF FIGURES

---

6.26	Y-slice of the rotor vorticity field of the fully developed wake, top: the CFCTT, bottom: the CFATT, $v_{tip}/v_{hub} = 5.56$ . . . . .	167
6.27	Y-slice of the rotor vorticity field of the fully developed wake, top: the CFCTT, bottom: the CFATT, $v_{tip}/v_{hub} = 6$ . . . . .	168
6.28	Y-slice of the rotor vorticity field of the fully developed wake, top: the CFCTT, bottom: the CFATT, $v_{tip}/v_{hub} = 6.67$ . . . . .	169
6.29	Y-slice of the rotor vorticity field of the fully developed wake, top: the CFCTT, bottom: the CFATT, $v_{tip}/v_{hub} = 7$ . . . . .	169
6.30	X-slice of the rotor vorticity field of the fully developed wake down- stream of the CFCTT, $x = 8.72R$ , from top-left to bottom-right: $v_{tip}/v_{hub} = 4, 4.5, 5, 5.56, 6, 6.67, 7$ . . . . .	170
6.31	X-slice of the rotor vorticity field of the fully developed wake down- stream of the CFATT, $x = 8.72R$ , from top-left to bottom-right: $v_{tip}/v_{hub} = 4, 4.5, 5, 5.56, 6, 6.67, 7$ . . . . .	170
6.32	Y-slice of the tide induced wake vorticity field of the fully developed wake down-stream of the CFCTT, from top to bottom: $v_{tip}/v_{hub} =$ $4, 4.5, 5, 5.56, 6, 6.67, 7$ . . . . .	172
6.33	Y-slice of the tide induced wake vorticity field of the fully developed wake down-stream of the CFATT, from top to bottom: $v_{tip}/v_{hub} =$ $4, 4.5, 5, 5.56, 6, 6.67, 7$ . . . . .	173
6.34	Composition of the induced vorticity field of the fully developed wake, $\max \omega^* $ vs. $\max \omega_w $ . . . . .	174
6.35	The excess bed shear stress induced by the CFCTT, from top to bottom: $v_{tip}/v_{hub} = 4, 4.5, 5, 5.56, 6, 6.67, 7$ . . . . .	176
6.36	The excess bed shear stress induced by the CFATT, from top to bottom: $v_{tip}/v_{hub} = 4, 4.5, 5, 5.56, 6, 6.67, 7$ . . . . .	177
6.37	The AEXSS evolution for the CFCTT. . . . .	178
6.38	The AEXSS evolution for the CFATT. . . . .	178
6.39	The temporal mean of the AEXSS for the VATT, the CFCTT and the CFATT. . . . .	180

# Chapter 1

## Introduction

### 1.1 State of the Art

Although still young, the tidal energy industry has been developing rapidly over the last few years. Indeed, the variety of devices designed to harness energy from tides continues to expand every year. The enthusiasm for marine renewable energy technology in the United Kingdom and elsewhere has been fuelled by optimistic estimates of the tidal energy resources. These estimates have suggested that the amount of power available in tidal currents and waves could be, in combination with other renewable sources of power, sufficient enough to provide a realistic energy alternative to fossil fuels. In fact, the World Wide Fund for Nature (WWF) announced an ambitious goal of 100% energy to be obtained from renewable sources by 2050 [6]. According to the WWF and the Office for Metropolitan Architecture [6], an unprecedented increase in the number of renewable energy installations worldwide has to be accompanied by a reduction in the energy demand below the level of consumption in 2000. To achieve such an ambitious goal, the scenario of the WWF makes provision for large energy conservation schemes, improvements in the efficiency of energy use, intensive recycling of materials, a sharp reduction in food waste (presently, 50% of food is wasted and lost worldwide according to Lundqvist and Molden [7]) and halving the consumption of meat per person by 2050 in OECD countries.

The extent and distribution of tidal energy resources in the UK has been summarized in the Atlas of UK Marine Renewable Energy Resources [8]. The

UK Total Resource was estimated at approximately 110 TWh annually, a large proportion of which is from presently known locations. A comprehensive overview of the recent developments in the technology used to extract power from tides can be found in the study by Bahaj [9]. The so called Significant Impact Factor (SIF), which establishes how much of the energy can be extracted without significant economic or environmental effects, was introduced as a measure of the technically extractable power. The value of the SIF estimated by Black and Veatch [10] further limits the extractable power from tides around the UK to around 18 TWh every year. The current derivation of the SIF, however, requires revision - further research should determine more appropriate values of the SIF in light of projected technological developments [10]. The SIF is derived from an estimate of the number of locations suitable for power extraction, based on the current state of the technology. The estimated number of suitable sites is based on the speed of the tidal flow. The merit of sites with low-speed currents could be acknowledged if efficient 'low-speed' tidal energy converters were available. It could be argued that the perception of tidal power extraction has become distorted - instead of asking how the technology can be adapted to the character of the resource, the resource has been perceived to be 'limited'. Indeed, the extraction capacity of existing devices, which did, initially, bear a strong resemblance to wind turbines, has been used to identify potential resources of tidal energy to be flows faster than 2 m/s. Concerns about the environmental factors affecting the availability of the resource are understandable, nonetheless. It should be stressed, however, that the interactions between the devices and marine environment have to be properly understood in order to establish the available resource, i.e. the amount of power that can be extracted without harm to the environment.

The handful of companies devoted to the design and manufacture of tidal power extraction devices have drawn inspiration from the achievements of the wind energy industry. The industry of wind power extraction has become well established in the European Union over the last decade. In particular, the profusion of wind power installations has been impressive. According to the European Wind Energy Association [11], the percentage of total installed power capacity in the EU in the form of wind power increased from 2.2% in 2000 to 11.4% in 2012. At the end of 2012, a total of 106GW of wind power capacity was installed in the

EU. In sharp contrast, the installed ocean power capacity in the EU accounted for only 260MW in 2012 [11]. According to Bahaj [9], the state of the marine energy industry in 2012 can be compared to the state of the emerging wind energy industry in the 1980s. The progress in the marine energy sector is, however, expected to proceed at a much faster rate than the development of the wind energy industry given the commitment to tackle climate change. While the number of on-shore wind energy installations could reach saturation in the near future, the developments in tidal power extraction provide an opportunity to mitigate the intermittent nature of wind power and thus to help secure a continuous power supply from renewable sources. Positioning of arrays of tidal energy conversion devices in strategically distributed tidal sites could, indeed, even out the periodic nature of tidal power generation by phasing the periods when the velocity of the stream is at its peak [12]. The regularity of power extracted from tides on a daily basis could thus balance out the irregularity that is immanent to wind power generation.

The biggest advantage of tidal energy is its predictability. The tidal cycle has been observed over the ages for the purposes of navigation of marine and sub-marine vehicles, fishing and weather forecasting. The earliest record of tidal cycle observations dates back to the 2<sup>nd</sup> century BC [13]. Since then, detailed data collection has enabled researchers to develop complex oceanographic models, which can predict the behaviour of tidal currents with a good level of accuracy. State-of-the-art oceanographic models, verified against experimental measurements, predict tidal range, constituents of tidal currents, underwater pressure, temperature, turbulence and sediment transport. With such an amount of information it is not surprising that tidal currents should be considered a plausible source of power for the future.

Although the marine energy industry is in an early stage of its development, with many devices still in the testing phase, the prospect of such a reliable resource of power is promising. In addition to the previously mentioned advantages of tidal energy over wind, the companies that operate tidal turbines are not likely to face such a critical public opinion on the aesthetic qualities of the devices with respect to the landscape. Once the technology reaches commercial scale, the ratio of power generated from renewable sources is expected to rise, addressing

not only the looming energy crisis, but also the much needed boost to industrial infrastructure and employment. The energy independence of local communities, with the prospect of a shortage of natural resources, could help to avoid future conflicts in competition for scarce energy reserves. According to WWF and the Office for Metropolitan Architecture [6], accessible local renewable energy supplies provide a basis for stable future communities, clean means of transport, and the prevention of food crises by divorcing food and oil prices.

Arguably, renewable energy conversion poses little harm to the natural environment in comparison to coal mining and combustion, oil drilling and contamination, Hydraulic Fracturing and the damage to the landscape by the exploitation of bitumen deposits. The possible environmental impact of the devices for extracting power from renewable sources are, however, not to be neglected if a reliable power supply is to be secured in the future. The estimates of the achievable power output of tidal energy conversion devices have taken into account possible impacts of the devices on the marine environment. According to Iyer et al. [12], the estimated power capacity has included a limit to the number of installed devices to mitigate potential damage to the seabed. The devices and the environment in which they operate cannot be viewed separately since they form an interconnected system. As much as a device influences its surroundings, the changes in the environment can also affect the device in a ‘positive’ feedback loop, possibly resulting in profound damage to the seabed and causing an alteration of the natural conditions that motivated the placement of the device in the first instance. In this light, an investigation of the interactions between the device and the environment is necessary not only to protect the marine environment but also to ensure continuous power output of the device. The long term effects of tidal energy conversion technology on the marine environment have to be thoroughly studied to mitigate potential undesirable consequences.

The presence of a tidal energy conversion device (TECD) can affect the marine environment in a number of ways. The fluctuations in local pressure near an operating TECD are of particular concern. Cavitation on the blades of an operating TECD could damage the blades by the action of cyclic stress, and disturb the environment by implosion of the cavities with associated generation

of sound waves, causing a peak in local pressure and temperature. To date, research on the environmental impact of marine renewable energy conversion has been focused on the potential change in behaviour of marine fauna and damage to natural habitats. The placement of a TECD into large ocean estuaries could, indeed, reduce the abundance of migrating fish through high levels of pressure and mechanical strikes, in particular the species migrating through the estuary to local rivers for reproduction [14]. The study by the Electric Power Research Institute [15] investigated injuries and mortality of fish ‘injected’ into a rotor of an operating TECD. Less lethal research methods have been used in Scotland to investigate the influence of tidal energy installations on marine life. The Scottish Association for Marine Science conducts research in many areas related to the environmental interactions of marine renewable energy, including the collision risks for mega-vertebrates, acoustic footprints of renewable devices, reef effects of offshore structures, biofouling on the structures, impacts of mass macro-algal culture and use of the wild seaweed resource, and survey techniques for tidal sites (acoustics and marine mammal abundance) [16].

A structure mounted on the seabed can cause relocation of sediment, called scouring of the seabed. In fact, the scour phenomenon occurs around any structure mounted on the seabed, even under steady current conditions [17]. The scour near the foundations of off-shore wind turbines has been investigated repeatedly and has resulted in proposals for effective scour protection techniques to mitigate the impact of scour on the stability and dynamic behaviour of the wind turbine [18]. The foundation of an off-shore wind turbine and the seabed represent an interconnected system consisting of the device and the environment. The presence of the wind turbine tower causes the flow to change in such a way that the shear stress is increased near the foundation compared to the shear stress which would have occurred in the absence of the tower. The scouring of the seabed around the foundation might thus jeopardize the stability of the wind turbine itself. In the case of an underwater turbine, the nature of the interactions between the flow through the rotor and the seabed is unknown at present. In an analogy to the situation with wind turbine foundations, the presence of a TECD on the seabed could result in anomalous scour of the seabed. The TECD could influence the dynamics of sediment. The effect on the sediment dynamics might accumulate

and, over a period of years, result in an alteration to the local seabed morphology. The possible reaction of the marine environment to the TECD mounted on the seabed needs to be considered in order to assess the future state of the interconnected system

$$TECD \rightleftharpoons environment,$$

referred to as the ‘TE’ system in this dissertation.

The potential consequences of mounting a rotor near the seabed are closely related to the character of the flow velocity in the vicinity of the TECD. In large part, researchers have chosen to focus on the unidirectional problem - the influence of the presence of a TECD on the current velocity. The method has repeatedly been the same - to represent the foreseen effects of a TECD by introducing some form of simplified expression, e.g. a reduction in the velocity of the flow (sometimes referred to as a momentum sink), into an existing hydrodynamical model [19, 20, 21, 22, 23, 24, 25, 26]. None of these studies has, however, considered the three-dimensional nature of the flow at the scale of the rotor. Furthermore, the expressions used to represent a TECD in the computer models have not been experimentally justified. In comparison, studies focusing on the detailed structure of the wake of a TECD are rare. One such study applied the Large-Eddy Simulation technique to examine the interactions between the wakes produced by multiple rotors in a turbulent flow [27]. The main purpose of the study was however to assess the changes in power production due to the turbulent inflow.

The assumption that large-scale hydrodynamical models, particularly those which have approximated the influence of TECDs on the environment as a reduction of the flow velocity, produce realistic data has to be questioned before any of the predictions are employed to regulate the deployment of TECDs. For instance, in the case of the island of Alderney, Neill et al. [22] conclude that the deployment of an array of tidal energy converters could lead to a considerable change in the maintenance of headland sand banks over a spring-neap cycle and advise the developers of the devices to re-examine the positioning of the array. These conclusions should be confirmed by small-scale modelling and measurements of the flow down-stream of TECDs before an appropriate location of the array can be determined, since the three-dimensional, small-scale fluid phenomena were omitted from consideration in Neill et al. [22].

A detailed three-dimensional study of the flow through the rotor of a TECD has to be conducted, both by computational and experimental means, to understand the nature of the flow. An empirical representation of the impact of TECDs on the seabed, i.e. a relationship between physical quantities of the flow and the device, should be derived from the results of computational investigations. Predictions of computational models need to be, however, subjected to verification against experiments, whenever relevant experimental data is available. The reaction of the environment to the changes caused by the presence of the TECD on the seabed should be examined as well. After the interactions within a TE system have been analysed, the temporal changes of the seabed can be assessed.

A variety of computational models are being used to simulate TECDs in studies focused on performance of the devices with the aim of maximizing the power extracted from tides. The information about the velocity field further from the rotor is not needed to evaluate the performance of a TECD, thus most of the previous computational studies have not focused on the detailed structure of the velocity field more than few diameters down-stream of the rotor. Previous experimental investigation of the velocity field down-stream of TECDs used techniques that emphasised the average of the velocity instead of recording the data in short enough time intervals so that the temporal characteristics of the wake could be captured. The scale used for simulations presented in this dissertation have been smaller than the resolution of velocity measurements available at present. The available experimental data include that presented by Myers and Bahaj [28], where the velocity field down-stream of the two porous discs has been recorded. Arguably, the flow down-stream of a static porous disc does not contain the effects induced by the rotation of individual blades. Both computational investigation of small-scale phenomena in the wake of a TECD further from the rotor and experiments designed to capture the evolution of the wake are essential steps on the path to a complete understanding of the TE system.

The dynamics of the TE system is likely to entail changes in current velocity, sediment concentration, temperature, pressure and turbulence. The variation in the velocity of the tidal current can be perceived as the primary measure of the interactions within the system because each of the other quantities depends in

some way on the velocity. The relationship between the current velocity and sediment concentration down-stream of the TECD could be approximated without detailed information about the temperature and the pressure in the current. Indeed, until small-scale measurements of sediment transport by a rapidly changing (turbulent) flow are available, computational investigations of sediment motion in the flow down-stream of a TECD have to rely on an approach which does not require information about turbulence. A suitable version of the sediment transport model coupled to a detailed simulation of the changes in current velocity could uncover the nature of the interactions within the TE system.

## 1.2 Research Objectives

The main purpose of the present research is to contribute to the knowledge about the connection between a TECD and the Environment (TE system). The first stage of the investigation proposed earlier is a detailed three-dimensional study of the flow through the rotor of a TECD. This dissertation presents a visualisation of the flow through the rotor obtained from a state-of-the-art computer model, an inviscid analysis of the three-dimensional phenomena occurring in the rotor wake and an investigation of the interactions between the wake and marine environment. The existence of a simplified algebraic expression which approximates well the effect of a generic TECD on the marine environment, assumed by Ahmadian et al. [19] and Neill et al. [21] among others, is challenged in this dissertation. The validity of a single algebraic expression for all TECD configurations is questioned and the existence of configuration-specific expressions is investigated. The main task of the present research is to uncover the physics of the small-scale three dimensional phenomena in the flow through the rotor of a TECD. The small-scale phenomena have not been previously studied in such detail. The three-dimensional effect in the flow down-stream of the rotor could influence the environment over scales of a few centimetres. The research focus is on the nature of the interactions within the TE system, with the premise that the local small-scale interactions play a crucial role in any assessment of the environmental impact of TECDs.

This dissertation attempts to provide answers to the following research questions:

- What does **the wake** of a TECD look like?
- How does the wake affect **the flow velocity** close to the seabed?
- What effects do the devices have on **the sediment**?
- Can **the change of these effects over time** be approximated by an algebraic expression?
- Does the expression apply for **all configurations** of a TECD?
- Which are **the key factors** influencing the effects of the devices on the seabed?
- What could be **the long term consequences** of the presence of TECDs on the seabed?
- How could the marine environment **change** due to the presence of the TECD?

The outcomes presented in this dissertation provide a fundamental understanding of the physics of the small-scale interactions within the TE system. The indicators of the environmental impact of TECDs are identified. The evolution of the velocity field of the flow through the rotor of a TECD, which influences a number of natural processes in the marine environment, is presented. Particular attention is paid to the effects of a TECD on the motion of sediment into suspension. The relation between the erosion of the sediment and the velocity of the flow down-stream of a TECD is studied. The motion of sediment is analysed by computer simulations of the evolution of the flow velocity down-stream of the TECD. The possibility of expressing the key aspects of the interaction of the device and the seabed as simplified formulas, and the conditions for the applicability of these formulas, are examined. Future applications of the findings presented in this dissertation are suggested.

## 1.3 Synopsis

This dissertation has following structure. Chapter 2 presents in detail the Vorticity Transport Model, modified to suit the purpose of modelling of the flow through a TECD. Chapter 3 contains the description of the sediment model used to simulate the effect of a TECD on the sediment down-stream of a TECD. In Chapter 4, the flow down-stream of a horizontal-axis TECD is analysed under the assumption that the inflow velocity is uniform. The influence of this flow on the seabed is discussed and the reasons for the utilisation of a more realistic inflow model are presented. Chapter 5 contains the analysis of the flow down-stream of the horizontal-axis TECD, predicted by the modified VTM which employs the inflow model in the form of a velocity profile. The predicted effects of the device on the seabed are analysed and compared with the results obtained for the uniform inflow approximation. Furthermore, the dependence of these effects on the phase of the tidal cycle and the position of the device is discussed. In Chapter 6, vertical-axis and cross-flow configurations of TECDs are compared with the horizontal axis configuration in terms of their influence on the seabed. And finally, the findings of the present research are concluded in Chapter 7.

## Chapter 2

# Hydrodynamic model

The nature of the small-scale interactions between the tidal flow and a tidal energy conversion device (TECD) mounted on the seabed is unknown at present. Prototypes of TECs undergo a testing period before their commercial deployment. The largest facility for testing of TECs is the European Marine Energy Centre (EMEC) Ltd, a not-for-profit private company, which provides services to developers of TECs. The EMEC does not provide the knowledge gained from the tests freely to the public, however. The main objective of the research at the EMEC is to support the marine energy industry. Furthermore, the design of existing TECs is intellectual property of private enterprises.

Consequently, the detailed experimental data, required for a reliable assessment of the interactions between the flow and TECs, are rarely available in public domain. The lack of publicly available information about existing prototypes of TECs motivated the design of the TECs in the present research. The need for the assessment of the impact of TECs on the marine environment inspired the development of computer models of the flow through TECs.

A TEC is subjected to an inflow, whose direction, speed and profile depends on the phase of the tidal cycle. For a TEC deployed in a tidal channel, i.e. between two islands or an island and the mainland, the direction of the flood tide is approximately opposite to the direction of ebb tide. In such a case a horizontal-axis TEC can adapt the pitch of the blades (180 degrees change) to extract power from the opposite direction. In a more complicated case when the flood tide direction is not simply the opposite to the ebb tide direction,

a horizontal-axis TECD would also need to yaw to face the inflow. Locations with a significant tidal asymmetry, i.e. the difference between the ebb and flood velocities, would require a device with variable rotational speed to keep the TSR constant, rather than a fixed speed TECD, to maximize the power output. The importance of tidal asymmetry in sediment transport is described in [29].

This dissertation presents the research on the interactions between the flow and a variety of community-sized (i.e. with rated power below 500kW) TECDs by the means of high-resolution three-dimensional computer simulations.

## 2.1 Studied Turbine Configurations

A number of community-sized TECDs are in use, notably the 300kW device, called HS300, installed by Andritz Hydro Hammerfest off-shore northern Norway [30], 250kW open-centre turbine by Open Hydro and 250kW turbine by Scotrenewables Tidal Power Ltd, called SR250, both installed in Fall of Warness off the island of Eday, Orkney Islands for purposes of testing [31], [32]. A device even smaller, the world's first community-owned tidal turbine of 30kW, called Nova-30, was deployed by Nova Innovation Ltd. in the Bluemull Sound in Shetland [33]. Despite the presented examples of isolated, community-sized devices, most of the planned tidal developments are large-scale turbine arrays. Marine Current Turbines Ltd, in partnership with RWE npower renewables, plan to install a 10MW array of seven twin rotor turbines in an area of 0.56km off the North West coast of Anglesey, Wales, in 2015 [34], [35]. Meygen Ltd. is going to deploy a large array of 1MW devices in the Inner Sound, Pentland Firth, Scotland [36]. An array of four AS1000 and four HS1000 turbines (both 1MW) in the sound of Islay is planned by ScottishPower Renewables [37].

From these examples it follows that the majority of TECDs will operate in arrays. The present study is focused on the wake of an isolated device to uncover the small-scale hydrodynamics of the rotor wake. This study indicates the importance of investigating near wake of TECDs and the value of expanding this research focus in future work on tidal arrays. A TECD positioned in an array is likely to experience the influence of the neighbouring wakes. This influence would depend on the mutual position of the rotors. In a simplified case of a number of

## 2.1 Studied Turbine Configurations

---

identical TECDs positioned so that their wakes extend down-stream in parallel, the effect of the neighbouring wakes on the TECD's wake could be captured by 'mirror' boundary conditions on appropriate walls of the computational domain shown in Fig. 2.7. Details of such boundary conditions are described in section 2.4.5. Sediment composition at turbine deployment locations can vary from sand banks to non-erodible bed rock (as described in section 3.1). The studied case of sediment erosion is concerned with a small, isolated 150kW device on an erodible bed, in a stream of 1-1.5m/s, in contrast with an array of large 1.5MW devices on non-erodible bed rock, in streams 2.5-4m/s.

The near-field effects of an isolated TECD on its surroundings, studied in this dissertation, do not necessarily indicate the large-scale impact of tidal arrays on the marine environment. Indeed, for example a local disruption of seabed morphology may level out over greater distances from the device. Moreover, small-scale changes in the flow observed within a few diameters down-stream of the rotor might have only a small influence on the flow some kilometres away from a tidal array. From the far-field perspective, the detailed knowledge of the wake of a TECD is likely to offer little insight into the changes in tidal range and speed due to a tidal array and its effects on the nearest coastline over a period of years.

The interactions of the flow and three types of TECDs are analysed in this dissertation, a horizontal axis tidal turbine (HATT), a vertical axis tidal turbine (VATT) and a cross-flow tidal turbine (CFTT), all community-sized, isolated devices. Geometry of these rotors is shown in Fig. 2.1, Fig. 2.2 and Fig. 2.3 and their parameters are presented in Tables 2.1 and 2.3 respectively.

The wake of the HATT was simulated for a range of positions above the seabed,  $z_{hub} = 1.01R - 2R$ . The 10 m diameter HATT is rated for 150kW power output in a stream of 2 m/s. Table 2.2 shows power output of the HATT in streams between 1 m/s and 5 m/s as well as the power output of the HATT, scaled between 10 m and 50 m diameter. The parameters of the HATT are presented in Table 2.1,

## 2.1 Studied Turbine Configurations

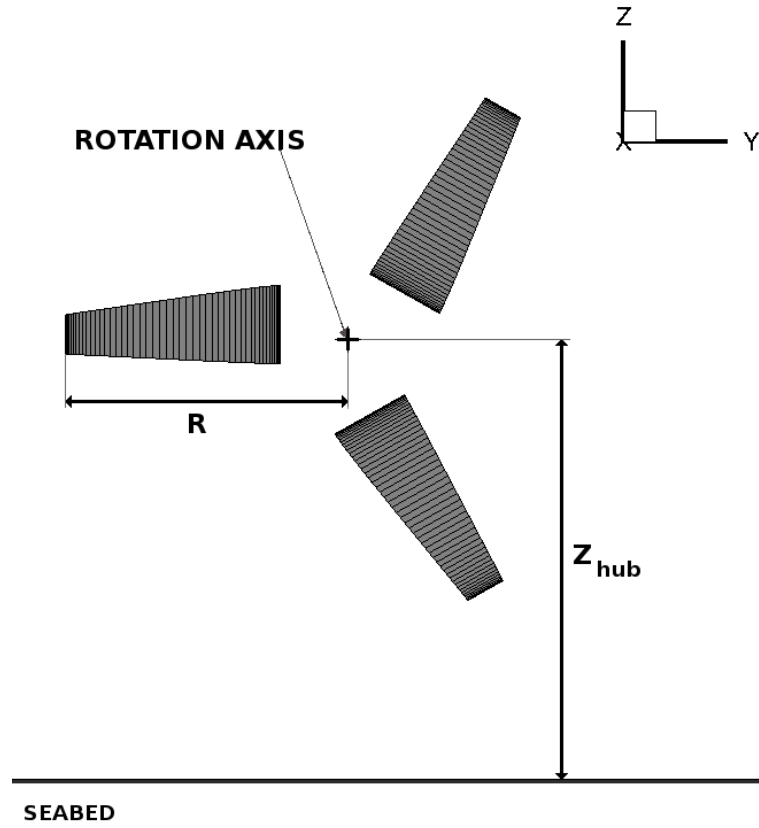


Figure 2.1: Position of the blades of the HATT in the coordinate system.

$R$ [m]	$N_b$	Aerofoil	AR
5	3	NACA0012	4.65

Table 2.1: Parameters of the HATT

## 2.1 Studied Turbine Configurations

---

where  $R$  is the rotor radius,  $N_b$  is the number of blades and  $AR = l^2/S$  is the aspect ratio of the blades.  $S$  is the surface area and  $l$  is the length of the blades, which have a twist of 18.58 degrees from root to tip.

$v_{hub}$ [m/s] \ $R$ [m]	5	10	15	20	25
1	0.019	0.076	0.172	0.306	0.478
2	0.153	0.612	1.376	2.447	3.823
3	0.516	2.065	4.645	8.258	12.904
4	1.224	4.894	11.011	19.575	30.586
5	2.390	9.558	21.506	38.233	59.739

Table 2.2: Variation of the HATT's power output with the flow speed at the rotor hub,  $v_{hub}$ , and the rotor radius,  $R$ . The values are presented in  $MW$ .

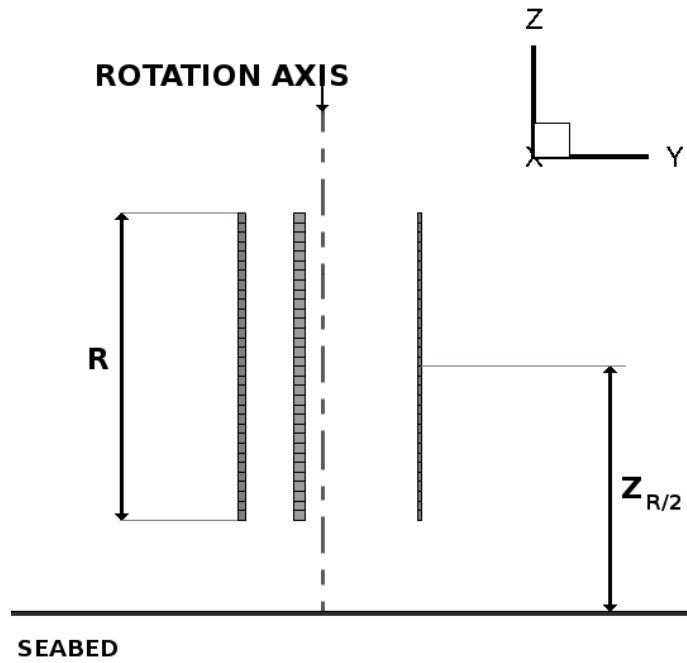


Figure 2.2: Position of the blades of the VATT in the coordinate system.

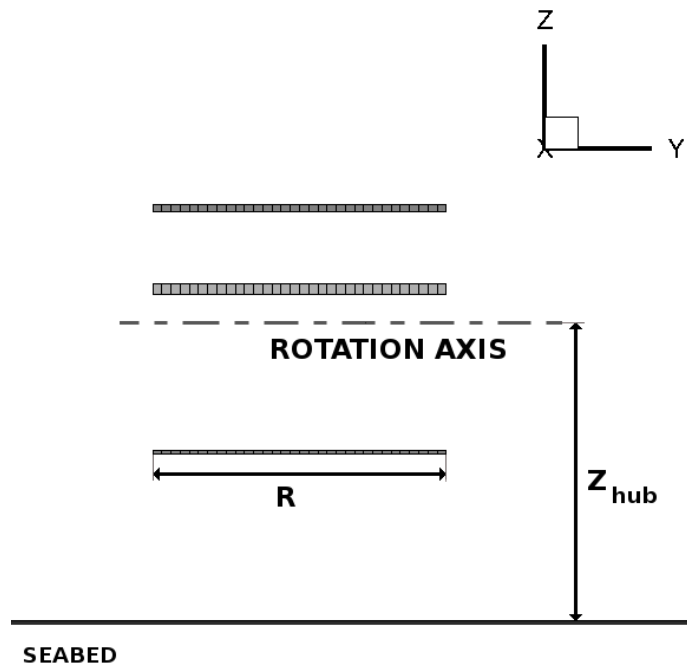


Figure 2.3: Position of the blades of the CFTT in the coordinate system.

$R_{VATT}$ [m]	$l_{VATT}$ [m]	$N_b$	Aerofoil	AR
1.65	5	3	NACA0015	25.85

Table 2.3: Parameters of the VATT and the CFTT.

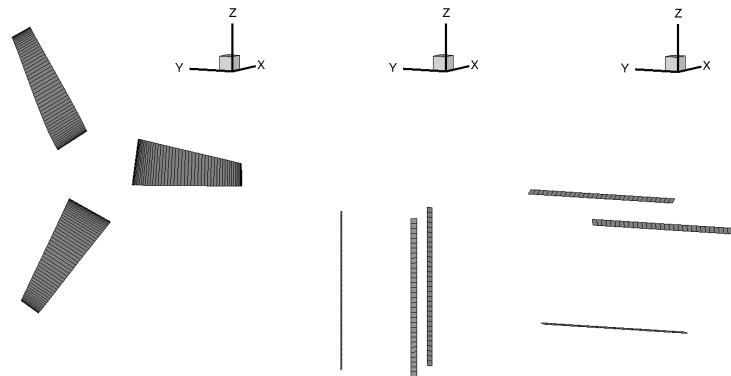


Figure 2.4: Scale comparison of the studied devices.

As indicated in Fig. 2.1 - Fig. 2.4, the present research has not included a sub-structure of the TECDs.

## 2.2 Wake of a TECD

The configuration of one of the modelled devices, a horizontal axis TECD, is illustrated in Fig. 2.5 for a uniform inflow and in Fig. 2.6 for a more realistic inflow condition.

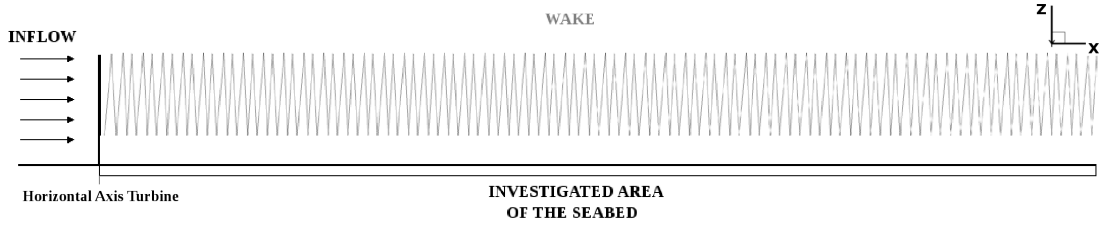


Figure 2.5: Schematic representation of the wake of a horizontal axis turbine in uniform flow

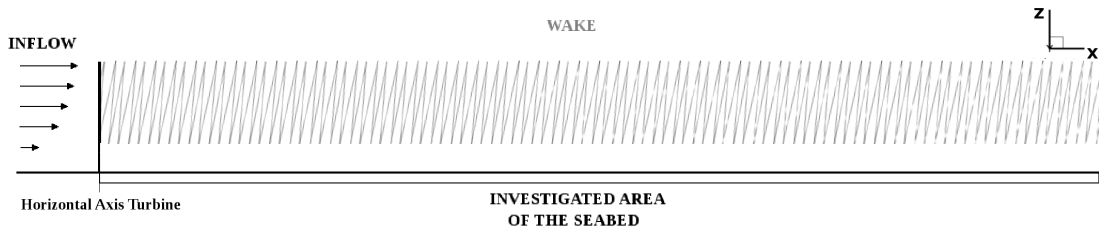


Figure 2.6: Schematic representation of the wake of a horizontal axis turbine for a non-uniform inflow model, where the inflow velocity increases with the height above the seabed

The flow enters the computational domain from the left in the schematic representations of the system shown in Fig. 2.5 and Fig. 2.6. The Cartesian coordinate system used throughout this dissertation was set so that the  $x$ -axis is aligned with the direction of the inflow and the  $z$ -axis with the height above the seabed, with positive sense upward. The water depth is assumed to be large enough so that surface effects can be omitted from consideration.

Fig. 2.7 shows the chosen computational domain. At the inlet boundary, the velocity and vorticity are prescribed. At the boundary faces 2) - 5) the condition of zero curvature of the induced vorticity is imposed. The top boundary is assumed not to be influenced by surface waves, i.e. no free-surface model is used in this study. The seabed boundary is modelled by the method of images - details are provided in section 2.4.5 - which ensures the velocity component normal to the seabed is zero. The boundary conditions employed are fully described in section 2.4.5.

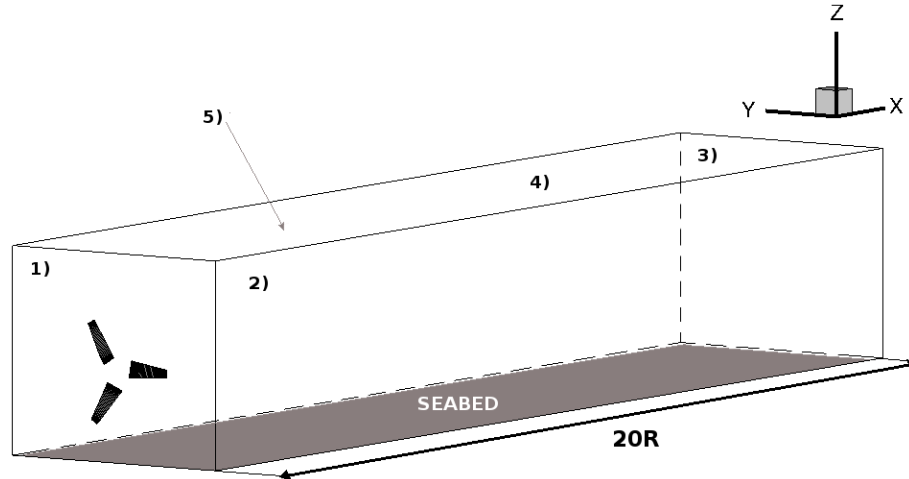


Figure 2.7: Computational domain with marked boundaries - 1) inlet; 2) right wall (from down-stream direction); 3) outlet; 4) left wall; 5) top.

This dissertation does not consider the influence of a supporting structure of TECDs on the seabed since the flow down-stream of static objects mounted on the seabed has been investigated previously in the research on the scouring around towers (monopiles) of wind turbines by Matutano et al. [17].

The effect of the presence of a turbine sub-structure depends on the geometry of the sub-structure. The research conducted previously on scour down-stream of wind turbine monopiles with circular cross-section has shown that the sediment around the monopile is eroded and transported away by the flow. Furthermore, the measured 'scour depth' is proportional to the monopile diameter,  $D_m$ , and reaches  $1.66D_m$  according to Matutano et al. [17]. A similar effect is to be expected to occur around foundations of TECDs. A simplified TECD foundation which consists of a circular monopile subjected to a realistic inflow would induce vorticity trailed down-stream. Such a wake of a monopile would inflict stress on the seabed and likely cause erosion around the monopile. In the present research these effects are assumed to be small in comparison with the influence of the rotor wake on the seabed. In this dissertation, the small-scale phenomena caused by the rotating blades of a TECD, which have not been investigated previously in such detail, are described.

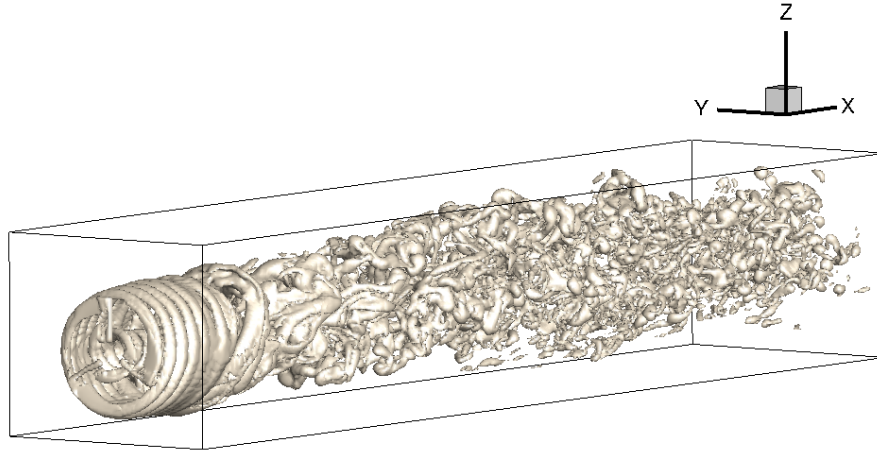


Figure 2.8: An iso-surface of rotor vorticity in the computational domain.

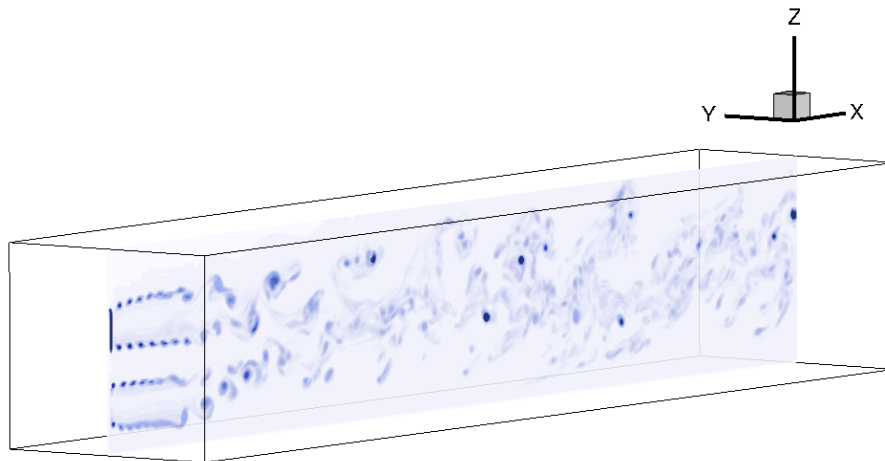


Figure 2.9: A section of rotor vorticity in the computational domain.

## 2.3 Vorticity Transport Model

The Vorticity Transport Model (VTM) was originally developed to study various conditions of helicopter flight. The VTM has been used and improved by many researchers over the past decade. Its numerous applications include studies of the Vortex Ring Phenomenon, helicopter noise, rotor-rotor interactions, helicopter

brownout and the aerodynamics of wind turbines [1, 38, 5, 3].

The above mentioned applications of the VTM have all been simulations of the high-Reynolds-number flow around a rotor in operation under the assumption that the fluid is incompressible. Seawater can be well approximated as an incompressible fluid, hence the flow around a TECD is governed by the same equations as the flow of air around a wind turbine. Moreover, the value of Reynolds number relevant to a wind turbine of 50 m diameter and wind speed of 10 m/s is less than three times greater than the Reynolds number for a tidal turbine of 10 m diameter subjected to an inflow of 2 m/s, since the kinematic viscosity of seawater is actually smaller than kinematic viscosity of air.

The VTM has been enhanced by the implementation of a number of specialized modules over the time of its development. The essential components of the model include an inner model, where the hydrodynamic loads on the blades are calculated, providing a source of vorticity, which feeds into an outer model that advances the vorticity field in time and space within a Computational Fluid Dynamics (CFD) framework.

The inner model used to calculate the source of vorticity is described in the following section together with the structural dynamics of the rotor. In section 2.3.2, the mathematical formulation of the equation which governs the evolution of the wake vorticity is presented, followed by section 2.3.3 with a description of the methodology employed to calculate the flow velocity down-stream of a TECD.

### 2.3.1 Rotor Model

The motion of the blades in the flow generates a reaction, simulated by the inner model in the VTM. At the start of the simulation, a vortex appears, ‘bound’ to each blade of the rotor. The fluid cannot penetrate the blade, which presents a barrier to the flow, thus the local flow velocity  $\mathbf{u}_b$  has zero normal component. The vorticity source,

$$S_\omega = -\frac{d\omega_b}{dt} + \mathbf{u}_b \nabla \cdot \omega_b, \quad (2.1)$$

consists of the temporal and the spatial variation of the bound vorticity  $\omega_b$ .

The model of the blade hydrodynamics in the VTM is based upon a modified Weissinger-L lifting line method. Each blade of the rotor is represented by a

## 2.3 Vorticity Transport Model

set of panels with collocation points placed at the three quarter chord location on the blade as shown in Fig. 2.10. The local flow velocity  $\mathbf{u}_b$  consists of the free-stream velocity, the structural motion of the panel and the wake induced velocity. The condition of zero flow through the blade at the collocation point yields an equation for the strength of the bound vortex. The vortex is attached to each of the panels at the one quarter chord location. The resulting discrete representation of the source of vorticity then detaches at the separation line and is convected as a sheet by the local flow. The sheet of vorticity is convected within the dynamic grid of the inner model, depicted in Fig. 2.10. The vortex structures in the grid of the inner model are then interpolated to the grid of the outer model as described in Line [1].

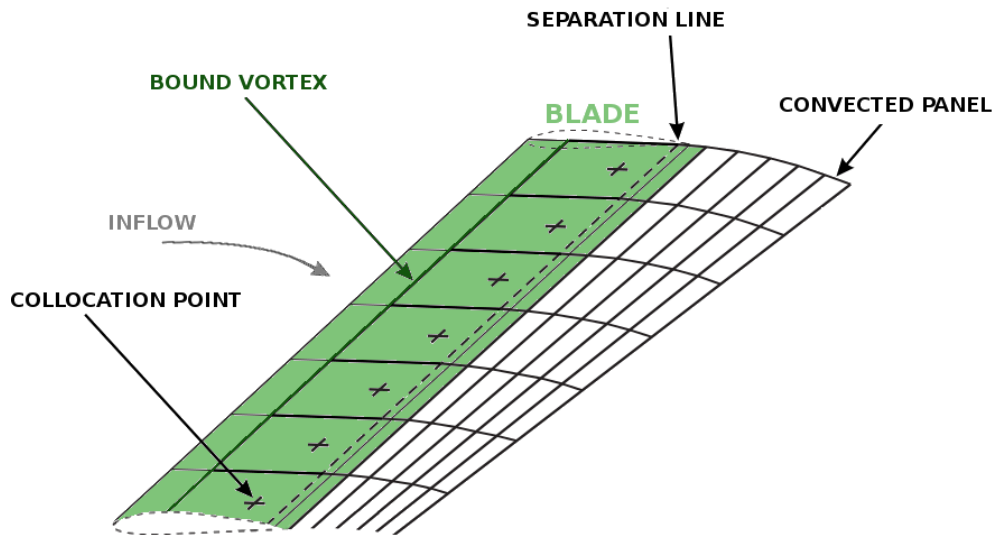


Figure 2.10: Schematic representation of the inner model

According to the Lifting-line theory, the approximation of the blades as a set of two-dimensional panels allows the lift on the panels to be determined from the velocity induced by the vortical wake and the variation of the angle of attack along the blades. In the VTM, the described approach was complemented to account for real blade loading by modification of the strength of the bound vorticity using an alternative lift coefficient, obtained either from aerofoil look-up tables

## 2.3 Vorticity Transport Model

---

of experimental values measured statically in a wind tunnel (to allow arbitrary aerofoils) or by a dynamic stall model.

The angle between the rotational velocity of the blades of a vertical axis turbine and the inflow velocity is continuously changing. Hence, the task of the calculation of the blade loading is more complicated than in the case of a horizontal axis turbine. In order to study the dynamics of the wake of vertical axis wind turbines a model of **dynamic stall** was implemented into the version of the VTM, described in Scheurich [3].

A semi-empirical model of dynamic stall, called the Leishman-Beddoes-type dynamic stall model, was incorporated into the Weissinger-L lifting-line method described earlier. In the Leishman-Beddoes-type dynamic stall model, the lift and drag coefficients are calculated and subsequently used within the blade model to simulate blade loading more accurately than can be obtained using the static aerofoil data alone. The blade loading model enhanced by the model of dynamic stall was validated by comparison of the simulated blade loading with experimental measurements of dynamic stall for wind turbines [3]. The version of the VTM adapted to model dynamic stall predicts well the blade loading of a vertical-axis turbine, and is thus an appropriate tool for the investigation of hydrodynamics of a vertical axis tidal turbine (VATT), whenever the tidal flow can be categorized by a Reynolds number similar to the typical values for wind turbines.

The dynamic stall model used in the VTM relies on the availability of relevant experimental data. In principle, however, the model could be generalised to arbitrary aerofoils if the data were available. At present, the semi-empirical model is based on the experimental data for the NACA0015 aerofoil [3].

The VTM employs a simplified representation of the rotor system in order to limit the computational cost of the simulations. Reducing the computational cost of the rotor model enables the allocation of the computer resources to the high-resolution simulation of the flow through the rotor and further down-stream, and to resolving the small-scale flow phenomena needed in the present research.

A conventional rotor system is treated as a collection of rigid blades. The blades are allowed to move with respect to the rotor hub; and the motion is expressed in terms of lag, flap and feather angles. These three degrees of freedom

## 2.3 Vorticity Transport Model

---

together with the azimuth of the blade define the position of a blade. A generalised approach is chosen in the VTM to model the structural dynamics of the rotor, using Lagrangian Dynamics. The motion of the rotor system is determined by the evolution of quantities identified with the various degrees of freedom of the system. These quantities are regarded as generalised coordinates,  $q = q(q_j, t)$ ,  $j = 1 \dots s$ , and together with their time derivatives,  $\dot{q} = dq/dt$ , these fully define the structural dynamics of the rotor blades.

The Lagrangian function which summarizes the dynamics of the system at time  $t$  is defined as<sup>1</sup>

$$\mathcal{L}_D = \mathcal{T} - \mathcal{V} + \int_{t_0}^{t_0+t} \mathcal{D}_\sigma d\sigma \quad (2.2)$$

where

$$\mathcal{T}(q, \dot{q}) \quad \text{is kinetic energy of the blades,} \quad (2.3)$$

$$\mathcal{V}(q, \dot{q}) \quad \text{is potential energy} \quad (2.4)$$

and

$$\mathcal{D}_t(q, \dot{q}) \quad \text{is the rate of dissipation.} \quad (2.5)$$

Hamilton's principle of stationary action, sometimes referred to as the 'Principle of Least Action',

$$\delta \left( \int_{t_0}^{t_0+\Delta t} \mathcal{L}_D - \mathcal{W} d\sigma \right) = 0 \quad (2.6)$$

determines the evolution of the system, where  $\delta$  denotes the variation with respect to the trajectory of the system through the space defined by  $(q, \dot{q})$ . The symbol  $\mathcal{W}$  denotes the work done by the external generalised forces  $\mathcal{Q}$  on the system. In the context of the rotor of a turbine,  $\mathcal{Q}$  represents the fluid forces on the blades. The substitution of Eq. 2.2 into Eq. 2.6 yields the Euler-Lagrange equations of the rotor system

$$\frac{d}{dt} \left( \frac{\partial \mathcal{L}_D}{\partial \dot{q}} \right) - \frac{\partial \mathcal{L}_D}{\partial q} = \mathcal{Q}. \quad (2.7)$$

---

<sup>1</sup>The subscript  $D$  emphasises the inclusion of dissipation into the Lagrangian function

The total time derivative in Eq. 2.7 can be expanded to give

$$\frac{\partial^2 \mathcal{L}_D}{\partial \dot{q}_i \partial \dot{q}_j} \ddot{q}_j + \frac{\partial^2 \mathcal{L}_D}{\partial \dot{q}_i \partial q_j} \dot{q}_j - \frac{\partial \mathcal{L}_D}{\partial q_j} = Q. \quad (2.8)$$

After evaluating all the derivatives, this can be solved directly for the accelerations  $\ddot{q}$ . The generalised coordinates at the next time step can then be approximated as

$$q^{n+1} = q^n + \dot{q}^n \Delta t \quad (2.9)$$

$$\dot{q}^{n+1} = \dot{q}^n + \ddot{q}^n \Delta t \quad (2.10)$$

using Euler integration.

The Lagrangian approach is chosen for its generality. The Lagrangian formulation of the structural dynamics of the rotor system makes it very easy to accommodate changes in the mechanical design of the system by a straightforward modification of the generalised coordinates and the associated energy functions.

### 2.3.2 Governing Equations

Once the source of vorticity is evaluated by the rotor model and interpolated into the outer grid of the VTM, the vorticity field is transported down-stream by the fluid. The motion of a Newtonian, incompressible fluid around the rotor is governed by the Navier-Stokes equations

$$\frac{\partial \mathbf{v}}{\partial t} + (\mathbf{v} \cdot \nabla) \mathbf{v} = -\frac{\nabla p}{\rho} + \nu \nabla^2 \mathbf{v} \quad (2.11)$$

$$\nabla \cdot \mathbf{v} = 0, \quad (2.12)$$

where  $\mathbf{v}$  is the velocity of the flow and  $p$  is the pressure. By taking the curl of Eq. 2.11 the pressure term disappears. The resulting Vorticity Transport Equation is

$$\frac{\partial \boldsymbol{\omega}}{\partial t} + (\mathbf{v} \cdot \nabla) \boldsymbol{\omega} - (\boldsymbol{\omega} \cdot \nabla) \mathbf{v} = \nu \nabla^2 \boldsymbol{\omega}, \quad (2.13)$$

where  $\boldsymbol{\omega}$  is the vorticity of the fluid.

The flow around the blades of the rotor of a TECD is dominated by inertial forces of the fluid rather than viscous forces. This observation can be expressed

## 2.3 Vorticity Transport Model

---

by a large Reynolds number. Since the Reynolds number depends on the characteristic length of the system and the characteristic flow velocity, the value relevant to a particular TECD relates to the size of the device as well as the velocity of the flow. Since the velocities characteristic for the flow near the rotor blades are typically smaller than the inflow velocity, the local Reynolds number is smaller than the Reynolds number of the inflow. The flow through the rotor of a TECD can thus be modelled using the high-Reynolds number approximation. Here, the flow is assumed to be inviscid everywhere except at the rotor blades, where the effect of the local viscous forces is modelled by the inclusion of the source of vorticity  $S_\omega$  into Eq. 2.13.

In this formulation of the equations of the fluid motion, the vorticity and velocity fields are coupled by the definition of vorticity,  $\omega = \nabla \times \mathbf{v}$ . This coupling and the vector identity

$$\nabla \times (\nabla \times \mathbf{v}) = \nabla(\nabla \cdot \mathbf{v}) - \nabla^2 \mathbf{v} \quad (2.14)$$

justifies using the Poisson equation

$$\nabla^2 \mathbf{v}_r = -\nabla \times \omega \quad (2.15)$$

to obtain the rotational part of the velocity field,  $\mathbf{v}_r$ , since the fluid is considered to be incompressible (i.e. the velocity field is solenoidal).

The velocity field can, however, comprise an irrotational component as well as the rotational one, according to the Helmholtz decomposition theorem [39]. The velocity of the flow is then composed of the rotational velocity and the gradient of a scalar harmonic function <sup>1</sup>

$$\mathbf{v} = \mathbf{v}_r + \nabla \phi. \quad (2.16)$$

The scalar field  $\phi$  is sometimes called a velocity potential. When a rotor is exposed to an inflow that does not vary in space, the irrotational part of the velocity field, represented by  $\nabla \phi$  in Eq. 2.16, equates to the velocity of the inflow.

---

<sup>1</sup> $\nabla^2 \phi = 0$

### 2.3.3 Velocity Calculation

In all previous applications of the VTM, the vorticity-velocity coupling, introduced in section 2.3.2, was considered for uniform inflow conditions. The original version of the VTM contained the boundary condition at the rotor plane in the form of a uniform inflow velocity. The irrotational part of the velocity field was then attributed to the uniform inflow velocity. In the original VTM, the velocity of the fluid passing through the rotor was assumed to be a composition of two independent components, the uniform free-stream velocity,  $\mathbf{v}_{fs}$ , and the rotor induced (rotational) velocity,  $\mathbf{v}_r$ , that was obtained as solution of

$$\nabla^2 \mathbf{v}_r = -\nabla \times \omega. \quad (2.17)$$

The velocity used to transport the vorticity field in Eq. 2.13 was the total velocity,  $\mathbf{v} = \mathbf{v}_r + \mathbf{v}_{fs}$ .

The outer model of the VTM performs the calculation of the coupled quantities,  $\omega$  and  $\mathbf{v}_r$ , every time step. The primary quantity to be obtained is the vorticity field as a solution of Eq. 2.13. The rotor induced velocity is then determined from Eq. 2.17. The solution of Eq. 2.17 has the form of the Biot-Savart law

$$\mathbf{v}_r(\mathbf{x}) = -\frac{1}{4\pi} \int_{supp(\omega)} \frac{(\mathbf{x} - \mathbf{x}') \times \omega(\mathbf{x}')}{|\mathbf{x} - \mathbf{x}'|^3} \mathbf{d}\mathbf{x}'. \quad (2.18)$$

In order to avoid the singularity at  $\mathbf{x} = \mathbf{x}'$ , the Rosenhead-Moore regularisation is applied in the numerical evaluation of Eq. 2.18 by addition of an artificial parameter  $\delta$  (for details see [40] and [41]).

In the VTM the support of the vorticity field,  $supp(\omega)$ , is composed of  $N_\Omega$  computational cells of a predefined volume  $V_i$ , for  $i = 1 \dots N_\Omega$ . Then the integral in Eq. 2.18 can be written as a sum of integrals, each calculating the contribution of an individual cell to the velocity field at  $\mathbf{x}$ . The regularised version of Eq. 2.18 then becomes

$$\mathbf{v}_r(\mathbf{x}) = \sum_{i=1}^{N_\Omega} \int_{V_i} K_\delta(\mathbf{x}, \mathbf{x}') \times \omega(\mathbf{x}') \mathbf{d}\mathbf{x}' \quad (2.19)$$

where

$$K_\delta(\mathbf{x}, \mathbf{x}') = -\frac{1}{4\pi} \frac{(\mathbf{x} - \mathbf{x}')}{(|\mathbf{x} - \mathbf{x}'|^2 + \delta^2)^{3/2}}. \quad (2.20)$$

## 2.3 Vorticity Transport Model

---

Each of the individual integrals is then approximated by evaluating the integrand at the centre of the computational cell,  $\mathbf{c}_i$ . The integral of vorticity over one cell is represented simply by  $\omega(\mathbf{c}_i)V_i$  since the distribution of vorticity within the cell is assumed to be uniform. The contribution to the total velocity at the point  $\mathbf{x}$  by the vorticity in cell  $i$  is

$$(\Delta \mathbf{v}_i)(\mathbf{x}) \approx K_\delta(\mathbf{x}, \mathbf{c}_i) \times [\omega]_i. \quad (2.21)$$

where  $[\omega]_i = \omega(\mathbf{c}_i)V_i$ . The rotor induced velocity field is then calculated as the sum of the contributions of all individual cells in the computational domain.

$$\mathbf{v}_r = \sum_{i=1}^{N_\Omega} (\Delta \mathbf{v}_i). \quad (2.22)$$

The computational cost of the direct summation in Eq. 2.22 would be very high since the corresponding algorithm would contain  $N_\Omega^2$  ‘cell-cell’ interactions, whereby each cell interacts with every other cell in the domain. The routines based on the Fast Multipole Method, implemented into the VTM by A. J. Line [1], replace some of the cell-cell interactions by a smaller number of cell-cluster and cluster-cluster interactions, thus reducing the computational cost of the velocity calculation. A cluster is a group of neighbouring cells containing vorticity.

### 2.3.4 Discretization of the Governing Equations

The vorticity transport equation Eq. 2.13 is solved numerically in a finite volume formulation. The computational domain is partitioned into a finite number of identical discrete cubes known as computational cells. The distribution of vorticity within each computational cell is assumed to be uniform. As well as the vorticity, the local velocity field is recorded for each cell. The vorticity and the velocity in neighbouring cells are also recorded for each cell. The management of the grid is described in section 2.3.7. The overall vorticity is preserved in the velocity-vorticity formulation. Numerical diffusion can, however, reduce the compactness of the vortical structures by smoothing the vorticity distribution. The effects of numerical diffusion are minimised by the Total Variation Diminishing (TVD) numerical scheme used in the VTM. The evolution of the velocity and

## 2.3 Vorticity Transport Model

---

vorticity through time is discretized into time steps or intervals of length  $\Delta t$ . The vorticity transport equation becomes

$$[\omega]^{n+1} - [\omega]^n = \int_n^{n+1} \{[(\omega \cdot \nabla)\mathbf{v}]^n - [(\mathbf{v} \cdot \nabla)\omega]^n + [S_\omega]^n\} dt, \quad (2.23)$$

where the operator  $[\cdot]^n$  denotes integration over a cell with volume  $V$  at the  $n$ -th time step  $n\Delta t$ . The integral on the right hand side of Eq. 2.23 can be split into three terms, each contributing to  $\Delta^n[\omega] = [\omega]^{n+1} - [\omega]^n$ . The relation Eq. 2.23 is used to obtain the vorticity at time step  $n + 1$ . First, the velocity field  $\mathbf{v}^n = \mathbf{v}(\omega^n)$  is evaluated as a superposition of the free-stream and rotor induced velocity, obtained from Eq. 2.22. Then, the three terms can be dealt with separately, using the operator splitting approach. The vorticity field at time  $(n + 1)\Delta t$  is constructed in three consecutive steps, here denoted symbolically as  $n + 1/3$ ,  $n + 2/3$  and  $n + 3/3$

$$[\omega]^{n+1/3} = [\omega]^n + \Delta^n[\omega]_{source} \quad (2.24)$$

$$[\omega]^{n+2/3} = [\omega]^{n+1/3} + \Delta^n[\omega]_{stretch} \quad (2.25)$$

$$[\omega]^{n+3/3} = [\omega]^{n+2/3} - \Delta^n[\omega]_{advect} \quad (2.26)$$

where

$$\Delta^n[\omega]_{source} = \int_n^{n+1} [S_\omega]^n dt \quad (2.27)$$

$$\Delta^n[\omega]_{stretch} = \int_n^{n+1} [(\omega \cdot \nabla)\mathbf{v}]^n dt \quad (2.28)$$

$$\Delta^n[\omega]_{advect} = \int_n^{n+1} [(\mathbf{v} \cdot \nabla)\omega]^n dt \quad (2.29)$$

The source of vorticity is calculated from the blade loading in the rotor model, as explained in section 2.3.1. The second term, Eq. 2.28, called the stretching operator is evaluated by Runge-Kutta integration. The third term, Eq. 2.29, the advection operator, is evaluated by the Weighted Average Flux (WAF) scheme, devised originally to resolve hyperbolic conservation laws [42]. The three-dimensional WAF scheme used in the VTM is described in detail in the following section.

### 2.3.5 Advection Scheme

The Weighted Average Flux scheme was developed to resolve shock waves in a compressible gas [43]. Consequently, the scheme was primarily used for hyperbolic conservation laws in one dimension. Its ability to resolve flow near abrupt changes in the quantities which represent the characteristics of the fluid makes it an appropriate tool to calculate potentially steep vorticity gradients within the rotor wake. The non-linear advection equation

$$\frac{\partial \omega}{\partial t} + (\mathbf{v} \cdot \nabla) \omega = 0 \quad (2.30)$$

is solved in the last of the three steps, Eq. 2.29. The change of the vorticity in cell  $i$  between the  $n$ -th and  $(n + 1)$ -th time step is determined by the vorticity flux from cell  $i - 1$  to  $i$ , denoted as  $F_{i-1/2}$ , and the vorticity flux from cell  $i$  to  $i + 1$ , denoted as  $F_{i+1/2}$ .

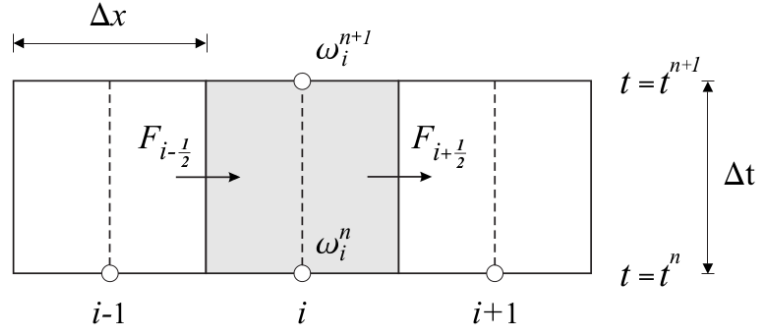


Figure 2.11: Schematic representation of the intercell vorticity fluxes, figure taken from [1]

The change of  $[\omega_i]$  in the  $n$ -th time step is

$$\Delta^n [\omega_i] = -\frac{\Delta t}{\Delta x} (F_{i+1/2} - F_{i-1/2}), \quad (2.31)$$

where  $\Delta^n [\omega_i] = [\omega_i]^{n+1} - [\omega_i]^n$ . The WAF scheme evaluates the vorticity flux as

$$F_{i+1/2} = \frac{1}{2} \left( (1 + \lambda\mu) \mathbf{v}_{i+1/2} [\omega_i]^n + (1 - \lambda\mu) \mathbf{v}_{i+1/2} [\omega_{i+1}]^n \right) \quad (2.32)$$

## 2.3 Vorticity Transport Model

---

where  $\mathbf{v}_{i+1/2}$  is the velocity at the cell face between cells  $i$  and  $i + 1$ , and

$$\mu = \mathbf{v}_{i+1/2} \frac{\Delta t}{\Delta x} \quad (2.33)$$

is the Courant-Friedrich-Lewy (CFL) number.  $\lambda$  is a wave amplifier function which depends on CFL number and the vorticity distribution ratio

$$r_{i+1/2}^n = \frac{[\omega_i]^n - [\omega_{i-1}]^n}{[\omega_{i+1}]^n - [\omega_i]^n}. \quad (2.34)$$

The calculation of vorticity from the intercell vorticity fluxes is illustrated by Fig. 2.11 taken from [1].

Unlike first order linear schemes, the second-order WAF scheme is prone to non-physical oscillations in areas where the difference between vorticity in neighbouring cells is large. To ensure that monotonicity of the solution is preserved, the chosen scheme has to be Total Variation Diminishing. The total variation of the vorticity field at time step  $n$  is defined as [44]

$$TV^n(\omega) = \int_{-\infty}^{+\infty} \left| \frac{\partial \omega}{\partial x} \right| dx, \quad (2.35)$$

which in discretized form becomes

$$TV^n(\omega) = \sum_{i \in \Omega} |[\omega_{i+1}]^n - [\omega_i]^n|, \quad (2.36)$$

where  $\Omega$  denotes the computational domain. The condition for the scheme to be TVD is then expressed as

$$TV^{n+1}(\omega) \leq TV^n(\omega) \quad (2.37)$$

The wave amplifier functions used in the VTM are based on the SUPERA wave amplifier introduced by Toro in [43] to ensure that the advection scheme of the VTM satisfies the condition 2.37.

The one-dimensional WAF scheme is then applied to the three dimensional problem approached as three one-dimensional problems, as described in [45], ensuring the resulting routine still qualifies as a TVD scheme. The condition of stability of the explicit WAF numerical scheme described in section 2.3.5 is expressed in terms of the local flow velocity, cell size and time step as

$$\left| \mathbf{v} \frac{\Delta t}{\Delta x} \right| \leq 1 \quad (2.38)$$

and is called the Courant-Friedrichs-Lewy (CFL) condition.

### 2.3.6 Adaptive Computational Grid

An adaptive meshing system was implemented into the VTM by A.J Line and R.E. Brown in order to study high-frequency dynamics of the wake of a helicopter [1]. An auxiliary structured grid was used in the rotor model described in section 2.3.1 to calculate the source of vorticity on the rotor blades, given by Eq. 2.1. The wake vorticity was then transferred to an adaptive grid, sometimes referred to as ‘Semi-Lagrangian’, where only the cells with vorticity were present. In the adaptive grid, the evolution of the vorticity field further from the rotor led to creation of new computational cells while cells, which no longer contained vorticity, were erased from computer memory. This resulted in a computational grid which required an update every time step. The adaptive management of the grid had advantages when employed to investigate the high-frequency dynamics of helicopter flight, for example when the geometry of the wake vorticity field could not be envisioned prior to the simulation. The adaptive grid enabled the wake of the rotor to grow arbitrarily in space and thus eliminated the need for boundary conditions on the vorticity field. In order to prevent exhaustion of the memory of a computer by the ever expanding computational grid, a limit is set in the VTM for the maximal number of cells. The details of the adaptive grid system used previously in the VTM are presented in [1].

The effectiveness of the computation was improved by an adaptation of the grid resolution. The VTM includes the option of up to four sizes of grid cells to be created. This allows the vorticity close to the rotor to be resolved in greater detail and the resolution to be reduced further from the rotor. The original application of the VTM, i.e. to study the wake of a helicopter, motivated this grid feature, since the area of interest of the previous application was, indeed, close to the rotor. For the investigation of the interactions between the wake of a TECD and the seabed, which includes small-scale phenomena further from the rotor, the decreasing resolution of the computational grid with the distance down-stream of the rotor is rather undesirable. Fortunately, the original VTM offers the option of a uniform, ‘isotropic’, grid geometry as well. The isotropic grid consists of more cells than a grid with decreasing resolution. As a result, the investigation of the

small-scale flow phenomena imposes higher demands on computer resources than the previous applications of the VTM.

### 2.3.7 Octree Data Storage

For each cell within the grid described in 2.3.6, the vorticity in the centre of the cell, the local velocity on the surfaces of the cell (for easier calculation of the advection) and the information about the neighbouring cells has to be stored. The grid of the VTM is handled as an octree data structure with all the connections realized by pointers. In the base level of the structure, each cell is connected to its six immediate neighbours and to its parent cluster. The next level is composed of the parent clusters, each parent having at most eight children. The structure of an octree data storage is illustrated in Fig. 2.12 from [1].

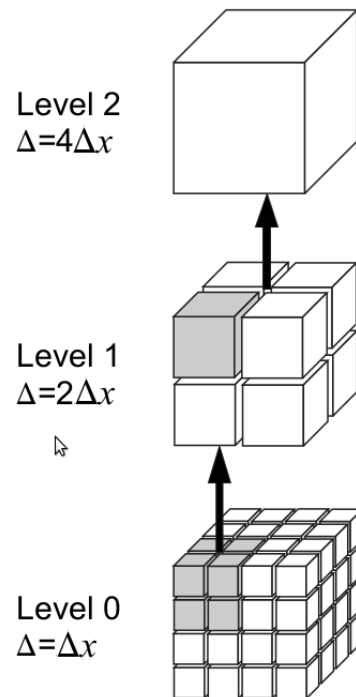


Figure 2.12: Schematic representation of an octree grid structure, figure taken from [1]

Each of the parent clusters is linked to its neighbours, its children and its

parent. The levelling up continues until the whole computational domain is embedded in one large cluster. This organization of the grid proved to be convenient in conjunction with the adaptive nature of the grid as the cells and clusters do not always have eight children, but rather less, depending on the local geometry of the vorticity field. The octree structure of the grid is well suited for the use of the fast multipole method for the calculation of the rotor induced velocity.

### 2.3.8 Fast Multipole Method

This section explains how the rotor induced velocity is calculated in the VTM. In section 2.3.3, the velocity produced by the rotor at the point  $\mathbf{x}$  is approximated as

$$\mathbf{v}(\mathbf{x}) \approx \sum_{i=1}^{N_\Omega} K_\delta(\mathbf{x}, \mathbf{c}_i) \times [\omega]_i. \quad (2.39)$$

In order to evaluate the velocity Eq. 2.39 it is necessary to calculate the sum of the contributions from all the cells in the computational domain. If that was to be done for  $j = 1 \dots N_\Omega$ , then the computational cost of such a routine would be of order  $N_\Omega^2$ . In other words, there would be  $N_\Omega^2$  cell-cell interactions. In the VTM, a less computationally expensive, but approximate approach is chosen. The Fast Multipole Method (FMM), introduced in [46], is employed to evaluate the rotor induced velocity. The FMM takes advantage of the octree structure that is imposed on the grid as described in section 2.3.7 and reduces the computational cost by replacing a portion of the cell-cell interactions with a smaller number of cell-cluster and cluster-cluster interactions. A cluster is defined as a group of neighbouring cells in the adaptive grid (details of the nature of the computational grid are presented in section 2.3.6), i.e. region  $\tau \subset \Omega$ . The contribution of the vorticity contained in the cluster to the velocity field at point  $\mathbf{x}$  is

$$\Delta \mathbf{v}_\tau \approx \sum_{i=1}^{N_\tau} K_\delta(\mathbf{x}, \mathbf{c}_i) \times [\omega]_i. \quad (2.40)$$

The Rosenhead-Moore kernel,  $K_\delta$ , is expanded into its Taylor series around the centre of the cluster,  $\mathbf{c}_\tau$ , as follows

$$K_\delta(\mathbf{x}, \mathbf{c}_i) = \sum_{l=0}^{\infty} \frac{1}{l!} D_c^l K_\delta(\mathbf{x}, \mathbf{c}_\tau) (\mathbf{c}_i - \mathbf{c}_\tau)^l. \quad (2.41)$$

## 2.3 Vorticity Transport Model

---

The expansion is three-dimensional, so the index of each term is a vector  $\mathbf{l} = (l_1, l_2, l_3)$ , with the factorial  $\mathbf{l}! = l_1!l_2!l_3!$ . The differential operator is defined as

$$D_c^{\mathbf{l}} = \frac{\partial}{\partial c_1^{l_1} \partial c_2^{l_2} \partial c_3^{l_3}} \quad (2.42)$$

and  $\mathbf{c}^{\mathbf{l}}$  stands for  $c_1^{l_1} c_2^{l_2} c_3^{l_3}$ . A further approximation to the contribution of the cluster to the velocity field is then made by truncating the Taylor expansion after the  $\mathbf{p}$ 'th term. This can be written as

$$\Delta \mathbf{v}_\tau(\mathbf{x}) \approx \sum_{l=0}^{\mathbf{p}} \mathbf{a}_l(\mathbf{x}, \mathbf{c}_\tau) \times \mathbf{m}_l(\tau), \quad (2.43)$$

where

$$\mathbf{a}_l(\mathbf{x}, \mathbf{c}_\tau) = \frac{1}{\mathbf{l}!} D_c^{\mathbf{l}} K_\delta(\mathbf{x}, \mathbf{c}_\tau) \quad (2.44)$$

are tensors of the Taylor series and

$$\mathbf{m}_l(\tau) = \sum_{i=1}^{N_\tau} (\mathbf{c}_i - \mathbf{c}_\tau)^l [\omega]_i \quad (2.45)$$

are moments of vorticity. The task of the calculation of the cluster velocity is divided into two independent parts, namely, the calculation of the tensors and the moments. The tensors represent the effect of the distance between the cluster and the point  $\mathbf{x}$  where the velocity contribution  $\Delta \mathbf{v}_\tau(\mathbf{x})$  is evaluated. The moments, on the other hand, express the distribution of vorticity internal to the cluster and are independent of the interaction distance. It is possible to write the moments of a cluster recursively as a binomial sum of the moments of its children, for details see Line [1]. Replacing the evaluation of  $N_\Omega^2$  cell-cell interactions with the calculation of the moments of large clusters allows the cost of the velocity calculation to be reduced.

Whether the velocity at point  $\mathbf{x}$  can be approximated by a truncated multipole series or not depends on the distance between the point  $\mathbf{x}$  and centre of the clusters,  $\mathbf{c}_\tau$ . An estimate of the truncation error of the approximation is, according to Krasny and Lindsay [47]

$$\epsilon_{\mathbf{p}} = \max_{i=1,2,3} \left( \frac{(p_i + 1)^2 d_\tau^{p_i} |\mathbf{m}_0(\tau)|}{4\pi(|\mathbf{x} - \mathbf{c}_\tau|^2 + \delta^2)^{p_i/2+1}} \right). \quad (2.46)$$

The Multipole Acceptance Criterion, based upon the error measure given by Eq. 2.46, is used in the VTM to decide if the loss of accuracy resulting from the approximation Eq. 2.43 is acceptable. The required level of accuracy of the expression Eq. 2.43 is specified by a maximum acceptable error and the maximal truncation order  $\mathbf{p}_{max}$  is chosen accordingly. Equation Eq. 2.46 is used to find such a  $\mathbf{p}$  for which the error is below  $\epsilon_{max}$ . If no such  $\mathbf{p}$  is found then the interaction is not considered *well separated* [1].

The cost of the velocity calculation is further reduced by introducing so called cluster-cluster interactions. When the velocity at the point  $\mathbf{x}$  is evaluated using Eq. 2.43, the velocity in the ‘sibling’-cells (the cells which share their parent cluster) can be approximated locally as

$$\Delta\mathbf{v}(\mathbf{x}_s) \approx \Delta\mathbf{v}(\mathbf{x}) + \sum_{l=1}^p \frac{1}{l!} D_s^l \mathbf{v}(\mathbf{x})(\mathbf{x}_s - \mathbf{x})^l \quad (2.47)$$

where  $\mathbf{x}_s$  denotes the position of a sibling cell.

In the VTM, two routines to evaluate the rotor induced velocity are implemented. Both make use of the same theory described earlier in this section. The first routine calculates velocity in the adaptive computational grid (described in section 2.3.6). This routine benefits from the interactions between clusters of cells. The information about the interactions which involve a cluster is summarized in the cluster’s interaction list. The interaction list is based on the decomposition of the grid into three parts - near, intermediate and far-field. The near-field contains the nearest neighbours of  $i$ . The intermediate field contains all of the children of the nearest neighbours of  $i$ ’s parent (see section 2.3.7 for details about the grid structure), except those that are already accounted for in the near-field. The far-field is defined as the whole computational grid excluding the near and the intermediate fields. The interaction list of cluster  $i$  is then defined as all of the clusters in the intermediate field of  $i$ .

In the first stage of the calculation the moments of every cluster in the octree (described in section 2.3.7) are calculated, starting with the parents of the computational cells, in an upward sweep. Note that the moment of cell  $i$  is equal to  $[\omega_i]$ . In the second stage, the interaction lists of the clusters are used to chose the relevant moments to evaluate the velocity field in every cell of the grid in a sweep

down through the levels of the grid starting at the root cluster which encapsulates the whole grid. Both the far-field and the intermediate-field components of the velocity field of the root cluster and its children are by definition zero. When the far-field component of the velocity of a cluster  $i$  is known, its intermediate-field velocity component is evaluated from cluster-cluster interactions with clusters given by  $i$ 's interaction list. The sum of  $i$ 's far-field and intermediate-field components of the velocity field are then stored as far-field components of the child clusters of  $i$ . The same process is repeated, descending down the octree, until the lowest level, inhabited by the computational cells, is reached. The process is completed by evaluating the contribution of the intermediate and near-fields of each cell as cell-cluster interactions. The described decomposition is illustrated in Fig. 2.13.

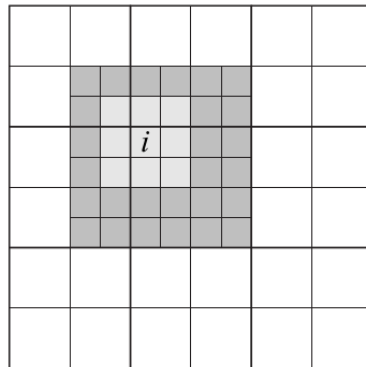


Figure 2.13: Decomposition of the vorticity field into the far field (white), intermediate field (dark grey), near field (light grey) of cluster  $i$ , figure taken from [1]

The advantage of the described algorithm is that in the second stage, the velocity in the whole computational domain ( $N_\Omega$  cells) can be evaluated simultaneously thus reducing the computational cost to  $\mathcal{O}(N_\Omega)$ .

The velocity field cannot be calculated by the above described two-stage algorithm outside of the computational domain (i.e. where the vorticity induced by the rotor is zero), since the information provided by the interaction lists of clusters is not available outside of the grid. In the VTM, an alternative two-stage routine has been used to evaluate the velocity where the interaction lists

## 2.3 Vorticity Transport Model

---

are undefined. The first stage of the alternative routine is the same as described above, i.e. the calculation of the moments of vorticity in an upward sweep. The difference between the two algorithms lies in the second stage - the sweep down through the levels of the grid. The alternative routine evaluates the velocity at the point  $\mathbf{x}$  as

$$\mathbf{v}(\mathbf{x}) \approx \sum_{\tau \in S_1} \mathbf{v}_\tau(\mathbf{x}) + \sum_{i \in S_2} \mathbf{v}_i(\mathbf{x}) \quad (2.48)$$

where the part of the computational domain, denoted  $S_1$ , contains all the well-separated clusters  $\tau$ . The velocity contribution of these clusters can be then approximated by cell-cluster interactions. In the domain  $S_2 = \Omega \setminus S_1$ , the velocity has to be calculated directly via cell-cell interactions. The velocity at any point other than  $\mathbf{x}$  can then be calculated by repeating the downward sweep. To calculate velocity using the alternative routine in a domain,  $\Phi$ , composed of  $N_\phi$  cells, the routine has to perform the downward sweep  $N_\phi$  times, thus a total of  $\mathcal{O}(N_\phi \log N_\phi)$  interactions must be evaluated [1]. Since the alternative routine is used only outside of the computational grid, the number  $N_\phi$  is several orders smaller than the number of the cells in the adaptive grid  $N_\Omega$ , the overall computational cost of the velocity calculation is thus relatively low, yet dependent on the extent of the domain  $\Phi$ .

The need to evaluate velocity outside of the computational grid arises when the loading on the blades is required for the calculation of the source of vorticity, given by Eq. 2.1 in section 2.3.1.

## 2.4 Tidal Flow Model

In all applications of the VTM prior to the present research, the inflow velocity,  $\mathbf{v}_{fs}$ , (sometimes referred to as the free-stream velocity) was a constant vector field

$$\mathbf{v}_{fs} = (V_{in}, 0, 0). \quad (2.49)$$

$$\frac{\partial V_{in}}{\partial x_i} = 0, \text{ for } i = 1, 2, 3. \quad (2.50)$$

Since the uniform inflow velocity is irrotational, i.e.

$$\nabla \times \mathbf{v}_{fs} = 0, \quad (2.51)$$

the vorticity in the uniform inflow is identically zero.

When a uniform flow is disturbed by a TECD the nature of the flow changes and the fluid is diverted around the blades of the TECD. The velocity of the flow is no longer irrotational, since the flow around each blade contains vorticity induced by the change in the flow velocity. The vorticity is then transported down-stream of the TECD by the flow. The important point is that the vorticity down-stream of a rotor, exposed to an uniform inflow, arises purely due to the presence of the device in the flow. Such vorticity is called rotor vorticity in this dissertation. The rotor vorticity induces a velocity  $\mathbf{v}_r$  which is, by definition, rotational. Under uniform inflow conditions, the induced velocity determines the flow through a TECD.

The assumption, that the rotor is the sole source of the vorticity in the flow, motivated the implementation of the adaptive computational grid (described in section 2.3.6) and the routines used for the calculation of the velocity field. This implementation made good sense when relatively large regions down-stream of the rotor were free of vorticity. The routines used to calculate the velocity field took advantage of the uniform nature of the inflow and treated the rotor induced velocity and the inflow velocity separately. As explained earlier, the velocity which transports the vorticity was calculated by an efficient grid-based routine, and to evaluate the velocity of the flow in regions with zero vorticity was computationally more expensive. The velocity outside of the adaptive grid was, however, originally needed only to evaluate the source of vorticity on the rotor blades, using

Eq. 2.1. Further need for velocity calculation close to the ground plane, generally located outside of the adaptive grid, had arisen in the research into helicopter brownout [5]. The increased computational cost indicated an inefficiency of the grid management and the grid-based velocity calculation routine for applications which required the knowledge of the velocity in areas without rotor vorticity.

The objective of the present research is to investigate various aspects of the flow through the rotor of a TECD. As the name suggests, the device is mounted on the seabed and subjected to a tidal flow. In the first approximation, the inflow is treated as uniform. The uniform inflow approximation has its limits, however. A number of research points, which are discussed in detail in section 1.2, need to be addressed by a more realistic inflow model to provide a reliable assessment of the environmental impact of a TECD on the seabed.

As will be shown in chapter 4, the results of the uniform inflow approach indicate that a more realistic model of the inflow would profoundly influence the simulation of the flow down-stream of the TECD. The uniform inflow condition used in chapter 4 is presented to show the sensitivity of results to the choice of inflow conditions. Real flows suitable for power extraction are generally varying with water depth.

The defining feature of the tidal flow is its variability in space, particularly near the seabed where the flow velocity decreases. In this section, the tidal flow over a flat seabed is assumed to vary only in the vertical direction. The approximation of the inflow that varies with water depth, but not laterally or longitudinally is called *a velocity profile* in this dissertation. To model even a simplified non-uniform inflow, the velocity profile, has required non-trivial modifications of the VTM.

In the following section 2.4.1 is introduced the approximation of a spatially varying inflow, the velocity profile. The notion of the free-stream vorticity, innate to the tidal flow, is presented in section 2.4.2. A new quantity, representing the interaction between the wake of a TECD and the tidal flow is defined in section 2.4.3. Subsequently, a new approach to the vorticity and velocity calculation is proposed. The required modification of the grid management is explained in section 2.4.4.

### 2.4.1 Velocity Profiles

The tidal flow generally varies in space. A more realistic model of tidal flow which represents the momentum loss in the boundary layer is considered in the simulation of the flow through the TECD. The loss of momentum in the boundary layer can be represented by an inflow velocity which decreases closer to the seabed. The variation of the velocity in the directions parallel to the ground plane depends on the particular morphology of the seabed. In the first approximation, the seabed is considered flat and the horizontal variation of the inflow velocity can thus be omitted from consideration. The term *velocity profile* used throughout this dissertation signifies an inflow velocity which varies only with water depth,  $z$ , but is invariant to the horizontal position (latitude, longitude)  $(x, y)$ .

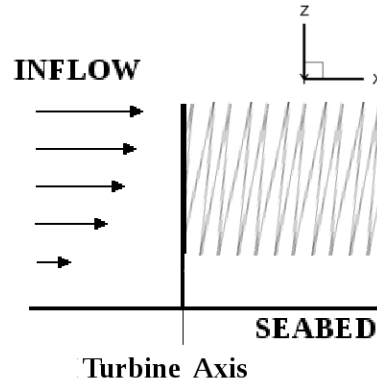


Figure 2.14: Illustration of a velocity profile as an inflow condition

The velocity profile is defined as a vector field of a fixed direction but variable magnitude

$$\mathbf{v}_{fs} = (V_{in}(z), 0, 0), \quad (2.52)$$

$$\frac{\partial V_{in}}{\partial z} > 0, \quad (2.53)$$

$$\frac{\partial V_{in}}{\partial x} = \frac{\partial V_{in}}{\partial y} = 0. \quad (2.54)$$

The increase of the inflow velocity with the distance from the seabed is expressed as the condition Eq. 2.53. The velocity profile satisfies the incompressibility condition  $\nabla \cdot \mathbf{v}_{fs} = 0$ . Despite the relative simplicity of this inflow model, its

incorporation into the VTM presented a challenge since the model was developed to benefit from the properties of the wake of a rotor subjected to a uniform inflow. In particular, the computational efficiency of the VTM, associated with the adaptive grid management and the routines used to evaluate the velocity, depended upon the uniform nature of the inflow.

In contrast to the uniform inflow approximation, Eq. 2.49-Eq. 2.50, the velocity profile, Eq. 2.52-Eq. 2.53, contains a rotational component **everywhere in the flow**, i.e.

$$\nabla \times \mathbf{v}_{fs} \neq 0, \forall \mathbf{x} \in \Omega \quad (2.55)$$

The new inflow approximation complicates the velocity calculation in the VTM. Prior to the present research, the rotational and the irrotational components of the velocity field could have been managed separately. It is implied within the uniform inflow model of rotor hydrodynamics that the vorticity is localised in the vicinity of the rotor. Helmholtz's Theorem states that a smooth vector field,  $\mathbf{u}$ , for which both  $\nabla \times \mathbf{u}$  and  $\nabla \cdot \mathbf{u}$  vanish at infinity, can be split into a rotational and an irrotational component [48]. The latter condition is satisfied by the incompressibility assumption. The velocity profile framework, however, needs to accommodate the curl of the velocity field that does not vanish at infinity. The velocity of the flow through the rotor of a TECD subjected to a velocity profile contains an unbounded vorticity field. The composition of the unbounded vorticity field is presented in sections 2.4.2 and 2.4.3.

### 2.4.2 Free Stream Vorticity

To simulate the flow down-stream of a TECD subjected to tidal flow which generally varies in space, a new model of the inflow has been implemented into the VTM. The situation of the rotor exposed to an inflow which is not uniform affects the manner in which the velocity and the vorticity is calculated.

The model of a more realistic inflow involves new quantities, not considered in the original VTM which employs the uniform inflow approximation. The first quantity is called *the free-stream vorticity* and is defined as

$$\omega_{fs} = \nabla \times \mathbf{v}_{fs} \quad (2.56)$$

in this dissertation. The second quantity innate to the new model of the inflow, called *the tide induced wake vorticity* in this dissertation, is introduced in section 2.4.3. As mentioned earlier, the flow near the flat seabed is approximated by a velocity profile. Then, the free-stream vorticity field takes the form

$$\omega_{fs} = (0, W_{in}(z), 0), \quad (2.57)$$

where  $W_{in}(z) = dV_{in}/dz$ . Note that  $W_{in}(z) > 0$  for  $z > 0$ . That is, the free-stream vorticity field is positive above the seabed with the axis parallel to the rotor plane and the seabed (the  $y$  axis). Temporal changes of the free-stream are discussed in section 2.4.3.

### 2.4.3 Tide Induced Wake Vorticity

The free-stream vorticity complicates the vorticity calculation in the VTM. Furthermore, the influence of the progress of the tidal cycle on the flow down-stream of a TECD needs to be considered in a realistic model of the tidal flow.

When the free-stream vorticity varies in time and space the vorticity down-stream of the TECD reflects the more complex nature of the inflow. The evolution of the vorticity in the flow, or the ‘total vorticity’, remains governed by the linear partial differential equation Eq. 2.13. The total vorticity can thus be written as a superposition of the free-stream vorticity,  $\omega_{fs}$ , and the induced vorticity,  $\omega_I = (\omega - \omega_{fs})$ . The vorticity transport equation yields

$$\frac{\partial \omega_I}{\partial t} + (\mathbf{v} \cdot \nabla) \omega_I - (\omega_I \cdot \nabla) \mathbf{v} = S_R - (\mathbf{v} \cdot \nabla) \omega_{fs} + (\omega_{fs} \cdot \nabla) \mathbf{v} - \frac{\partial \omega_{fs}}{\partial t}, \quad (2.58)$$

where the velocity field,  $\mathbf{v}$ , includes the free-stream velocity. The terms on the right hand side containing  $\omega_{fs}$  can be viewed as additional sources of the induced vorticity field. The induced vorticity is different from the rotor vorticity modelled for a uniform inflow. It is now possible to distinguish three sources of the induced vorticity,  $\omega_I$ : the source due to the rotor,  $S_R = S_\omega$  (defined in section 2.3.1); the source due to the progression of the tidal cycle

$$S_{TC} = -\frac{\partial \omega_{fs}}{\partial t}; \quad (2.59)$$

and the source due to the interaction of the free-stream vorticity and the velocity field that is induced by the rotor

$$S_{int}(\mathbf{v}) = (\omega_{fs} \cdot \nabla)\mathbf{v} - (\mathbf{v} \cdot \nabla)\omega_{fs}. \quad (2.60)$$

As mentioned above, the differential operator<sup>1</sup>

$$L(\mathbf{v}) = \frac{\partial}{\partial t} + (\mathbf{v} \cdot \nabla) - [\nabla\mathbf{v}] \quad (2.61)$$

where  $[\nabla\mathbf{v}]\mathbf{a} = (\mathbf{a} \cdot \nabla)\mathbf{v}$ ,  $\forall \mathbf{a} \in \mathbb{R}^3$ , is linear. To identify the difference between the vorticity generated down-stream of a rotor in a uniform flow and the vorticity down-stream of a TECD in a spatially varying flow, the induced vorticity field,  $\omega_I$ , is viewed as a composition of two vector fields  $\omega_w$  and  $\omega^*$ , defined as the solutions of the two equations

$$L(\mathbf{v})\omega_w = S_R \quad (2.62)$$

and

$$L(\mathbf{v})\omega^* = S_{TC} + S_{int}(\mathbf{v}), \quad (2.63)$$

so that

$$L(\mathbf{v})(\omega_w + \omega^*) = S_R + S_{TC} + S_{int}(\mathbf{v}), \quad (2.64)$$

which is an alternative form of Eq. 2.58. The equation Eq. 2.13 is a special case of the equation Eq. 2.62, when the inflow is uniform and the vorticity comes from the vorticity source, Eq. 2.1. The vorticity component  $\omega_w$  is thus equivalent to the rotor vorticity studied in the case when the rotor is subjected to a spatially uniform free-stream velocity. The quantity  $\omega_w$ , which originates from the source Eq. 2.1, is referred to as the rotor vorticity in an analogy to the case of the uniform inflow. The free-stream vorticity is present everywhere in the flow, i.e. the velocity of the free-stream is rotational. The velocity is evaluated from the total vorticity,  $\omega = \omega_{fs} + \omega_w + \omega^*$  as the solution of

$$\nabla^2\mathbf{v} = -\nabla \times \omega. \quad (2.65)$$

---

<sup>1</sup>formally  $L(\mathbf{v}) : \mathcal{H}^1(\mathbb{R}^3 \times (0, \infty)) \rightarrow \mathcal{H}^1(\mathbb{R}^3 \times (0, \infty))$ , the space  $\mathcal{H}^1$  contains ‘weakly smooth’ functions.

The structure of the vorticity field down-stream of a TECD in tidal flow is very different from the structure of the rotor vorticity in the case of a uniform inflow. This is because the vorticity component  $\omega^*$  has no equivalent in the uniform inflow case. When the free-stream contains no vorticity, both  $S_{TC}$  and  $S_{int}(\mathbf{v})$  are zero. Thus, the homogeneous equation

$$L(\mathbf{v})\omega^* = 0 \tag{2.66}$$

yields the solution  $\omega^* = 0$ . The vorticity  $\omega^*$  thus embodies the effect of the tide on the flow down-stream of the TECD and, consequently, the influence of the device on its environment. In this dissertation,  $\omega^*$  is called *the tide induced wake vorticity*.

The tide induced wake vorticity occurs as a result of the interaction between the tidal flow, which varies over time, and the rotor. The temporal variation of the free-stream represents the progression of the tidal cycle. The time scale investigated by the VTM is adjusted to span the development of the wake of a rotor. Typically, the rotor wake under a static (time invariant) inflow condition is studied over an interval of minutes. The exact time interval depends on the parameters of the flow.

It can be safely assumed that the variation of the velocity profile over the period of the tidal cycle is very slow compared to the time-scales that are relevant to the development of the wake of the TECD. In fact, according to Morris et al. [49], the change of the tidal velocity at 10 m above the seabed is typically of order  $10^{-4}\text{ms}^{-1}$  per second, whereas the wake develops over time scales of the order of 10 seconds. The free-stream vorticity is thus considered time invariant over the interval relevant for the development of the wake, i.e.

$$\frac{\partial\omega_{fs}}{\partial t} = 0. \tag{2.67}$$

The source of the tide induced wake vorticity attributed to progression of the tidal cycle is thus negligible relative to the source resulting from the interaction between the free-stream and the rotor. The tidal cycle can, therefore, be discretized and represented as a set of consecutive velocity profiles, which correspond to a range of inflow conditions for the VTM.

### 2.4.4 Fixed Computational Grid

The spatial extent of the tide induced wake vorticity,  $\omega^*$ , is generally larger than the spatial extent of the rotor vorticity field,  $\omega_w$ . The induced vorticity field,  $\omega_I = \omega_w + \omega^*$ , thus lacks the compactness of the rotor vorticity field associated with the uniform inflow case. The support of the induced vorticity needs to be included in an expanded grid within the VTM to facilitate the computations. The total vorticity field  $\omega = \omega_{fs} + \omega_w + \omega^*$ , is required to calculate the velocity as

$$\mathbf{v}(\mathbf{x}) = -\frac{1}{4\pi} \int_{supp(\omega)} \frac{(\mathbf{x} - \mathbf{x}') \times \omega(\mathbf{x}')}{|\mathbf{x} - \mathbf{x}'|^3} d\mathbf{x}', \quad (2.68)$$

where  $supp(\omega)$  is larger than  $supp(\omega_w)$  at any time during the simulation of the wake of a TECD in tidal flow.

In the original version of the VTM, the adaptive grid was updated every time step through deletion and insertion of cells, depending on the spatial distribution of the rotor vorticity field. Extension of the adaptive grid approach for the tidal flow simulations has proven computationally expensive, a problem which has been addressed by the implementation of a new computational grid of fixed (time invariant) geometry. It is of relevance that a fixed grid arrangement existed in the VTM prior to the implementation of the adaptive grid, described in [1]. The new fixed grid management, however, benefits from the utilisation of the octree data structure and the efficient velocity calculation, described in sections 2.3.7 and 2.3.3. The new grid is created at the beginning of the simulation and remains unchanged.

### 2.4.5 Boundary Conditions

The fixed grid is defined by its limits in the Cartesian stencil,  $[-x_0, x_{max}] \times [-y_{max}, y_{max}] \times [0, z_{max}]$ . This modification requires a definition of boundary conditions on the new, time invariant boundaries. The condition of zero curvature on the induced vorticity field,  $(\nabla\omega_I \cdot \mathbf{n})|_{\partial\Omega} = 0$ , is imposed on the boundaries  $x = x_{max}$ ,  $|y| = y_{max}$  and  $z = z_{max}$ , so that there is no change in the vorticity field passing through the boundary out of the computational grid. The rotor plane, at

$x = 0$ , does not represent a boundary. The condition at  $x = -x_0$ , i.e. up-stream from the rotor plane, is  $\omega = \omega_{fs}$ .

The argument used in [1] in favour of a boundary-free grid over a fixed grid is the influence of the boundary conditions on the flow in situations where the wake induces a velocity of magnitude similar or greater than the free-stream (for a graphical example see [1], page 35).

The adaptive grid could extend to contain all of the vorticity produced by the rotor, which meant that possible disadvantages associated with fixed boundaries were avoided. The nature of the Biot-Savart relationship Eq. 2.18 implies that all of the vorticity needs to be included in the calculation of the velocity field and omitting a region containing vorticity in the velocity calculation could result in a solution which is not physical. Hence, the implementation of fixed boundaries could introduce an error into the velocity calculation if the extent of the induced vorticity field is larger than the size of the fixed grid. When the free-stream contains vorticity, however, the adaptive grid formulation outlined in section 2.3.6 is no longer appropriate. The free-stream vorticity needs to be considered for the simulation of a TECD placed into a boundary-layer flow.

The boundary condition of zero penetration at the ground plane ( $z = 0$ ) is modelled in the VTM by the method of images [5]. A vortex approaching a solid surface behaves as if there were another vortex below the ground plane, rotating in the opposite sense. In the presence of a solid surface, the induced vorticity is obtained as a solution of Eq. 2.13, following which the vorticity of the mirror wake is evaluated. The velocity field of the wake near the ground plane is then calculated from the superposition of the two vorticity fields. The method of images is capable of representing the ground plane as a boundary to a high Reynolds number (inviscid) flow. An approximation of the viscous boundary condition at the seabed is incorporated into the VTM via the inclusion of a free-stream vorticity field corresponding to an empirical velocity profile as explained in section 2.4.1. However, this implementation of the seabed boundary condition is not equivalent to a full no-slip condition.

The imposed boundary condition implies that the component of the velocity field normal to the seabed is zero, i.e. the flow does not penetrate the seabed, and that the tangential component of the wake induced velocity near the seabed is

amplified. However, the inflow model in the form of a velocity profile implemented into the VTM helps to reduce this effect by ensuring that the flow velocity close to the seabed decelerates. The amplified tangential component of the wake induced velocity field could lead to some over-prediction of the erosion of the seabed by the wake of a TECD. Without the reduction of the amplification effect the over-prediction of the seabed erosion would be more pronounced. Nevertheless, the modified VTM provides novel qualitative predictions of the wake structure and the erosion of the seabed by the wake of a TECD.

In a first approximation, free surface could be modelled by another mirror plane located at  $z = z_{max}$  to ensure no-penetration condition  $\mathbf{v}_I \cdot \mathbf{n} = 0$  at the upper boundary. Two vortices which represent a section of an inclined vortex ring and their mirror images are depicted in Fig. 2.15,

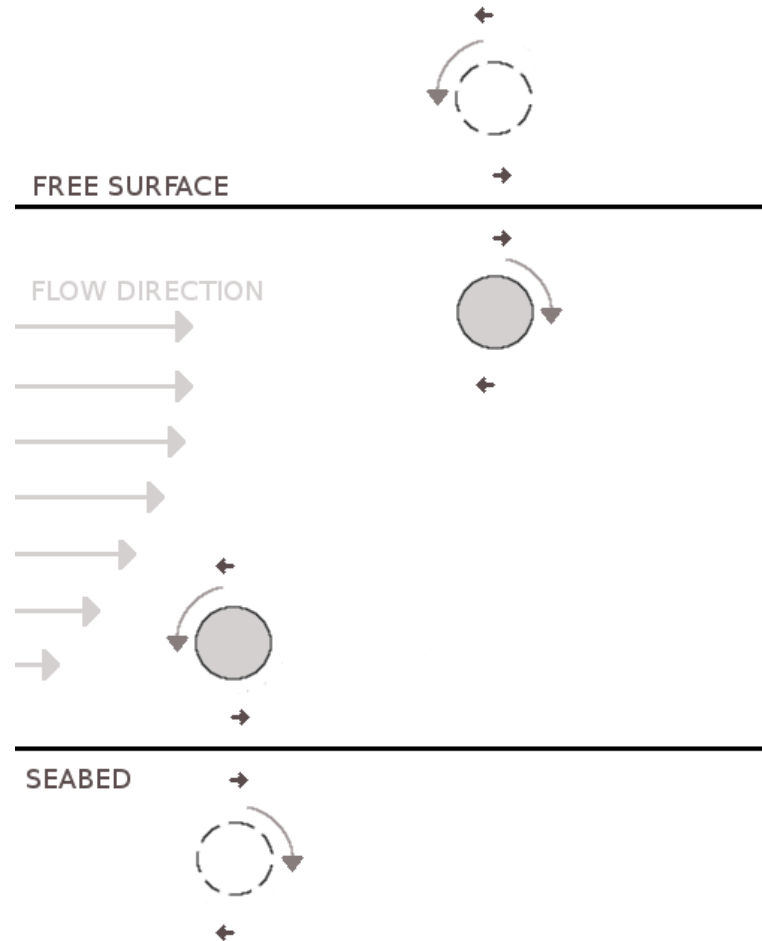


Figure 2.15: Illustration of the implemented seabed boundary condition and a possible free-surface representation.

where the small black arrows indicate the direction of the vortex induced velocity. An alteration of the wake induced velocity field due to the simplified representation of free-surface is illustrated in Fig. 2.16.

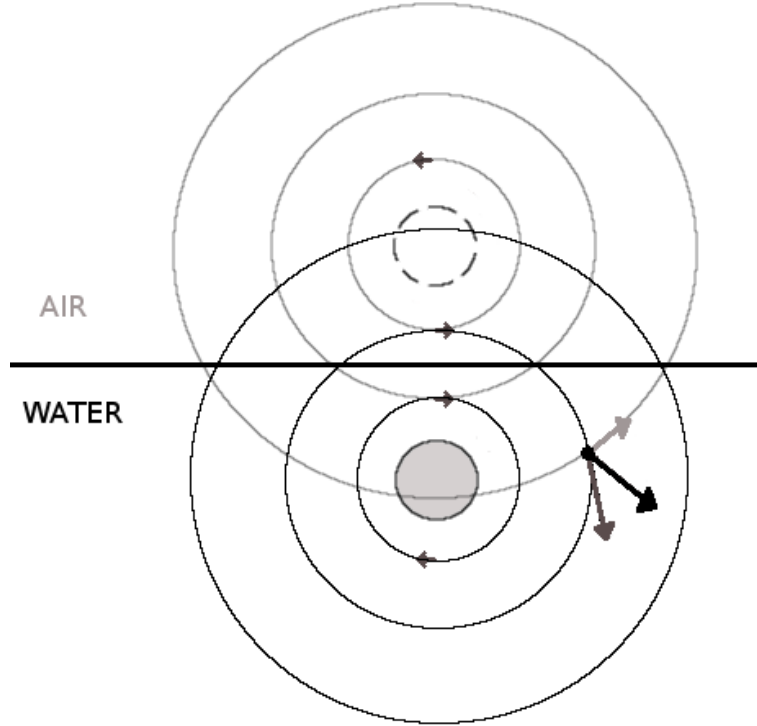


Figure 2.16: Illustration of the influence of the mirror vortex on the flow. The dark grey arrow represents the wake induced velocity vector without an influence of free surface, the light grey arrow represents the velocity induced by the mirror vortex and the black arrow indicates the wake induced velocity vector affected by the simple free-surface model.

### 2.4.6 Sediment in the VTM

A sediment transport model has been implemented into the VTM to simulate the evolution of sediment concentration,  $c$ , using the pre-existing routines. The VTM now contains a module to solve the transport equation

$$\frac{\partial c}{\partial t} + (\mathbf{v} + \mathbf{w}_s) \cdot \nabla c = \nabla \cdot (\epsilon \nabla c) + S_c, \quad (2.69)$$

where  $\epsilon$  is the sediment diffusivity,  $\mathbf{w}_s$  is the settling velocity and  $S_c$  is the source of sediment due to the presence of the TECD on the seabed. The settling velocity and the source of sediment are calculated from semi-empirical formulas

and depend on the parameters of the sediment, as described in chapter 3. The advection of the sediment concentration is evaluated by the routine described in section 2.3.5, employing less compressive wave amplifier than the advection of vorticity, since the calculation of sediment concentration is less likely to be affected by spurious oscillations. Unlike the vorticity transport equation, Eq. 2.69 contains a diffusion term. The sediment diffusivity is treated as a parameter due to the lack of empirical data. The calculation of the sediment concentration is fully explained in section 3.4.

### 2.4.7 Turbulent Diffusion Effects

While the viscous effects are small in high-Reynolds number flows and can thus be omitted from consideration, the effects of turbulent diffusion generally are not. Therefore, an implementation of a suitable turbulence model would be a valuable future amendment to the VTM as discussed in chapter 7. The turbulent diffusion effects may include earlier disintegration of the vortex structure and vortex decay in general. This has implications for the predictions of the erosion inflicted by the wake of a TECD on the seabed since turbulent diffusion might cause lower rates of seabed erosion than is suggested by the results presented in this dissertation. Furthermore, a turbulent inflow could affect the wake down-stream of TECDs. In such a case the inflow could not be approximated as quasi-steady. The degree of the influence of a turbulent inflow on the wake of a TECD is indicated by turbulence intensity at tidal sites. Turbulence intensity is defined as ratio of the magnitude of the velocity fluctuations,  $|\mathbf{v}'|$ , and the magnitude of the mean velocity,  $|\bar{\mathbf{v}}|$ , [50]. The turbulence intensity during strong tides is consistently around 10% according to Thomson et al. [50], who analysed the data from a tidal power site in Puget Sound, WA, USA, where maximum spring velocity magnitude reaches almost 2 m/s. The velocity fluctuations were measured in 64 s periods [50]. Arguably, measurements over different time periods could result in different values of the turbulence intensity. The 10% variation of the inflow velocity which is likely to occur during the period of wake development is not captured by the VTM's simulations at present. A turbulent inflow containing large eddies could disturb the formation of the ordered vortical structure down-stream of TECDs.

Nevertheless, the VTM's predictions were validated previously as discussed in the following section.

## 2.5 Model Validation

The predictions of the VTM in terms of rotor loading and wind turbine performance have been validated previously and repeatedly against experimental data. Of most relevance to the current study, the comparison between the VTM's predictions of the blade loading and experiments has been done by Scheurich [3] for wind turbines. A comparison between the loading on the blades predicted by the VTM and experimental data from [3] is presented in Fig. 2.17. The ability of the VTM to simulate accurately the wake further from the rotor was confirmed by comparison between the simulations and relevant experimental data [5]. For example the structure of the vorticity field for a typical case modelled by the VTM by Phillips [5] is presented in Fig. 2.19 and compared to experimental data from Lee et al. [4] presented in Fig. 2.18.

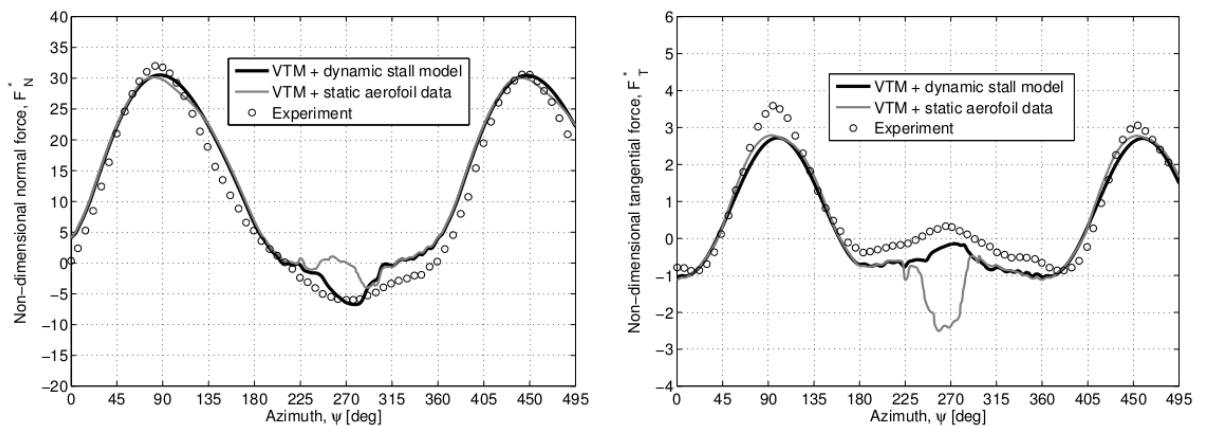


Figure 2.17: Comparison between the variation in VTM-predicted aerodynamic loading and experimental measurements made by Strickland et al. [2] for  $TSR = 5$ , left: normal force, right: tangential force. Image taken from Scheurich [3].

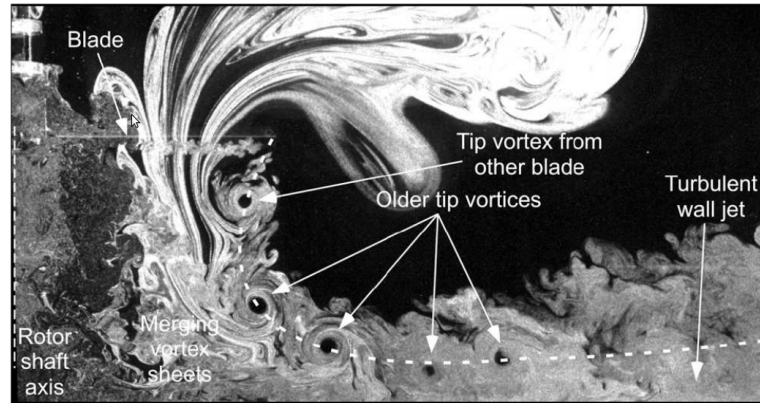


Figure 2.18: Smoke flow visualisation of the wake produced by a two bladed rotor in ground effect. Image taken from Lee et al. [4]

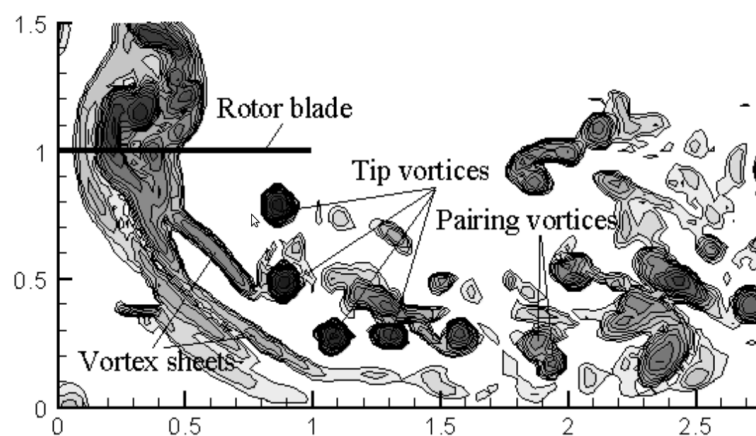


Figure 2.19: Vorticity distribution from a two bladed rotor in proximity to the ground plane as calculated using the VTM. Image taken from Phillips [5]. (The rotor was hovering one radius above the ground)

The VTM's predictions of blade loading for a wind turbine using relatively thick NREL S809 aerofoil were previously compared with experimental data by T.M. Fletcher in [51]. Moreover, the wake structure predicted by the VTM was compared with predictions of a three-dimensional, incompressible, Reynolds-Averaged Navier-Stokes flow solver in [51]. This comparison encourages the use of the VTM to simulate the flow around TECDs.

## 2.6 Summary

The Vorticity Transport Model is a complex modelling system, consisting of many modules, developed over the years to simulate various configurations of the rotor, for a variety of helicopter flight conditions, and the performance of vertical-axis wind turbines. The core of the VTM is the solution of the vorticity transport equation Eq. 2.13, a form of the equations of motion of an incompressible fluid, that explicitly conserves vorticity within the flow. The vorticity transport equation governs the evolution of the wake vorticity field and the wake induced velocity field, which is coupled to the vorticity by the Biot-Savart relationship, Eq. 2.18. The source of vorticity is identified with the strength of the circulation around the blades of the rotor. The vorticity source is evaluated by the modified version of the Weisinger-L lifting-line method. The calculation of the transport of vorticity is split into advection and stretching parts. The advection in three-dimensions is treated as a sequence of three one-dimensional applications of the WAF scheme, equipped with the SUPERA-type wave amplifier functions with the Total Variation Diminishing property to preserve monotonicity of the solution. The octree structure of the grid in conjunction with the velocity calculation by the Fast Multipole Method reduces computational cost, since the costly cell-cell interactions are replaced with faster cell-cluster and cluster-cluster interactions. The truncation error of the multipole expansion is smaller than a pre-set value, ensuring the chosen degree of accuracy. The semi-empirical Dynamic Stall Model allows for the wake of a vertical axis turbine to be studied, predicting the unsteady attached flow, the unsteady separated flow and the formation of the dynamic stall vortex.

To study the impact of a TECD on the marine environment, the more realistic inflow condition in the form of a velocity profile, defined in section 2.4.1, was considered. The spatial variation of the inflow has been accounted for by introducing a free-stream vorticity into the model, which significantly alters the nature of the flow. Extending the previous modelling strategy, two essential components of the vorticity field have been identified - the rotor vorticity, which resembles the vorticity field occurring under the uniform inflow condition, and the tide induced wake vorticity. The latter component is zero in the uniform inflow case. Furthermore, two sources of the tide induced wake vorticity have been identified, one

attributed to the progression of the tidal cycle and the other to the interaction between the tide and the rotor. The free-stream vorticity was assumed to be time independent during the VTM simulations. To accommodate the spatially varying inflow the VTM required a modification to incorporate the simulation of the new variables, which are defined in sections 2.4.2 and 2.4.3. A new time-invariant grid geometry has been developed to replace the previous adaptive grid, which proved to be unsuitable for the simulation of the flow down-stream of a TECD subjected to a velocity profile. The new grid management has reduced the length of the simulations below the time typically required by the original VTM to investigate the uniform inflow cases. The new version of the VTM, adapted to simulate the spatially variable inflow, is used to model the flow through a rotor for a range of the inflow conditions.

# Chapter 3

## Sediment Model

The hydrodynamics of a tidal energy conversion device (TECD), simulated by the Vorticity Transport Model (VTM), needs to be put into the context of sediment transport in order to study the interaction within the TECD-environment (TE) system. The character of sediment and the seabed morphology in potential future locations of TECs is discussed in section 3.1.

The flow through the rotor of a TECD governs the influence of the device on the seabed. As mentioned in section 2.4, the seabed is approximated as a flat plane, which poses an impenetrable boundary to the flow. In the absence of the TECD, the tidal flow contains the free-stream vorticity. The concept of the free-stream vorticity, which was introduced in section 2.4.2, encapsulates the reaction of the flow to the presence of a barrier – the seabed. If the TECD were not in close proximity to the seabed the inflow to the rotor could be approximated as uniform. The motion of sediment from the flat seabed needs to be modelled with the consideration of viscous effects if the influence of the TECD wake on the marine environment is to be understood.

When a realistic velocity profile (based on experimental data) is chosen as an inflow model for the VTM, additional sources of vorticity have to be defined consistently with the selected profile. The definition of the empirical velocity profile includes the assumption that the free-stream velocity is zero on the seabed. This approach does not, however, enforce the no-slip condition at the seabed.

In the present model of a flow through the rotor of a TECD, the seabed interacts with the flow in two ways. On one hand, the rotor is exposed to the

---

spatially variable inflow in the form of a velocity profile. On the other hand, the induced vorticity field (that is caused by the presence of the rotor in the tidal flow) produced down-stream of the device interacts with the seabed. A model of such interactions is described in section 2.4.5.

Both the uniform inflow approximation and the more realistic inflow model (i.e. the free-stream velocity in the form of a velocity profile) are investigated in this dissertation. In both scenarios, the interaction of the flow through the rotor of a TECD with the seabed is governed by the velocity field. Surface shear forces on the seabed (related to the flow velocity above the seabed) initiate motion of sediment, which is then transported by the flow in the layer just above the seabed. The process of the initiation of the sediment motion varies with the parameters of the sediment.

The characteristic time-scales of the different processes involved in the sediment transport in the wake of the HATT are listed in Table 3.1 to put the present study into the context of large-scale sediment transport and changes in the seabed morphology. The period of short-term changes of the seabed morphology is 1 year according to van Rijn [52]. The time needed to complete one rotor revolution of the HATT described in section 2.1 is  $T_{rr} = 6.28$  s. The eddy turnover time is of the order of the lifetime of the largest eddies occurring in the flow, hence it depends on the flow and typically varies between 0.1 s - 1 s according to Zimberg et al. [53].

Eddy turnover time	$T_{rr}$	Tidal Cycle	Morphodynamic short-term period
0.1-1 s	6.28 s	12 hours	1 year

Table 3.1: Comparison of the time scales of the processes involved in the sediment transport in the wake of the HATT.

As explained in section 2.4.3, for the purposes of the present research, the tidal cycle can be discretized and the wake development can be treated as quasi-steady, since the change of the tidal velocity at 10 m above the seabed is typically of order  $10^{-4}\text{ms}^{-1}$  per second [49]. If an explicit turbulence model were used and a turbulent inflow were considered, the quasi-steady approximation of the inflow

### 3.1 Sediment Characteristics at Potential Tidal Sites

---

would not be possible given the eddy turnover times, which imply even faster changes of small eddies. In such a case, also the use of static aerofoil data to obtain the source of vorticity on the blades should be questioned. Since the model used here does not provide for a turbulent inflow and the inflow velocity is assumed to be time invariant over the period of wake development ( $\sim 50$  s), the use of the static aerofoil data is justified.

Sediment characteristics of potential future locations of TECDs are discussed in section 3.1. The concept of a threshold of sediment uplift and its connection to the parameters associated with the sediment particles are discussed in section 3.2. Erosion of sediment and the types of sediment motion are introduced in section 3.3. The notion of an ‘excess bed shear stress’ is defined as a measure of the impact of the flow on the seabed. The excess bed shear stress is assumed to determine the erosion flux from the seabed and to influence the concentration of sediment in the flow, i.e. the amount of sediment in motion. The sediment concentration depends also on the rate of deposition of sediment back on the seabed and the sediment diffusivity. A model of sediment settling is defined in section 3.4.1. The relationship between turbulence and sediment diffusivity is discussed in section 3.5. A model of the evolution of the sediment concentration is presented in section 3.4.

### 3.1 Sediment Characteristics at Potential Tidal Sites

In the extreme tidal conditions of the Pentland Firth (maximal stream velocity of 4.5 m/s) the seabed is characterized as non-erodible bed rock [54]. Indeed, with an exception of small areas near the shore and around the islands, where accretion of sediment is predicted, the sediment was completely removed by the tidal streams [26]. In other areas, suitable for power extraction by TECDs, the composition of sediment varies, from non-erodible bed rock to the Alderney South Bank sandbanks, where a tidal development is planned [22]. According to the British Geological Survey [54], the composition of sediment on the seabed off the west coast of Scotland includes sand and mud.

A clear distinction needs to be made between large-scale tidal arrays, which are likely to be installed in faster streams, and community-sized isolated devices, placed to slower streams relatively close to shore. This dissertation is focused on the latter case - a single TECD with rated power below 200kW. In slower streams an accumulation of sediment on the seabed is predicted [26]. Hence, the seabed near a community-sized TECD is more likely to be erodible than the seabed near a tidal array.

### 3.2 Initiation of Sediment Motion

The nature of the interaction between the seabed and the flow depends on the properties of the fluid. A viscous fluid moving over a surface generates shear forces on the surface. The magnitude of the shear is related to the local near-bed velocity [55]. In fact, the velocity of the flow just above the seabed and the parameters of the fluid, principally its viscosity and density, determine the shear forces on the seabed. The initiation of sediment motion depends not only on the action of the shear forces, however. The properties of the sediment and morphology of the seabed also influence the process of the initiation of the sediment motion.

In reality, how the seabed responds to the fluid forces depends on the shape of sediment particles and local geometry of the seabed. The most often used models of the initiation of sediment motion are the so called *threshold models*. In such models, sediment particles are assumed to leave the seabed when a physical quantity related to the surface shear forces generated by the fluid exceeds a threshold value. The threshold value of sediment uplift has been found to depend not only on the size of the particles, but also on the geometry of the particles as well as the micro-structure of the surface and the local electrostatic field [56]. The vegetation on the seabed is known to change the bed roughness coefficient [57]. The flat-seabed approximation, which is consistent with the definition of the free-stream velocity in section 2.4.1, focuses attention on the basic principles of sediment uplift. On a flat seabed, it is the character of the sediment which determines whether or not a sediment particle leaves the seabed. Furthermore, the properties of the sediment influence the type of motion which a sediment particle undergoes once it has left the surface.

## 3.2 Initiation of Sediment Motion

---

The seabed generally hosts a variety of sediment, from clay to boulders. The range of sizes of sediment on the seabed is usually characterized by a single parameter called the median sediment diameter [55]. The representative size of the sediment particles then presents an indicator of the type of sediment motion. The diversity of sediment is categorized according to the dominant type of motion the particles are likely to adopt. Larger particles will roll and hop along the seabed while others will, under the same shear forces, leave the seabed to be suspended into the flow.

The behaviour of the sediment depends on the relative amounts of the sediment types present. Since the inter-particle force dominates the gravitational force when the surface area of a particle is significantly larger than its volume [58], the sediment is categorized either as ‘cohesive’ or ‘non-cohesive’ depending on the size of the sediment particles. The particles of diameter larger than  $62\ \mu\text{m}$  are classified as non-cohesive sediment [55]. If the mud (cohesive sediment) content (defined by so called clay-silt ratio) is below a critical value, the entrainment of the sand particles is assumed to be the dominant erosion mechanism according to Van Rijn [55]. Fine and coarse sand (non-cohesive sediment smaller than  $2\ \text{mm}$ ) is characterized by motion into suspension. Apart from the size of sediment particles, the sediment is characterized by its density on the seabed.

The existence of a threshold of sediment uplift has been postulated by many studies over the years to simplify the description of such motion for applications in engineering, oceanography, geology, geochemistry and sedimentology [59]. The relationship between the sediment parameters and the fluid shear forces (related to the flow velocity above the seabed) is highly complex. Given the variability of the hydrodynamic environment, many different empirical threshold curves have been devised and used [60, 61, 62, 63, 64, 65].

The Shield’s curve, introduced by Shields [61], has been repeatedly revised as more and more experimental data have become available. The modifications have, however, brought ‘little more than scatter’ according to Miller et al. [64], because, as is pointed out by Paphitis [59], the notion of a threshold is rather subjective. The commonly used definitions of a threshold were based on visual assessment. Such an assessment depends, indeed, on how the individual investigators perceived the moment at which particle motion is initiated [59]. Based

### 3.2 Initiation of Sediment Motion

---

upon their perception, some investigators even argued that sediment motion is observable at any unidirectional current velocity greater than zero.

The research into the fluctuations of bed shear stress indicated the difficulty of defining a unique threshold under turbulent flow conditions. The instantaneous stresses have been observed to entrain sediment [66, 67, 68], even when the temporal mean of the stress was below the threshold condition. An experimental study on near-bed turbulence suggests that the threshold of sediment motion is related to the flux of turbulent kinetic energy [69]. A direct numerical simulation (DNS) conducted to determine the forces acting on the sediment particles indicated that two distinct ways of initiation of sediment motion, ‘pick-up’ and ‘roll-over’, have to be taken into account to capture the entrainment of gravel by turbulent flow in an open channel [70]. Furthermore, threshold velocity-based models have been experimentally validated only for large-scale, steady flows and therefore their applicability to more complex, small-scale unsteady flows, such as those caused by the interaction of the flow down-stream of a TECD and the seabed, is unknown at present. The applicability of threshold velocity-based erosion models to small-scale fluid phenomena requires future experimental verification.

Nevertheless, due to the lack of consensus within the scientific community on the process of initiation of sediment motion under rapidly changing flow conditions, the original Shield’s definition of the threshold, reformulated by van Rijn [55] to depend on dimensionless sediment size, is adopted here as a primary threshold condition.

The Shield’s function is widely accepted among researchers to provide a simple algebraic expression of sediment entrainment for a variety of types of sediment [55]. This choice of threshold model thus makes the present research compatible with sediment models currently in use. The sediment motion is assumed to initiate when a critical value of bed shear stress is reached. The shear stress on the seabed,  $\tau_b$ , can be expressed as

$$\tau_b = \rho C_D |\mathbf{v}_b| \mathbf{v}_b, \quad (3.1)$$

where  $\mathbf{v}_b$  is the flow velocity at the friction height, and  $C_D$  is a drag coefficient of the fluid [71]. The friction height is defined as the position of the sediment particles before they are moved by the flow. The relation Eq. 3.1 was chosen

### 3.2 Initiation of Sediment Motion

---

over the classical form of the shear stress,  $\tau_b = \rho\nu\nabla\mathbf{v}_b \cdot \mathbf{n}$ , since the latter is used less than the former within the field of sedimentology. The choice of Eq. 3.1 ensures compatibility of the present research with oceanographic sediment transport models, which makes the output of the presented model suitable as an input into large-scale models of sediment motion.

The dimensionless bed shear stress,  $\theta$ , is given by

$$\theta = \frac{\tau_b}{(\rho_s - \rho)gd}, \quad (3.2)$$

where  $\rho_s$  is the density of sediment,  $\rho$  is the fluid density,  $g$  is the gravitational acceleration and  $d$  is the mean diameter of the sediment [71]. In this dissertation,  $d$  was chosen to represent fine to medium sand particles. This type of sediment is present in British coastal seas, in particular in headland sand banks [22].

The threshold for initiation of sediment motion adopted in the present research

$$\theta_{cr} = \theta_0(d^*)^\sigma, \quad (3.3)$$

is based on the data of Miller et al. [64], where  $d^*$  is the dimensionless sediment diameter [55]

$$d^* = d \left( \left( \frac{\rho_s}{\rho} - 1 \right) \frac{g}{\nu^2} \right)^{1/3}, \quad (3.4)$$

where  $\nu$  denotes the viscosity of the fluid. The coefficients in Eq. 3.3 vary with the sediment parameters as presented in table 3.2 [72, 73, 64].

	$1 < d^* \leq 4$	$4 < d^* \leq 10$	$10 < d^* \leq 20$	$20 < d^* \leq 150$	$d^* > 150$
$\theta_0$	0.24	0.14	0.04	0.013	0.055
$\sigma$	-1	-0.64	-0.1	0.29	0

Table 3.2: Empirical relationship between the coefficients,  $\theta_0$ ,  $\sigma$  and the dimensionless sediment size

In the article by Zhang et al. [74], the critical bed shear stress,  $\theta_{cr}$ , is influenced by the local geometry of the bed material. Since only flat beds were studied, this influence was not considered here.

The threshold model Eq. 3.3 was chosen due to its widespread use within the field of sedimentology and therefore to facilitate the comparison of the results with other research studies. Nevertheless, to investigate the sensitivity of the model to the choice of threshold condition, another threshold formula was adopted in the form of the threshold velocity

$$v_t = \sqrt{K \frac{\rho_s}{\rho} g d} \quad (3.5)$$

where  $K = \mu_0/c_d$ ,  $c_d$  is the particle drag coefficient and  $\mu_0$  is a coefficient of static friction [75]. The threshold condition Eq. 3.5 was devised for models of dust and debris transport from the desert surface by helicopter rotors [75]. Since this expression was specifically devised to approximate the entrainment of particles by the unsteady flow through the rotor,  $|\mathbf{v}| \geq v_t$  could be seen as more appropriate threshold condition than  $\theta \geq \theta_{cr}$  for the purposes of the present research.

### 3.3 Erosion and Sediment Load

A sediment is generally composed of bed load and suspended load, depending on the type of motion which the sediment particles undergo. Both bed load and suspended load are strongly related to the choice of the threshold model of sediment uplift (conceivably, two threshold models suited to the two types of motion could be used as proposed by Ma et al. [70]). The two mechanisms of sediment motion depend on each other - the bigger grains of sediment which roll and hop cause the smaller particles to move into suspension.

The erosion of sediment, studied By Huang et al. in [58], depends on a relative measure  $\xi$ ,

$$\xi = \left( \frac{\theta}{\theta_{cr}} - 1 \right), \text{ when } \theta \geq \theta_{cr}, \quad (3.6)$$

for the threshold model Eq. 3.3. The alternative threshold condition Eq. 3.5 yields

$$\xi = \left( \frac{|\mathbf{v}|^2}{v_t^2} - 1 \right), \text{ when } |\mathbf{v}| \geq v_t, \quad (3.7)$$

since the bed shear stress is proportional to square of the flow velocity [73].

The relative quantity,  $\xi$ , is called *the excess bed shear stress* in this dissertation. Ribberink [73] suggests that the instantaneous value of the excess bed shear stress,  $\xi = \xi(t)$ , rather than the temporal mean thereof, needs to be taken into account in modelling of sediment motion in an unsteady flow. The excess bed shear stress is related to a number of quantities used to describe the sediment motion, including the erosion flux of cohesive sediment [76], the bed load,  $q_b$ , [73, 55], and the concentration of the suspended load,  $c_s$ , [77].

The commonly accepted relation between the erosion flux and the excess bed shear stress is

$$E = E_0 \xi^f, \quad f > 0 \quad (3.8)$$

where  $E_0$  is an empirical constant [76]. The application of Eq. 3.8 relies on knowledge of the constant,  $E_0$ , which is affected by a number of factors of physical, electrochemical and biological nature. Hence, the value of the erosion-flux constant has to be determined from experiments for each particular flow situation that is of interest [76].

Van Rijn [55] concluded that the bed load  $q_b$  is related to the excess bed shear stress as

$$q_b \approx \tau_b^{1/2} \xi. \quad (3.9)$$

Earlier, in [78], he defined the concentration of bed load,  $c_b$ , as

$$c_b = \frac{q_b}{|\mathbf{v}_b| \delta_b}, \quad (3.10)$$

where  $\delta_b$  is the thickness of the bed load layer. From Eq. 3.9, Eq. 3.1 and Eq. 3.10 it follows that the concentration of bed load is proportional to the excess bed shear stress

$$c_b \approx \xi. \quad (3.11)$$

According to [73], the bed load is proportional to  $\xi(t)^m$  even for unsteady flows and the parameter  $m$  is determined by experiments. In oscillatory flows the instantaneous value of the excess bed shear stress determines the bed load [73].

Furthermore, the excess bed shear stress is related to the motion of sediment suspended in the flow. The concentration of suspended sediment depends on the excess bed shear stress  $c = c(\xi)$ . In particular, according to Van Rijn [77]

$$c_{ref} \approx \frac{\xi^{1.5}}{z_{ref}} \quad (3.12)$$

at a reference level  $z_{ref} < 0.01$  m above the seabed. The reference concentration,  $c_{ref}$ , is used to evaluate the sediment concentration,  $c$ , at all heights above the seabed. The sediment concentration depends further on environmental parameters: the sediment size; the sediment density; the fluid viscosity and the fluid density.

To summarize, the excess bed shear stress,  $\xi$ , determines the erosion flux of the sediment, the concentration of bed load and the concentration of the sediment in suspension. The instantaneous value of  $\xi$  has to be taken into account for unsteady flow. This observation motivates the calculation of the excess bed shear stress in every time step of the simulation. The instantaneous value,  $\xi(t)$ , is used herein to evaluate the source of sediment in the model of sediment transport used in the present research.

## 3.4 Sediment Transport

Unlike the bed load concentration,  $c_b$ , which can be evaluated by a rather simple algebraic formula Eq. 3.10 (even in the case of oscillatory flows), the concentration of the sediment in suspension,  $c$ , is calculated as a solution of a differential equation. In most of the literature on sediment transport, the one-dimensional advection-diffusion equation is employed to resolve the evolution of the concentration of the sediment in suspension.

Since the flow through the rotor of a TECD is inherently unsteady and since the three-dimensional nature of the flow is of particular interest in the present research, the evolution of the sediment concentration is modelled as

$$\frac{\partial c}{\partial t} + (\mathbf{v} + \mathbf{w}_s) \cdot \nabla c = \nabla \cdot (\epsilon \nabla c) + S_c, \quad (3.13)$$

where  $\epsilon$  is the sediment diffusivity,  $S_c$  is the source of sediment, evaluated from the erosion flux Eq. 3.8. The process of sediment deposition is expressed by the vertical convection of the sediment concentration by the settling velocity  $\mathbf{w}_s = (0, 0, -W_s)$ .

The Eq. 3.13 is the generalisation of the time-averaged one-dimensional sediment transport equation used in [78].

$$\epsilon \frac{dc}{dz} + cW_s = 0, \quad (3.14)$$

### 3.4.1 Settling Velocity

The deposition of sediment is modelled by the inclusion of a semi-empirical settling velocity into the sediment transport equation Eq. 3.13. The settling velocity is essentially a *threshold of sediment deposition*. A sediment particle is assumed to settle back on the seabed when the velocity of the moving particle decreases below the settling velocity.

Several formulae have been devised over the years to quantify the process of sediment leaving suspension. A detailed overview of the formulae used to evaluate settling velocity is provided in Cheng [79]. Similarly to the threshold model for the initiation of sediment motion, Eq. 3.3, the commonly used model of the threshold of sediment deposition depends on the sediment size [79, 80]. The following expressions were considered here [79, 80, 81].

$$W_s = \frac{(d^*)^3}{18d} \nu \quad d < 100\mu m \quad (3.15)$$

$$W_s = \frac{10\nu}{d} \left( \sqrt{1 + 0.1(d^*)^3} - 1 \right) \quad 100\mu m \leq d \leq 1mm \quad (3.16)$$

$$W_s = 1.1 \frac{\nu}{d} (d^*)^{3/2} \quad d > 1mm \quad (3.17)$$

## 3.5 Turbulence and Sediment Diffusivity

The sediment transport equation Eq. 3.13 contains the sediment diffusivity. If the dependence of sediment diffusivity on the water-depth is known, a one-dimensional approximation of the sediment concentration in a steady flow can be obtained as the solution of Eq. 3.14. Such a solution obtained for a sediment diffusivity parabolic with water depth is called the Rouse profile. The Rouse profile is widely accepted to represent sediment concentration in a steady river flow [82, 80, 83]. Given the experience with the experimentally confirmed Rouse profile for sediment concentration, the sediment diffusivity in more complicated flows is needed to evaluate the sediment concentration therein.

The sediment diffusivity and the reference concentration Eq. 3.12 determine the concentration of suspended sediment. As explained earlier, the flow influences the reference concentration through the excess bed shear stress,  $\xi$ , defined in section 3.3. An approximation of the sediment diffusivity is needed to evaluate

### 3.5 Turbulence and Sediment Diffusivity

---

the concentration of suspended sediment at all heights above the seabed from Eq. 3.13.

The roughness of the seabed causes eddies to occur in the boundary layer [84]. In fact, diffusion of physical quantities transported by the flow, like salinity, temperature and sediment concentration, is related to the turbulent eddy viscosity, [74, 71, 84]. In the study by Holmedal et al. [84], the sediment diffusivity was approximated as the sum of the turbulent eddy viscosity and the viscosity of the fluid. The argument for this approximation is articulated by Zhang et al. [74]. The calculation of sediment diffusivity requires knowledge of the turbulent eddy viscosity, which is normally obtained from a turbulence closure model [74, 71]. The VTM does not contain an explicit eddy simulation scheme in the form of the evolution of turbulent kinetic energy, which is required to evaluate the turbulent eddy viscosity and, consequently, the sediment diffusivity.

Instead, the sediment diffusivity is treated here as a parameter in the equation of sediment transport Eq. 3.13. The inclusion of a value of sediment diffusivity calculated by a large-scale model of sediment transport to the sediment transport of the VTM was contemplated in the course of the present research. Such a possibility is, however, not feasible due to the relatively coarse resolution of common large-scale models (hundreds of metres), given the focus of the present research on small-scale phenomena (centimetres). An approximation of the sediment diffusivity by a constant can seem relatively crude, given the dynamic nature of turbulence and thus the diffusivity. Such an approximation is, however, the first step on the way to understanding the sediment transport by the wake of a TECD. A turbulence modelling scheme which would provide a realistic sediment diffusivity in the appropriate spatial scale remains among the tasks for future research.

The results presented in this dissertation might be later translated into larger-scale, far-field models, which use depth-averaged analysis. Spatial averaging of the velocity field smoothens out the small-scale features, however, the effect of the TECD on the flow could be approximated by a horizontal and a vertical velocity profiles down-stream of the device. Moreover, in a model using a greater time step the influence of the wake on the flow could be expressed by the inclusion of a source of turbulent kinetic energy into the model (given there is an explicit

turbulence scheme), if the turbulent kinetic energy was calculated from the difference between magnitude of the flow velocity averaged over the large time step and the maximum of the magnitude of the flow velocity predicted by the VTM over the larger time step. The predicted erosion due to the presence of a TECD can be also treated as a source of sediment into a large-scale sediment transport model.

## 3.6 Summary

A model of sediment uplift by the tidal flow described in section 2.4.1, has been devised. Two threshold conditions for the initiation of sediment motion were considered. The applicability of threshold models for initiation of sediment motion to small-scale unsteady flows, such as those caused by the interaction between the flow down-stream of a TECD and the seabed, is however unknown at present. The critical bed shear stress Eq. 3.3 was chosen as the primary threshold condition because of its wide-spread use to ensure the compatibility of the present study with other research on sediment motion. The secondary threshold condition Eq. 3.5 was chosen to investigate the sensitivity of the sediment model to the choice of a threshold condition. The excess bed shear stress, Eq. 3.6, Eq. 3.7, was selected as an indicator of changes in the motion of sediment. The instantaneous value of the excess bed shear stress is assumed to determine the erosion flux, the concentration of bed load and the reference concentration of suspended sediment.

The transport of sediment in the unsteady flow is governed by the transport equation for the sediment concentration Eq. 3.13. The process whereby the sediment particles leave suspension has been modelled as vertical convection by the settling velocity. The sediment diffusivity in the sediment transport equation Eq. 3.13 is treated as a parameter in the present model of sediment transport.

# Chapter 4

## TECD in Uniform Flow

The flow through the rotor of a TECD is analysed for two types of inflow models in this dissertation. The two inflow models result in qualitatively different behaviour of the wake of a TECD. The simpler of the two approaches is to set the inflow velocity as a uniform vector field. The research presented in this chapter shows, however, that the simpler approximation of the inflow velocity does not necessarily lead to a realistic representation of the influence of the TECD on the seabed. In this chapter, the results for a uniform approximation of the inflow velocity are presented. The flow through a TECD was investigated by the means of high-resolution, three-dimensional simulations conducted using the VTM, described in chapter 2.

The uniform inflow model is based on the assumption that the velocity of the inflow does not vary with water depth. The inflow velocity (which is identical to the velocity of the stream in the absence of a TECD) is assumed to be a constant vector

$$\mathbf{v}_{fs} = (V_{in}, 0, 0), \quad \forall \mathbf{x} \in \Omega, \quad (4.1)$$

where  $V_{in} = \text{const}$ . In the absence of a TECD, the stream does not contain any vorticity because the velocity of the free-stream,  $\mathbf{v}_{fs}$ , is irrotational. The uniform inflow condition Eq. 4.1 and the zero free-stream vorticity provide the simpler of the two inflow models for the VTM. Such an inflow model could be used for TECDs placed further above the seabed, where the differences between the flow velocity at the bottom of the rotor disc does not differ greatly from

---

the flow velocity at the top of the rotor disc. The gradient of the tidal velocity across the rotor thus indicates whether the inflow model Eq. 4.1 should be used to simulate the hydrodynamics of the TECD. The results presented in this chapter help to identify the limits of the uniform inflow model, and decide whether a more realistic model of the inflow, which would take into account the variation of the inflow velocity with depth, should be developed.

The high Reynolds number approximation could be seen as unsuitable for flows close to the seabed, where the viscous forces cause deceleration of the flow. To assess the erosion of the seabed by the flow in the case of the uniform free-stream velocity, the interactions between the flow and the sediment on the seabed are simulated by the sediment model, described in chapter 3.

The presence of a TECD in the uniform stream induces vorticity in the flow. The vorticity occurs as a reaction between the rotating blades and the stream. Since the free-stream contains no vorticity, the source of the tide induced wake vorticity is zero. The total vorticity in the flow is, therefore, equal to the rotor vorticity. The source of the vorticity, which is located at the rotor blades, is calculated as described in section 2.3.1.

The motion of the flow in the presence of the TECD, depicted in Fig. 4.1, is simulated by the VTM, which predicts the evolution of the rotor vorticity. The structure of the vorticity field determines the velocity field down-stream of the TECD in a uniform flow and thus the impact of the flow on the seabed. The changes in the structure of the vorticity field with the value of the inflow velocity are discussed in section 4.2. The results are analysed to establish, or otherwise, any connection between the erosion of the seabed and the structure of the vorticity field. The the evolution of the velocity field predicted by the VTM is presented in section 4.3, where a relative quantity called Relative Excess Erosion Flux (REEF) is defined and used to express the effect of the presence of the TECD on the sediment erosion flux. The limits of the uniform inflow approximation are discussed in section 4.4.

## 4.1 Specifications of the TECD

In this chapter, results of simulations conducted on a TECD which is representative of conservative design practice are presented. The TECD analysed in this chapter is a three-bladed, horizontal-axis device. The rotor is modelled as a constant-speed device, i.e. a predefined speed of rotation is assumed here. The TECD in the coordinate system used in this (and the following) chapters is shown in Fig. 4.1. The parameters of the device are listed in Table 4.1,

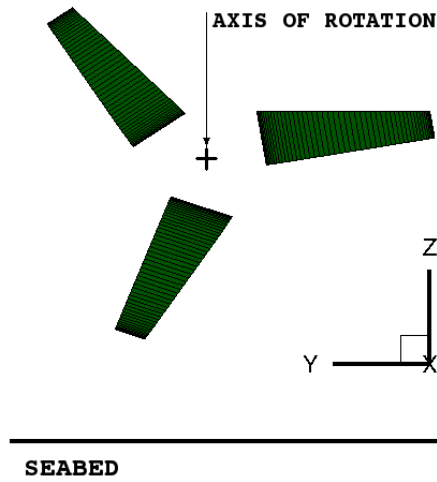


Figure 4.1: Position of the blades of the horizontal-axis TECD in the coordinate system.

$R$ [m]	$N_b$	Aerofoil	AR
5	3	NACA0012	4.65

Table 4.1: Parameters of the TECD

where  $R$  is the rotor radius,  $N_b$  is the number of blades and  $AR = l^2/S$  is the aspect ratio of the blades.  $S$  is the surface area and  $l$  is the length of the blades, which have a twist of 18.58 degrees from root to tip.

Various blade configurations have been modelled to investigate how the parameters of the rotor affect the power output of the device. The loading on the

blades for each configuration was examined and the blade parameters, i.e. chord, twist, pitch and aerofoil, were chosen such that the device has a realistic power output without compromising its structural integrity by the fluid forces. The in-flow velocity is chosen big enough to represent flow conditions suitable for power extraction. The power coefficient of the TECD is shown in Fig. 4.2 for a range of values of the tip speed ratio  $TSR = v_{tip}/v_{fs}$ . At its best operating conditions (in uniform flow 2 m/s) the TECD is capable of producing about 157 kilowatts of power. Such a device represents a community-sized TECD with approximately half of the power extracting capability of the first TECD connected to grid [85], which is deployed in northern Norway.

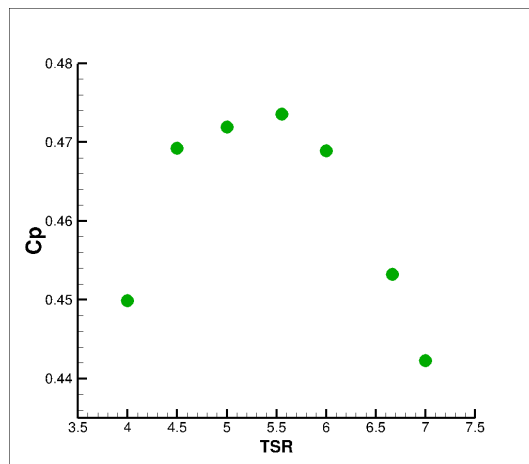


Figure 4.2: Dependence of the power coefficient of the TECD on TSR.

## 4.2 Structure of the Wake

The vorticity field induced by the presence of the TECD in a uniform flow dominates the flow down-stream of this device. Fig. 4.3 shows the evolution of the rotor vorticity field predicted by the VTM. The forces on the blades, which are rotating with a predefined speed, are calculated in the first time step, which is equivalent to the sudden appearance of the operating rotor in the previously

undisturbed flow. The vortical structure which emerges from the blades at the beginning of the simulation results from the fact that the simulations were initiated impulsively and is called the starting vortex.

Three vortex sheets which originate on the rotor blades roll up to create concentrated tip vortex filaments. The filaments form a helical structure which is transported by the flow down-stream of the rotor. The vortical structure is transported by the velocity field. The velocity field consists of the free-stream velocity and the velocity induced by the vorticity. The vortex induced velocity can locally exceed the mean velocity of the flow. A vortex filament which is affected by the high local velocities exhibits a deformation. The deformation of the vortical structure generates a ‘positive’ feedback by affecting the local flow velocity. This behaviour leads to more deformations of the vorticity structure over time. As a result, the helical vortical structure loses coherence further from the rotor. The initially regular structure eventually disintegrates into fragments of the vortex filaments. The fragments of vorticity exhibit seemingly random motion, while being transported further down-stream of the device.

The initial unsteadiness in the flow which is caused by assuming an impulsive start has little influence on the behaviour of the fully developed wake. The starting vortex dissolves at a distance down-stream of the rotor which depends on the inflow velocity. For velocities investigated in the present research the starting vortex disintegrated within the distance of  $20R$  down-stream of the rotor. Hence, when the vorticity reaches the distance of  $20R$  down-stream of the rotor, the wake is considered to be fully developed.

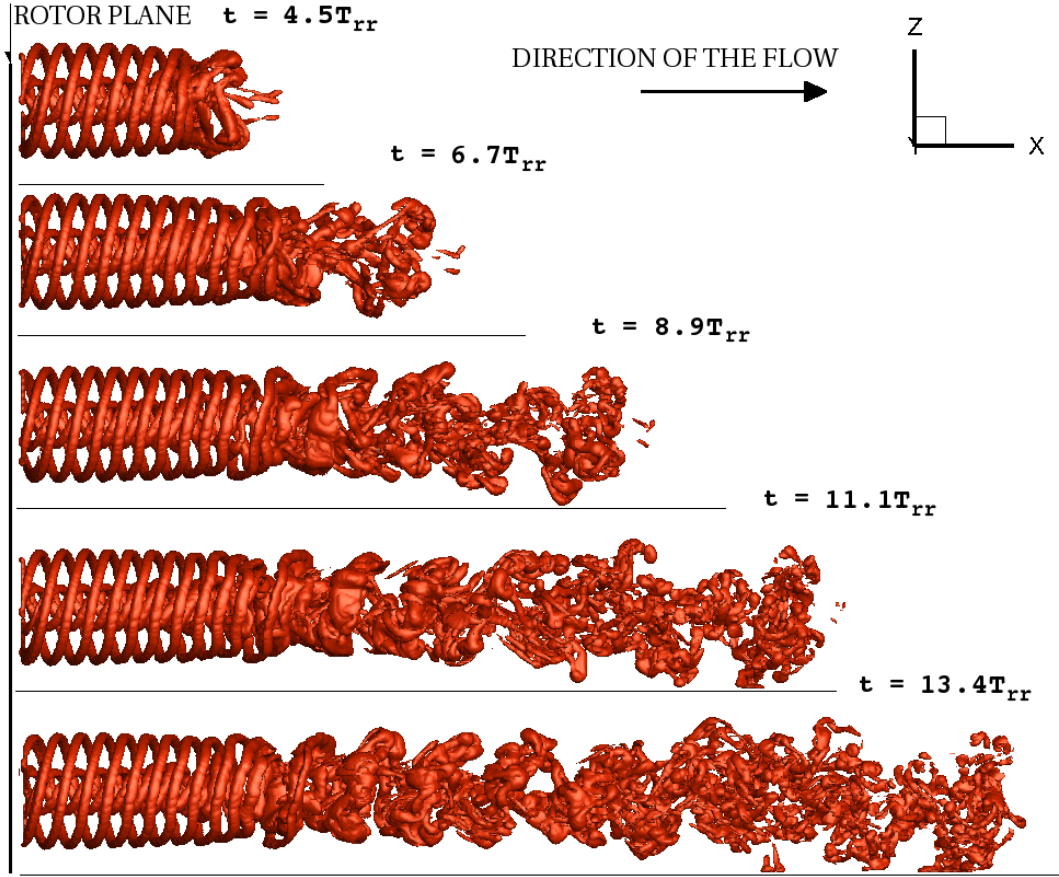


Figure 4.3: Three-dimensional representation of the rotor vorticity field evolving in time, the black lines denote the position of the seabed ( $z = 0$ ).

The strength of the vorticity field depends on the tip speed ratio. For the TECD with 5 m radius and rotational frequency  $1 \text{ rads}^{-1}$ , the velocity of the blade tip is  $v_{tip} = 5 \text{ m/s}$ . Table 4.2 contains the values of the TSR and the corresponding inflow velocities investigated in this chapter.

The relative strength of the vorticity field for the TSRs listed in Table 4.2 is illustrated in Fig. 4.4 by a surface of a constant value of the vorticity (an iso-surface) equal to 10% of the maximal magnitude of the vorticity for  $TSR = 4$ . The strength and the structure of the vorticity field varies with the TSR. The vorticity ‘filaments’ in Fig. 4.4 (the helical tubes of the presented iso-surface) appear to be thicker for faster flows, which corresponds to higher values of the

## 4.2 Structure of the Wake

---

$V_{in}$ [m/s]	0.71	0.75	0.83	0.90	1.00	1.11	1.25
<i>TSR</i>	7.00	6.67	6.00	5.56	5.00	4.50	4.00

Table 4.2: The inflow conditions represented by the TSR and the inflow velocity

magnitude of vorticity. As expected, for faster inflow the ordered helical structure is relatively longer with wider gaps between the individual loops of the filaments. The process of disintegration of the helical structure is accelerated by the mutual proximity of the filament loops. The loops formed by the filaments in slower flow are closer together. As a result, the ordered part of the wake is shorter for lower inflow velocities.

## 4.2 Structure of the Wake

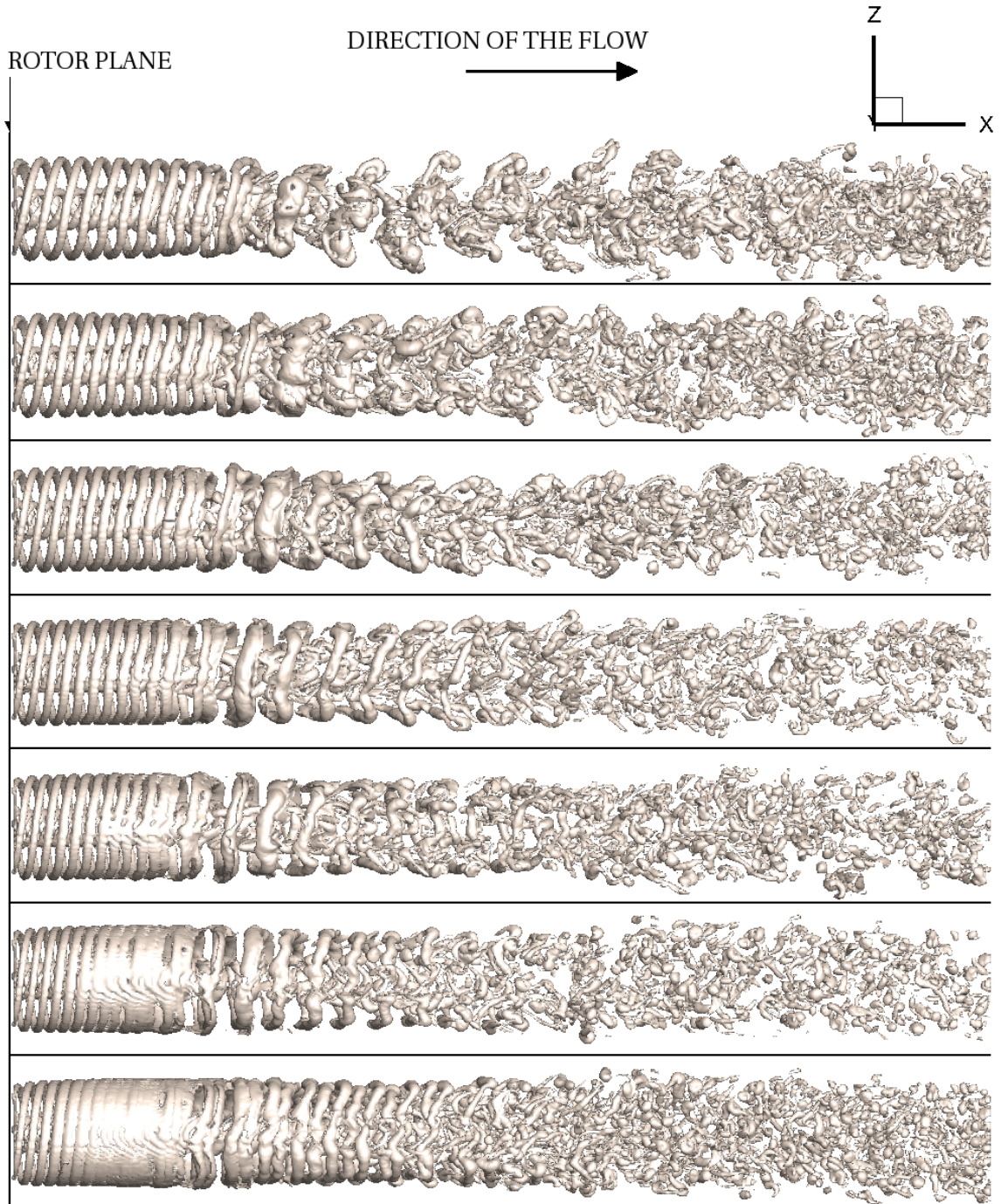


Figure 4.4: The iso-surface of the vorticity field, equal to 10% of the maximal magnitude of the vorticity for  $TSR = 4$ , of the fully developed wake; from top to bottom:  $TSR = 4, 4.5, 5, 5.56, 6, 6.67, 7$ .

The vortical structure down-stream of the rotor subjected to the inflow of 1.25 m/s (i.e.  $TSR = 4$ ) shows a high level of disintegration within a distance of 3 rotor diameters. An intermediate phase, when the loops of the filaments have been deformed by the flow but have not yet fragmented, is observable in Fig. 4.4 for TSRs higher than 5. The number of the deformed vortex loops yet to fragment increases with the TSR. The deformed loops fragment within a distance of 10 rotor diameters down-stream of the TECD for all investigated values of the TSR, and the spatial distribution of the fragmented vorticity also shows a dependence on the TSR. For higher TSRs, the filaments which originated at the roots of the blades (thus are closer to the axis of rotation) seem to disintegrate shortly before the filaments which originated at the tips of the blades. When all of the filaments have disintegrated within a few rotor diameters, most of the fragments gather into a formation which is spatially confined around the rotational axis of the TECD. A small number of fragments are, however, moving towards the seabed.

The impact of the flow down-stream of the TECD on the seabed is indicated, in Fig. 4.5, by the velocity field at the friction height of  $0.02R$ , referred to as the ‘near-bed’ velocity throughout this dissertation. The spatial distribution of the high values of the near-bed velocity is consistent with the structure of the vorticity field shown in Fig. 4.4. The near-bed velocity is influenced by both the ordered vortical structure immediately down-stream of the rotor and the fragments of the vorticity filaments approaching the seabed further down-stream of the rotor. The effect due to the ordered vortical structure predominates and the near-bed velocity exceeds the free-stream velocity immediately down-stream of the TECD for each of the TSRs listed in Table 4.2. For the inflow of  $TSR = 6.67$  and 7, however, the maximum near-bed velocity occurs further from the rotor, confined to a number of peaks disturbing the seabed.

## 4.2 Structure of the Wake

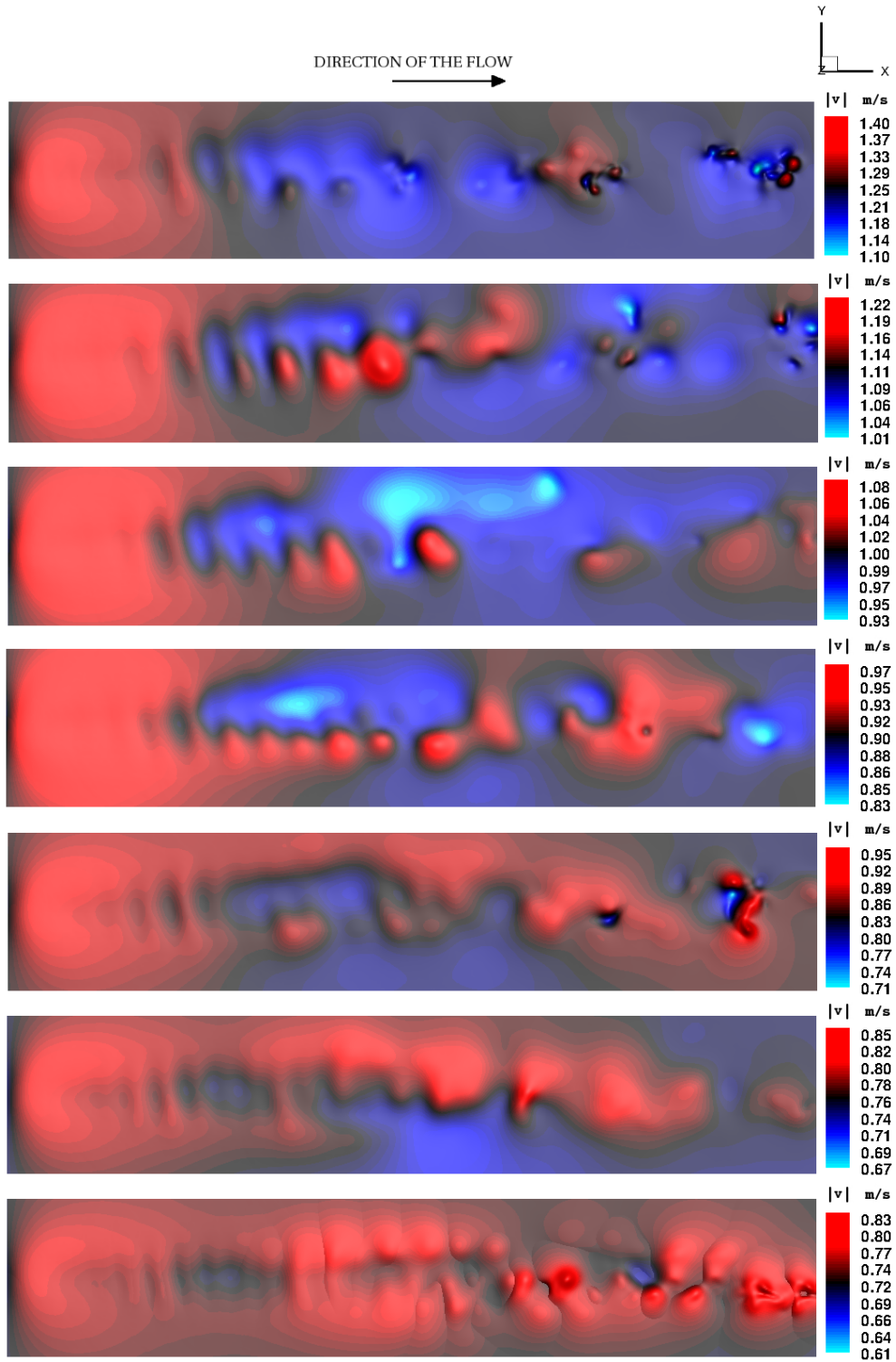


Figure 4.5: The near-bed velocity induced by the fully developed wake, from top to bottom:  $TSR = 4, 4.5, 5, 5.56, 6, 6.67, 7$ . The value of the free-stream velocity is depicted by black colour, the regions where the near-bed velocity exceeds the free-stream value are red.

The near-bed velocity, at the same time as the vorticity shown in Fig. 4.4, is depicted in Fig. 4.5. The value of the free-stream velocity is depicted in black and the regions where the near-bed velocity exceeds the free-stream velocity are depicted in red in Fig. 4.5 for each of the TSRs. The behaviour of the fully developed wake, illustrated by the vorticity and the near-bed velocity, indicates the character of the impact on the seabed. The velocity field changes in fractions of seconds together with the vorticity field, making the impact of the TECD on the seabed variable in time. The local flow velocity can change significantly in a short period of time, as a result of the rapidly moving fragments of vorticity filaments approaching the seabed. The results suggest that the variable nature of the flow down-stream of the TECD should not be neglected in the investigation of the impact of this device on the seabed.

### 4.3 Relative Erosion Flux

The near-bed velocity has been observed to vary significantly over a period of minutes. Indeed, the near-bed velocity is predicted to fluctuate between values below and above the free-stream velocity during a period of less than 50 s. The variability of the near-bed velocity over time is illustrated in Fig. 4.6 for the TSR of 4. The colour range is consistent with the top diagram in Fig. 4.5. The snapshots in Fig. 4.6 are chosen to emphasise the contrast of the extremes of the near-bed velocity.

The impact of the flow on the seabed is quantified by the erosion flux,  $E$ , defined as  $E = E_0\xi$ . The dependence of the erosion flux on the value of the empirical constant,  $E_0$ , limits the applicability of the model to the flow conditions for which the value of  $E_0$  is known. Unfortunately,  $E_0$  for the unsteady flow down-stream of a TECD or a relevant equivalent unsteady flow is not available at present.

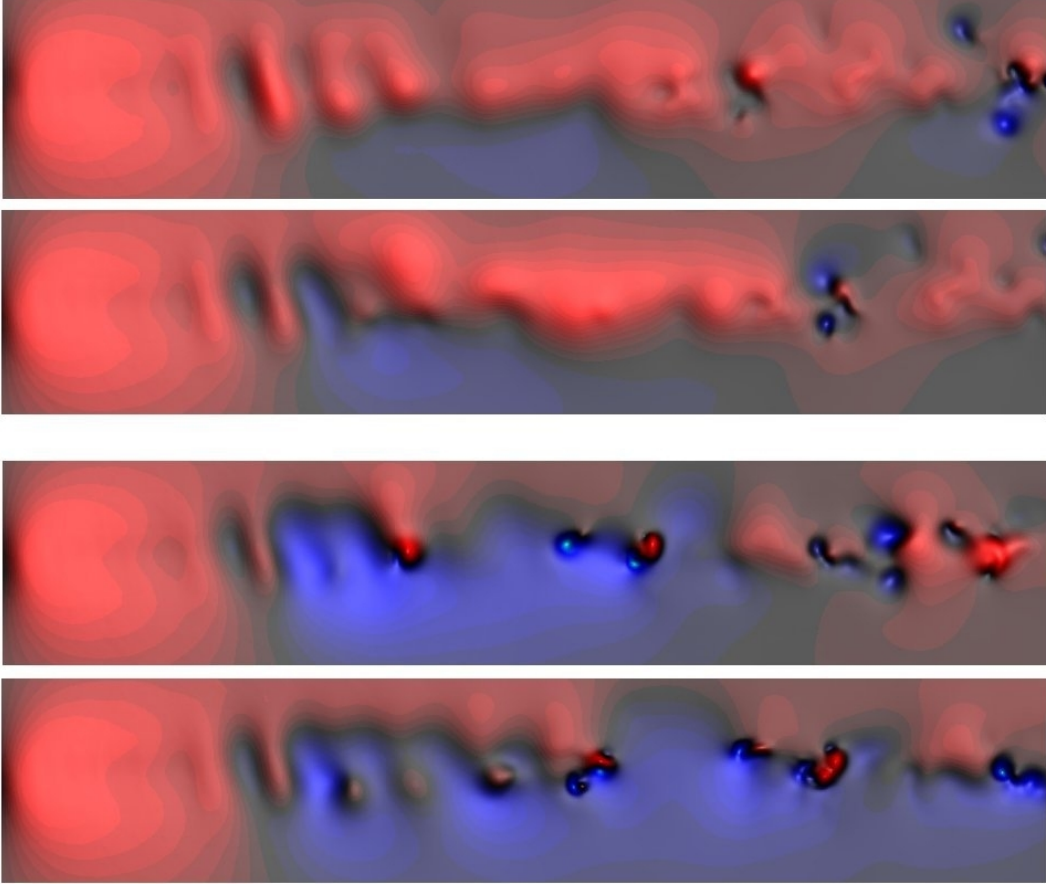


Figure 4.6: Illustration of the abrupt changes in the near-bed velocity,  $TSR = 4$ , from top to bottom:  $25.6 T_{rr}$ ,  $26.7 T_{rr}$ ,  $34.5 T_{rr}$ ,  $36.8 T_{rr}$ , where  $T_{rr}$  denotes the time of one rotor revolution.

To circumvent the need for the empirical constant,  $E_0$ , the influence of the TECD on the seabed is expressed by a relative quantity called the Relative Excess Erosion Flux (REEF)

$$R_f = \left( \frac{\bar{E}}{E_{fs}} - 1 \right), \text{ for } \bar{E} \geq E_{fs} > 0, \quad (4.2)$$

where  $\bar{E}$  is the average of the erosion flux over the studied area of the seabed. The REEF can be used as an indicator of the change in the seabed erosion due to the TECD when the free-stream is strong enough to erode the seabed ( $E_{fs} > 0$ ). The REEF indicates the relative difference between the erosion of the seabed

### 4.3 Relative Erosion Flux

due to the TECD and the erosion which would have been caused by the uniform free-stream in the absence of the TECD.

The behaviour of the REEF has been investigated with the anticipation of observing a pattern in the evolution of the erosion flux caused by the presence of the TECD, a pattern which would have been observed for all the investigated TSRs. For example, the REEF could have been found to reach a representative value which could have been then taken as a measure of the impact on the seabed. Or, if the REEF were periodic in time, its frequencies and its amplitude could have been used to indicate the impact. The REEF has been recorded throughout the simulation for the values of the TSR listed in Table 4.2. Among other parameters, the impact on the seabed is thought to be influenced by the distance of the rotor from the seabed. To study this influence, the simulation of the flow through the TECD was conducted for two positions of the rotor hub,  $1.5R$  and  $1.2R$ , above the seabed. The evolution of the REEF is depicted in Fig. 4.7 - Fig. 4.13. The REEF for  $z_{hub} = 1.5R$  does not exceed 6.3%, while the REEF for  $z_{hub} = 1.2R$  is smaller than 3.5%, for any of the TSRs listed in Table 4.2.

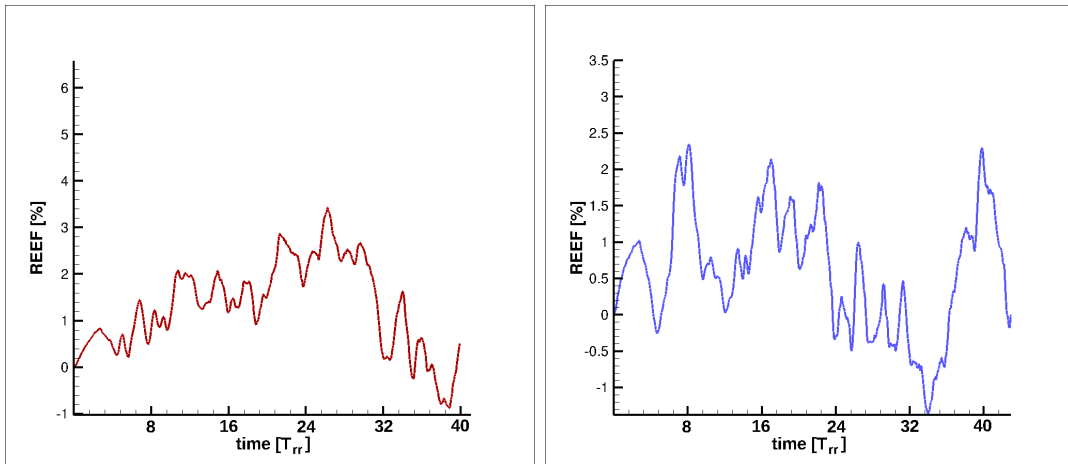


Figure 4.7: REEF for  $TSR = 4$ , left:  $z_{hub} = 1.5R$ , right:  $z_{hub} = 1.2R$ .

### 4.3 Relative Erosion Flux

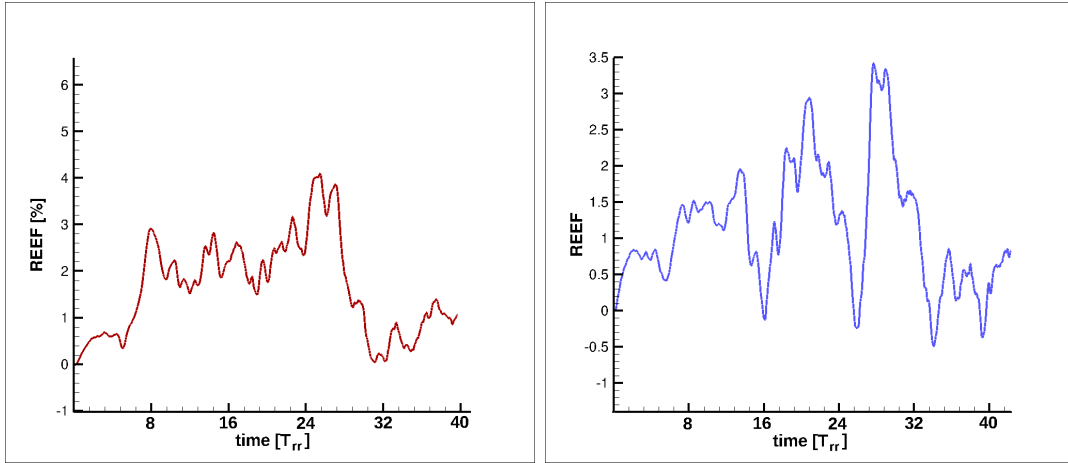


Figure 4.8: REEF for  $TSR = 4.5$ , left:  $z_{hub} = 1.5R$ , right:  $z_{hub} = 1.2R$ .

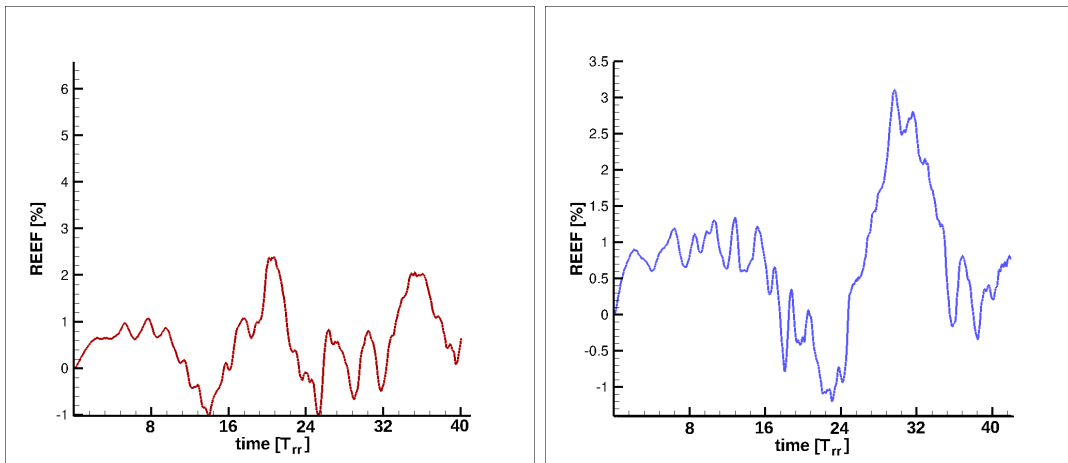


Figure 4.9: REEF for  $TSR = 5$ , left:  $z_{hub} = 1.5R$ , right:  $z_{hub} = 1.2R$ .

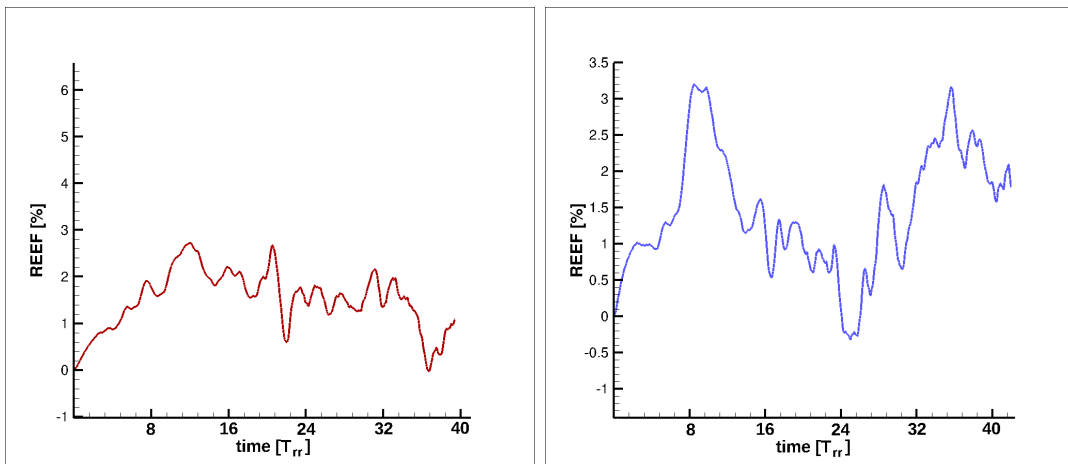


Figure 4.10: REEF for  $TSR = 5.56$ , left:  $z_{hub} = 1.5R$ , right:  $z_{hub} = 1.2R$ .

### 4.3 Relative Erosion Flux

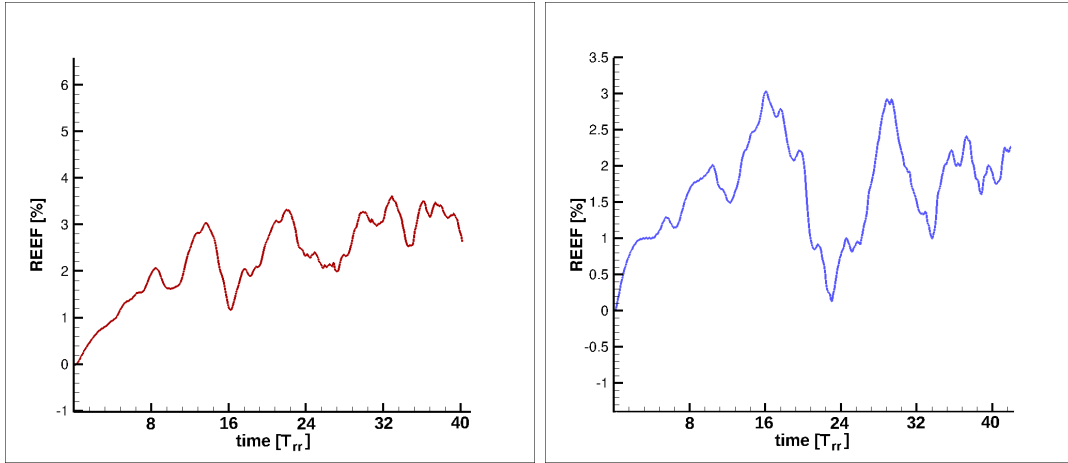


Figure 4.11: REEF for  $TSR = 6$ , left:  $z_{hub} = 1.5R$ , right:  $z_{hub} = 1.2R$ .

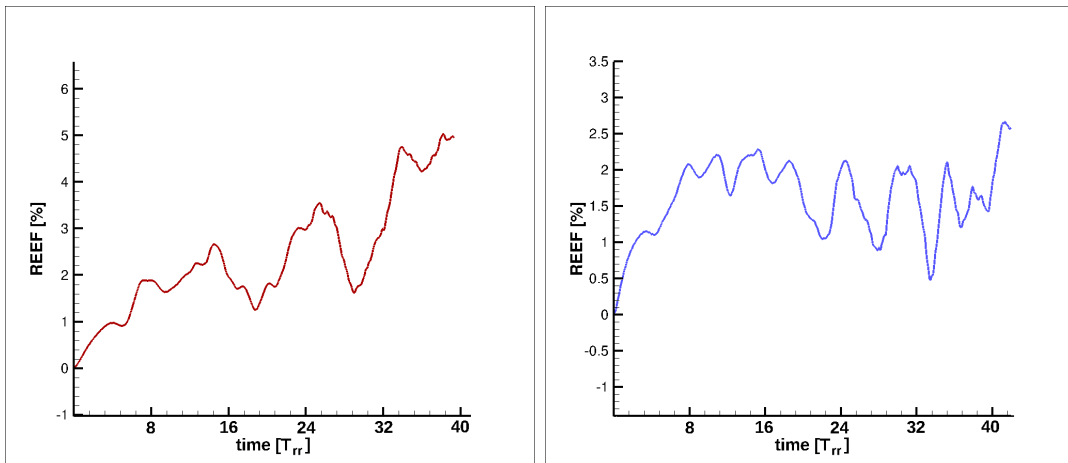


Figure 4.12: REEF for  $TSR = 6.67$ , left:  $z_{hub} = 1.5R$ , right:  $z_{hub} = 1.2R$ .

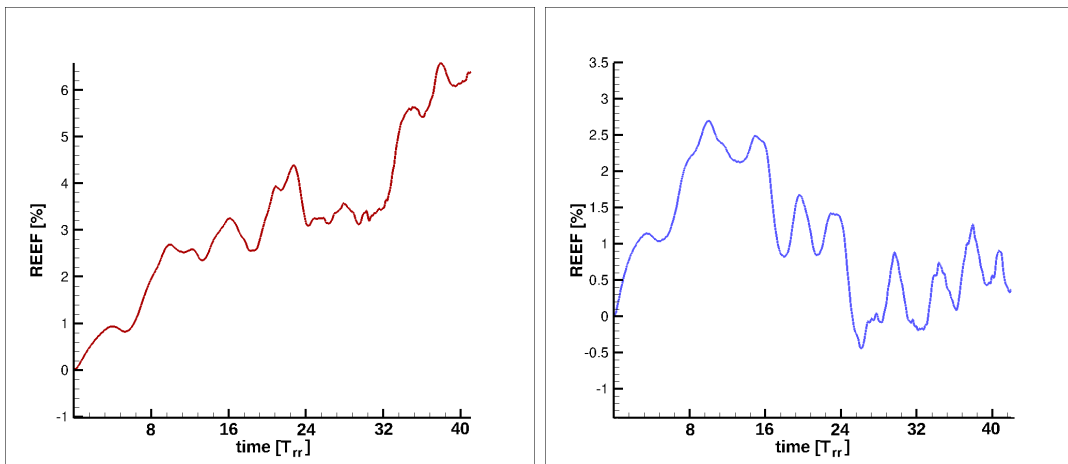


Figure 4.13: REEF for  $TSR = 7$ , left:  $z_{hub} = 1.5R$ , right:  $z_{hub} = 1.2R$ .

The curves in Fig. 4.7 - Fig. 4.13 reflect the fluctuations of the near-bed velocity, caused by fragments of the vortex filaments approaching the seabed. The positive values of the REEF indicate a promotion and the negative values of the REEF indicate a reduction in the sediment erosion relative to the erosion by the uniform free-stream in the absence of a TECD. The REEF attains positive but also negative values over the studied period of time. The fluctuations in the REEF reveal the uncertainty in the impact of the TECD on the seabed.

After more than 250 s of the simulation time have passed (equivalent to approximately 4 months of run time), it has become clear that from the available information about the temporal variation of the REEF, that it is not possible to describe the REEF as periodic in time with a number of characteristic frequencies. The typical run times of the VTM are presented in appendix B. In fact, none of the investigated uniform inflow cases resulted in a pattern in the evolution of the REEF. The REEF evolution appears to be a stationary process, i.e. the data do not follow any trends and have time-invariant mean. The wake of the TECD in uniform flow has thus been deemed unlikely to reach a quasi-steady state, represented by a pattern in the evolution of the REEF.

The REEF is averaged over the time interval,  $[t_0, t_{END}]$ , where  $t_0$  is the point when the wake reaches the fully developed state and  $t_{END}$  is the end of the simulation. The fluctuations of the REEF, observed in Fig. 4.7 - Fig. 4.13, are used to define the (un-)certainty of the mean value (sometimes referred to as the confidence interval). Fig. 4.14 depicts the temporal mean of the REEF. The error bars in Fig. 4.14 denote the confidence intervals. The error bars which extend below zero suggest that the outcome of the simulation is inconclusive, since the TECD could cause promotion as well as reduction of the sediment erosion in comparison with the free-stream erosion. Although the mean of the REEF seems to increase with the TSR in the case when the TECD is mounted  $1.5R$  above the seabed, the large fluctuations in the REEF over the time of the simulation make the assessment of the impact of the TECD on the erosion difficult.

## 4.4 Motivation for Tidal Flow Simulations

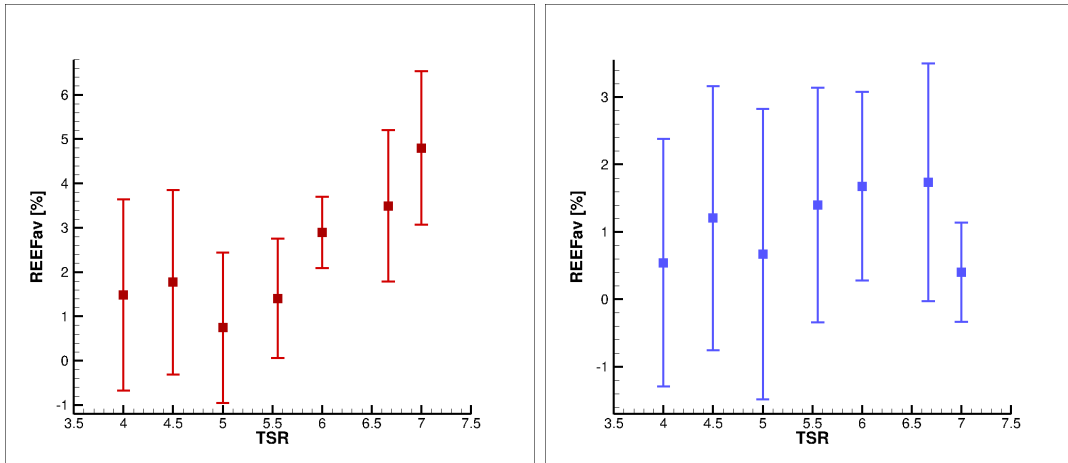


Figure 4.14: The mean value of REEF of the fully developed wake, left:  $z_{hub} = 1.5R$ , right:  $z_{hub} = 1.2R$ .

A possibility of investigating the REEF further would be to generate a number of REEF curves from the results of the VTM's simulations for perturbed initial conditions (for example for the inflow velocity  $1.00 + 0.01k$  m/s for  $k = -5, \dots, 5$ ). This range of the REEF data could then be averaged and the mean REEF could be used to represent the impact of the TECD on the seabed for the uniform inflow of 1 m/s. The simulations would be required to run long enough to cover the period of wake development and beyond to capture the fluctuations in the REEF. For such a statistical study of the REEF, however, considerable computer resources would need to be allocated. Indeed, a single VTM simulation of the wake of the TECD which encompass 250 s required a run-time of a number of months. Hence, the generation of reliable statistical REEF data is not practical with the present level of computer resources.

## 4.4 Motivation for Tidal Flow Simulations

Although the study of the flow down-stream of the TECD presented in this chapter provided initial insight into the interactions between the wake of the TECD and the seabed, the simulations revealed a number of aspects of the model indicating the inadequacy of the uniform inflow approximation.

In a real flow, the velocity near the seabed decreases because of the friction between the seabed and the flow. The flow in proximity of the seabed forms a boundary layer. A more realistic inflow model should reflect the viscous nature of the seawater by simulating a boundary layer flow. The decrease of the velocity close to the seabed could have an effect on the flow down-stream of the TECD. Such an effect is neglected by the uniform inflow approximation.

The flow close to the seabed is responsible for the erosion of the sediment. Once the sediment is lifted from the seabed, the nature of the flow velocity in the boundary layer determines the subsequent motion of the sediment. The model of sediment transport by the flow down-stream of the TECD should include the effects caused by the boundary layer to provide a realistic assessment of the interactions within the TE system. The uniform inflow approximation applied to sediment transport could result in an unrealistic distribution of the sediment concentration.

The simulations of a TECD in a uniform flow did not yield a connection between the environmental conditions and the motion of sediment. Such a connection could have led to a quantification of the impact of the TECD on the seabed. A possible reason why the simulations presented in this chapter did not lead to a better understanding of the environmental impact of TECDs is that the uniform inflow model was too simplistic, as discussed above. To investigate this possibility, the model of the flow through the rotor of a TECD needed to be modified to include the effects of an inflow velocity which decreases in the vicinity of the seabed.

## 4.5 Summary

The first TECD presented in this dissertation is a three-bladed, horizontal-axis, constant-speed device. The horizontal-axis TECD (referred to as the HATT) is representative of conservative design practice. The flow down-stream of this device and its interactions with the seabed were investigated for two positions of the rotor,  $1.2R$  and  $1.5R$ , above the seabed and a range of inflow conditions, listed in Table 4.2.

The wake of the HATT simulated by the VTM contains vorticity, induced by the presence of the device in the flow. The vorticity field is composed of filaments, which form a helical structure immediately down-stream of the rotor, whose strength depends on the TSR. The helical vortex structure becomes deformed further from the rotor. As the vorticity is transported down-stream, the deformed filaments disintegrate, leaving behind a cluster of fragments of the vorticity filaments. The fragments aggregate near the axis of the rotor for higher values of the TSR. The distance from the rotor where the helical structure starts to disintegrate also depends on the TSR.

The interactions between the flow down-stream of the HATT and the seabed are determined by the near-bed velocity, which is influenced by the structure of the vorticity field for all investigated values of the TSR. Indeed, the near bed velocity exceeds the free-stream velocity in the region immediately down-stream of the rotor, due to the presence of the helical vortical structure. For low values of the TSR the highest values of the near-bed velocity are to be found further from the rotor. The instantaneous near-bed velocity is used to evaluate the erosion flux. The influence of the HATT on the erosion of the seabed was expressed by the Relative Excess Erosion Flux (REEF). The mean of the REEF of the fully developed wake indicates the impact of the device on the seabed under the uniform inflow approximation, and the fluctuations in the evolution of the REEF are used to determine the confidence interval of the mean. The large confidence intervals suggest that the REEF can be positive as well as negative, implying the possibility of either a promotion or a reduction of the sediment erosion flux. The uncertainty in the mean value of the REEF leads to the conclusion that the uniform inflow approximation may not be suitable for the purpose of the assessment of the interaction within the TECD-Environment (TE) system.

The uniform inflow approximation was supposed to simplify the investigation of the environmental impact of the TECD. The results indicate, however, that this simplification was rather counter-productive since the outcome of the research presented in this chapter is inconclusive. The results presented in this chapter motivated the implementation of a more realistic model of tidal flow into the VTM, described in chapter 2, to achieve a better understanding of the environmental impact of TECDs.

# Chapter 5

## TECD in Tidal Flow

In the previous chapter, the flow through the rotor of a TECD was presented for the uniform inflow model. A more realistic approach is to model the inflow velocity as decreasing in proximity to the seabed. In this chapter, the results for a more realistic, non-uniform approximation of the inflow velocity are presented. Fig. 5.1 depicts the velocity at the rotor plane, which illustrates the inflow conditions used to represent the tidal flow. The flow through the TECD was investigated by the means of high-resolution, three-dimensional simulations conducted using the Vorticity Transport Model, described in chapter 2, equipped with the inflow model defined in section 2.4.1.

The inflow velocity is taken to depend on the water depth so that

$$\mathbf{v}_{fs} = (V_{in}(z), 0, 0), \quad (5.1)$$

where  $z > 0$ . The velocity profile,  $\mathbf{v}_{fs}$ , was defined to model the boundary layer flow which is observed near a solid surface. In the simplified case of the rotor plane parallel to a straight shoreline and the tidal stream perpendicular to the shoreline, the seabed would be eroded in the ‘to-shore’ direction during the flood tide and in the ‘from-shore’ direction during the ebb tide. The simplified geometry of the tidal current adopted here could also be relevant for TECDs placed into strong streams between two islands (or an island and the mainland). Generally, the position of the area of the seabed most affected by the TECD depends on the direction of the tidal current. The velocity profile is a non-negative, monotonically

---

increasing, concave function of  $z$ , i.e.

$$\frac{\partial^k V_{in}}{\partial z^k} \geq 0 \text{ for } k = 0, 1 \quad (5.2)$$

and

$$\frac{\partial^2 V_{in}}{\partial z^2} \leq 0, \quad (5.3)$$

above the seabed, so that the inverse function,  $z(V_{in})$ , is convex. The dependence of the magnitude of the inflow velocity on the distance between the rotor and the seabed is presented in Fig. 5.2.

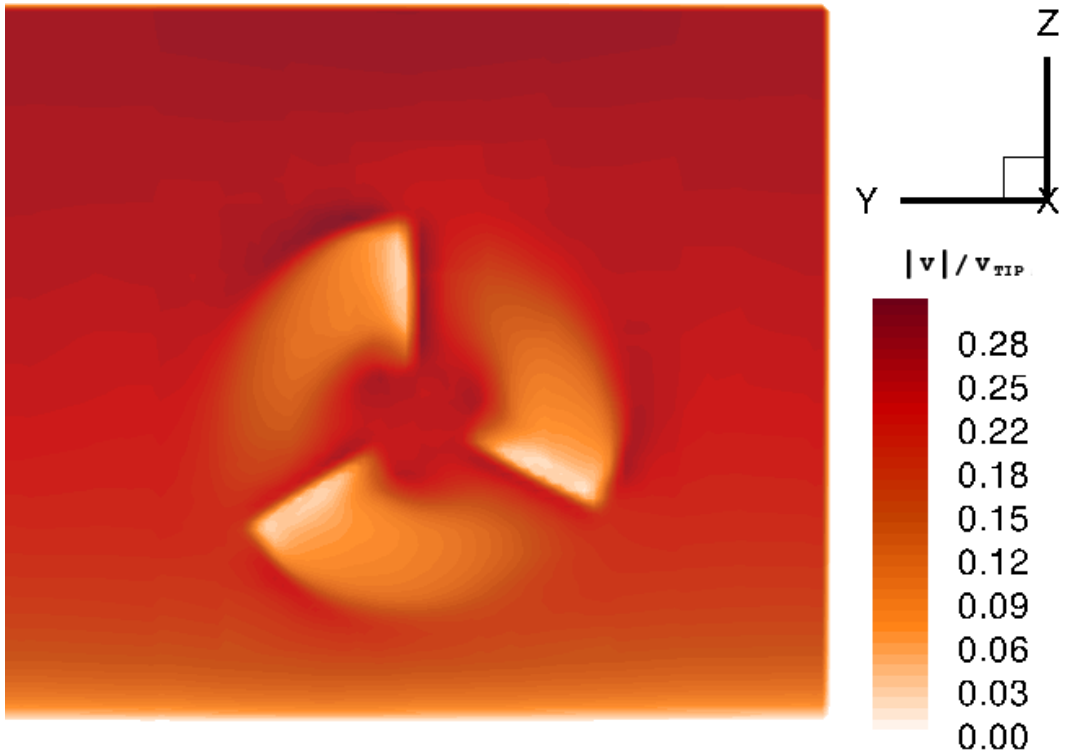


Figure 5.1: The velocity of the flow at the rotor plane ( $x = 0$ ),  $v_{hub}/v_{tip} = 0.2$ ,  $z_{hub} = 1.5R$ ,  $R = 5$  m.

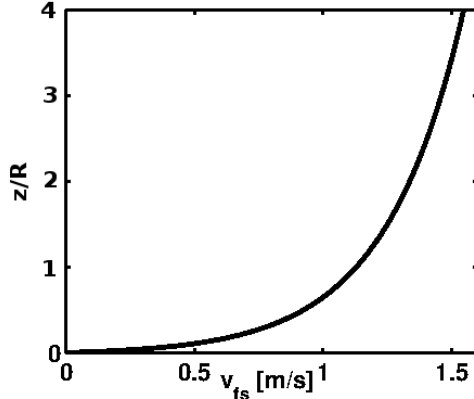


Figure 5.2: Boundary layer flow for  $v_{hub} = 1.25$  m/s.

The dependence  $z(V_{in})$  could be expressed by a number of functions. Among the models used in the literature, the most common is a logarithmic curve [78]. The model used here relies on a semi-empirical velocity profile, which was obtained by McIntosh et al. [86] from the velocity measurements in the Falls of Warness in the Pentland Firth, conducted by the EMEC. The semi-empirical velocity profile was a logarithmic curve taking into account surface roughness [87]. The range of the heights above the seabed where the velocity was measured did not include the heights below 0.5 m, however. The semi-empirical velocity profile was modified in the region close to the seabed to satisfy the no-slip condition on the seabed. The resulting modified velocity profile is

$$V_{in}(z) = A \log \left( \frac{z}{k_s} + 1 \right) \quad (5.4)$$

where  $k_s$  is an empirical constant. The value of  $A$ ,

$$A = \frac{v_{hub}}{\log \left( \frac{z_{hub}}{k_s} + 1 \right)}, \quad (5.5)$$

is chosen so that the inflow velocity at the rotor hub,  $v_{hub}$ , together with the condition that inflow velocity is zero on the seabed, determine  $V_{in}(z)$ . The velocity at the rotor hub,  $v_{hub}$ , is treated as an input parameter to the VTM.

---

Since the inflow velocity is not uniform, the free-stream (the stream in the absence of a TECD) contains free-stream vorticity

$$\omega_{fs} = (0, W_{in}(z), 0), \quad (5.6)$$

as explained in chapter 2.4. For the chosen form of the velocity profile it follows that

$$W_{in}(z) = \frac{A}{z + k_s}. \quad (5.7)$$

The free-stream vorticity as a function of  $z$  is illustrated in Fig. 5.3.

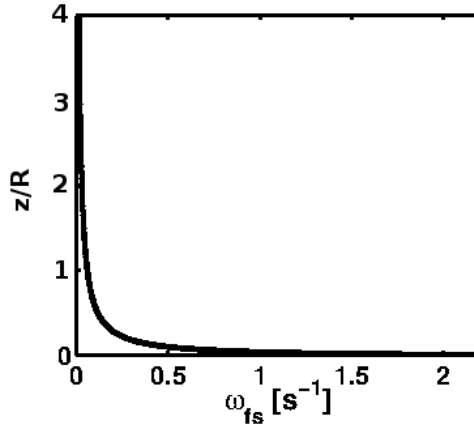


Figure 5.3: Free-stream vorticity for  $v_{hub} = 1.25$  m/s.

The free-stream vorticity appears in the flow due to the interaction between the flow and the seabed. The existence of this vorticity requires an addition into the VTM, which is necessary for the assessment of the impact of a TECD on the seabed. This vorticity is represented in the VTM via the formalism described in section 2.4. For the example of the inflow shown in Fig. 5.2 -Fig. 5.3 the free-stream vorticity decreases below  $0.1s^{-1}$  at the heights greater than 10 m above the seabed. If the rotor of a TECD was placed further than  $2R$  above the seabed, the flow down-stream could be sufficiently well approximated by the uniform inflow simulations discussed in chapter 4. Surface effects could however be found to alter the flow down-stream of a TECD in shallow water [88], and potentially contribute to the variability of the stresses on the seabed. Further work in this direction is proposed in section 7.2.

---

The presence of a TECD in the boundary layer induces vorticity in the flow down-stream of the device. The total vorticity field comprises the free-stream vorticity, the rotor vorticity and the tide induced wake vorticity. The tide induced wake vorticity,  $\omega^*$ , is defined as a solution of Eq. 2.63, and is identified with the influence of the velocity profile on the flow down-stream of the rotor, while the rotor vorticity,  $\omega_w$ , is analogous to the vorticity field in the uniform inflow case. The velocity field used to transport vorticity in Eq. 2.62 differs, however, from the velocity field used in Eq. 2.13, as explained in section 2.4.3. The source of the rotor vorticity is obtained from Eq. 2.1. The source of the tide induced wake vorticity is calculated from Eq. 2.60. The results presented here are for the same horizontal-axis TECD as in chapter 4, section 4.1, referred to as the HATT. In this chapter, the investigation of the role of the inflow velocity in the interactions within the TE system is presented. The non-uniform inflow velocity results in a qualitative change of the flow down-stream of the HATT in comparison with the uniform inflow case. The free-stream vorticity and the tide induced wake vorticity fields could affect the seabed significantly by inducing or reducing bed shear stress in comparison with the case of uniform inflow, in which neither of the two vorticity fields exists. The total vorticity field,  $\omega = \omega_{fs} + \omega_w + \omega^*$ , was studied to uncover the nature of the interactions between the flow down-stream of the HATT and the seabed.

The structure of the flow down-stream of the HATT, which determines the stresses on the seabed, is described in section 5.1. A measure of the impact of the HATT on the seabed, the excess bed shear stress is presented in section 5.2. The changes in the flow down-stream of the HATT during the tidal cycle, and the consequent changes of the excess bed shear stress, which are important for a long-term assessment of the impact, are presented in section 5.3. The degree to which the position of the HATT in the boundary flow influences the environmental impact of the device is described in section 5.4. Finally, the concentration of sediment in the flow down-stream of the HATT, described in section 3.4, and the variation of the sediment concentration with the sediment parameters, are presented in section 5.5.

## 5.1 Structure of the Wake

The flow down-stream of the HATT simulated by the VTM with the uniform inflow model, discussed in chapter 4, contains the rotor vorticity field. Similarly, the flow down-stream of the HATT, simulated by the VTM with the non-uniform inflow model Eq. 5.4, contains the vorticity field induced by the presence of the rotor in the flow. The vorticity filaments originate on the blades of the rotor and are transported down-stream by the flow, forming a helical structure immediately down-stream of the rotor. In contrast to the uniform inflow case, however, the vertical gradient of the inflow velocity causes the helical vorticity structure to incline because the vorticity closer to the seabed is transported more slowly than the vorticity further above the seabed. Moreover, the rotor vorticity field is transported approximately one rotor radius further from the seabed than is the case for uniform inflow due to the vertical gradient of the inflow velocity. This contrast is illustrated in Fig. 5.4 where the rotor vorticity for the uniform inflow model is compared to the rotor vorticity field for the velocity profile. The horizontal black lines in Fig. 5.4 denote the position of the seabed.

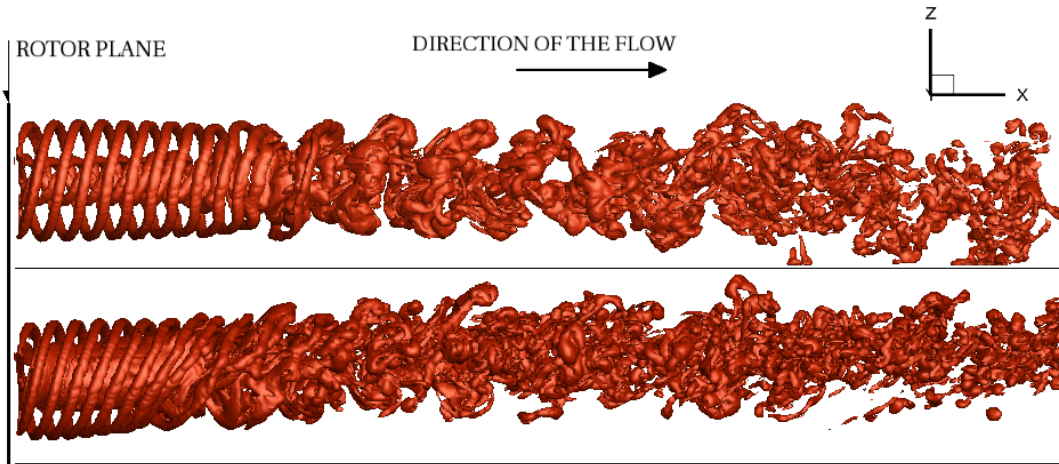


Figure 5.4: Comparison of the rotor vorticity field for the two inflow models, top: uniform inflow velocity,  $V_{uniform} = 1.25$  m/s, bottom: the velocity profile,  $v_{hub} = 1.25$  m/s.

The evolution of the rotor vorticity field is shown in Fig. 5.5. The vortex

## 5.1 Structure of the Wake

filaments assembled in the helical structure become increasingly inclined with distance down-stream of the rotor. The inclined helical structure starts to disintegrate down-stream of the HATT in less than 40 s of the simulation time at a distance approximately  $5R$  from the rotor plane. Consistently with the definition used in chapter 4, once the vorticity reaches  $20R$  down-stream of the rotor, the wake is considered to be fully developed. The size of the computational grid used in the modified VTM is presented in appendix A.

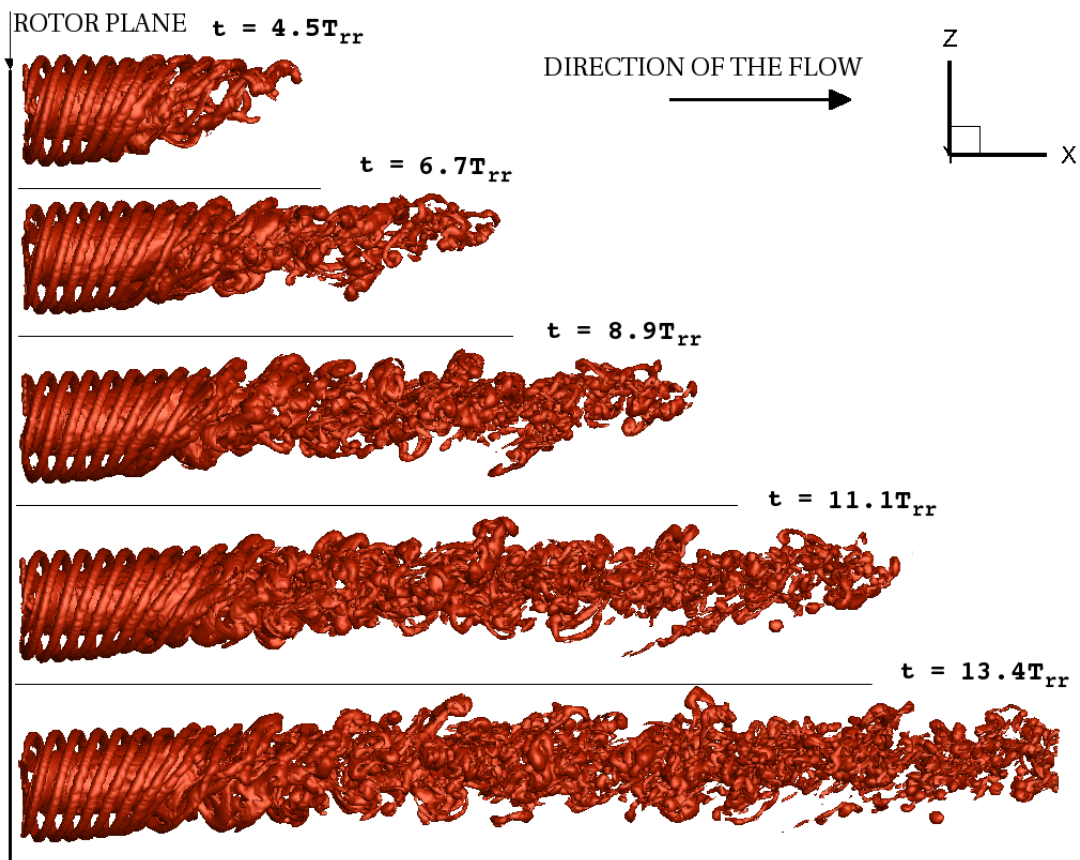


Figure 5.5: Illustration of the evolution of the rotor vorticity field, calculated by the modified VTM.

An example of the fully developed wake is shown in Fig. 5.6 and Fig. 5.7. The component of the vorticity field which represents the interaction between the free-stream and the rotor vorticity fields, called the tide induced wake vorticity, is

presented in Fig. 5.7. The maximal magnitude of the tide induced wake vorticity is less than 2% of the maximal magnitude of the rotor vorticity for the example presented in Fig. 5.6 (i.e. for  $v_{hub} = 1$  m/s and  $z_{hub} = 1.5R$ ). The flow downstream of the HATT is thus most influenced by the rotor vorticity.

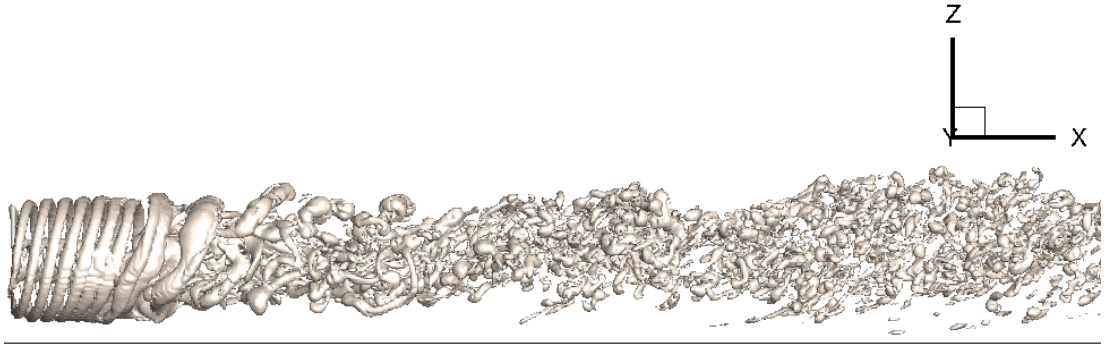


Figure 5.6: The rotor vorticity field of the fully developed wake,  $v_{hub} = 1$  m/s and  $z_{hub} = 1.5R$ .



Figure 5.7: The tide induced wake vorticity of the fully developed wake, planar section perpendicular to the seabed and the rotor plane,  $v_{hub} = 1$  m/s and  $z_{hub} = 1.5R$ .

Understanding the behaviour of the induced vorticity field beyond the point of disintegration is the key to understanding the environmental impact of the HATT. The fragments of the inclined vortical structure are transported away from the seabed by the flow, as shown in Fig. 5.5. Consequently, the inclination of the vorticity field results in a reduction of the influence of the fragments of the vortex filaments on the seabed in comparison with the uniform inflow case.

## 5.2 Excess Bed Shear Stress

The impact of the HATT on the erosion of the seabed is related to the near-bed velocity, i.e the velocity responsible for the uplift of sediment. The near-bed velocity varies in time in relation to the motion of the vortical structure. The temporal changes in the near-bed velocity are illustrated in Fig. 5.8. The region

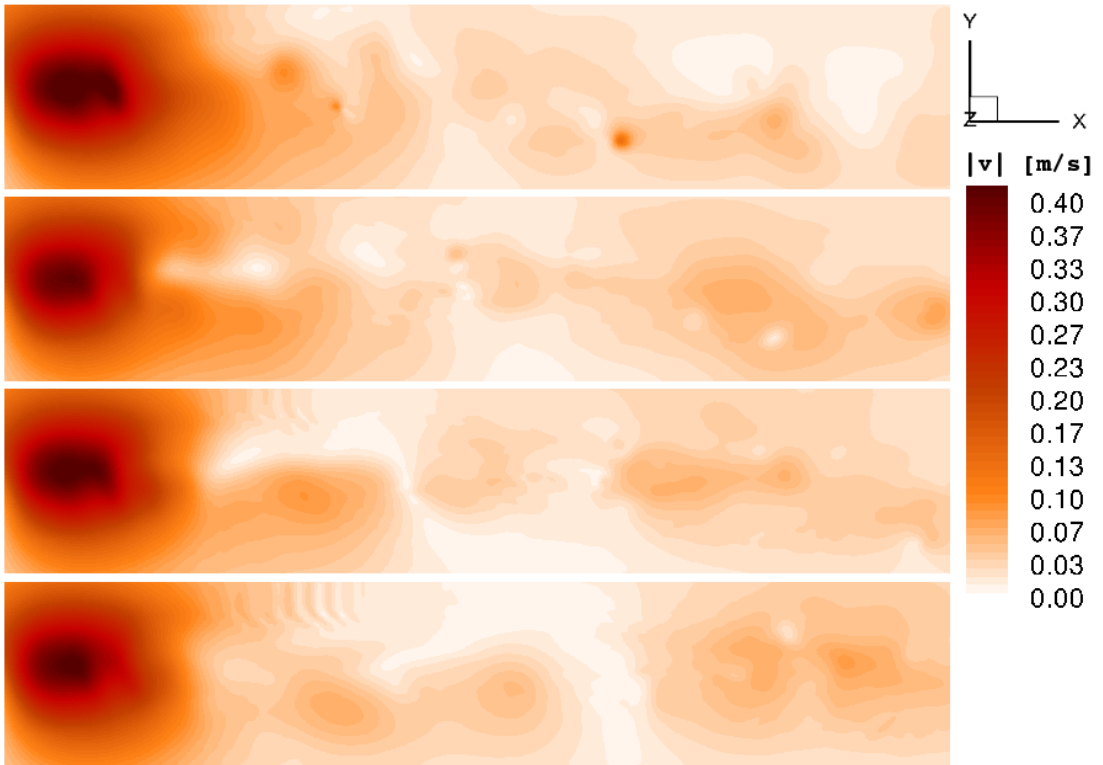


Figure 5.8: The near-bed velocity,  $v_{hub} = 1$  m/s and  $z_{hub} = 1.5R$ , from top to bottom:  $t = 20.2 T_{rr}$ ,  $27.9 T_{rr}$ ,  $32.3 T_{rr}$ ,  $36.8 T_{rr}$ , where  $T_{rr}$  denotes the time of one rotor revolution.

in which the near-bed velocity is greater than the free-stream velocity, shown in Fig. 5.8, is smaller in comparison with the location of high near-bed velocities observed for the uniform inflow approximation in Fig. 4.6.

When comparing the result for the uniform inflow a problem arises. The free-stream value of the erosion flux, Eq. 3.8, is zero when the inflow is approximated by the velocity profile, unlike in the case of the uniform inflow. If the free-stream

## 5.2 Excess Bed Shear Stress

erosion flux were positive, the relative excess erosion flux  $R_f = (\xi/\xi_{fs} - 1)$  would be used to indicate the impact of the flow down-stream of the HATT on the seabed. When the seabed is not eroded by the free-stream ( $\xi_{fs} = 0$ ), however, the relative excess erosion flux cannot be defined. Hence, another quantity, introduced in section 3.3, the excess bed shear stress,  $\xi$ , is chosen as a measure of the impact of the flow on the seabed.

The excess bed shear stress (EXSS) depends on the near-bed velocity. The spatial distribution of the EXSS is depicted in Fig. 5.9. The EXSS becomes large

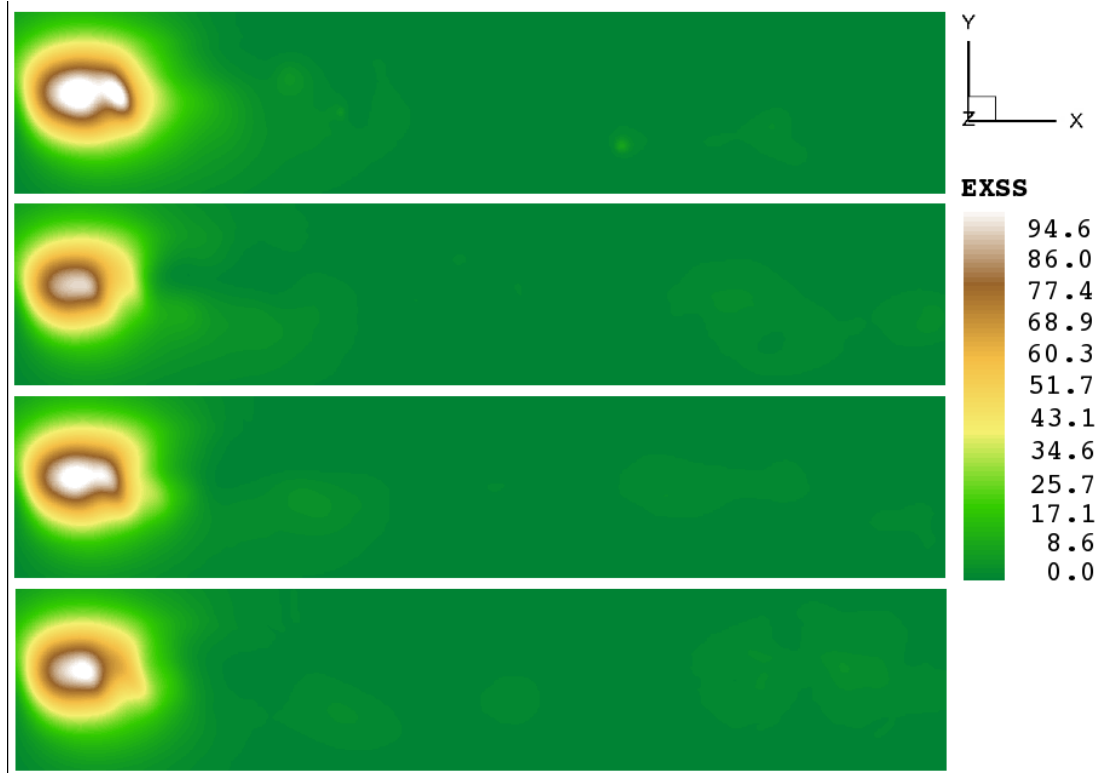


Figure 5.9: The excess bed shear stress,  $v_{hub} = 1$  m/s and  $z_{hub} = 1.5R$ , from top to bottom:  $t = 20.2 T_{rr}$ ,  $27.9 T_{rr}$ ,  $32.3 T_{rr}$ ,  $36.8 T_{rr}$ .

in the region immediately down-stream of the rotor. The high EXSS is caused by the ordered part of the rotor vorticity field (i.e. the helical structure before disintegration) in Fig. 5.6. An occasional spike in the EXSS further from the rotor can occur when a vorticity fragment approaches the seabed. The majority of the vorticity fragments are transported away from the seabed by the flow, however.

The EXSS, averaged over the studied area of the seabed is shown in Fig. 5.10. The initial increase of the averaged excess bed shear stress (AEXSS) corresponds to the establishment of the ordered part of the wake, illustrated by Fig. 5.5. The start of the fluctuations of the AEXSS around a mean value coincides with the disintegration of the ordered vortical structure observed in Fig. 5.5. The evolution of the AEXSS, illustrated in Fig. 5.9, reveals that the HATT promotes the erosion of the seabed in comparison with the free-stream erosion.

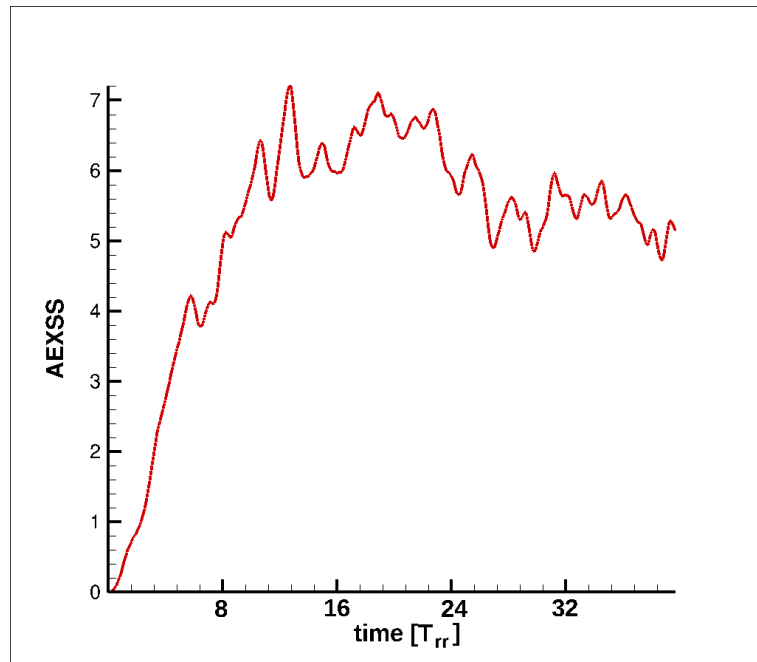


Figure 5.10: The averaged excess bed shear stress,  $v_{hub} = 1$  m/s and  $z_{hub} = 1.5R$ .

The relation between the phase of the tidal cycle and the EXSS, which is needed for an assessment of the impact of the HATT on the marine environment over the tidal cycle, is presented in section 5.3. The change of the impact with the position of the HATT is addressed in section 5.4, where a dependence of the EXSS on the distance of the rotor from the seabed is described.

## 5.3 Tidal Cycle

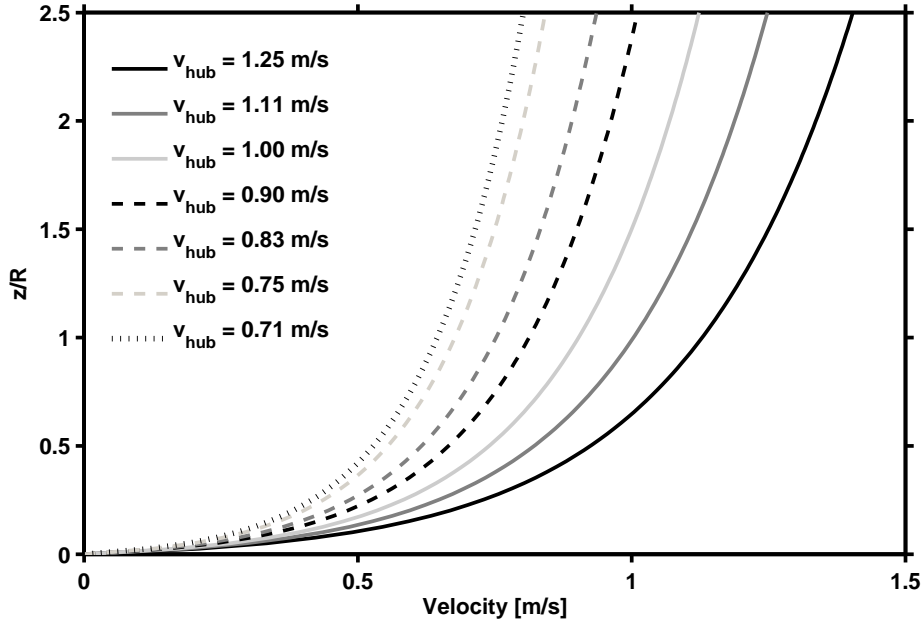


Figure 5.11: Set of velocity profiles used to represent subsequent stages of the tidal cycle,  $z_{hub} = 1.5R$ ,  $R = 5$  m.

The tidal velocity changes very slowly in comparison to the abrupt changes in the local velocity field down-stream of the HATT. Based on data presented in Morris et al. [49], the change of the tidal velocity at 10 m above the seabed per the time scale characteristic for wake development would be  $\partial \mathbf{v}_{fs} / \partial t \approx 10^{-2} \text{ m s}^{-2}$ . The influence of such a small quantity on the flow down-stream of the HATT can be safely omitted from consideration, and the inflow velocity can be approximated as time-invariant during the simulation. The details of the approximation are presented in chapter 2, section 2.4.3. The time-invariant inflow velocity is used to represent a phase of the tidal cycle. The tidal cycle can then be approximated by a set of consecutive velocity profiles. Such a representation of the tidal cycle can be found in Morris et al. [49], and the velocity profiles, which represent a later stage of the flood-tide in the Severn estuary site [49], are similar to the inflow conditions in Fig. 5.11.

In an analogy to the tip speed ratio defined for the uniform inflow, the ratio between the rotational speed of the blade tips and the inflow velocity at the rotor hub,  $v_{tip}/v_{hub}$ , is used to characterize the inflow conditions. The inflow velocity at the rotor hub is set so that  $v_{hub} = V_{uniform}$ , where  $V_{uniform}$  denotes the values of the inflow velocity investigated for the uniform inflow approximation. The resulting set of velocity profiles is depicted in Fig. 5.11.

The relationship between the power coefficient, which represents the power extracted by the HATT with respect to the power available in an uniform flow with speed  $v_{hub}$ , and the phases of the tidal cycle is illustrated in Fig. 5.12.

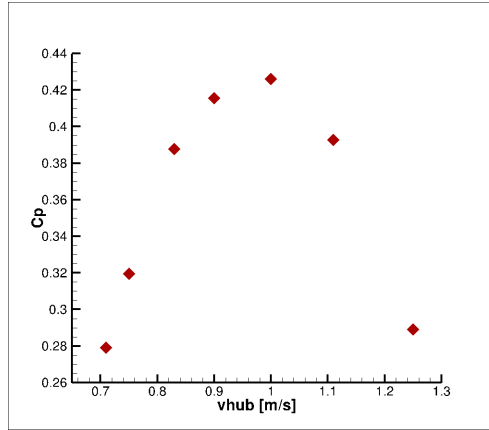


Figure 5.12: The power extracted by the HATT with respect to the power available in an uniform flow of speed  $v_{hub}$ .

The difference of the inflow velocity across the rotor,  $\Delta v_{2R}$ , defined as

$$\Delta v_{2R} = v_{fs}(z_{hub} + R) - v_{fs}(z_{hub} - R), \quad (5.8)$$

is presented in Table 5.1 for the set of velocity profiles in Fig. 5.11. From Eq. 5.4 it follows that  $\Delta v_{2R} = 0.383v_{z_{hub}}$  for  $R = 5$  m and  $z_{hub} = 1.5R$ , and this relationship is illustrated in Fig. 5.13.

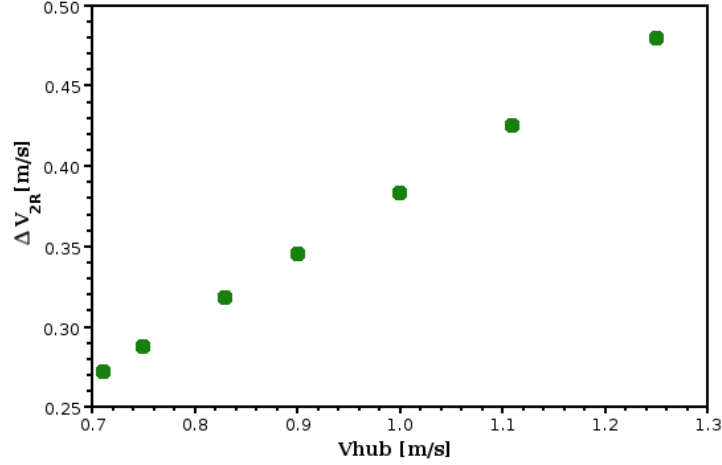


Figure 5.13: The difference of the inflow velocity across the HATT.

$v_{tip}/v_{hub}$	7.00	6.67	6.00	5.56	5.00	4.50	4.00
$v_{hub}$ [m/s]	0.71	0.75	0.83	0.90	1.00	1.11	1.25
$\Delta v_{2R}$ [m/s]	0.27	0.29	0.32	0.35	0.38	0.43	0.48

Table 5.1: The inflow conditions in relation to the difference of the inflow velocity across the rotor.

The rotor vorticity field, predicted by the VTM for the range of the inflow conditions listed in Table 5.1, is depicted in Fig. 5.14. Similarly to the rotor vorticity field in the uniform inflow simulations presented in chapter 4, the filaments of vorticity in Fig. 5.14 are closer together and the maximal magnitude of the vorticity is smaller for slower inflow. Furthermore, the inclination angle and strength of the vorticity filaments are higher for higher  $v_{hub}$ . The vortical structure is most inclined for the largest inflow velocity ( $v_{hub} = 1.25$  m/s), an important feature as the level of the inclination influences the interactions between the filaments and, consequently, their motion. The inner geometry of the rotor vorticity field is illustrated by the planar section which is perpendicular to the seabed and the rotor plane, in Fig. 5.15. This planar section is referred to as the ‘y-slice’ for convenience.

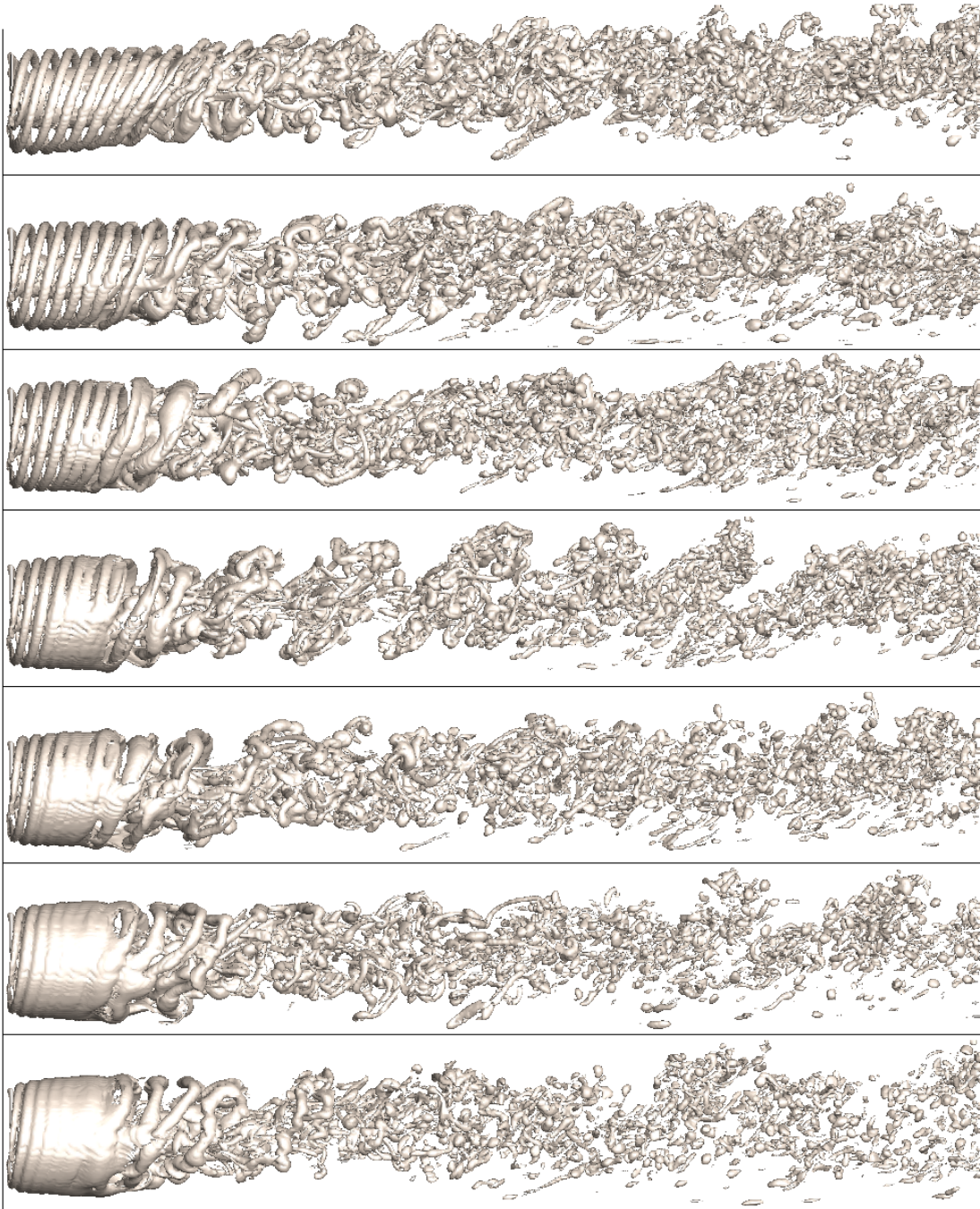


Figure 5.14: The rotor vorticity field of the fully developed wake, from top to bottom:  $v_{tip}/v_{hub} = 4, 4.5, 5, 5.56, 6, 6.67, 7$ .

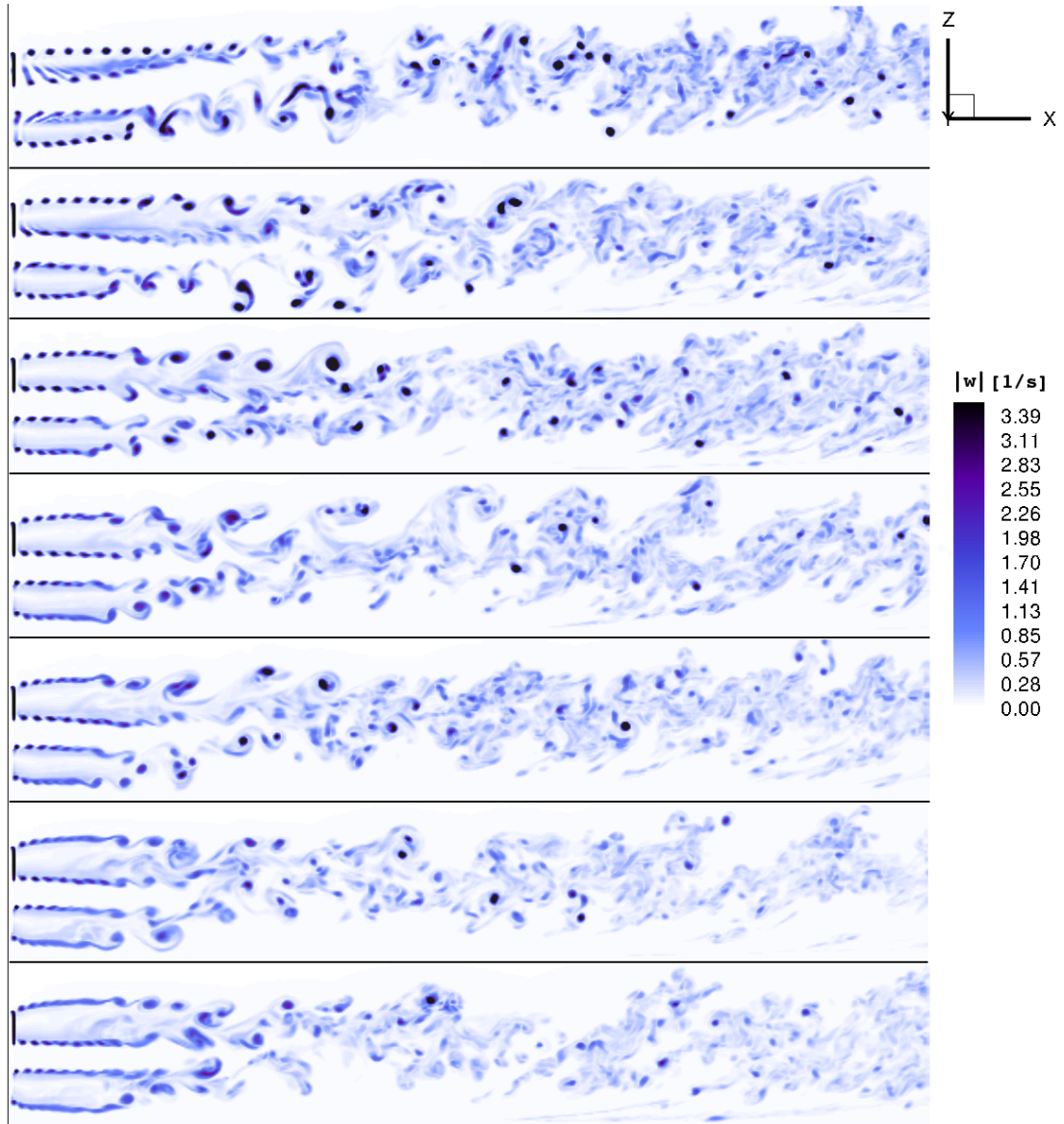


Figure 5.15: Y-slice of the rotor vorticity field of the fully developed wake, from top to bottom:  $v_{tip}/v_{hub} = 4, 4.5, 5, 5.56, 6, 6.67, 7$ .

The tide induced wake vorticity corresponding to the cases presented in Fig. 5.15 is depicted in Fig. 5.16. The magnitude of the tide induced wake vorticity is less than 2% of the maximal magnitude of the rotor vorticity field for all investigated velocity profiles. In comparison, the maximal value of the free-stream vorticity is less than 10% of the maximal magnitude of the rotor vorticity

predicted by the VTM. In other words, the rotor vorticity reaches a higher magnitude than the tide induced vorticity and the free-stream vorticity combined.

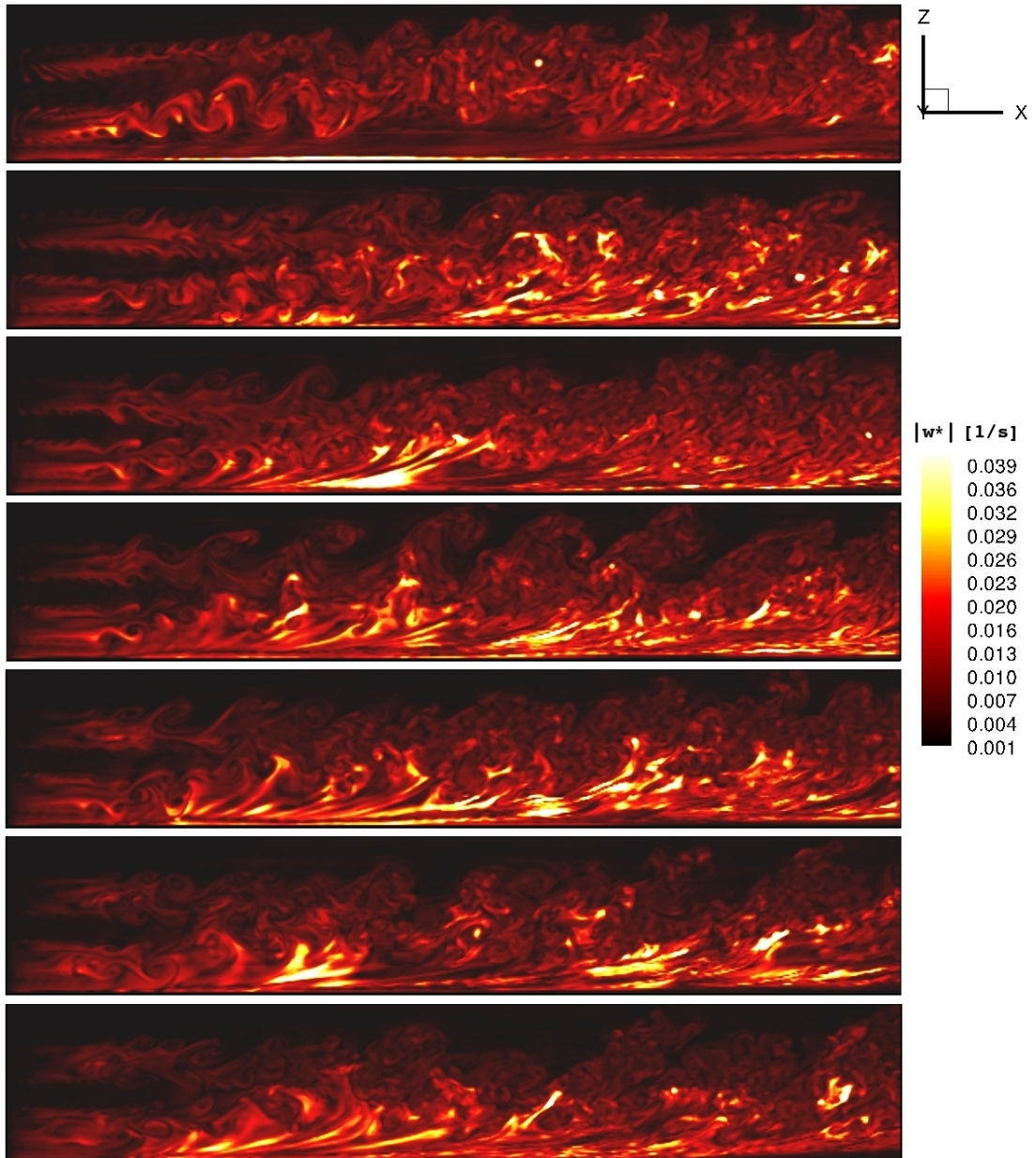


Figure 5.16: Y-slice of the tide induced vorticity field of the fully developed wake, from top to bottom:  $v_{tip}/v_{hub} = 4, 4.5, 5, 5.56, 6, 6.67, 7$ .

The vorticity field affects the flow close to the seabed, which is responsible for erosion of sediment. The structure of the vorticity field varies with the inflow, so does the near-bed velocity. The near-bed velocity, shown in Fig. 5.17, determines the EXSS, depicted in Fig. 5.18. The erosion flux depends on the EXSS through  $E = E_0\xi$ . It is, however, the empirical constant  $E_0$  which is needed for evaluation of the absolute value of the erosion flux. Hence, the erosion flux induced by a TECD can be estimated only after the  $E_0$  for unsteady flows governed by small-scale vortical structures is obtained.

The size of the most affected area of the seabed is related to the dimension of the rotor for all investigated velocity profiles. The spatial distribution of the excess bed shear stress suggests that the greatest impact of the HATT is to be expected in two areas of the seabed on either side of the rotor plane, associated with the ebb and flood parts of the tidal cycle. The size of the impacted areas is proportional to the square of the rotor radius. The effect on the seabed varies with the strength of the inflow, or in other words, with the phase of the tidal cycle.

To uncover patterns in the evolution of the EXSS, its average over the studied area of the seabed (denoted as the AEXSS) is presented in Fig. 5.19 for the inflow conditions listed in Table 5.1. The common feature of the evolution of the AEXSS is the initial increase associated with the development of the rotor vorticity field illustrated in Fig. 5.5. The AEXSS increases during the formation of the helical structure in the wake, and starts to fluctuate once the vorticity filaments begin to disintegrate. Although the data presented in Fig. 5.19 fluctuate, the value of the mean averaged excess bed shear stress (MAEXSS) of the fully developed wake is larger than the maximum of the fluctuations.

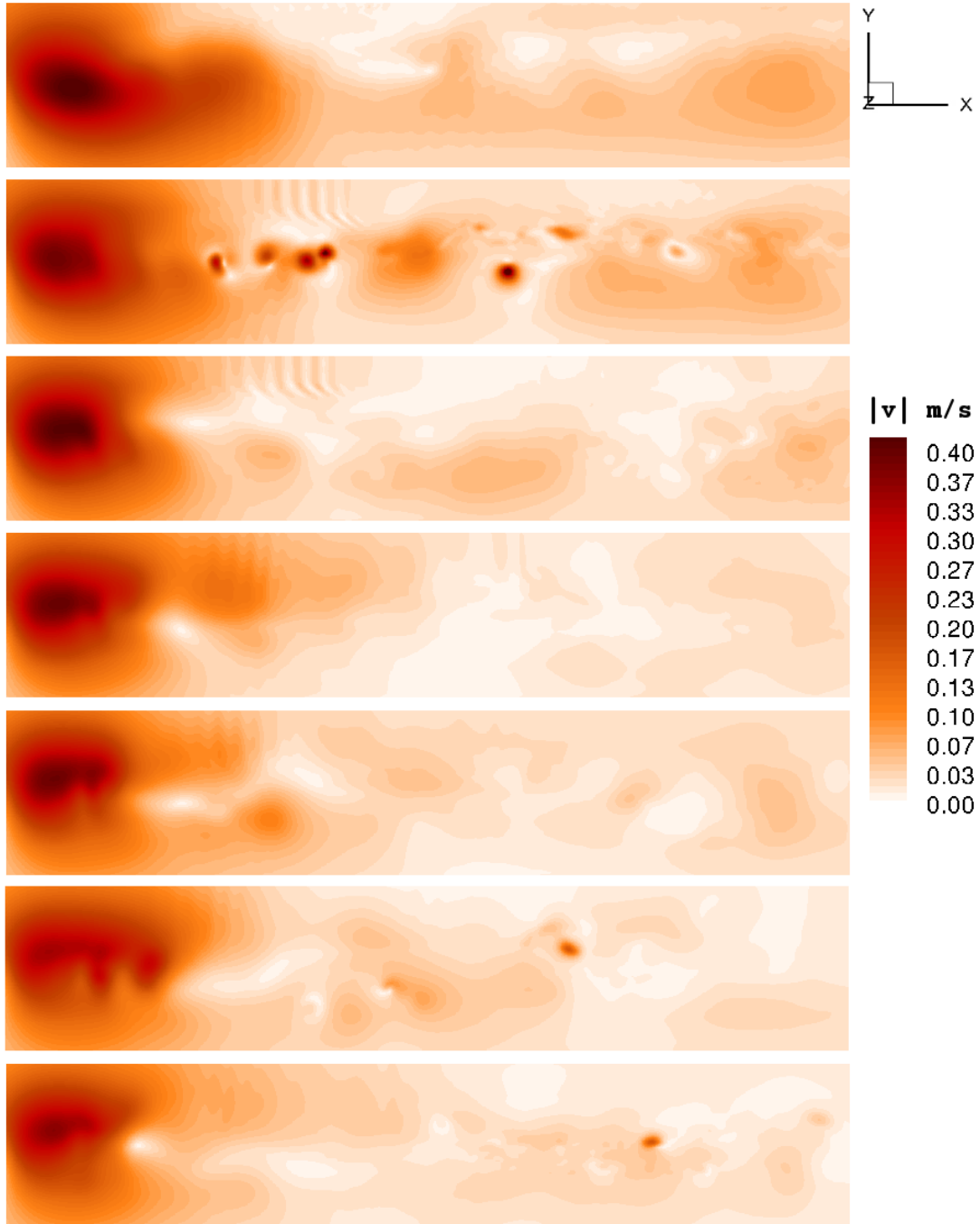


Figure 5.17: The near-bed velocity of the fully developed wake, from top to bottom:  $v_{tip}/v_{hub} = 4, 4.5, 5, 5.56, 6, 6.67, 7$ .

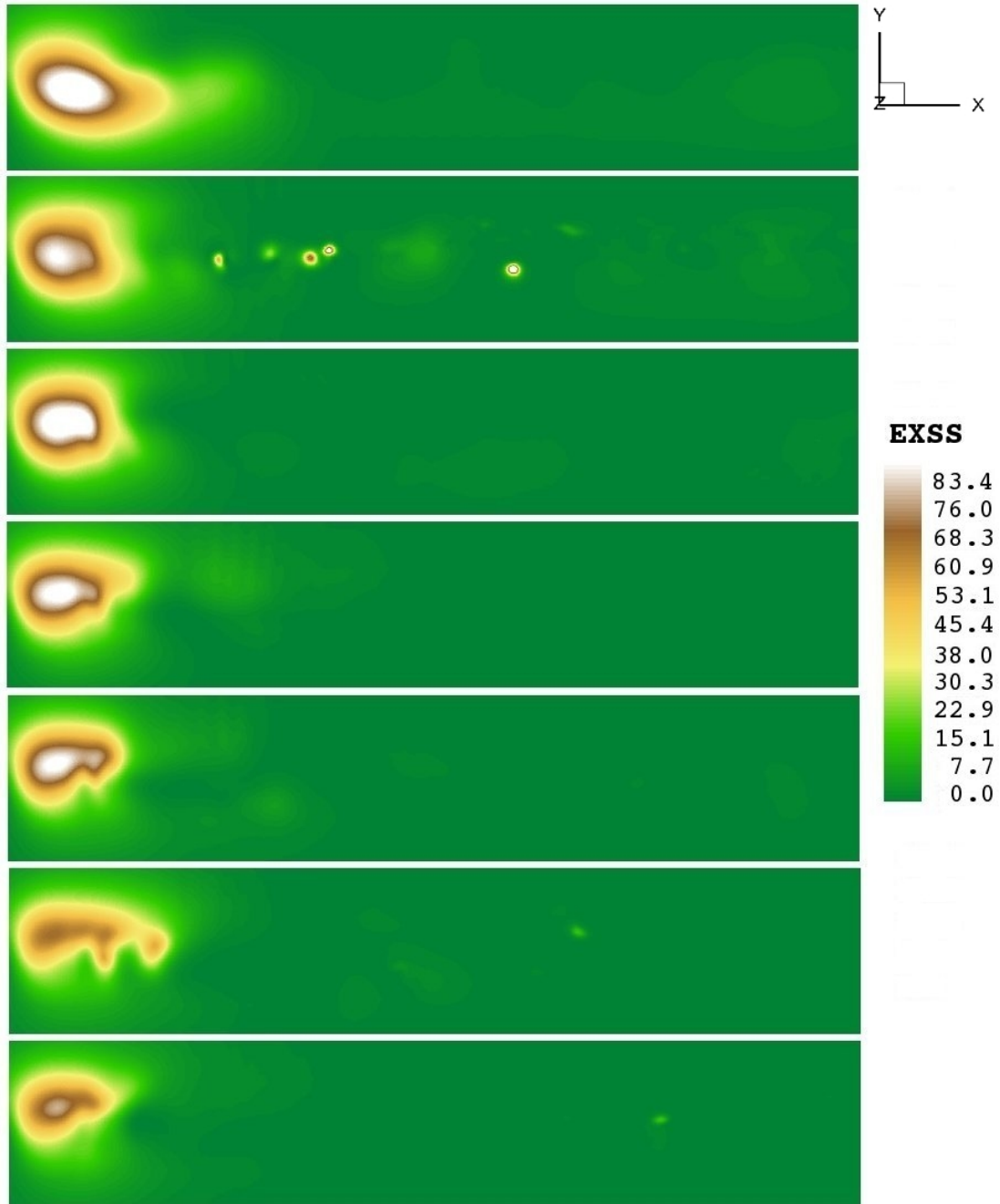


Figure 5.18: The excess bed shear stress once the wake is fully developed, from top to bottom:  $v_{tip}/v_{hub} = 4, 4.5, 5, 5.56, 6, 6.67, 7$ .

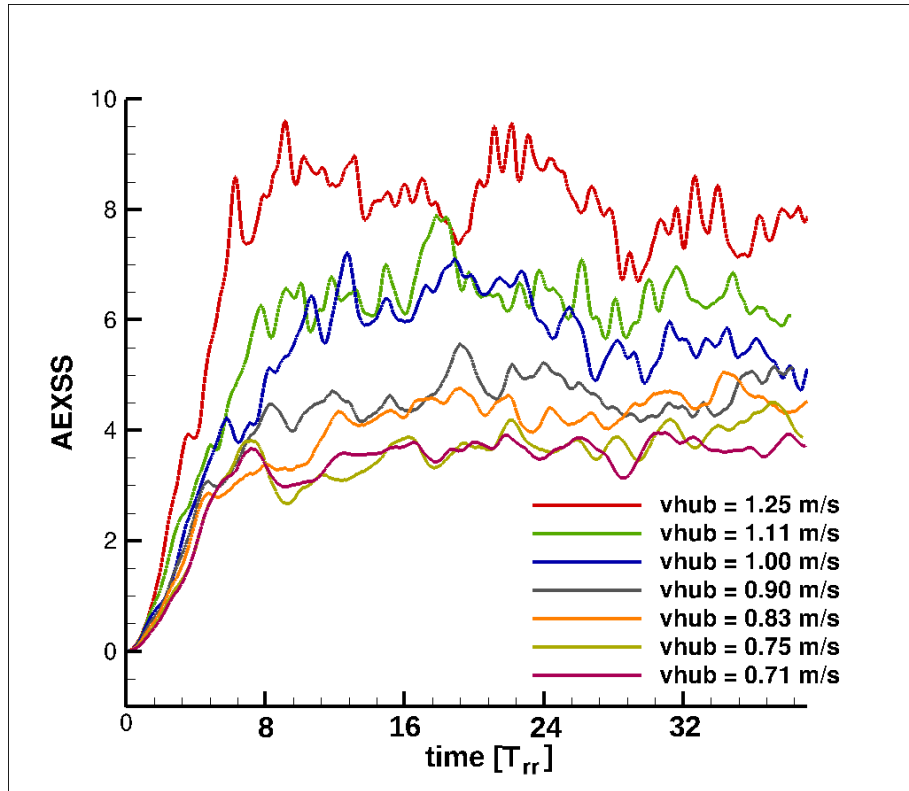


Figure 5.19: The AEXSS evolution for the HATT for the inflow conditions listed in Table 5.1.

The mean of the fluctuations is chosen to represent the impact of the fully developed wake on the seabed. The dependence of the MAEXSS on the inflow velocity is presented in Fig. 5.20. An estimate of the fluctuations in the AEXSS around the mean can be obtained as the difference between the maximal and the minimal AEXSS occurring between the point of establishment of the fully developed wake,  $t_0$ , and the end of the simulation,  $t_{END}$ .

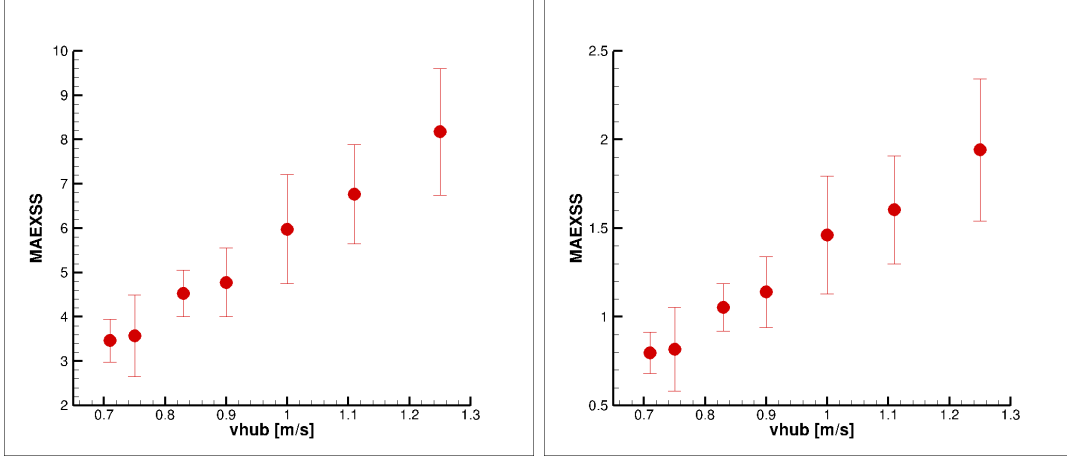


Figure 5.20: The dependence of the MAEXSS on the inflow velocity for the HATT under two threshold conditions described in section 3.2, left:  $\theta \geq \theta_{cr}$ , right:  $|\mathbf{v}| \geq v_t$ .

The dependence of the MAEXSS on the velocity at the rotor hub can be approximated using Eq. 5.4 and the definition of the EXSS  $\xi = (|\mathbf{v}_b|^2/v_t^2 - 1)$ , where  $\mathbf{v}_b$  is the near-bed velocity and  $v_t$  is the threshold velocity within the sediment uplift model introduced in section 3.2. The near-bed velocity can be written as a composition of the inflow velocity and the velocity induced by the presence of the HATT,  $\mathbf{v}_b = \mathbf{v}_{fs}^b + \mathbf{v}_I^b$ . Given that  $|\mathbf{v}_b|^2 = |\mathbf{v}_{fs}^b|^2 + 2\mathbf{v}_{fs}^b \cdot \mathbf{v}_I^b + |\mathbf{v}_I^b|^2$ , and that the first two terms contain the velocity at the rotor hub so that

$$|\mathbf{v}_{fs}^b|^2 = v_{hub}^2 \frac{\log(z_b/k_s + 1)}{\log(z_{hub}/k_s + 1)}, \quad (5.9)$$

the MAEXSS can be expressed as

$$\bar{\xi} = \xi_2^v v_{hub}^2 + \xi_1^v v_{hub} + \xi_0^v, \quad (5.10)$$

where

$$\xi_2^v = v_t^{-2} \left( \frac{\log(z_b/k_s + 1)}{\log(z_{hub}/k_s + 1)} \right)^2 \quad (5.11)$$

$$\xi_1^v = 2v_t^{-2} v_x^I \left( \frac{\log(z_b/k_s + 1)}{\log(z_{hub}/k_s + 1)} \right) \quad (5.12)$$

$$\xi_0^v = v_t^{-2} |\bar{\mathbf{v}}_I|^2 - 1. \quad (5.13)$$

The  $x$ -component of the temporal mean of the spatially averaged induced velocity at  $z_b$ ,  $\overline{v_x^I}$ , and its magnitude,  $|\overline{\mathbf{v}^I}|$ , are generally unknown. The coefficients in Eq. 5.10 for the single rotor device, described in section 4.1, mounted  $1.5R$  above the seabed, and  $z_b = 10$  cm are listed in Table 5.2.

	$\xi_2^v$	$\xi_1^v$	$\xi_0^v$
$\theta \geq \theta_{cr}$	0.4640	$6.543\overline{v_x^I}$	$23.07 \overline{\mathbf{v}^I} ^2 - 1$
$ \mathbf{v}  \geq v_t$	0.1271	$1.793\overline{v_x^I}$	$6.321 \overline{\mathbf{v}^I} ^2 - 1$

Table 5.2: Coefficients in the MAEXSS function Eq. 5.10.

The correlation of the expression Eq. 5.10 with the MAEXSS in Fig. 5.20 is illustrated in Fig. 5.21. The coefficients  $\xi_2^v = 0.4640$ ,  $\xi_1^v = 6.5$  and  $\xi_0^v = -0.95$ , which were used to define the curve in Fig. 5.21, suggest that the temporal mean of the spatial average of the induced velocity would be smaller than the downstream component of the mean averaged velocity  $\overline{v_x^I}$ .

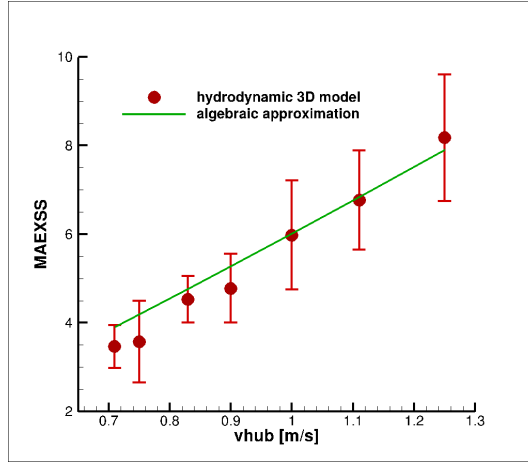


Figure 5.21: The dependence of the MAEXSS for the HATT on the inflow velocity, comparison of the VTM's simulations with the algebraic expression Eq. 5.10.

To summarize, the flow through the rotor of the HATT affects the immediate region of the seabed down-stream of the device. The results indicate that the erosion of the seabed would vary during the tidal cycle and that the scale of the

## 5.4 Effect of the Distance from the Seabed on the EXSS

erosion would be directly correlated to the local tidal velocity. A simple algebraic relation Eq. 5.10 was devised to approximate the connection between the phase of the tidal cycle and the impact of the HATT on the seabed.

The influence of the distance between the rotor and the seabed on the excess bed shear stress has been investigated by a series of simulations, the results from which are presented in section 5.4.

### 5.4 Effect of the Distance from the Seabed on the EXSS

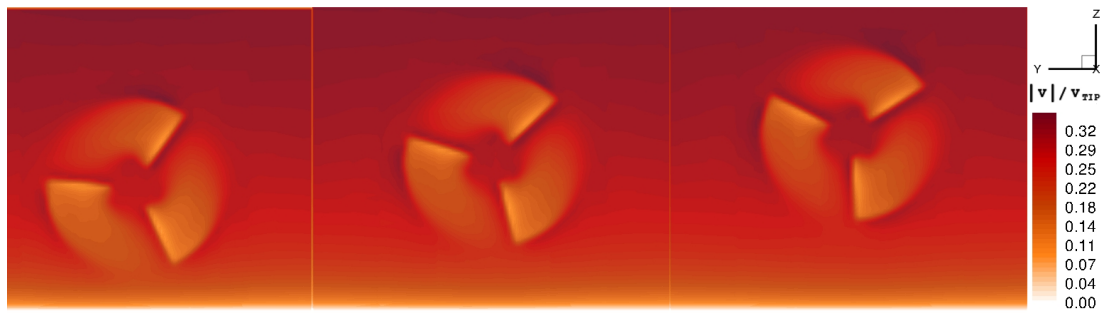


Figure 5.22: Velocity at the rotor plane, from left to right:  $z_{hub} = 1.4R, 1.7R, 2R$ .

Unlike in the uniform inflow case, the distance of the HATT from the seabed affects the nature of its environmental impact substantially. The effect of the presence of the HATT in a boundary layer flow was studied for a number of positions of the HATT above the seabed. The inflow velocity at the rotor plane for different positions of the HATT is illustrated in Fig. 5.22. Although the flow at the rotor blades decelerates, the flow just below the rotor disc accelerates in comparison with the flow in the absence of a TECD. The velocity profile, illustrated in Fig. 5.23, was defined to reach 2 m/s at 40 m, to represent flow conditions suitable for power extraction at different heights above the seabed.

## 5.4 Effect of the Distance from the Seabed on the EXSS

---

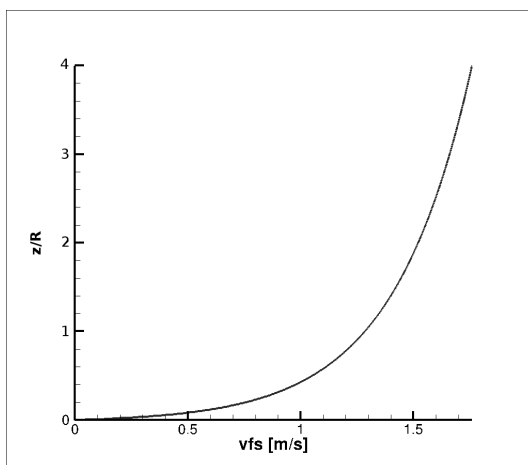


Figure 5.23: The investigated velocity profile,  $V_{in} = 2$  m/s at 40 m above the seabed.

The velocity at the rotor hub for the position of the HATT between  $1.3R$  and  $2R$  above the seabed is listed in Table 5.3.

$z_{hub}$	$1.3R$	$1.4R$	$1.5R$	$1.6R$	$1.7R$	$1.8R$	$1.9R$	$2R$
$v_{hub}$ [m/s]	1.37	1.40	1.42	1.45	1.47	1.49	1.50	1.52
$\Delta v_{2R}$ [m/s]	0.68	0.61	0.55	0.50	0.46	0.43	0.40	0.38

Table 5.3: The inflow conditions and the position of the rotor hub above the seabed.

The position  $z_{hub} = 1.3R$  signifies that the blade tips of the 5 m long blades pass as close as 1.5 m to the seabed. The quantity  $\Delta v_{2R}$ , defined in the previous section, indicates that the HATT closer to the seabed is subjected to a bigger gradient of the inflow velocity. The variation of the inflow velocity gradient with the position of the HATT is illustrated in Fig. 5.24.

The effect of mounting the rotor even closer to the seabed is presented in section 5.4.1. In contrast to the investigation of the tidal cycle where the rotational speed was kept constant, while the ratio  $v_{tip}/v_{hub}$  varied with inflow velocity, the ratio  $v_{tip}/v_{hub}$  is maintained at 5.56 for all the positions listed in Table 5.3 by modifying the rotational speed.

## 5.4 Effect of the Distance from the Seabed on the EXSS

---

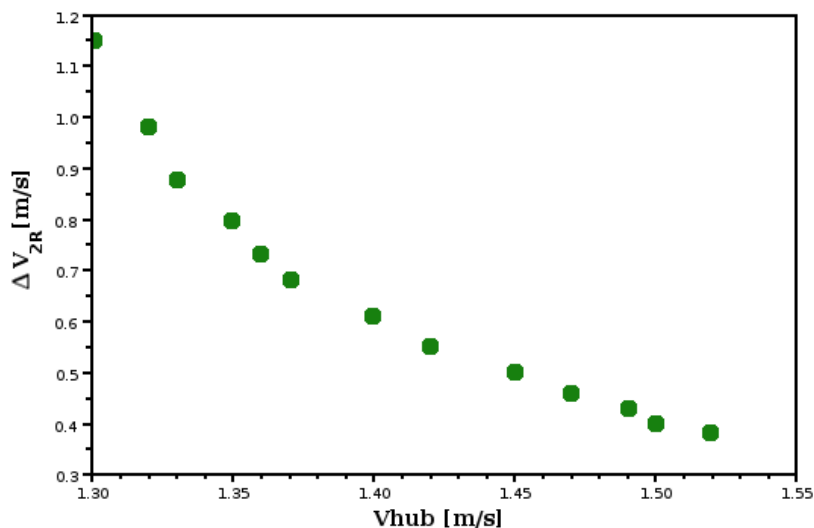


Figure 5.24: The difference of the inflow velocity across the rotor for the investigated positions of the HATT above the seabed, listed in Tables 5.3 and 5.4.

Consistently with the investigation of the variation of the excess bed shear stress during the tidal cycle, the structure of the induced vorticity field, i.e. the rotor vorticity and the tide induced wake vorticity fields, were studied. The rotor vorticity fields for the positions listed in Table 5.3 are shown in Fig. 5.25, where the horizontal black lines denote the positions of the seabed. It can be observed that the helical structure of the rotor vorticity field is more inclined for smaller distances between the rotor hub and the seabed. The strength of the rotor vorticity does not vary significantly with  $z_{hub}$  relative to the variation with  $v_{tip}/v_{hub}$  presented in Fig. 5.14. The ordered part of the rotor vorticity field extends further down-stream of the rotor in Fig. 5.25 than in Fig. 5.14 for all of the investigated positions of the HATT. The extent of the ordered vortical structure does not vary with  $z_{hub}$  relative to the variation with  $v_{tip}/v_{hub}$  observed in Fig. 5.14, i.e. during the tidal cycle. The influence of the inflow velocity on the structure of the rotor vorticity field is illustrated by comparison of the vorticity structure in the two cases when  $v_{tip}/v_{hub} = 5.56$  and  $z_{hub} = 1.5R$ , presented in Fig. 5.26.

## 5.4 Effect of the Distance from the Seabed on the EXSS

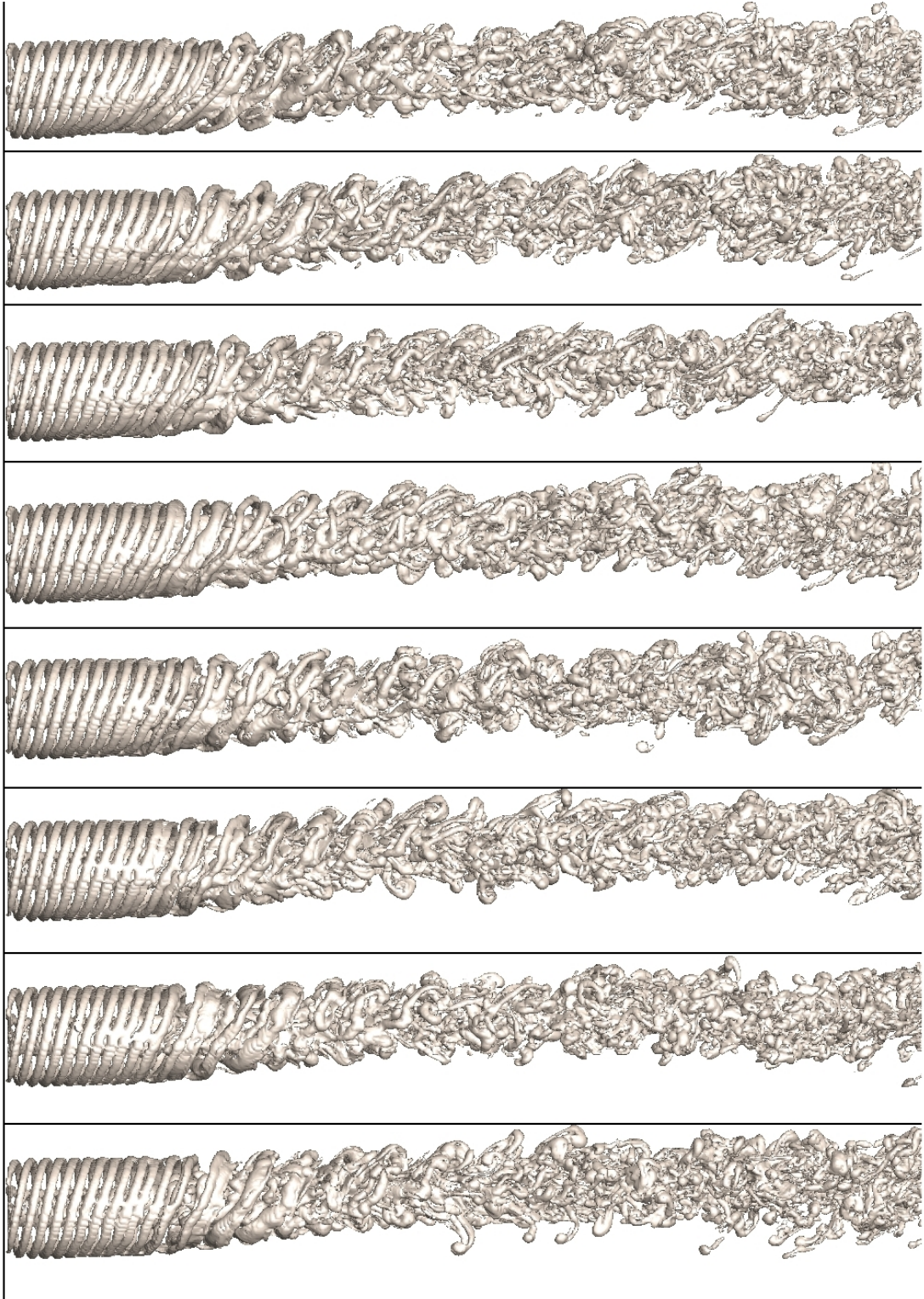


Figure 5.25: The rotor vorticity field of the fully developed wake, from top to bottom:  $z_{hub} = 1.3R, 1.4R, 1.5R, 1.6R, 1.7R, 1.8R, 1.9R, 2R$ .

## 5.4 Effect of the Distance from the Seabed on the EXSS

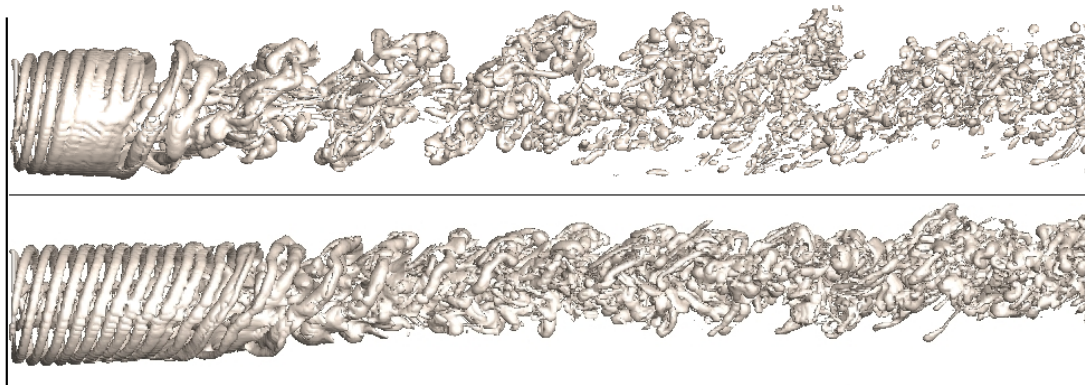


Figure 5.26: The rotor vorticity field of the fully developed wake,  $v_{tip}/v_{hub} = 5.56$ ,  $z_{hub} = 1.5R$ , top:  $v_{hub} = 0.90$  m/s, bottom:  $v_{hub} = 1.42$  m/s.

From Fig. 5.26 it follows that the location where the ordered vortical structure starts to disintegrate depends on  $v_{hub}$ , and the disintegration occurs further from the rotor for faster inflow velocities.

The rotor vorticity field in Fig. 5.25 is transported from the seabed by the boundary flow, causing a reduction of the area of the seabed affected by the rapidly changing flow in the wake of the HATT. The results, presented in Fig. 5.25, suggest that the process of the disintegration of the rotor vorticity field may depend on the position of the rotor, since the vorticity structure for  $z_{hub} \leq 1.7R$  contains a loop of the vortex filaments which is more deformed at  $z_{hub}$  than the filament loops down-stream of the rotor mounted further than  $1.7R$  above the seabed.

The detailed structure of the wake is illustrated by y-slice of the rotor vorticity field in Fig. 5.27, where the darker colours denote higher values of the rotor vorticity. The strength of the vortices is relatively similar for all investigated positions of the rotor, in contrast to the vortex strength observed in Fig. 5.15, where higher values of vorticity were correlated to smaller values of  $v_{tip}/v_{hub}$ .

## 5.4 Effect of the Distance from the Seabed on the EXSS

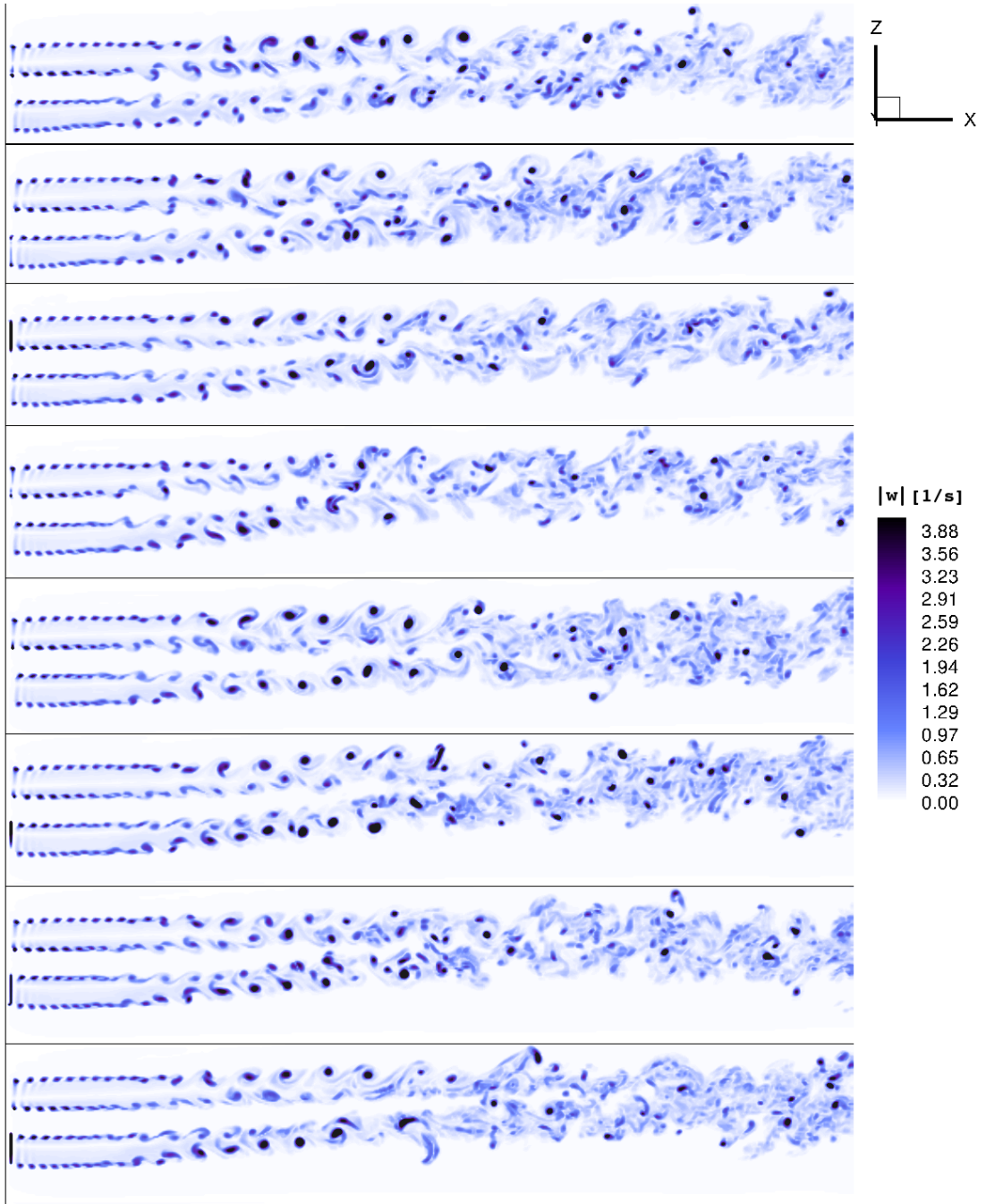


Figure 5.27: Y-slice of the rotor vorticity field of the fully developed wake, from top to bottom:  $z_{hub} = 1.3R, 1.4R, 1.5R, 1.6R, 1.7R, 1.8R, 1.9R, 2R$ .

## 5.4 Effect of the Distance from the Seabed on the EXSS

---

Y-slices of the tide induced wake vorticity are presented in Fig. 5.28. Unlike in Fig. 5.16, the tide induced wake vorticity contains high values further downstream of the rotor in a long narrow region a few centimetres above the seabed for  $z_{hub} \geq 1.5R$ . The vertical gradient of the inflow velocity causes the elevation of the induced vorticity away from the seabed in contrast to the case of uniform inflow. The magnitude of the induced vorticity is, however, little influenced by the variability of the inflow, since the maximal magnitude of the tide induced wake vorticity is less than 5% of the maximal magnitude of the rotor vorticity for any of the investigated positions of the rotor. Furthermore, the maximal magnitude of the tide induced wake vorticity is smaller than 10% of the maximal magnitude of the free stream vorticity.

The near-bed velocity, which is presented in Fig. 5.29 and related excess bed shear stress (EXSS), which is shown in Fig. 5.30, indicate that the impact of the flow on the seabed is confined into the region immediately downstream of the rotor for all values of  $z_{hub}$  listed in Table 5.3, similarly to the EXSS in Fig. 5.18 and Fig. 5.9 in the previous section. The high EXSS is located in the area of the seabed below the ordered helical structure in the induced vorticity. The extent of the high EXSS as well as the maximal EXSS appear to depend on the position of the rotor above the seabed. The seabed is affected by the highest EXSS, which extends up to  $6R$  downstream of the rotor, for  $z_{hub} = 1.3R$ , and the maximal EXSS is more than four times bigger than the maximal value of the EXSS for  $z_{hub} = 2R$ . The extent of the area exposed to the high EXSS is smaller when the HATT is mounted further above the seabed.

## 5.4 Effect of the Distance from the Seabed on the EXSS

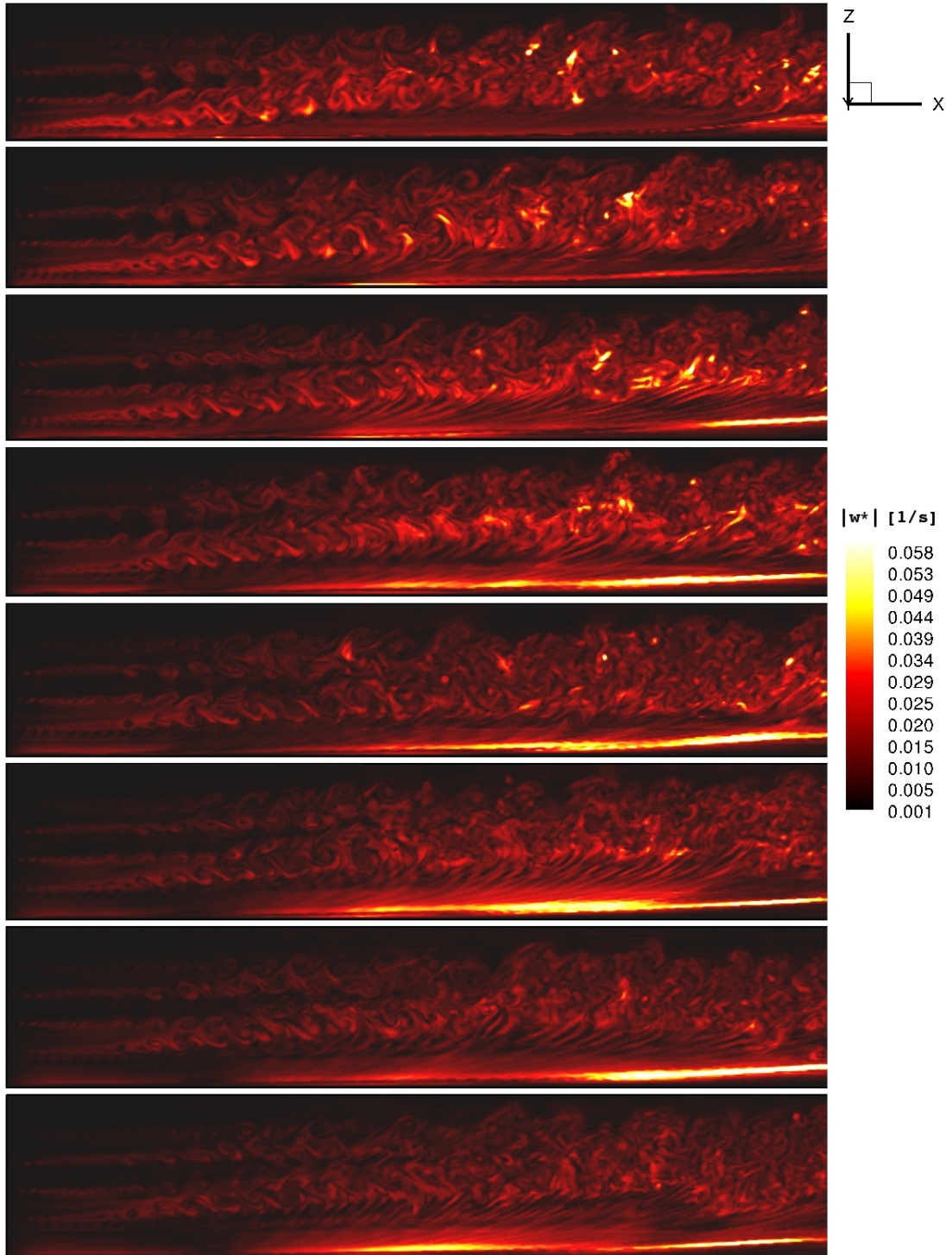


Figure 5.28: Y-slice of the tide induced wake vorticity of the fully developed wake, from top to bottom:  $z_{hub} = 1.3R, 1.4R, 1.5R, 1.6R, 1.7R, 1.8R, 1.9R, 2R$ .

## 5.4 Effect of the Distance from the Seabed on the EXSS

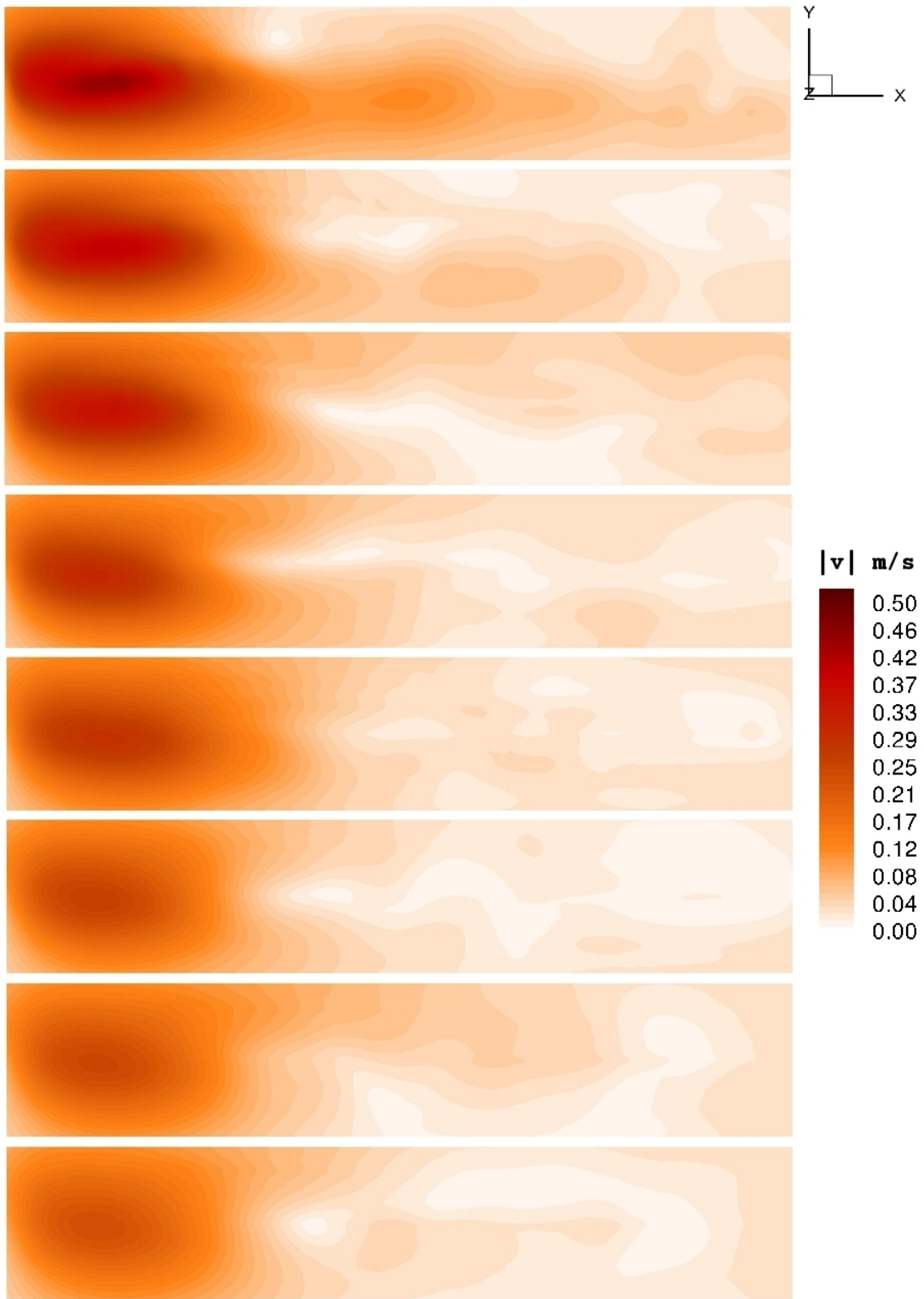


Figure 5.29: The near-bed velocity induced by the fully developed wake, from top to bottom:  $z_{hub} = 1.3R, 1.4R, 1.5R, 1.6R, 1.7R, 1.8R, 1.9R, 2R$ .

## 5.4 Effect of the Distance from the Seabed on the EXSS

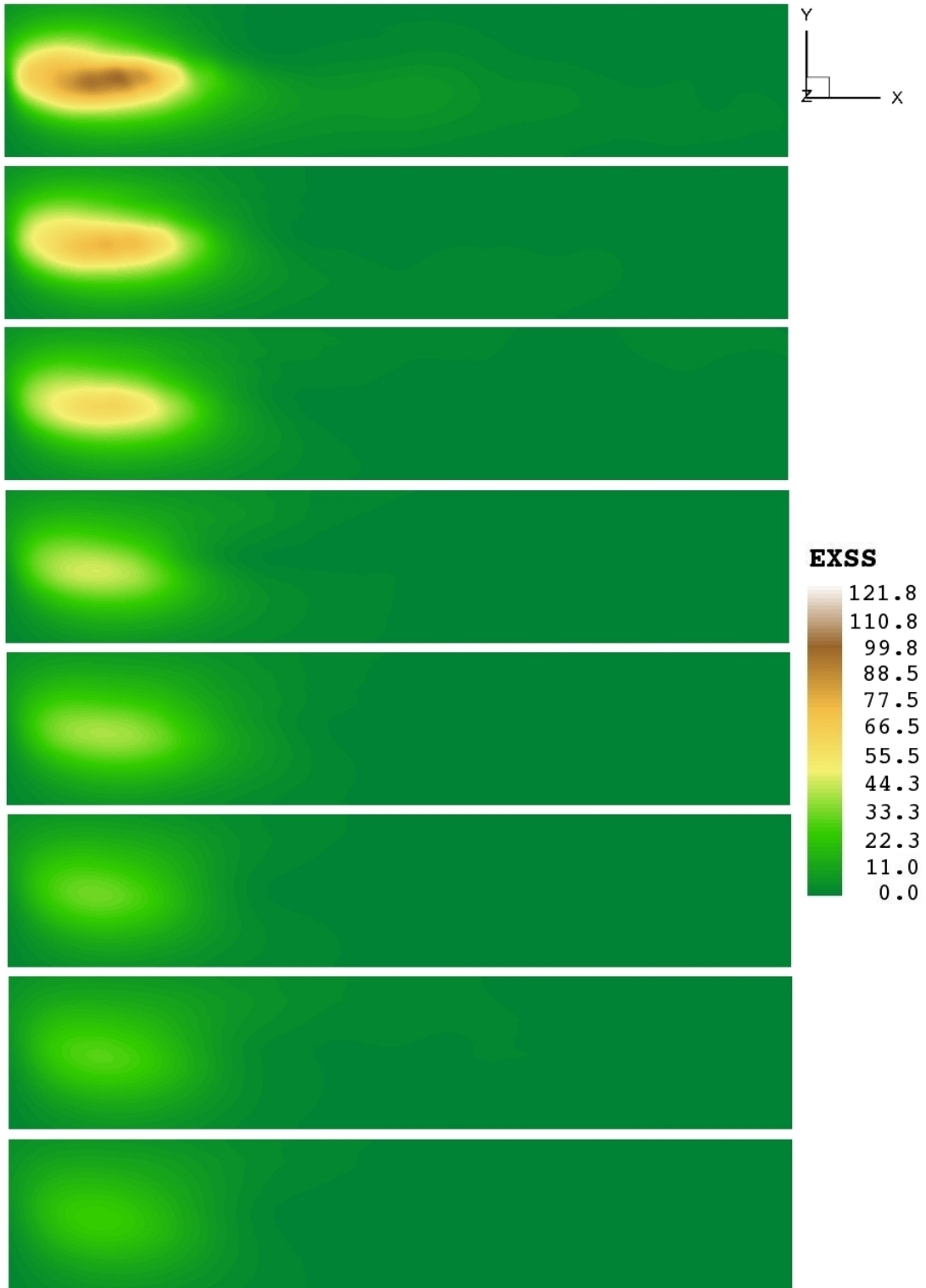


Figure 5.30: The excess bed shear stress once the wake is fully developed, from top to bottom:  $z_{hub} = 1.3R, 1.4R, 1.5R, 1.6R, 1.7R, 1.8R, 1.9R, 2R$ .

## 5.4 Effect of the Distance from the Seabed on the EXSS

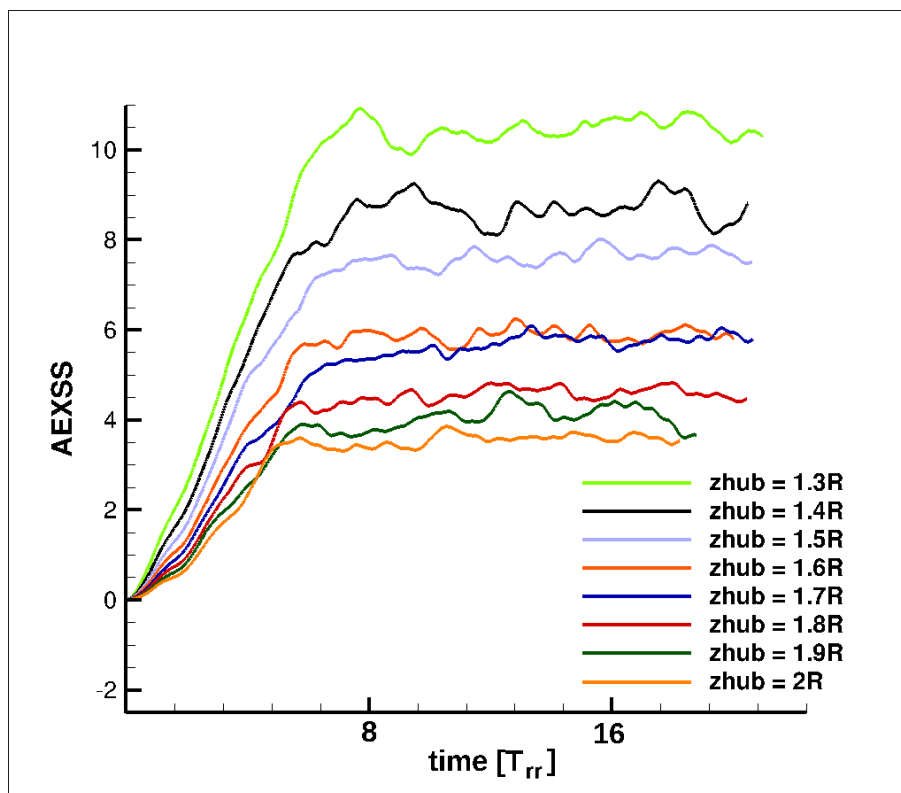


Figure 5.31: Variation of the AEXSS evolution with the position of the HATT above the seabed,  $z_{hub} \geq 1.3R$ .

The evolution of the excess bed shear stress, averaged over the studied area of the seabed, is presented in Fig. 5.31. The results shown in Fig. 5.30 suggest that the impact of the HATT on the seabed, expressed by the EXSS, decreases with the increasing distance of the rotor from the seabed for  $z_{hub} \in [1.3R, 2R]$ . This behaviour is well expressed by the dependence of the temporal mean of the averaged excess bed shear stress (MAEXSS) on  $z_{hub}$ . The relationship between the MAEXSS and  $z_{hub} \in [1.3R, 2R]$  is summarized in Fig. 5.32, in which the error bars of the MAEXSS are calculated as the difference between the maximum and the minimum AEXSS within  $[t_0, t_{END}]$ , consistently with the previous section.

## 5.4 Effect of the Distance from the Seabed on the EXSS

---

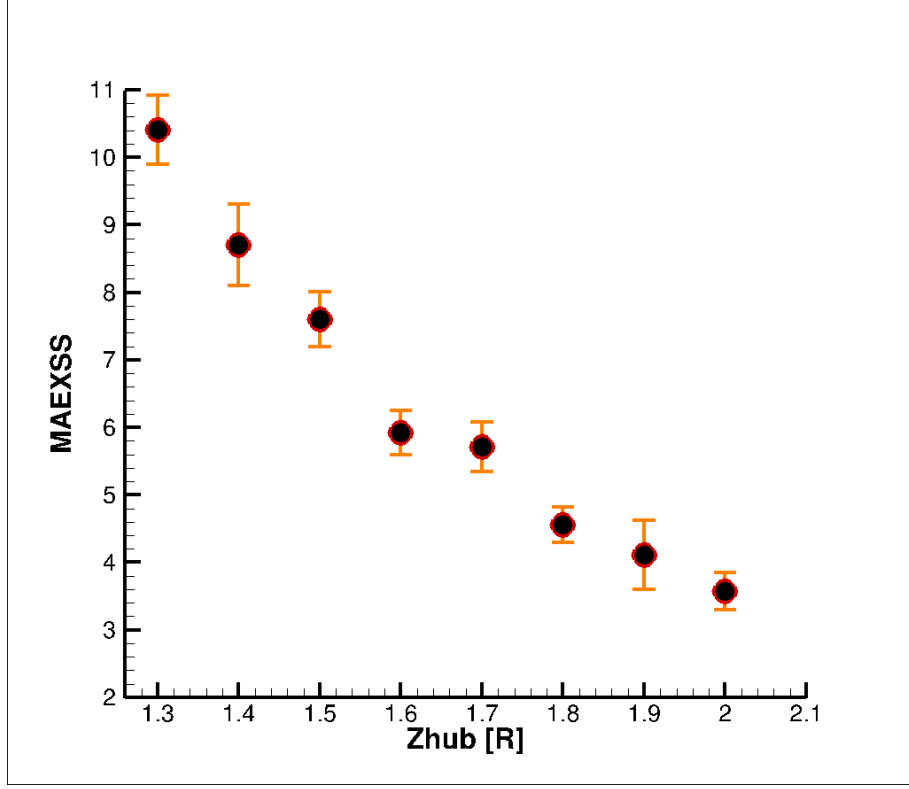


Figure 5.32: Dependence of the MAEXSS on the position of the HATT above the seabed.

In order to approximate the MAEXSS by a function of the distance between the rotor hub and the seabed, the induced vorticity can be represented by a series of single vortices at height  $z_b$  above the seabed, and the near-bed velocity down-stream of the HATT is expressed as a sum of the contributions of the single vortices. In two dimensions, a single vortex at height  $z_{hub}$  above the seabed induces a near-bed velocity  $v_b = \Gamma/2\pi(z_{hub} - z_b)$ , where  $\Gamma$  is the strength of the vortex. Under the assumption that the seabed at the point  $\mathbf{x}$  is influenced predominantly by the nearest single vortex, a dependence of the MAEXSS, denoted as  $\bar{\xi}$ , on  $z_{hub}$  then follows from the definition of the EXSS

$$\bar{\xi} \approx \frac{\xi_{-2}^z}{(z_{hub} - z_b)^2} - 1. \quad (5.14)$$

The constant  $\xi_{-2}^z$  depends on the strength of the vortex which would represent

## 5.4 Effect of the Distance from the Seabed on the EXSS

---

the wake of the HATT. The representative vortex strength can be obtained by a fit of the data points presented in Fig. 5.32. For  $\xi_{-2}^z = 16.5$ , the fitted curve is plotted against the three-dimensional results in Fig. 5.33. The relation Eq. 5.14 provides a simplified model of the MAEXSS.

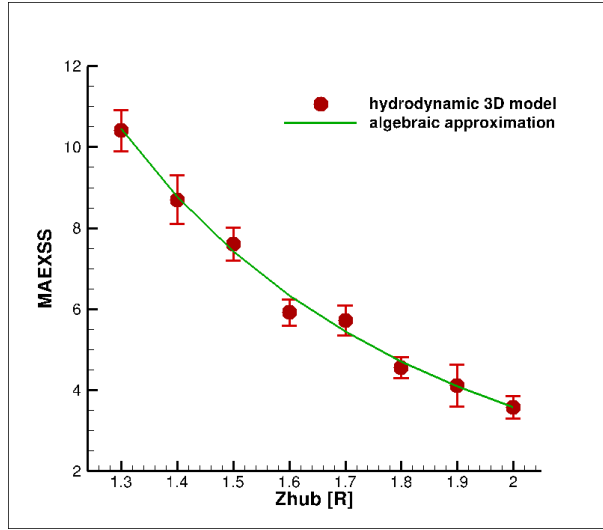
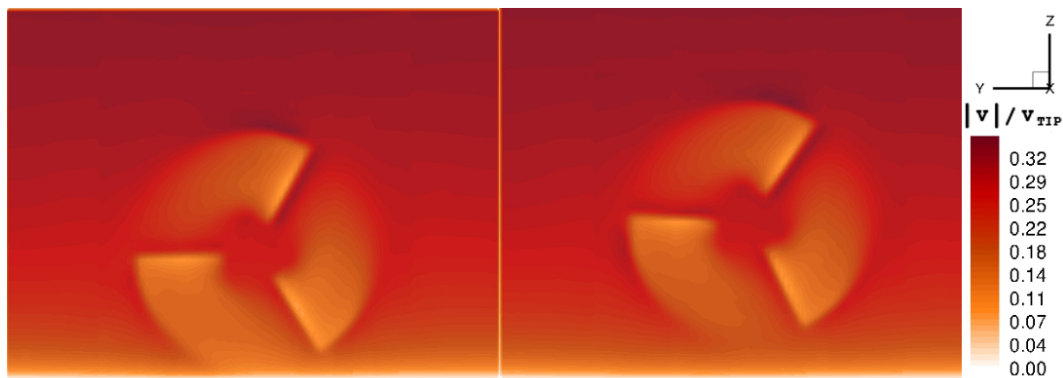


Figure 5.33: Dependence of the MAEXSS on the position of the HATT above the seabed, comparison with Eq. 5.14, where  $\xi_{-2}^z = 16.5$ .

The increased MAEXSS for the HATT closer to the seabed, shown in Fig. 5.32, indicates that the HATT would cause even bigger erosion flux if mounted closer than  $1.3R$  above the seabed. The applicability of the relation Eq. 5.14 for the HATT closer to the seabed, the impact on the seabed for  $z_{hub}$  in the interval  $[1R, 1.3R]$  is discussed in section 5.4.1. The placement of the rotor closer than  $1.3R$  above the seabed yields somewhat surprising results about the nature of the interaction between the flow down-stream of the HATT and the seabed, which are presented in section 5.4.1.

## 5.4.1 TECD close to the seabed


 Figure 5.34: Velocity at the rotor plane, left:  $z_{hub} = 1.05R$ , right:  $1.3R$ .

The flow velocity at the rotor plane for the range of distances between the rotor and the seabed presented in this section is illustrated in Fig. 5.34, where the legend is the same as in Fig. 5.29. The range of the inflow velocities at the rotor hub are listed in Table 5.4. The HATT mounted closer than  $1.3R$  above the seabed is exposed to a greater velocity gradient, than when the device is further above seabed (compare with the velocity in Table 5.3). The magnitude of vertical gradient of the inflow velocity is indicated by the quantity  $\Delta v_{2R}$ , which is listed in Table 5.1.

$z_{hub}$	$1.05R$	$1.10R$	$1.15R$	$1.20R$	$1.25R$
$v_{hub}$ [m/s]	1.30	1.32	1.33	1.35	1.36
$\Delta v_{2R}$ [m/s]	1.15	0.98	0.88	0.80	0.73

Table 5.4: Position of the rotor hub in the velocity profile.

The placement of the HATT at  $1.05R$  above the seabed signifies that the tips of the 5 metre-long blades pass as close as 25 cm above the seabed. The rotor vorticity field for the positions in Table 5.4 is presented in Fig. 5.35.

#### 5.4 Effect of the Distance from the Seabed on the EXSS

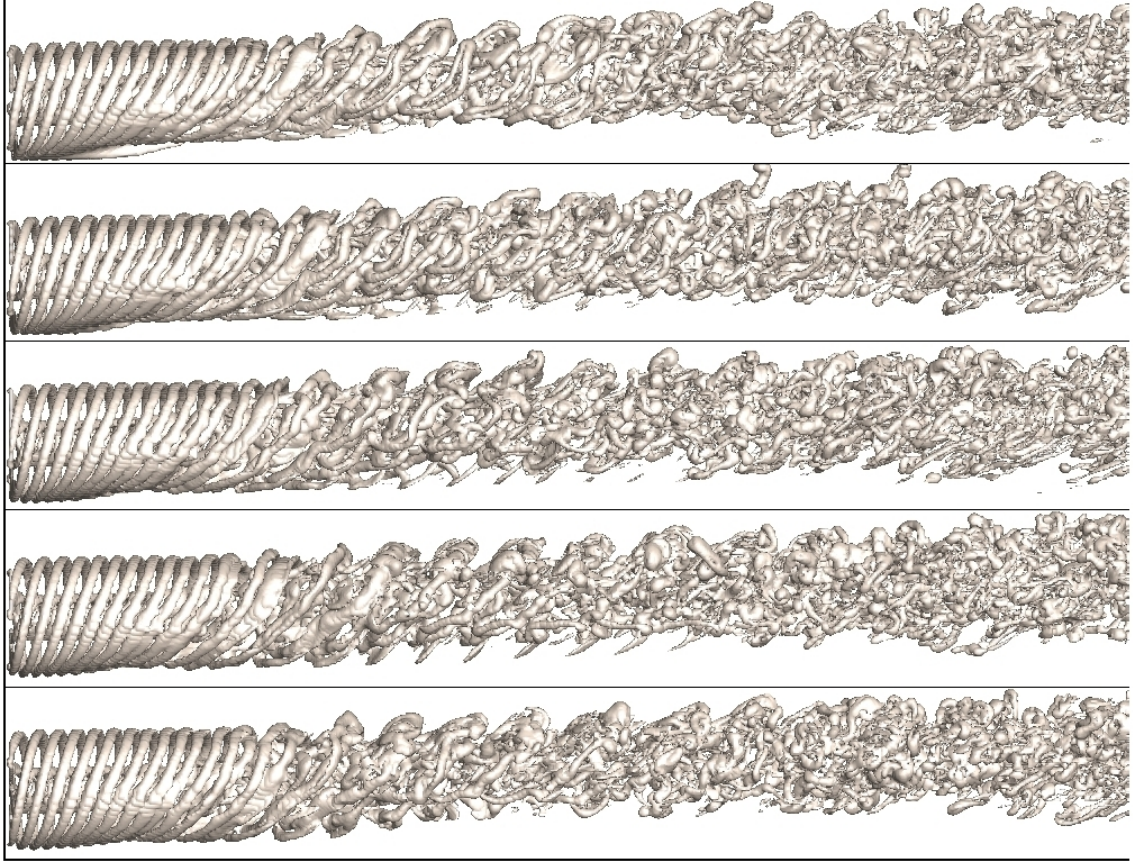


Figure 5.35: The rotor vorticity field of the fully developed wake, from top to bottom:  $z_{hub} = 1.05R, 1.1R, 1.15R, 1.2R, 1.25R$ .

The inclination of the ordered portion of the rotor vorticity field down-stream of the HATT closer to the seabed observed in Fig. 5.25 is even greater for  $z_{hub}$  less than  $1.3R$ . Indeed, the degree to which the wake inclines before it disintegrates is greatest for the minimum separation between the rotor and the seabed, i.e.  $z_{hub} = 1.05R$ . The details of the structure of the rotor vorticity are illustrated by the planar section through the rotor axis, perpendicular to the seabed and the rotor plane (y-slice) shown in Fig. 5.36. The larger gradient of the inflow velocity causes the vorticity to move away from the seabed within a distance of  $2R$  down-stream of the rotor, compared to the cases of  $z_{hub} \geq 1.3R$ , where the first sign of the elevation of the vorticity appears only at distances greater than  $4R$  from the rotor. (beyond the point where the ordered vortical structure disintegrated).

## 5.4 Effect of the Distance from the Seabed on the EXSS

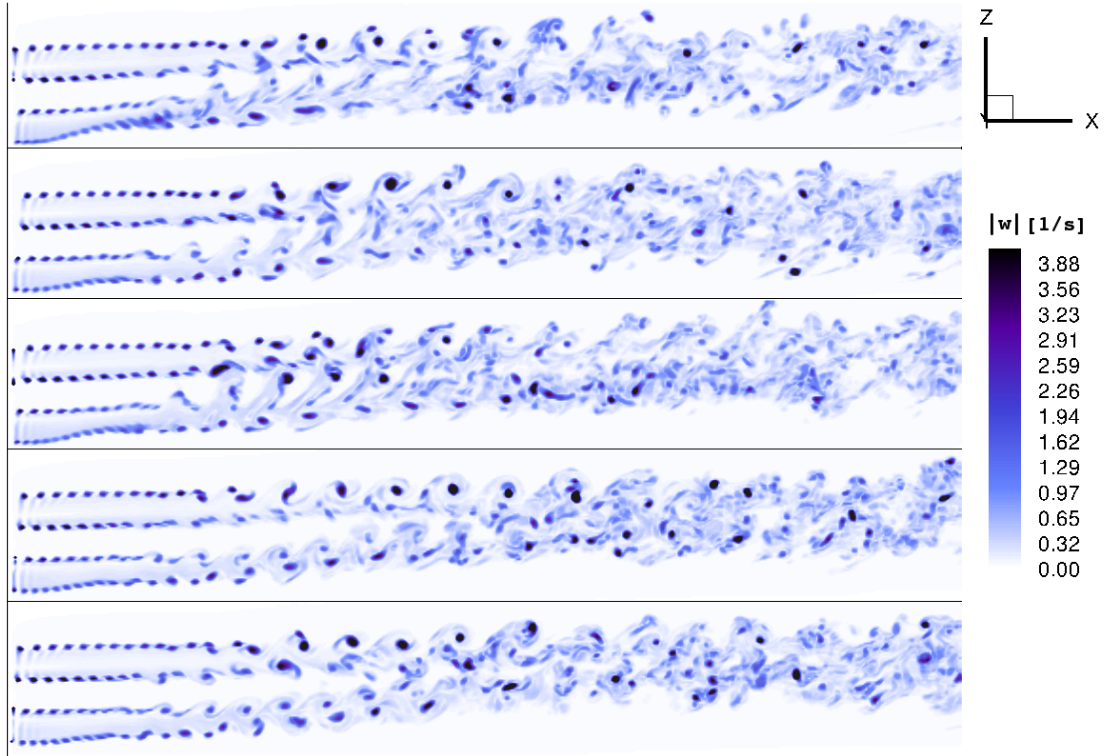


Figure 5.36: Y-slice of the rotor vorticity field of the fully developed wake, from top to bottom:  $z_{hub} = 1.05R, 1.1R, 1.15R, 1.2R, 1.25R$ .

The ordered vortical structure in the rotor vorticity field is deformed as a result of the very small distance from the seabed,  $z_{hub} = 1.05R$ . The deformation of this structure, observed in Fig. 5.36, is asymmetric, a feature which is illustrated further by z-slices of the rotor vorticity (planar sections parallel to the seabed and perpendicular to the rotor plane) in Fig. 5.37. The asymmetry is related to the sense of rotation of the HATT (i.e. clock-wise as seen in Fig. 5.34). X-slices of the rotor vorticity (planar sections perpendicular to the seabed and parallel to the rotor plane) are presented in Fig. 5.38.

## 5.4 Effect of the Distance from the Seabed on the EXSS

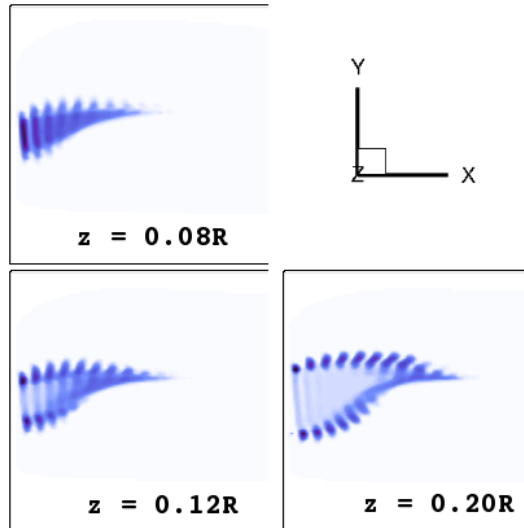


Figure 5.37: Z-slice of the rotor vorticity field of the fully developed wake, detailed behaviour of the wake close to the seabed.

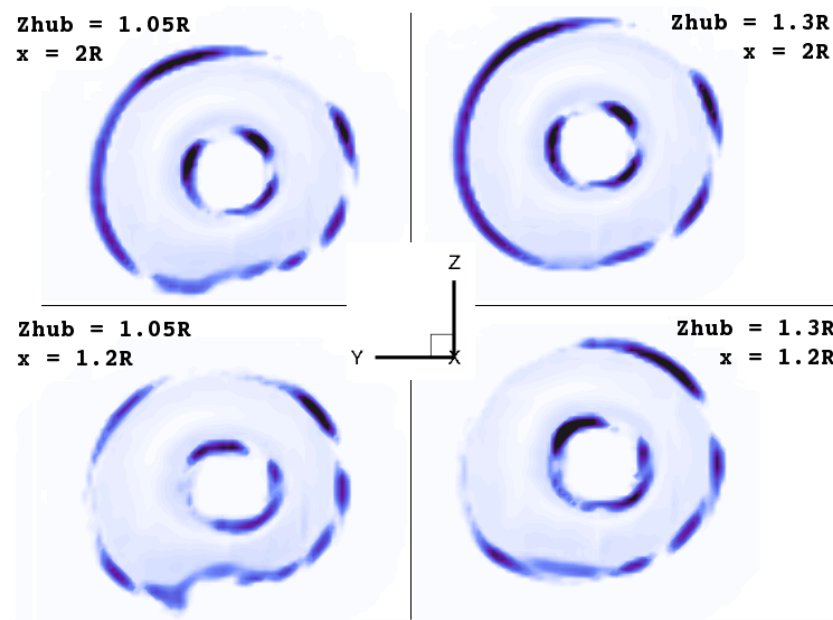


Figure 5.38: X-slice of the rotor vorticity field of the fully developed wake, comparison between cases  $z_{hub} = 1.05R$  and  $z_{hub} = 1.3R$ .

## 5.4 Effect of the Distance from the Seabed on the EXSS

From Fig. 5.37 and Fig. 5.38 it can be hypothesized that the strong vortices which are very close to the seabed are responsible for the asymmetric deformation of the ordered vortical structure. The interaction between the strong vortices and the solid surface results in the acceleration of the flow near the point of contact between the vortices and the seabed. The accelerated flow transports the rotor vorticity away from the seabed near the point of contact.

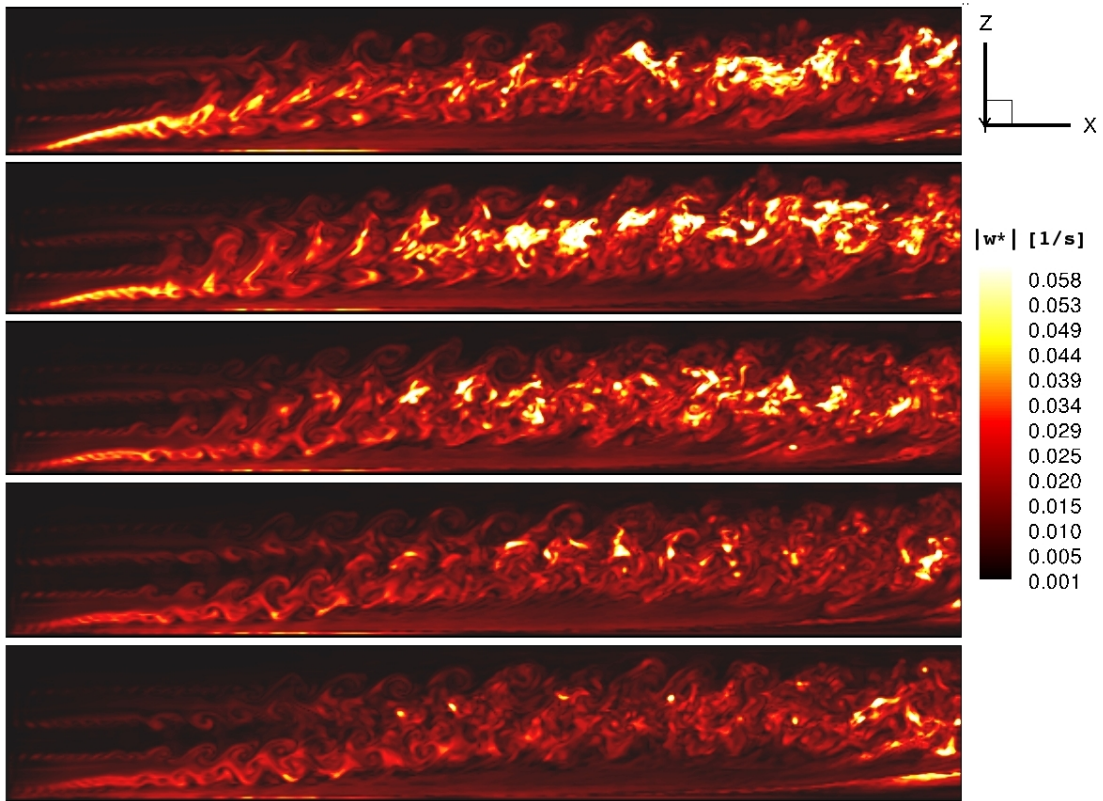


Figure 5.39: Y-slice of the tide induced wake vorticity of the fully developed wake, from top to bottom:  $z_{hub} = 1.05R, 1.1R, 1.15R, 1.2R, 1.25R$ .

The y-slice of the tide induced wake vorticity,  $\omega^*$ , is shown in Fig. 5.39. All positions of the rotor,  $z_{hub}$ , listed in Table 5.4, result in high  $\omega^*$  further from the rotor. The high  $\omega^*$  is observed immediately down-stream of the rotor only for  $z_{hub} \leq 1.1R$ . It can be seen that the tide induced wake vorticity is transported down-stream and away from the seabed by the flow. In contrast to the cases of  $z_{hub} \geq 1.3R$ , the high tide induced wake vorticity does not form a long narrow

## 5.4 Effect of the Distance from the Seabed on the EXSS

region close to the seabed as seen in Fig. 5.39. The relationship between the magnitudes of the fields  $\omega_w$  and  $\omega^*$  is, however, the same as in the cases  $z_{hub} > 1.3R$ . The maximal magnitude of the tide induced wake vorticity constitutes less than 5% and 10%, respectively, of that for the rotor vorticity and the free stream vorticity.

The near-bed velocity is shown in Fig. 5.40.

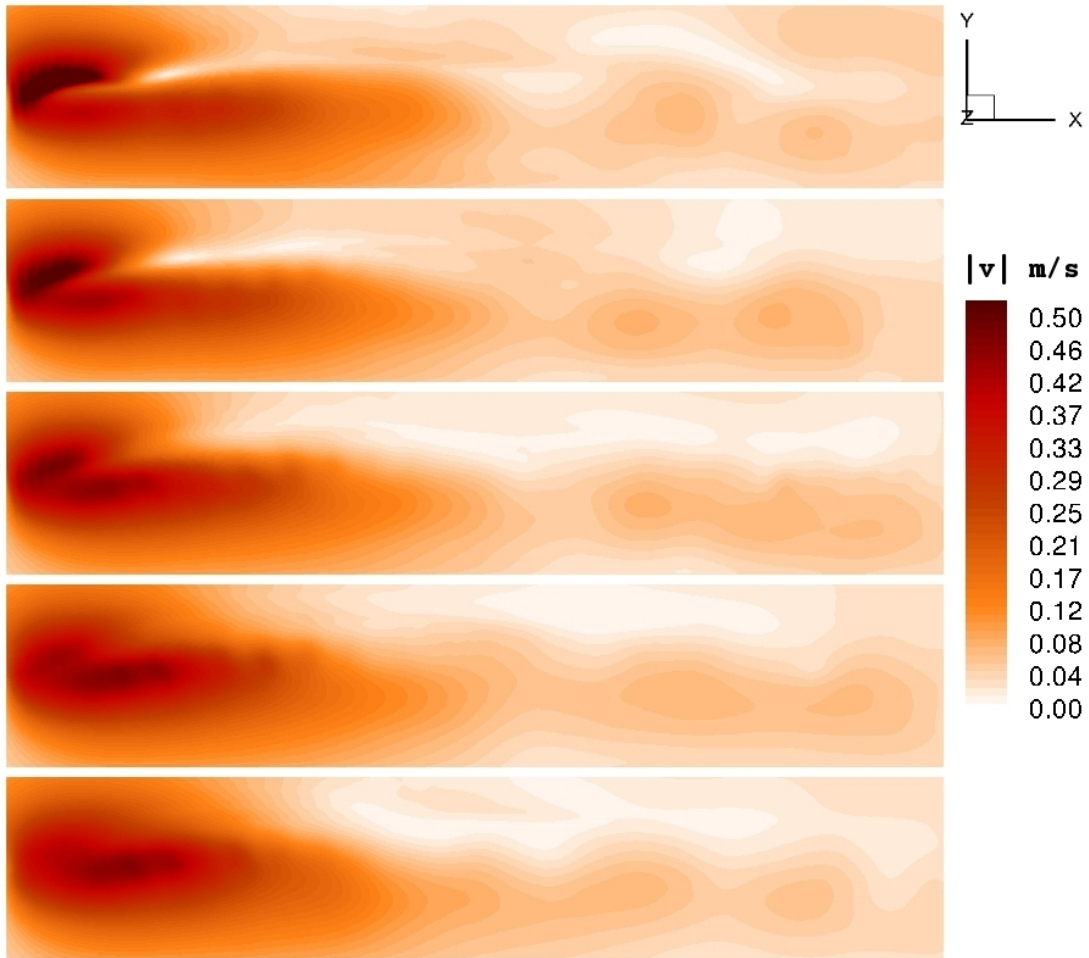


Figure 5.40: The near-bed velocity induced by the fully developed wake, from top to bottom:  $z_{hub} = 1.05R, 1.1R, 1.15R, 1.2R, 1.25R$ .

The region of the seabed immediately down-stream of the HATT is exposed to the highest flow velocities. The magnitude of the near-bed velocity is bigger for smaller distances of the rotor from the seabed, as expected.

## 5.4 Effect of the Distance from the Seabed on the EXSS

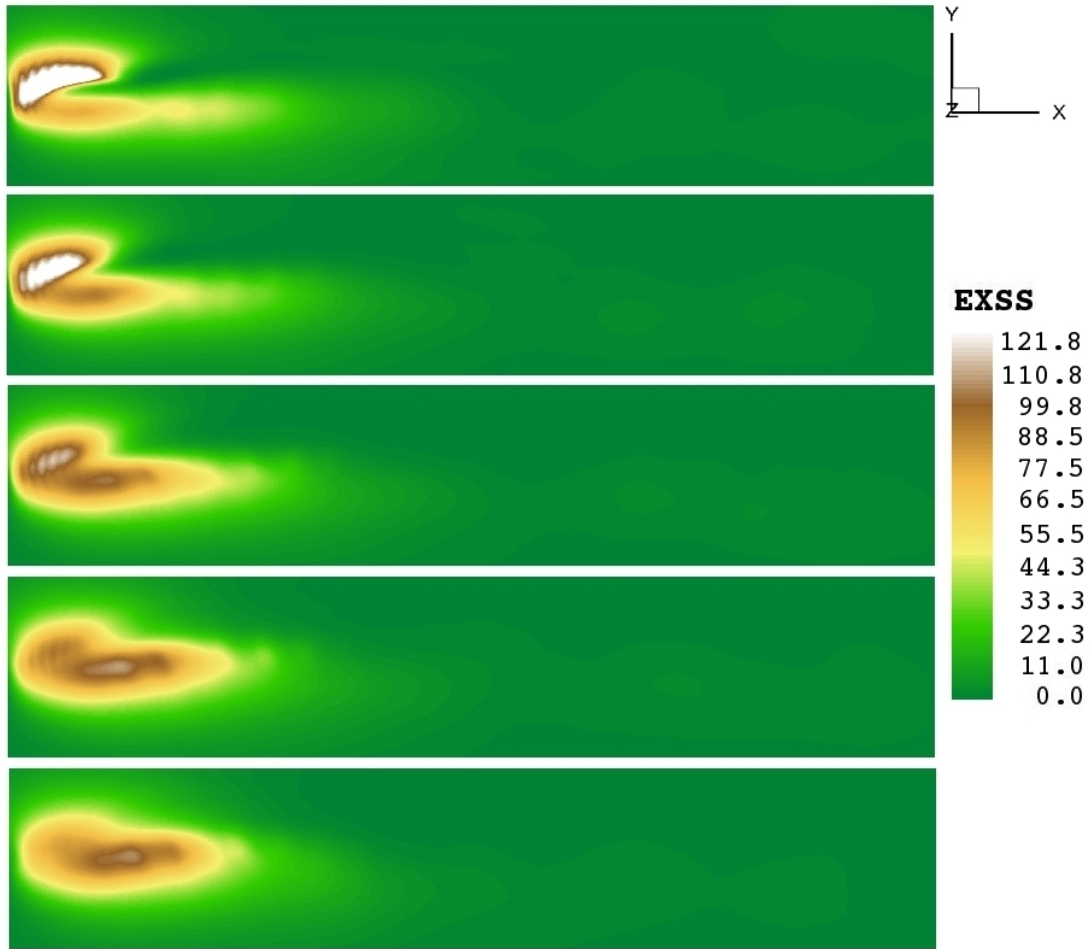


Figure 5.41: The excess bed shear stress once the wake is fully developed, from top to bottom:  $z_{hub} = 1.05R, 1.1R, 1.15R, 1.2R, 1.25R$ , showing the asymmetry of the exposed area of the seabed for small  $z_{hub}$ , caused by the local deformation of the rotor vorticity.

Rather unexpected is the reduction of the size of the affected area for the smallest values of  $z_{hub}$ . The reduction is a consequence of the elevation of the vorticity field above the seabed occurring closer to the rotor than is the case for  $z_{hub} \geq 1.3R$  because of the greater velocity gradient. The asymmetry of the exposed area is caused by the local deformation of the rotor vorticity field, shown in Fig. 5.37 and Fig. 5.38, which was discussed earlier.

The excess bed shear stress corresponding to the near-bed velocity, presented

## 5.4 Effect of the Distance from the Seabed on the EXSS

in Fig. 5.40, is shown in Fig. 5.41. The reduction of the area which is most affected by the presence of the HATT is emphasized in Fig. 5.41 by the color threshold between green and brown. The brown-white region, which indicates the highest stresses on the seabed, is considerably smaller for  $z_{hub} = 1.05R$  and  $1.10R$  than for  $z_{hub} = 1.25R$  and above.

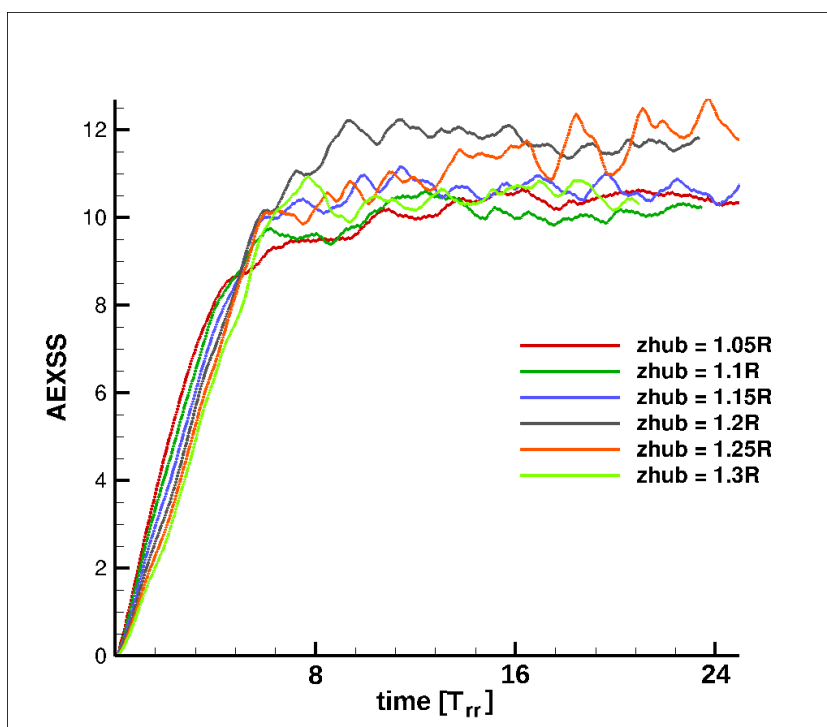


Figure 5.42: Variation of the AEXSS evolution with the position of the HATT above the seabed,  $z_{hub} \leq 1.3R$ .

The evolution of the excess bed shear stress averaged over the studied area of the seabed for  $z_{hub} < 1.3R$  is shown in Fig. 5.42. The evolution of the averaged excess bed shear stress (AEXSS) shows that as a result of the reduction in size of the area most exposed to the high values of the velocity, the EXSS is actually lower for  $z_{hub} = 1.05R$  than for  $z_{hub} = 1.25R$ .

The dependence of the MAEXSS on  $z_{hub}$ , evaluated from the data of the fully developed wake for  $z_{hub} < 1.3R$ , is displayed in Fig. 5.43, together with the MAEXSS for  $z_{hub}$  between  $1.3R$  and  $2R$  presented earlier in Fig. 5.32.

## 5.4 Effect of the Distance from the Seabed on the EXSS

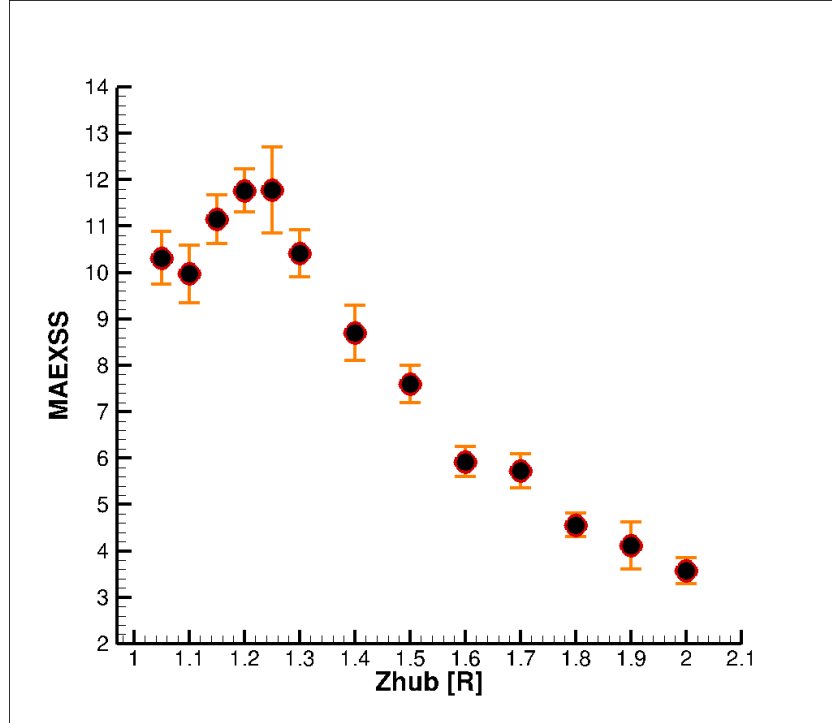


Figure 5.43: Dependence of the temporal mean of the AEXSS on the position of the HATT above the seabed.

Two intervals of a different nature of the excess bed shear stress have been identified from Fig. 5.43. The temporal mean of the excess bed shear stress averaged over the studied area of the seabed decreases with the increasing distance of the rotor from the seabed when the HATT is mounted at least  $1.3R$  above the seabed. The excess bed shear stress inflicted on the seabed by the HATT peaks when  $z_{hub} = 1.25R$ , and decreases for the smaller distances. This behaviour is a consequence of the asymmetry of the vorticity field close to the seabed discussed previously. The greater velocity gradient causes the rotor vorticity to start moving away from the seabed earlier than was the case for the HATT mounted at least  $1.3R$  above the seabed. As a result, the expression Eq. 5.14 is not applicable for the temporal mean of the excess bed shear stress when  $z_{hub} < 1.3R$ .

## 5.5 Sediment Concentration

As explained in chapter 3, section 3.3, the excess bed shear stress can be used to determine the source of sediment leaving the seabed into suspension,  $S_c$ . The motion of the sediment lifted from the seabed by the flow is modelled by the sediment transport equation

$$\frac{\partial c}{\partial t} + (\mathbf{v} - \mathbf{w}_s) \cdot \nabla c = \nabla \cdot (\epsilon \nabla c) + S_c, \quad (5.15)$$

by the evaluation of the evolution of sediment concentration  $c$ .

The inclusion of a realistic representation of the sediment diffusivity into the sediment transport model is needed to simulate the motion of sediment in the flow through the HATT. A realistic representation of sediment diffusivity  $\epsilon = \epsilon(\mathbf{x}, t)$  is however difficult to choose without an appropriate (explicit) model of turbulence implemented in the VTM, since the diffusion of sediment is generally associated with turbulent kinetic energy, as described in section 3.5. The parametric study of sediment diffusivity presented in this section provides, however, an insight into the variability of the motion of the sediment with the flow conditions.

The sediment diffusivity together with the settling velocity determines the evolution of sediment concentration, as described in chapter 3. Similarly to the model of sediment deposition where the settling velocity is defined in the  $z$ -direction, the vertical diffusion of sediment,  $\eta$ , is considered here. The sediment diffusivity is treated as a parameter in Eq. 5.15, with values  $\eta = 0.001, 0.002, 0.003, 0.004, 0.005, 0.006, 0.007, 0.008, 0.009, 0.01$  and  $0.05 \text{ m}^2/\text{s}$ .

The rotor vorticity field down-stream of the HATT is shown in Fig. 5.44 and the  $y$ -slice thereof in Fig. 5.45.

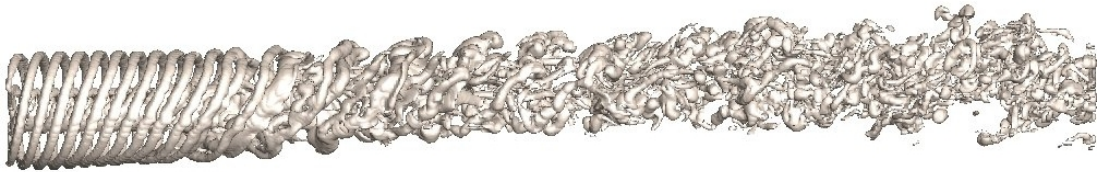


Figure 5.44: The rotor vorticity field of the fully developed wake.

## 5.5 Sediment Concentration

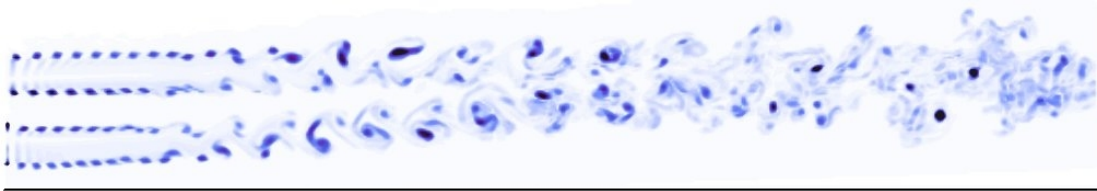


Figure 5.45: Y-slice of the rotor vorticity field of the fully developed wake.

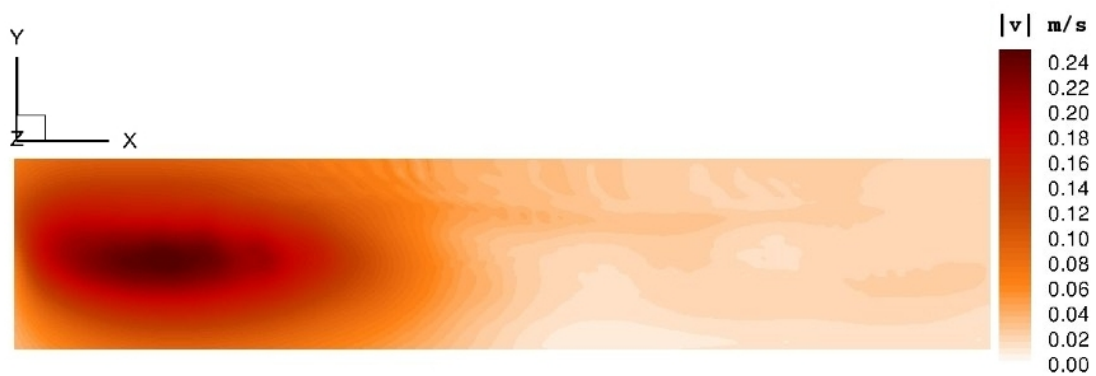


Figure 5.46: The near-bed velocity induced by the fully developed wake.

The near-bed velocity down-stream of the HATT is depicted in Fig. 5.46. The source of sediment moving into suspension depends on the EXSS, which depends on the near-bed velocity. The concentration of the sediment suspended in the flow is evaluated by the sediment transport model Eq. 5.15. The results indicate that the spatial distribution of the concentration of the sediment suspended in the flow, sometimes referred to as the ‘sediment cloud’, varies significantly with the choice of the vertical sediment diffusivity  $\eta$ . The y-slice through the sediment cloud is shown in Fig. 5.47 and Fig. 5.48 for the investigated values of the sediment diffusivity.

## 5.5 Sediment Concentration

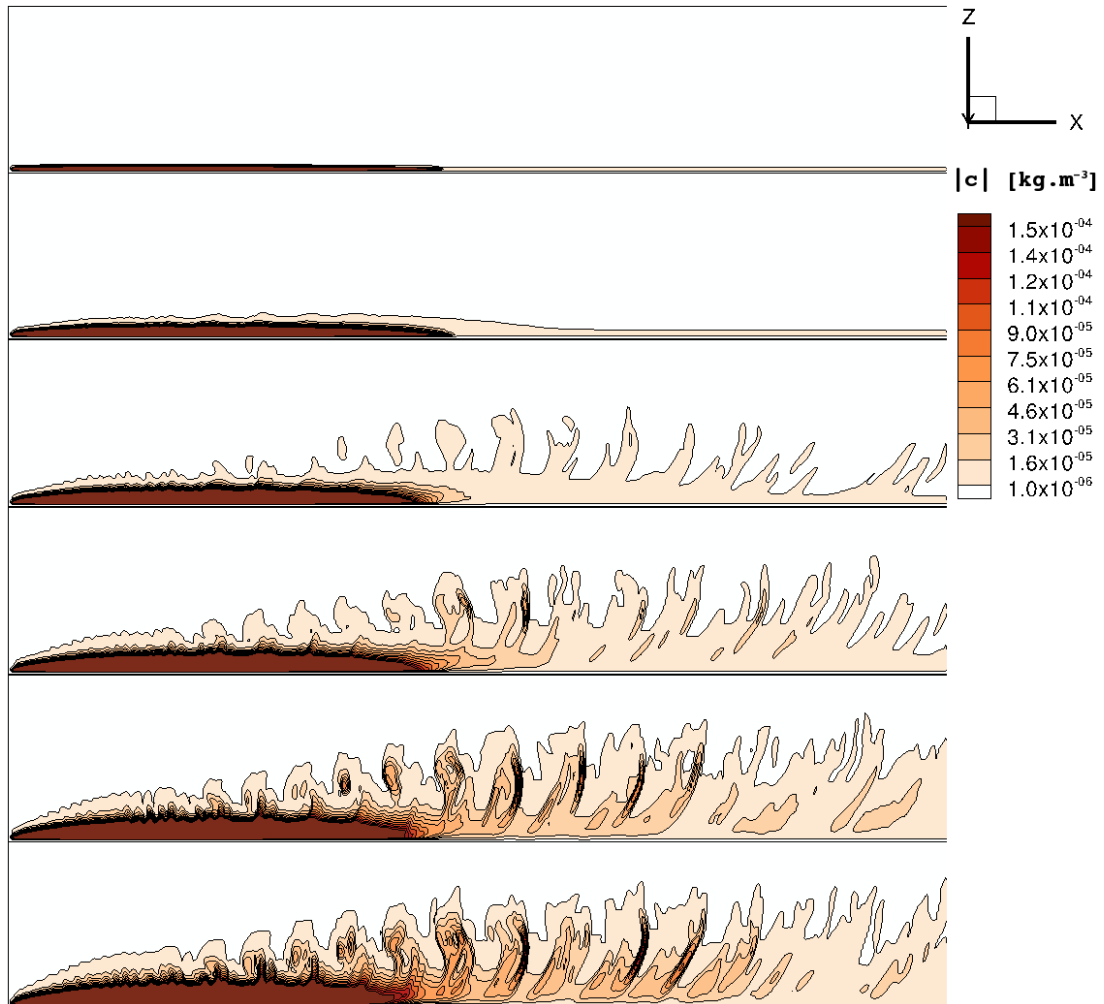


Figure 5.47: Y-slice of the sediment concentration  $c$ , from top to bottom:  $\eta = 0.001, 0.002, 0.003, 0.004, 0.005$  and  $0.006 \text{ m}^2/\text{s}$ .

For the case of  $\eta = 0.001 \text{ m}^2/\text{s}$ , the results indicate an initial uplift of sediment, which is then transported down-stream in a thin layer above the seabed without further motion up-wards. The sediment finally settles back onto the seabed approximately  $6R$  down-stream of the rotor. The displacement of the sediment is correlated with the extent of the ordered vortical structure of the rotor vorticity field. A particle of sediment representative of the case  $\eta = 0.001 \text{ m}^2/\text{s}$  would follow a simple trajectory - up into suspension, along the seabed in the down-stream direction and finally down onto the seabed. Such a trajectory is, however,

## 5.5 Sediment Concentration

not likely to represent a realistic example of the motion of sediment in the flow affected by the rotor vorticity field Fig. 5.44. The sediment concentration displays other possible behaviour of sediment particles for  $\eta > 0.001 \text{ m}^2/\text{s}$ . The case where the sediment disperses over the whole of the computational domain and beyond was observed for  $\eta = 0.05 \text{ m}^2/\text{s}$ .

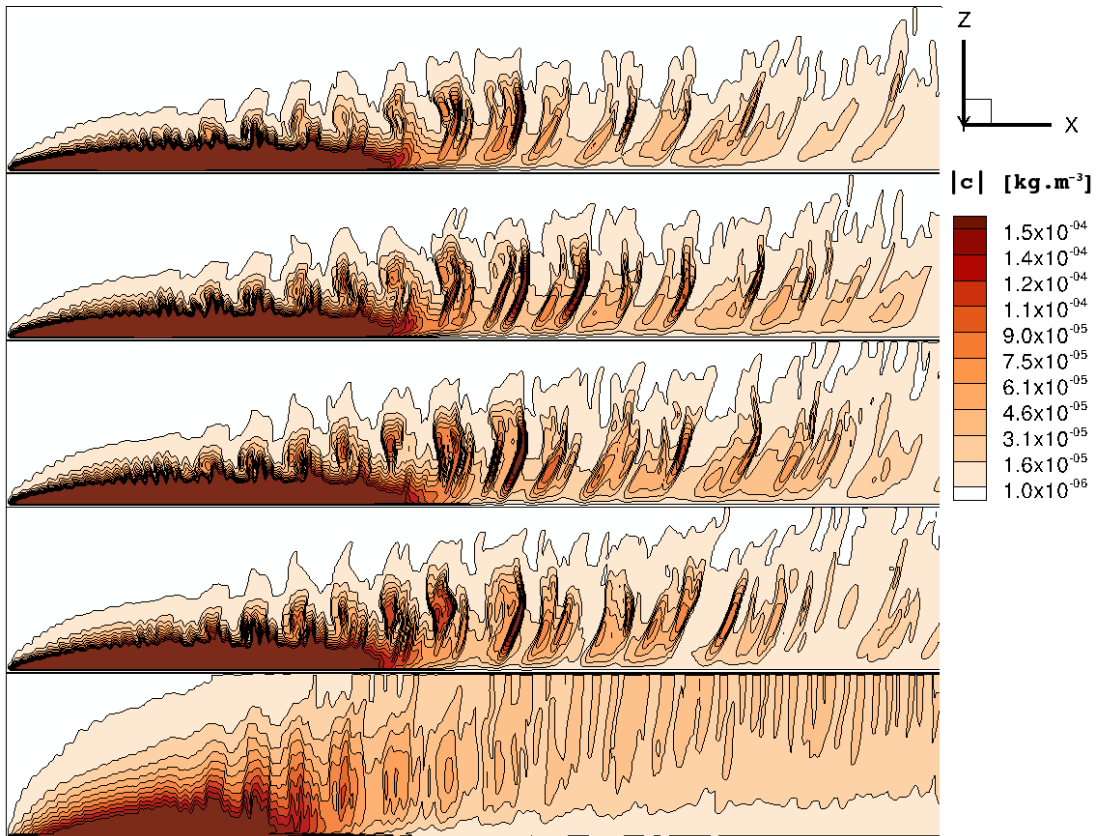


Figure 5.48: Y-slice of the sediment concentration  $c$ , from top to bottom:  $\eta = 0.007, 0.008, 0.009, 0.010$  and  $0.050 \text{ m}^2/\text{s}$ .

The differences between the structure of the sediment cloud are illustrated in Fig. 5.49 and Fig. 5.50 by the  $z$ -slice through the sediment cloud 1 m above the seabed. Consistent with the observations from Fig. 5.47 and Fig. 5.48, the sediment concentration in the layer 1 m above the seabed is lower for smaller values of  $\eta$  up to  $0.004 \text{ m}^2/\text{s}$ . The amount of sediment in the 1 m layer is similar for values of  $\eta$  between  $0.005 \text{ m}^2/\text{s}$  and  $0.007 \text{ m}^2/\text{s}$ . For  $\eta$  bigger than  $0.007 \text{ m}^2/\text{s}$  the sediment concentration in the 1 m layer decreases.

## 5.5 Sediment Concentration

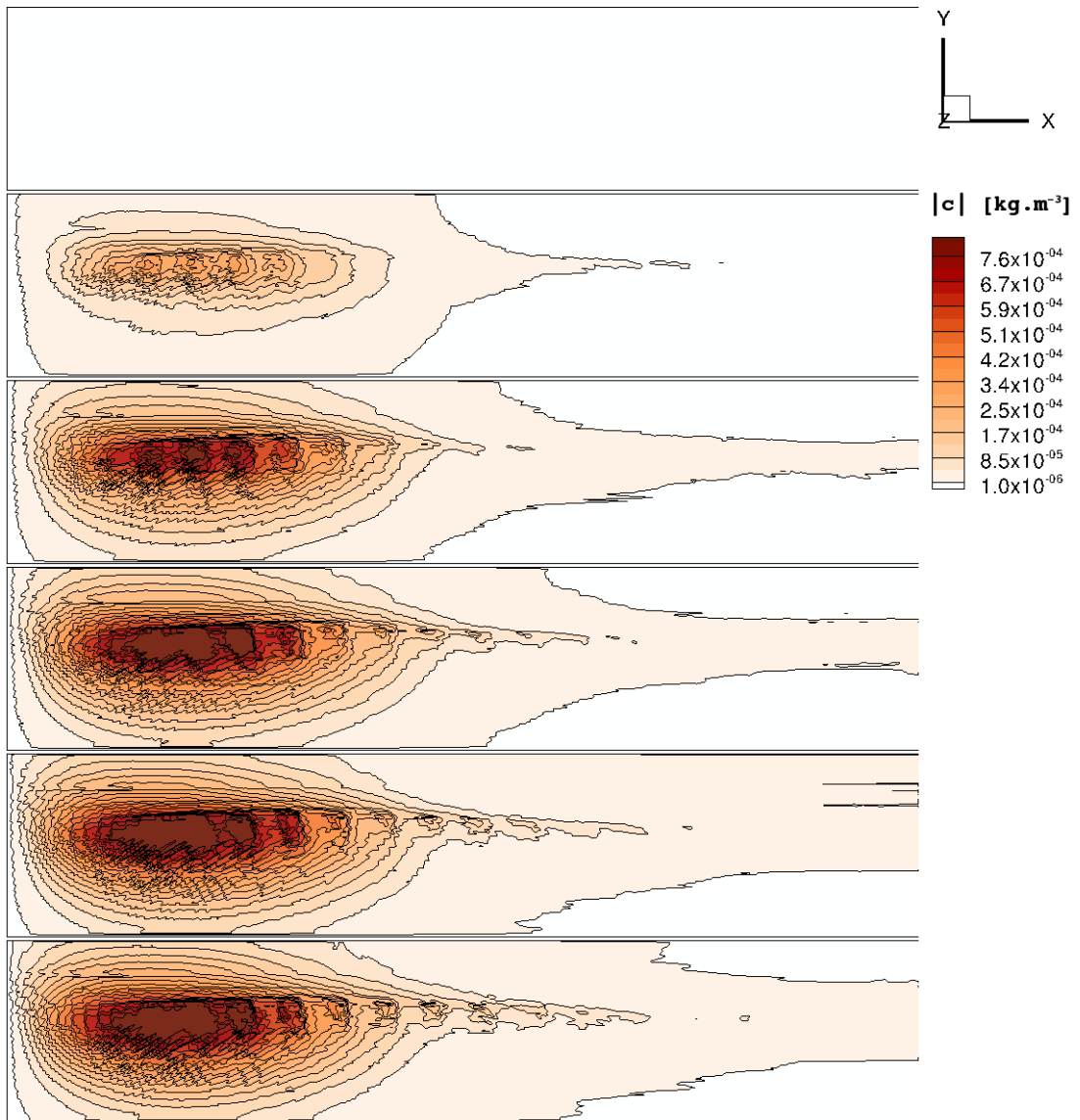


Figure 5.49: Z-slice of the sediment concentration  $c$  at height 1 m, from top to bottom:  $\eta = 0.001, 0.002, 0.003, 0.004, 0.005$  and  $0.006 \text{ m}^2/\text{s}$ .

## 5.5 Sediment Concentration

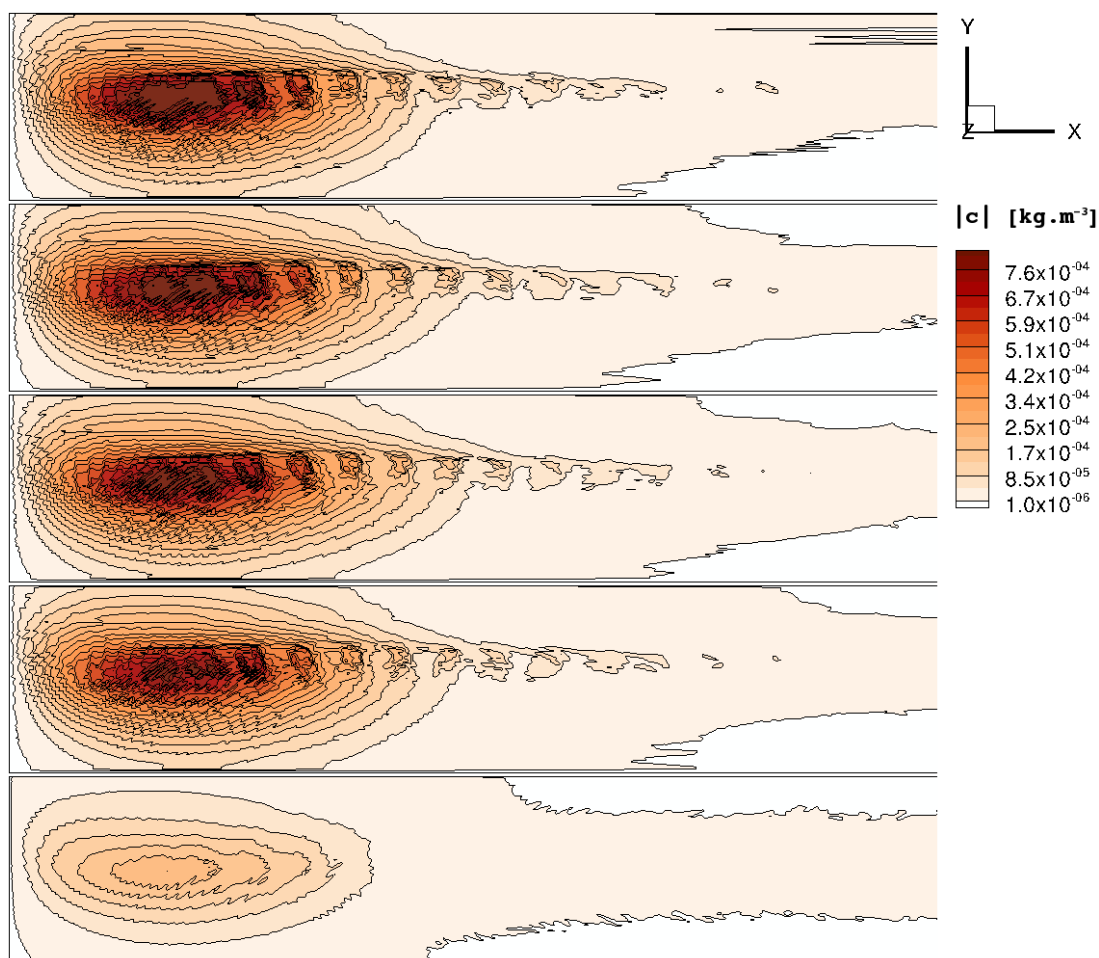


Figure 5.50: Z-slice of the sediment concentration  $c$  at height 1 m, from top to bottom:  $\eta = 0.007, 0.008, 0.009, 0.010$  and  $0.050 \text{ m}^2/\text{s}$ .

## 5.5 Sediment Concentration

The magnitude of the gradient of the sediment concentration  $|\nabla c|$  is illustrated in Fig. 5.51 and Fig. 5.52 by the y-slice of  $|\nabla c|$ .

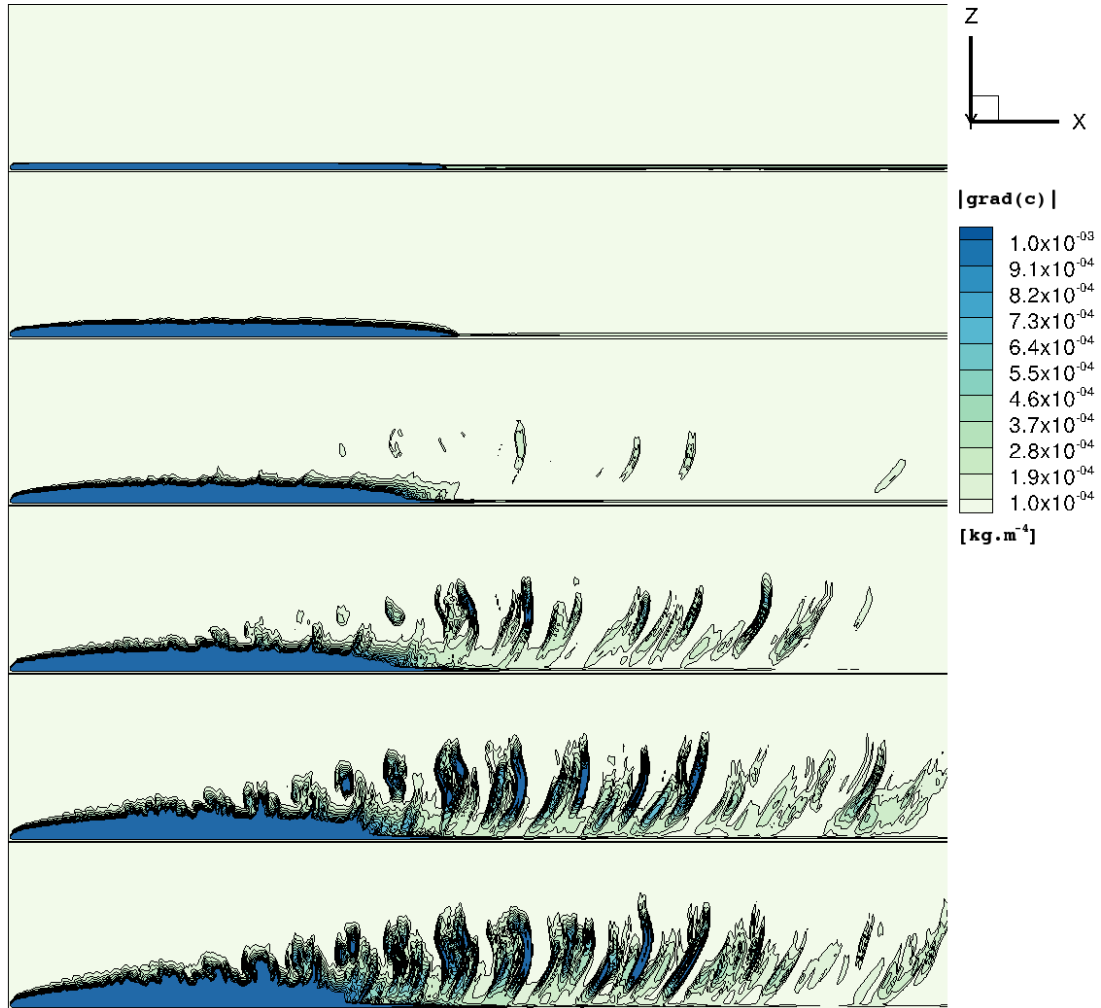


Figure 5.51: Y-slice of the magnitude of sediment concentration gradient  $|\nabla c|$ , from top to bottom:  $\eta = 0.001, 0.002, 0.003, 0.004, 0.005$  and  $0.006 \text{ m}^2/\text{s}$ .

The highest values of the concentration gradient for  $\eta = 0.001 \text{ m}^2/\text{s}$  are to be found in the thin layer above the seabed. The location of the high values of  $|\nabla c|$  coincides with the highest values of  $|c|$  in Fig. 5.47. The big concentration gradient for  $\eta = 0.001 \text{ m}^2/\text{s}$  is due to the difference between the concentration values in the thin layer, shown in Fig. 5.47, and the zero concentration above the thin layer. The high concentration gradient in the thin layer suggests that the

## 5.5 Sediment Concentration

value  $0.001 \text{ m}^2/\text{s}$  is indeed an unrealistic representation of sediment diffusivity. The concentration gradient indicates that the sediment is more evenly distributed in the flow when  $\eta > 0.001 \text{ m}^2/\text{s}$ .

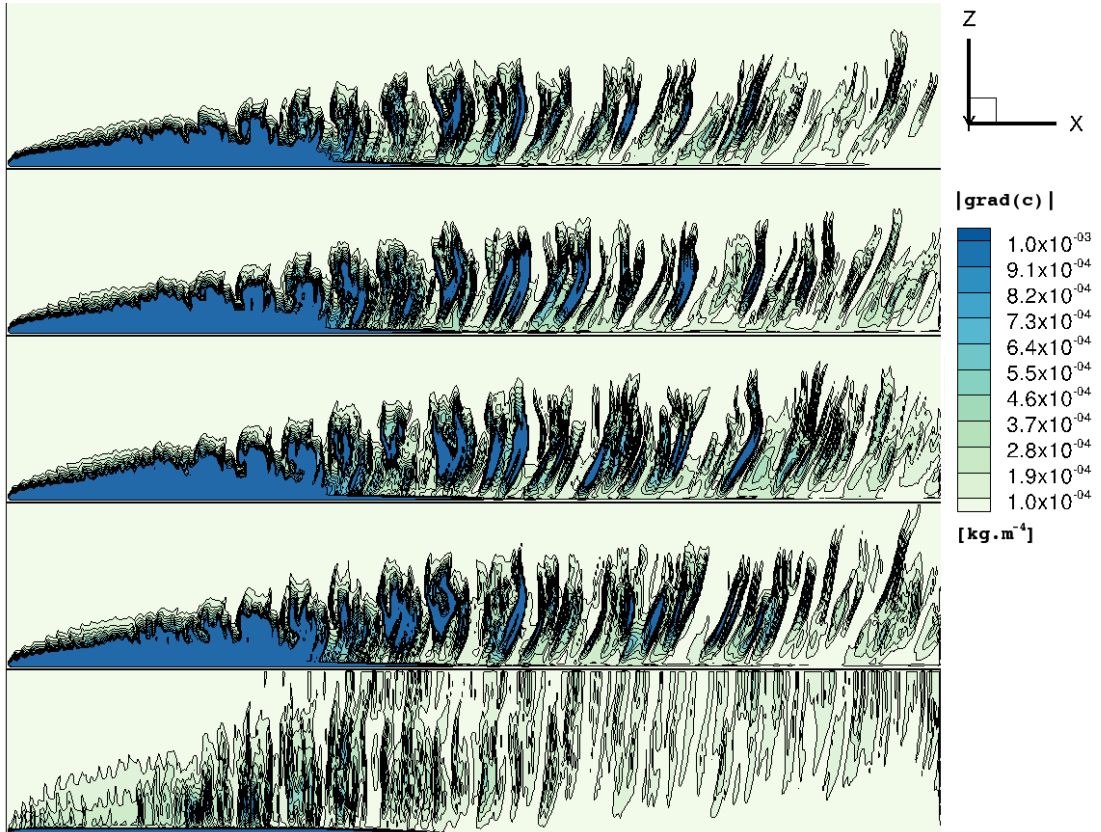


Figure 5.52: Y-slice of the magnitude of sediment concentration gradient  $|\nabla c|$ , from top to bottom:  $\eta = 0.007, 0.008, 0.009, 0.010$  and  $0.050 \text{ m}^2/\text{s}$ .

The magnitude of the concentration gradient for  $\eta = 0.05 \text{ m}^2/\text{s}$  is low in comparison with the other investigated cases. The low values of  $|\nabla c|$  for higher  $\eta$  resulted from two factors, firstly, the sediment is distributed more evenly in the flow and secondly, the sediment has been dispersed beyond the computational domain.

### 5.5.1 Sediment Size

The sediment concentration depends on the source of sediment, the fallout velocity and the sediment diffusivity. The sediment source and the fallout velocity vary with the size of sediment particles. The sensitivity of the model of sediment transport to the choice of sediment size can be determined from the simulations of three sizes of sediment particles,  $d = 0.25$  mm, 0.50 mm and 0.75 mm, all well within the definition of types of sand. The vorticity and velocity of the simulation are presented in Fig. 5.44, Fig. 5.45 and Fig. 5.46. The excess bed shear stress calculated for the three sediment sizes is presented in Fig. 5.53.

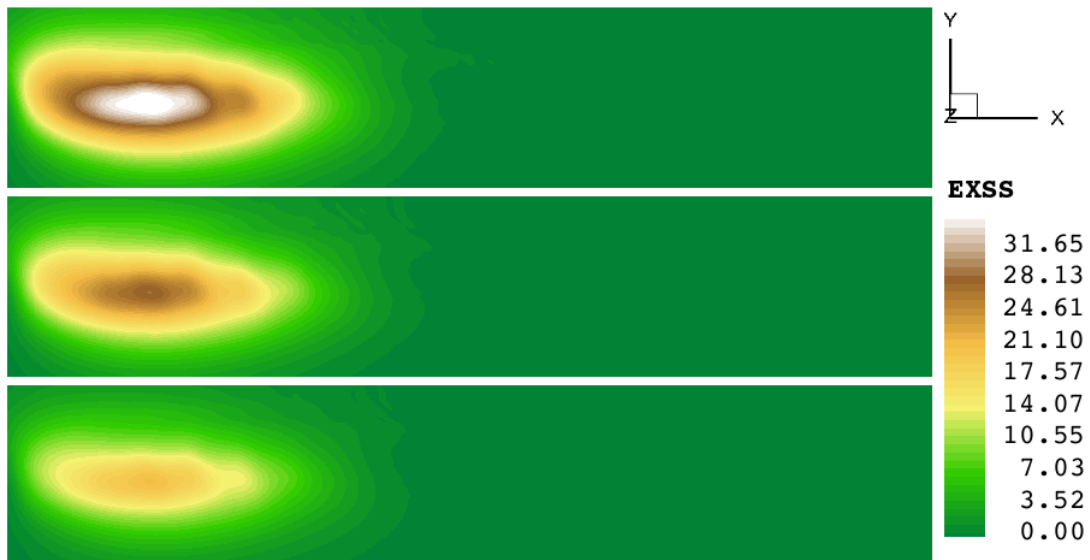


Figure 5.53: EXSS once the wake is fully developed, from top to bottom: Sediment size  $d = 0.25$  mm, 0.50 mm and 0.75 mm.

The lowest maximal value of the EXSS for  $d = 0.75$  mm corresponds to the higher value of the threshold which needs to be reached for the sediment particles to leave the seabed. The evolution of the EXSS averaged over the studied area of the seabed is shown in Fig. 5.54.

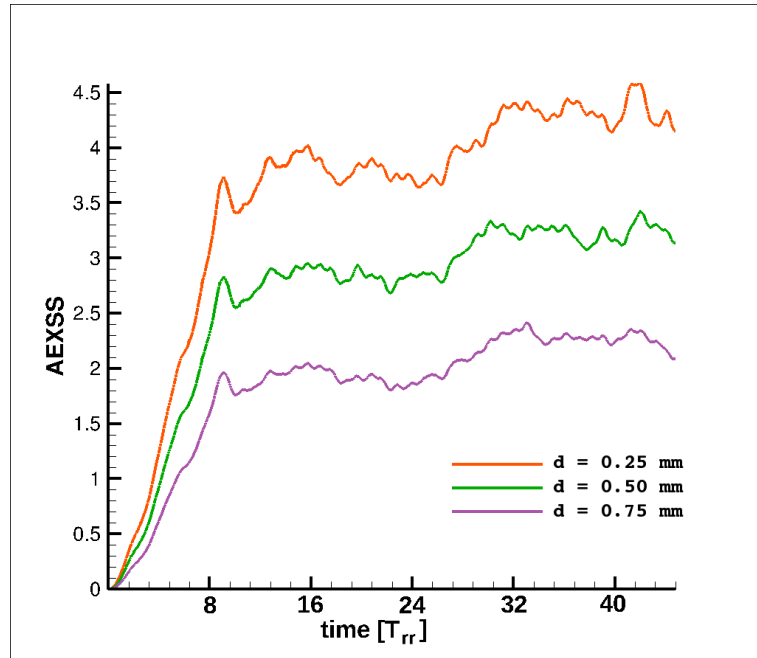


Figure 5.54: The evolution of the AEXSS for the three sediment sizes,  $d = 0.25$  mm, 0.50 mm and 0.75 mm.

The effect of the sediment size on the concentration of sediment is indicated by the averaged excess bed shear stress (AEXSS) for the three sediment sizes. The lower AEXSS for the larger sediment particles signifies that fewer larger sediment particles would be lifted into suspension by the same flow. The concentration of larger sediment particles in the flow would be lower, since fewer particles would leave the seabed and the particles in suspension would settle onto the seabed earlier due to larger settling velocity. Together with the sediment diffusivity, the sediment size and sediment density affect the motion of the sediment particles in the flow.

## 5.6 Summary

The flow through the rotor of the HATT was simulated by the VTM equipped with the non-uniform inflow model Eq. 5.4. The rotor vorticity field has a bigger influence on the flow down-stream of the HATT than the tide induced wake vorticity. The vertical gradient of the inflow velocity caused the rotor vorticity to incline in comparison with the uniform inflow case, leading to a reduction of the extent of the high near-bed velocity down-stream of the HATT. The excess bed shear stress (EXSS) was identified as a measure of the changes in the sediment erosion flux caused by the presence of the HATT in the flow. An area of the seabed proportional to the radius of the HATT is the most affected by the presence of the device. A representative value of the EXSS, the temporal mean of the average excess bed shear stress (MAEXSS), is chosen to assess the impact of the HATT on the seabed.

A sequence of velocity profiles has been used to represent stages of the tidal cycle in a series of simulations conducted to study the changes of the EXSS during the tidal cycle. The MAEXSS increases with increasing inflow velocity at the rotor hub, a relationship which can be approximated by the algebraic expression Eq. 5.10.

The effect of the position of the HATT in the boundary flow on the EXSS is predicted by the VTM's simulations. The simulations indicate that the distance between the rotor hub and the seabed influences the EXSS in two different ways. Firstly, when the HATT is placed so that  $z_{hub} \geq 1.3R$ , the MAEXSS decreases with increasing distance from the seabed and the relationship between the position of the rotor and the MAEXSS is well approximated by the expression Eq. 5.14. Secondly, when the rotor hub is closer than  $1.3R$  to the seabed, the large gradient of the inflow velocity across the rotor area deforms the rotor vorticity field, which for the minimum separation  $z_{hub} = 1.05R$ , is asymmetric and is transported by the flow away from the seabed within a distance of one rotor diameter down-stream of the HATT. The size of the area of the high EXSS is thus reduced in comparison with the case  $z_{hub} = 1.25R$ . In other words, the excess bed shear stress averaged over the investigated area of the seabed decreases with  $z_{hub}$  for the HATT closer than  $1.3R$  to the seabed.

The motion of the sediment lifted by the flow down-stream of the HATT is predicted by the sediment transport model. The role of the sediment diffusivity is assessed from the results of a parametric study. The highest concentration of sediment appears to be in the area below the ordered vortical structure observed in the rotor vorticity field for all of the investigated values of the sediment diffusivity. The distribution of sediment in the flow down-stream of the HATT is considered to be unrealistic for sediment diffusivity below  $0.002 \text{ m}^2/\text{s}$  because of the confinement of the sediment into the thin layer above the seabed. The AEXSS and its fluctuations are predicted to decrease with increasing size of sediment particles. To conclude, the sediment transport model is sensitive to the choice of the sediment parameters. Hence, the information about the composition of sediment in the vicinity of TECs is needed for a realistic assessment of the changes in the sediment motion caused by the presence of these devices on the seabed.

## Chapter 6

# Influence of Rotor Configuration on Sediment Motion

Whether a TECD would inflict detrimental changes on the seabed depends, undoubtedly, on the configuration of the rotor. The investigation of the impact of the horizontal axis tidal turbine (HATT), described in chapter 4, on the motion of sediment is presented in chapter 5. The HATT configuration is rather common among commercial designs of TECDs. The composition of the vorticity induced by the presence of the HATT in the boundary flow and the relationship between the rotor vorticity,  $\omega_w$ , and the tide induced wake vorticity,  $\omega^*$ , has been established for the HATT. The induced vorticity field,  $\omega_I = \omega_w + \omega^*$ , down-stream of the HATT determines the extent of sediment erosion.

A possible variation of the impact of a TECD on the seabed with the design of the device motivated the research presented in this chapter. The configuration of a vertical-axis tidal turbine (VATT) is introduced and the analysis of the flow through the rotor of the VATT, using the same approach as for the HATT in the previous chapter, is presented in section 6.1. The VATT configuration, studied in a horizontal position, simulating so called cross-flow tidal turbines (CF TTs), is likely to have a different impact on the seabed than the vertical configuration. Furthermore, the impact of the CF TT on the seabed could depend on the sense of rotation, hence this device is analysed for two operating conditions, clock-wise and anti-clock-wise rotation, in section 6.2.

## 6.1 Vertical Axis TECD

The flow down-stream of a vertical axis tidal turbine (VATT) was simulated by the modified version of the Vorticity Transport Model (VTM), described in chapter 2. The interactions of the flow down-stream of the VATT and the seabed were studied with the aim of comparing the findings with the investigation of the impact of the HATT presented in chapter 5.

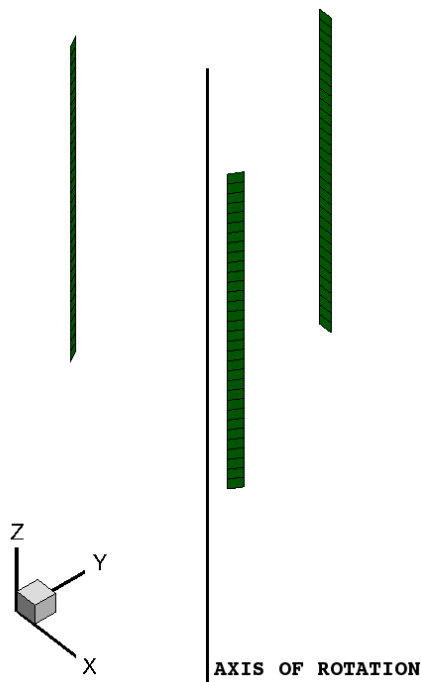


Figure 6.1: Position of the blades of the VATT in the coordinate system.

The blades, which are depicted in Fig. 6.1, of the VATT are not twisted and have constant chord. The length of the blades is equal to the radius of the HATT,  $l_{VATT} = R$ , while the distance between each blade and the rotation axis is  $R_{VATT} = 0.33R$ . The dynamic loading on the blades of this device does not compromise the structural integrity of the device, according to the analysis of the blade loading performed by the semi-empirical Dynamic Stall Model, which is described in chapter 2. The parameters of the VATT are listed in Table 6.1, where AR stands for the aspect ratio of the blades and  $N_b$  is the number of blades

of the device. The power coefficient of the device is presented in Fig. 6.2, where the error bars express the amplitudes of the oscillations due to the azimuthal variation in the blade loading during a single rotor revolution, as described in Scheurich [3].

$R_{VATT}$ [m]	$l_{VATT}$ [m]	$N_b$	Aerofoil	AR
1.65	5	3	NACA0015	25.85

Table 6.1: Parameters of the VATT.

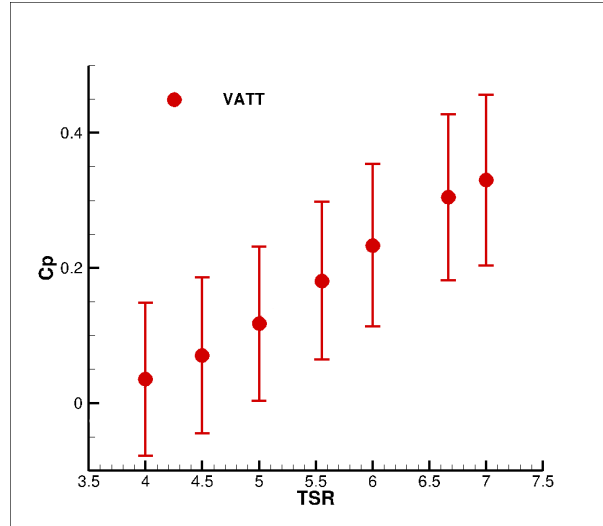


Figure 6.2: Power coefficient of the VATT.

The progress of the simulation of the rotor vorticity field is illustrated in Fig. 6.4. The rotor vorticity is transported by the boundary layer flow, defined by Eq. 5.4 with

$$A = \frac{v_{R/2}}{\log\left(\frac{z_{R/2}}{k_s} + 1\right)}, \quad (6.1)$$

which is chosen so that the inflow velocity in the middle of the vertical blades,  $v_{R/2} = |\mathbf{v}_{fs}(z_{R/2})|$ , together with the condition that the inflow velocity is zero on the seabed, determine the function Eq. 5.4.

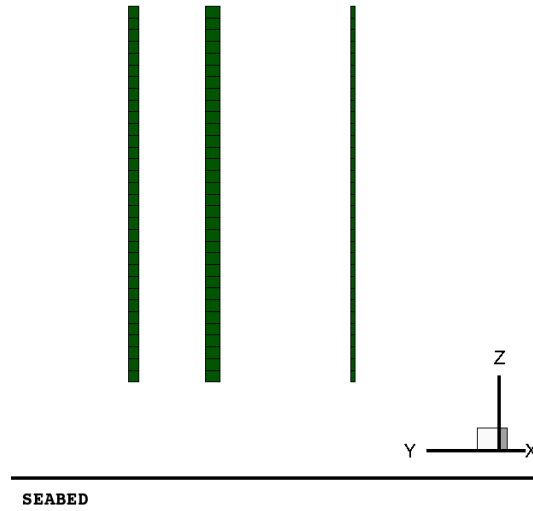


Figure 6.3: Position of the blades of the VATT above the seabed.

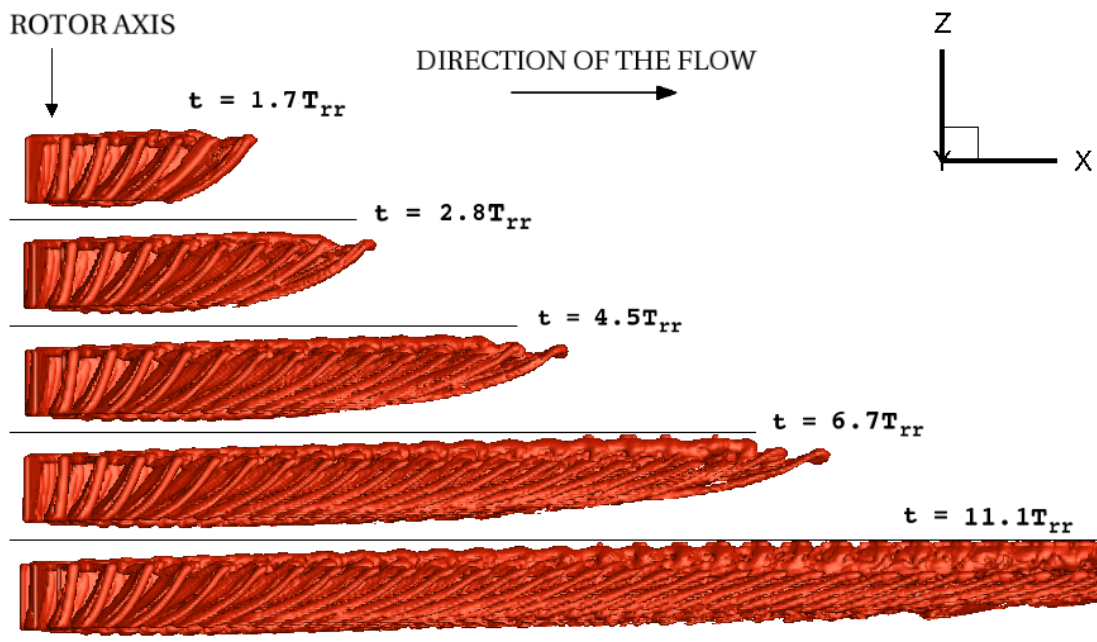


Figure 6.4: Illustration of the evolution of the rotor vorticity field for the VATT, simulated by the modified VTM.

The VATT is positioned so that the separation between the blade tips and the seabed is  $0.26R$ , i.e. the centre of the blades is located at  $z_{R/2} = 0.76R$  above the seabed, as shown in Fig. 6.3.

The rotor vorticity leaves the blades concentrated into blade-shaped structures of trailed vorticity, which are attached to sheets of shed vorticity. The blade-shaped structures incline down-stream of the VATT and the inclination angle increases with the distance from the device. The increasingly inclined vorticity structure expands further above the seabed, as seen in Fig. 6.5.

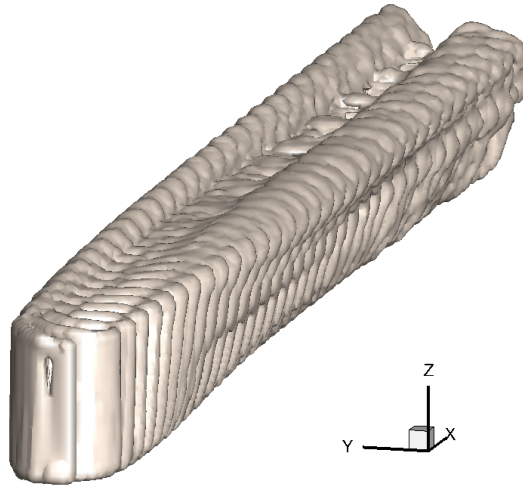


Figure 6.5: The rotor vorticity field of the fully developed wake down-stream of the VATT.

$v_{tip}/v_{R/2}$	7.00	6.67	6.00	5.56	5.00	4.50	4.00
$v_{R/2}$ [m/s]	0.71	0.75	0.83	0.90	1.00	1.11	1.25
$\Delta v_R$ [m/s]	0.19	0.20	0.22	0.24	0.26	0.29	0.33

Table 6.2: The inflow conditions in relation to the difference of the inflow velocity across the VATT.

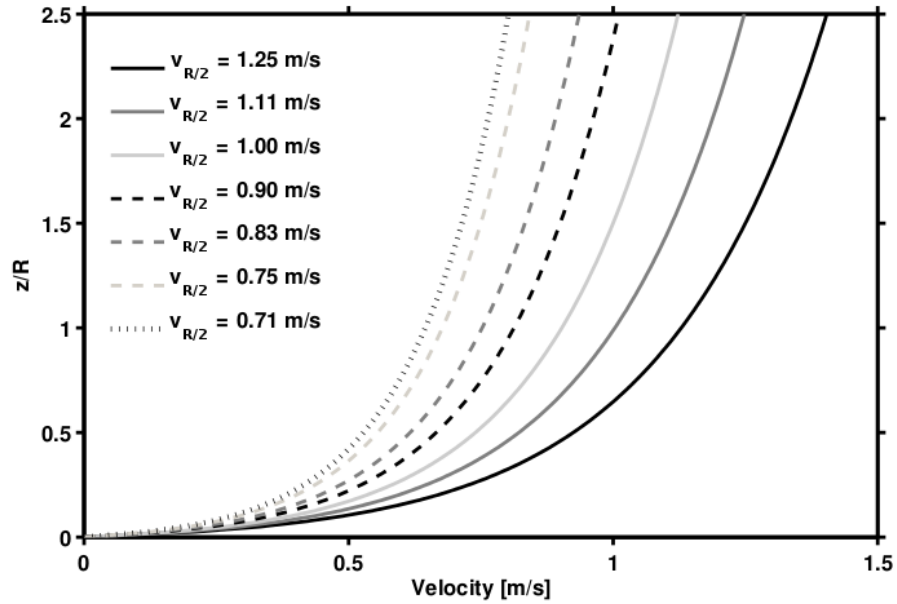


Figure 6.6: Set of velocity profiles used to represent a part of the tidal cycle.

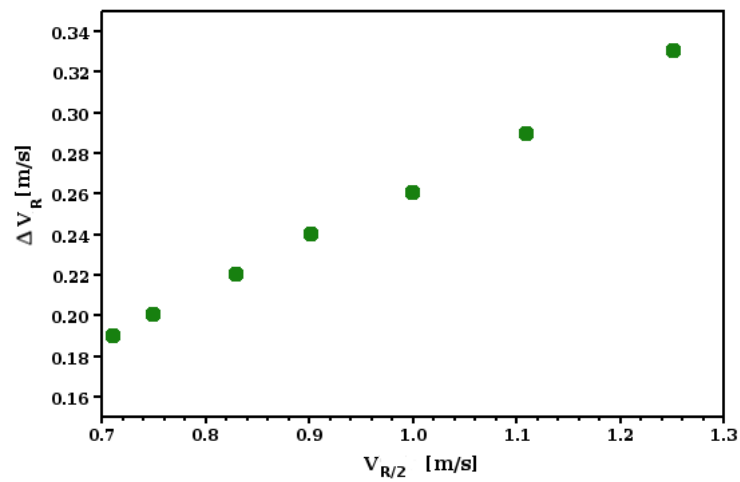


Figure 6.7: The difference of the inflow velocity across the VATT.

In a similar vein to the study of the seabed erosion during the tidal cycle conducted for the HATT, the flow through the VATT during the tidal cycle is analysed here. The set of velocity profiles, which are used to represent the tidal

cycle, is presented in Fig. 6.6 and the gradient of the inflow velocity across the rotor is illustrated in Fig. 6.20.

The speed of rotation is set at  $1\text{rads}^{-1}$  for each of the inflow conditions, listed in Table 6.2. The rotor vorticity field for the set of velocity profiles is presented in Fig. 6.8 as the iso-surface of 10% maximal vorticity for  $v_{tip}/v_{R/2} = 4$ . The detailed structure of the rotor vorticity field is compared in Fig. 6.9 for the inflow conditions listed in Table 6.2.

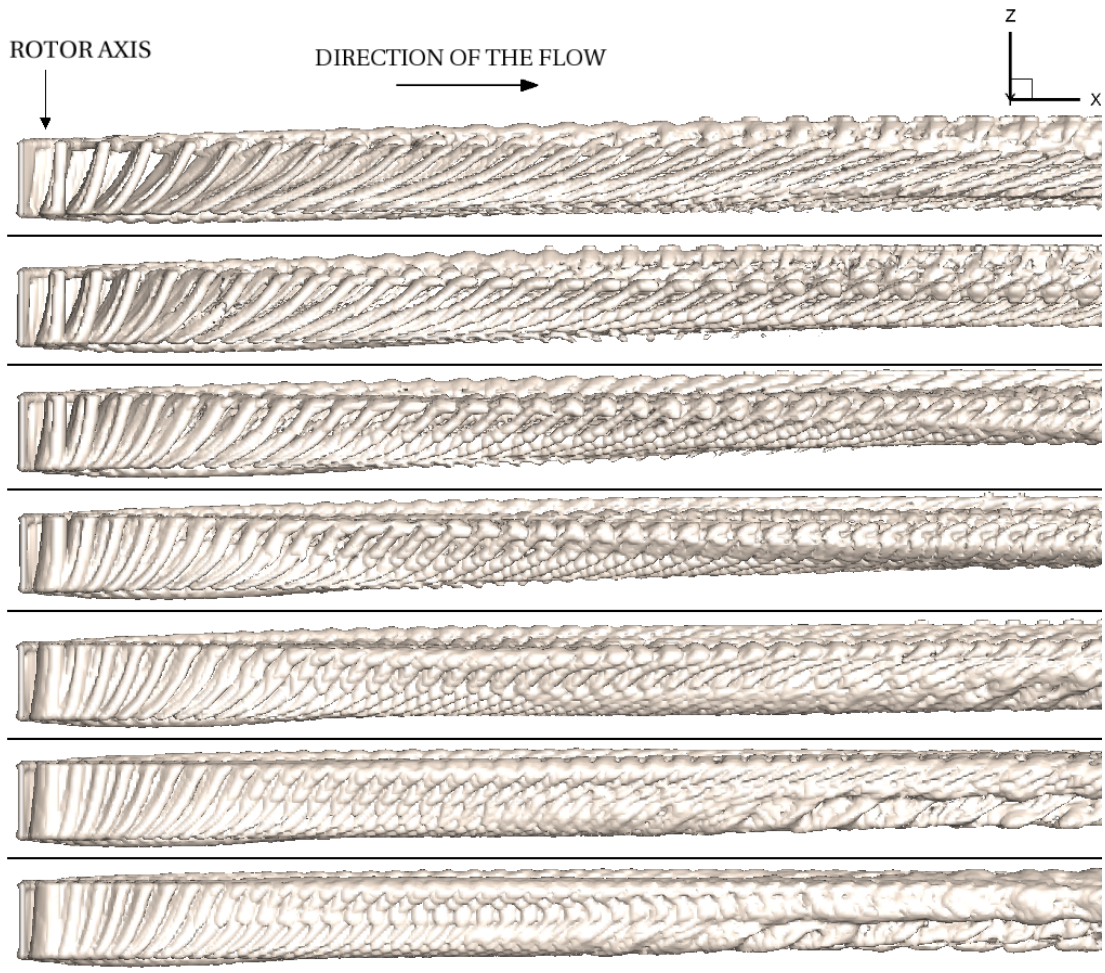


Figure 6.8: The rotor vorticity field of the fully developed wake, from top to bottom:  $v_{tip}/v_{R/2} = 4, 4.5, 5, 5.56, 6, 6.67, 7$ .

The presented iso-surface of the rotor vorticity for lower  $v_{tip}/v_{R/2}$  comprises the blade-shaped formations, where the magnitude of the rotor vorticity,  $|\omega_w|$ , is high, and the regions where  $|\omega_w|$  is less than 10 % of the maximal vorticity. Similarly to the rotor vorticity field down-stream of the HATT, the inclination angle of the vorticity structure is greater for lower values of the ratio  $v_{tip}/v_{R/2}$ , which corresponds to faster inflows and greater vertical gradients of the inflow velocity across the rotor.

The rotor vorticity is elevated from the seabed by the flow within a distance  $2R$  down-stream of the VATT, however the dissolving vortices approach the seabed again beyond a distance  $4R$  down-stream of the device. The described behaviour is most pronounced for  $v_{tip}/v_{R/2} = 4.5$  in Fig. 6.9.

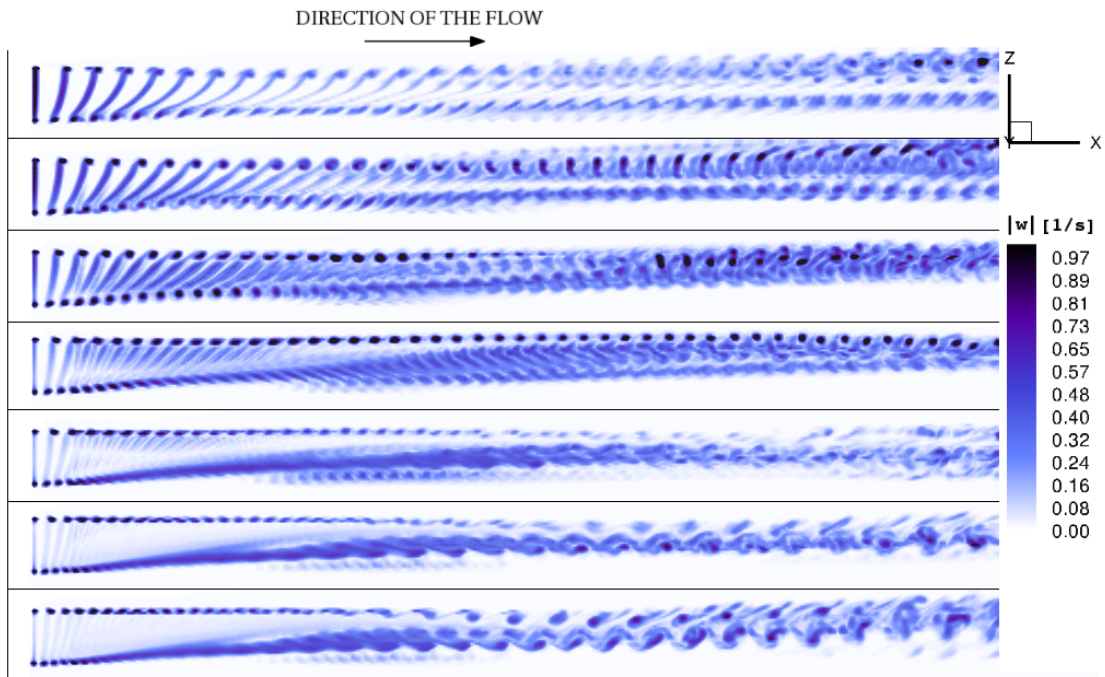


Figure 6.9: Y-slice of the rotor vorticity field of the fully developed wake, from top to bottom:  $v_{tip}/v_{R/2} = 4, 4.5, 5, 5.56, 6, 6.67, 7$ .

The results presented in chapter 5 suggest that the highest rotor vorticity down-stream of the HATT occurs for the fastest inflow. Down-stream of the VATT, however, the fastest inflow does not appear to cause the highest values of the rotor vorticity, despite the strong vortex bound to the blades of the rotor. The strongest vortices, observed in Fig. 6.9, are located down-stream of the rotor for  $v_{tip}/v_{R/2} = 4.5, 5$  and  $5.56$  at approximately  $z_{R/2} + R/2$  above the seabed. The rotor vorticity field for  $v_{tip}/v_{R/2} \geq 6$  is dominated by dissolving vortices which are transported away from the seabed.

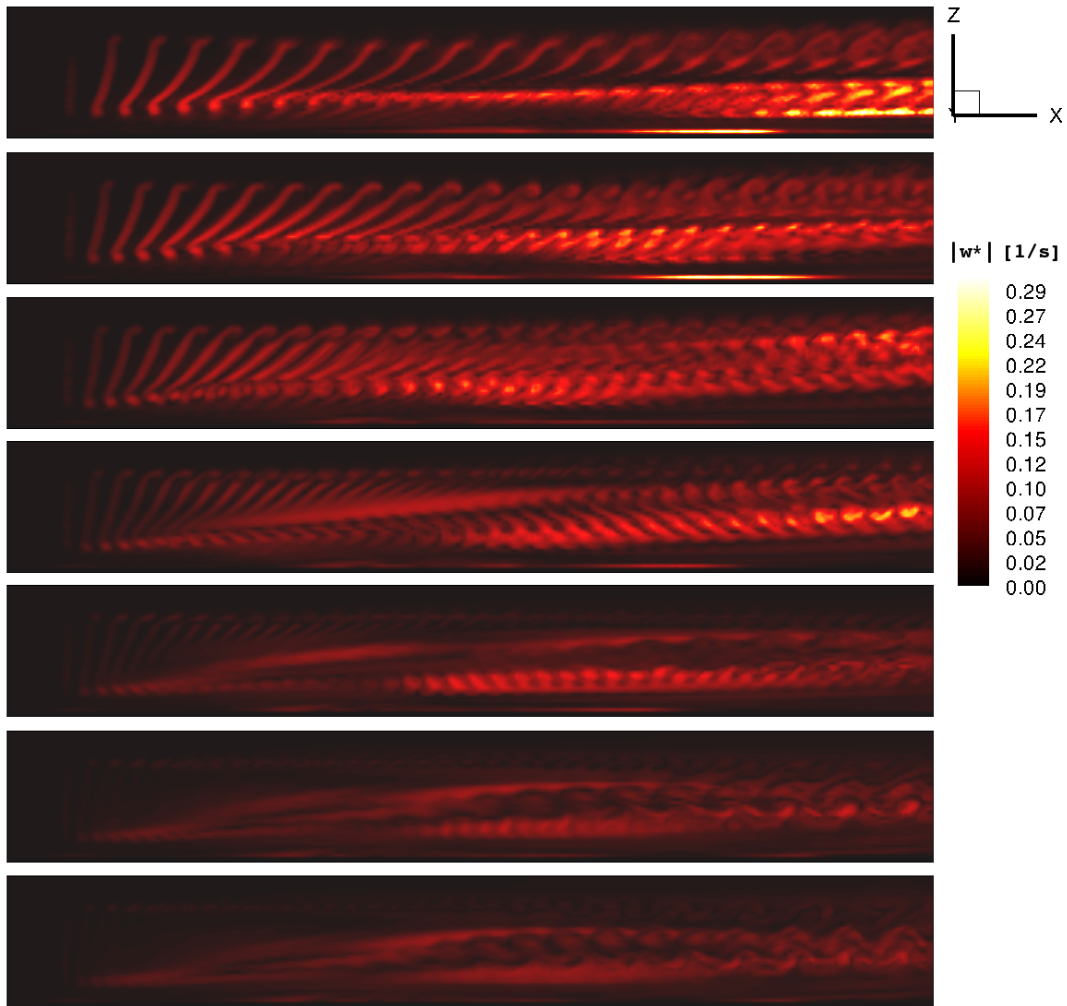


Figure 6.10: Y-slice of the tide induced wake vorticity field of the fully developed wake, from top to bottom:  $v_{tip}/v_{R/2} = 4, 4.5, 5, 5.56, 6, 6.67, 7$ .

The planar section (y-slice) through the tide induced wake vorticity,  $\omega^*$ , is shown in Fig. 6.10. Similarly to the rotor vorticity field,  $\omega_w$ , presented in Fig. 6.9, the tide induced wake vorticity contains a row of long, narrow regions of high  $|\omega_w|$ , which are increasingly inclined. The pattern observed in Fig. 6.10 loses coherence further down-stream of the rotor, where the vorticity structure starts to disintegrate.

The structure of the rotor vorticity down-stream of the VATT appears to be more ordered than the rotor vorticity down-stream of the HATT, where the initially regular helical structure breaks down at a distance proportional to the rotor radius. The contrast between the two presented structures could be due to the relative levels at which the vorticity iso-surfaces are selected since the vorticity magnitude of the VATT and the HATT are of a different order. The strongly structured wake of the VATT might not be realistic, however, since the wake development does not account for the turbulence in the tidal stream as discussed in section 2.4.7. In real flows at tidal sites, the turbulence intensity varies between 50% in slack waters and 10% during strong tides according to Thomson et al. [50]. The non-zero turbulent intensity suggests an earlier disintegration of the vorticity structure would occur if turbulent effects were considered.

The presence of the VATT in the flow induces the tide induced wake vorticity, which has a bigger influence on the flow than in the case of the HATT (presented in chapter 5). Up to 13% of the induced vorticity occurred due to the reaction of the boundary flow to the presence of the device in operation, which would not have occurred if the flow had been approximated as uniform. The maximal magnitude of  $\omega^*$  is compared to the maximal magnitude of  $\omega_w$  in Fig. 6.11 for the set of the velocity profiles presented in Fig. 6.6.

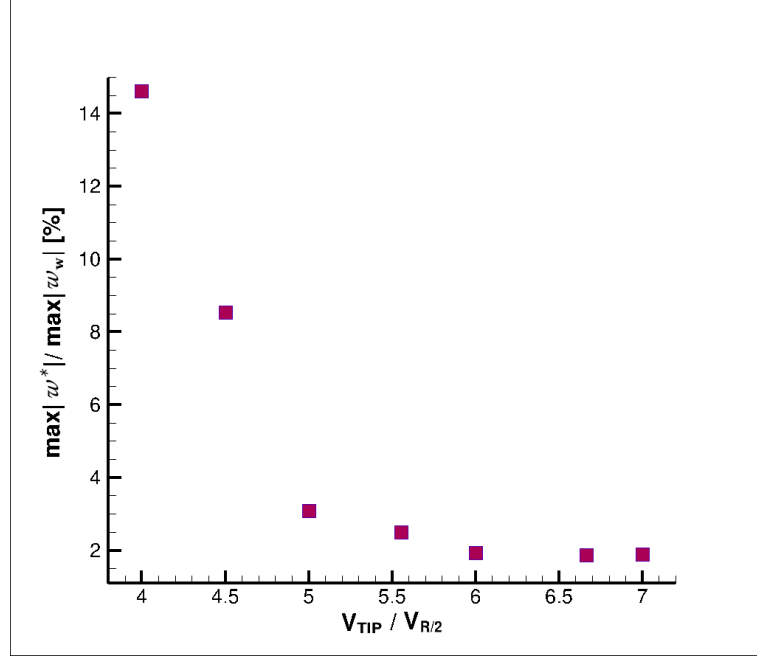


Figure 6.11: Composition of the induced vorticity  $\omega_I = \omega^* + \omega_w$  of the fully developed wake,  $\max |\omega^*|$  vs.  $\max |\omega_w|$ .

From Fig. 6.10 it follows that the tide induced wake vorticity field for  $v_{tip}/v_{R/2} = 4$  has the most influence on the flow down-stream of the VATT among the investigated inflow conditions. Indeed, the highest tide induced wake vorticity occurs close to the seabed for  $v_{tip}/v_{R/2} = 4$  and 4.5.

The induced vorticity  $\omega_I = \omega^* + \omega_w$  is responsible for changes in the velocity close to the seabed. The near-bed velocity determines the excess bed shear stress (EXSS). The EXSS is zero where the flow is not strong enough to erode sediment from the seabed, according to the model for the sediment uplift. On the other hand, a positive EXSS indicates the motion of sediment into suspension. The spatial distribution of the EXSS of the fully developed wake is shown in Fig. 6.12, from which it can be observed that the high values of the EXSS are concentrated immediately down-stream of the VATT for all investigated inflow conditions.

The magnitude of the EXSS within the area proportional to  $R^2$  down-stream of the device is expected to be bigger for faster inflow conditions, i.e. lower values of  $v_{tip}/v_{R/2}$ . This is, however, not the case for  $v_{tip}/v_{R/2} = 4$ , where the smaller

EXSS can be attributed to the smaller magnitude of the rotor vorticity observed in Fig. 6.9.

Further down-stream of the VATT, the positive EXSS persists, in contrast to the zero EXSS further down-stream of the HATT, presented in chapter 5. It should be noted that for  $v_{tip}/v_{R/2} = 4$  and  $4.5$  the EXSS reaches more than 50% of its maximal magnitude at a distance approximately  $4R$  from the rotor, where the dissolving vortices re-approach the seabed, as observed in Fig. 6.9. At a distance approximately  $6R$  down-stream of the rotor, the EXSS contains streaks of higher and lower values, effectively reducing the average EXSS. The position of the streaks coincides with the highest values of the tide induced wake vorticity, presented in Fig. 6.10 for  $v_{tip}/v_{R/2} = 4$  and  $4.5$ . Such an observation suggests that the tide induced wake vorticity could act against the rotor vorticity, lowering the impact of the VATT on the seabed for the two fastest inflow velocities (i.e.  $v_{tip}/v_{R/2} = 4$  and  $4.5$ ).

The evolution of the EXSS averaged over the studied area of the seabed is illustrated in Fig. 6.13. The EXSS varied in time even after the induced vorticity reached the end of the computational domain. Fig. 6.13 shows that the averaged excess bed shear stress (AEXSS) for  $v_{tip}/v_{R/2} = 4.5$  is bigger than the AEXSS for  $v_{tip}/v_{R/2} = 4$ , in contrast to the AEXSS for the HATT, presented in Fig. 5.19.

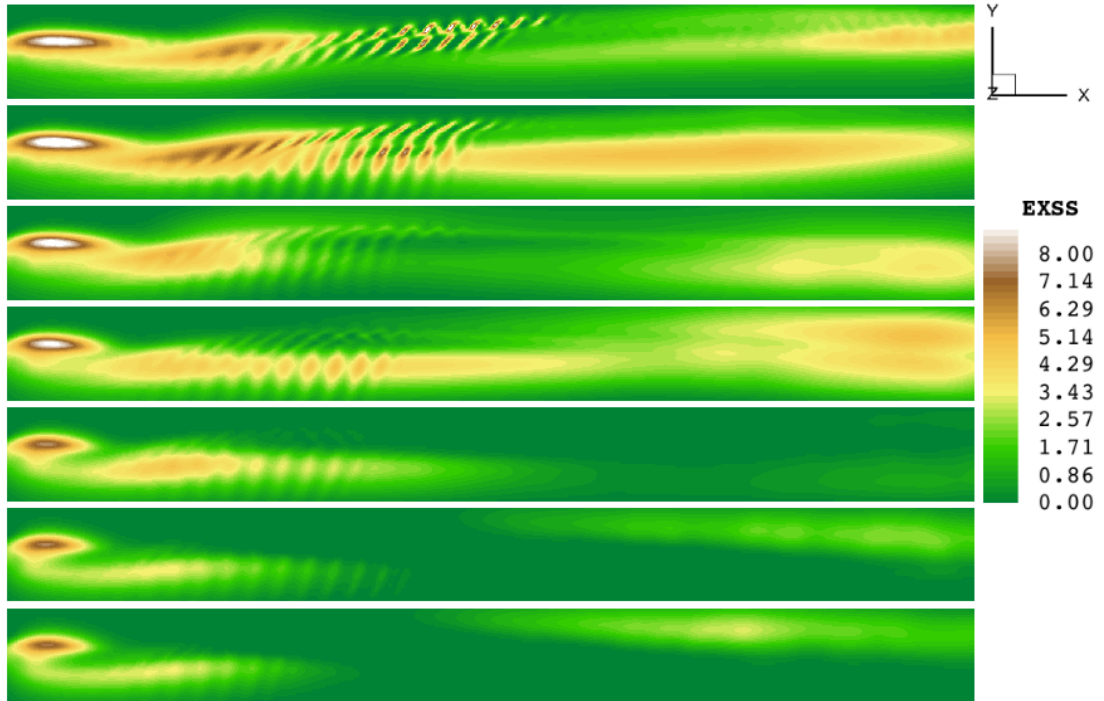


Figure 6.12: The excess bed shear stress induced by the fully developed wake, from top to bottom:  $v_{tip}/v_{R/2} = 4, 4.5, 5, 5.56, 6, 6.67, 7$ .

To express the over-all impact of the VATT on the seabed, the mean of the AEXSS over the time interval which represents the final stage of wake development shown in Fig. 6.4 was evaluated. The temporal mean of the averaged excess bed shear stress (MAEXSS) is presented in Fig. 6.39 for the inflow conditions listed in Table 6.2. The MAEXSS increases with the inflow velocity when  $v_{R/2} \leq 1$  m/s, i.e.  $v_{tip}/v_{R/2} \geq 4.5$ . In contrast to the MAEXSS down-stream of the HATT, the MAEXSS down-stream of the VATT, which is presented in Fig. 6.39, did not show a simple dependence on the inflow velocity. Instead, the impact of the VATT on the seabed is reduced for the inflow of  $v_{R/2} = 1.25$  m/s to the level observed for  $v_{R/2} = 0.90$  m/s.

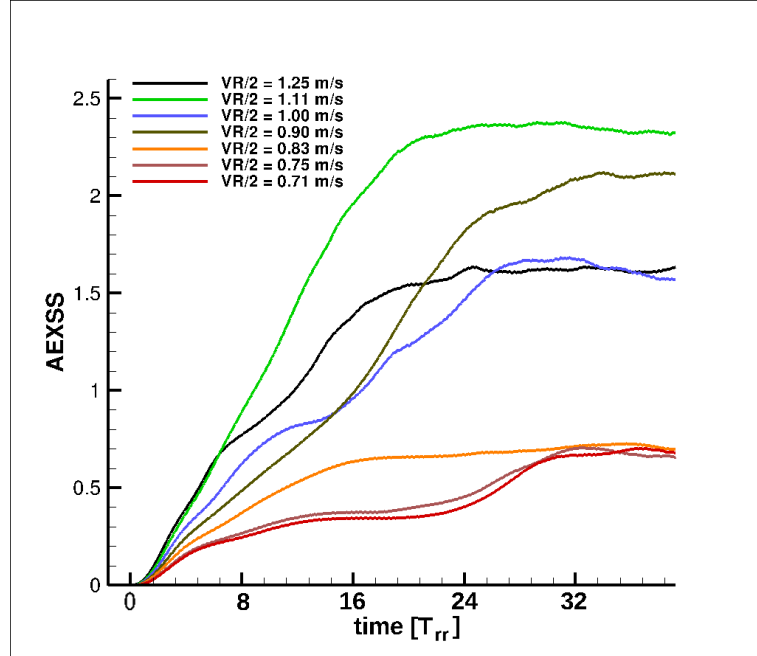


Figure 6.13: The AEXSS evolution for the VATT.

The choice between the HATT and the VATT configurations of the TECD could mitigate the impact of the device on the seabed. The flow down-stream of the VATT could be more influenced by the tide induced wake vorticity than the flow down-stream of the HATT. The impact of the VATT on the seabed, which is represented by the EXSS averaged over the studied area of the seabed, appears to be lowest for the inflow faster than  $v_{R/2} = 0.90$  m/s, i.e.  $v_{tip}/v_{R/2} \leq 5.56$ . Higher EXSS might occur further from the VATT, beyond the computational domain, however, since the cases when the inflow velocity is smaller than  $v_{R/2} = 1$  m/s suggest that the affected area down-stream of the VATT is limited and its extent depends on the inflow.

Indeed, the rotor vorticity, which affects the flow the most, is elevated by the boundary flow further down-stream of the VATT (as seen in Fig. 6.9 for  $v_{R/2} < 1$  m/s). Moreover, the rotor vorticity starts to disintegrate further down-stream of the device. This results in a shorter extent of the region of positive EXSS, observed for  $v_{R/2} < 1$  m/s in Fig. 6.12.

## 6.2 Cross-Flow TECD

The vertical axis turbine defined in section 6.1 is placed horizontally into the tidal flow, so that the position of the rotor hub is  $z_{hub} = 0.85R$ . The impact of such an arrangement on the seabed is the focus of this section. The horizontal VATT is referred to as the cross-flow tidal turbine (CFTT) in this dissertation.

Similarly to the VATT, the CFTT is placed in the boundary flow, defined by Eq. 5.4 with

$$A = \frac{v_{hub}}{\log\left(\frac{z_{hub}}{k_s} + 1\right)}. \quad (6.2)$$

The cross-flow geometry has advantages over the vertical configuration. Although a CFTT does not benefit from the ability to extract power from multiple directions, the horizontal orientation permits a row of CFTTs to be installed on the seabed, using one generator for two CFTTs. The CFTT is considered here in two operating conditions, clockwise and anti-clockwise rotation. The clock-wise sense of rotation is defined in Fig. 6.14.

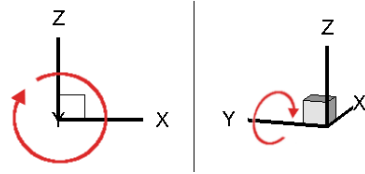


Figure 6.14: Clock-wise sense of rotation of the CFTT.

The power extraction capacity of the CFTT is illustrated in Fig. 6.15, where the error bars express the oscillations caused by the azimuthal variation in the blade loading during a single rotor revolution, as described in Scheurich [3].

The progress of the VTM-simulated rotor vorticity field down-stream of the CFTT, which operates clock-wise (CFCTT) is presented in Fig. 6.16, and the corresponding development for the device in anti-clock-wise operation (CFATT) is presented in Fig. 6.18. The structure of the rotor vorticity field down-stream of the CFCTT is illustrated in Fig. 6.17.

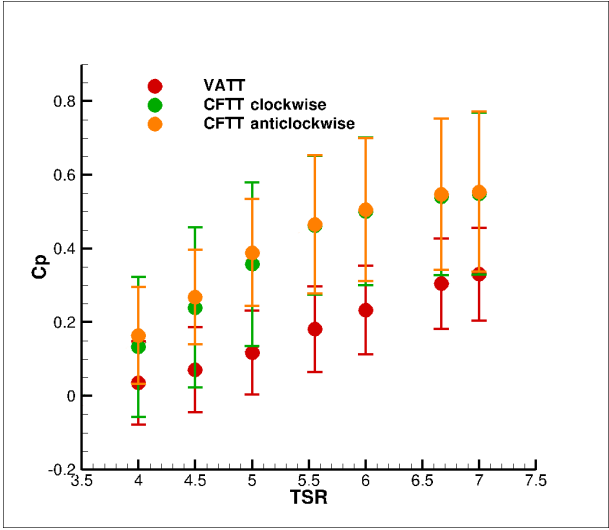


Figure 6.15: Power coefficient of the CFTT and the VATT.

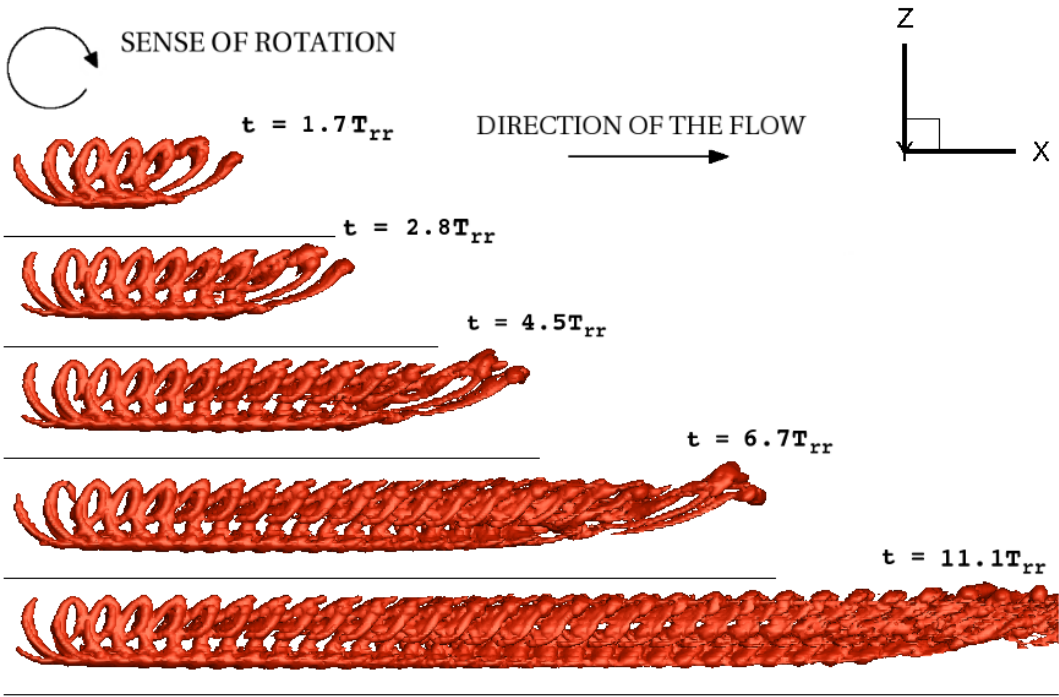


Figure 6.16: Illustration of the evolution of the rotor vorticity field for the CFCTT, simulated by the modified VTM.

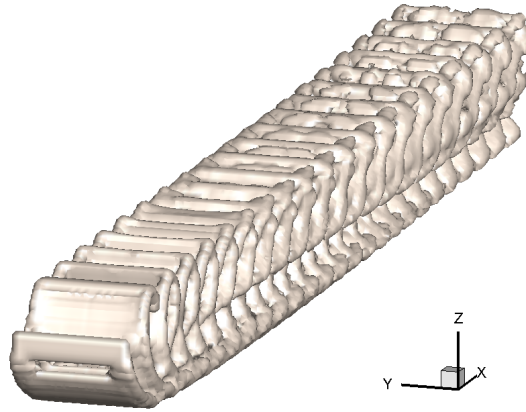


Figure 6.17: The rotor vorticity field of the fully developed wake down-stream of the CFCTT.

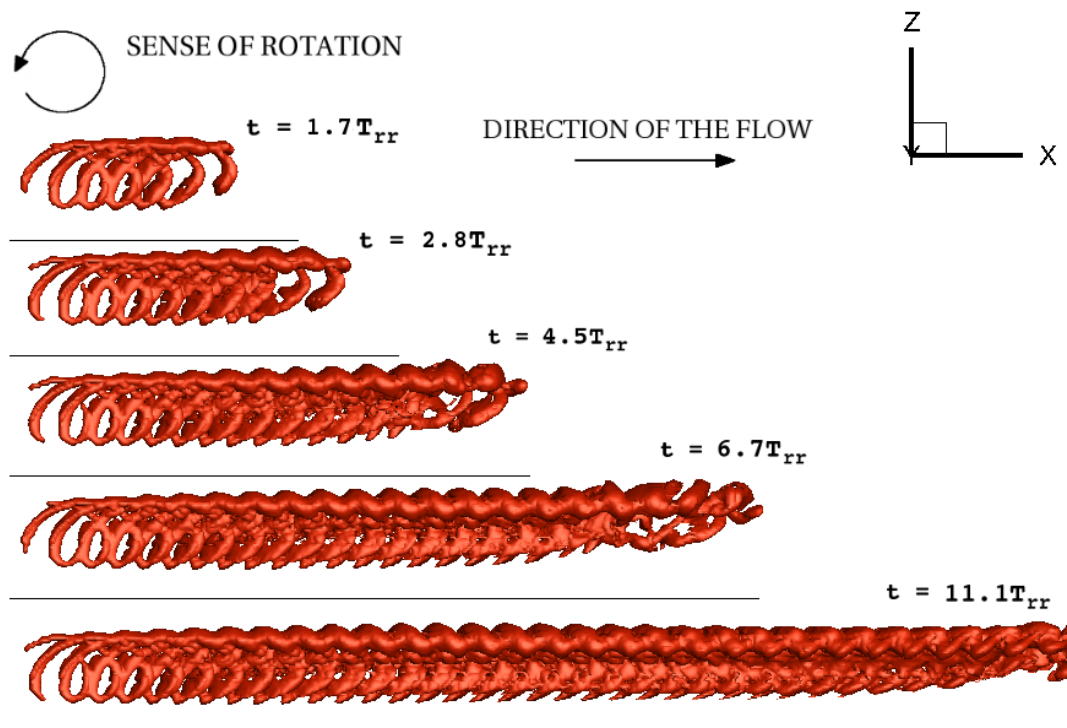


Figure 6.18: Illustration of the evolution of the rotor vorticity field for the CFATT, simulated by the modified VTM.

The rotating blades of the CF TT induce trailed and shed vorticity which is transported down-stream by the boundary flow. The induced vorticity structure becomes increasingly inclined with increasing distance from the rotor due to the vertical gradient of the inflow velocity.

In an analogy to the investigation of the changes in the flow down-stream of the VATT during the tidal cycle, the flow down-stream of the CFCTT and the CFATT was studied for the set of inflow conditions presented in Fig. 6.19. The vertical gradient of the inflow acting on the CF TT is illustrated by the difference of the inflow velocity across the rotor in Fig. 6.20 for the inflow conditions listed in Table 6.3.

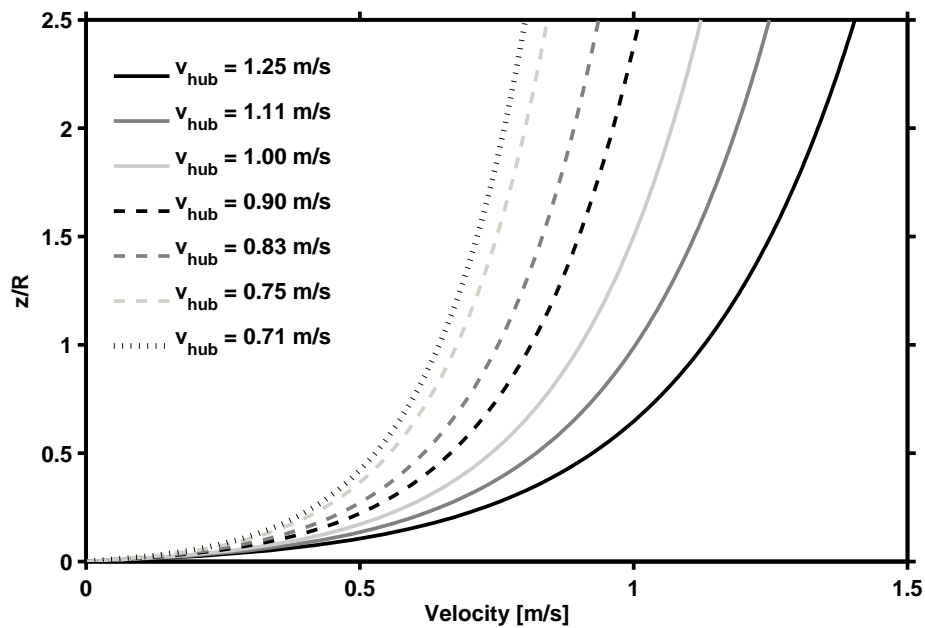


Figure 6.19: Set of velocity profiles used to represent a part of the tidal cycle.

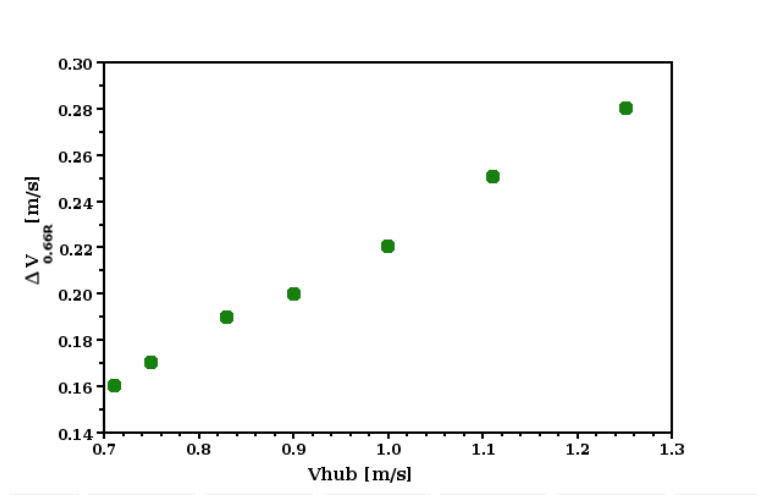


Figure 6.20: The difference of the inflow velocity across the CFCTT.

$v_{tip}/v_{hub}$	7.00	6.67	6.00	5.56	5.00	4.50	4.00
$v_{hub}$ [m/s]	0.71	0.75	0.83	0.90	1.00	1.11	1.25
$\Delta v_{0.66R}$ [m/s]	0.16	0.17	0.19	0.20	0.22	0.25	0.28

Table 6.3: The inflow conditions in relation to the difference in the inflow velocity across the CFCTT.

The structure of the rotor vorticity field for the investigated set of velocity profiles is shown in Fig. 6.21 and Fig. 6.22. The rotor vorticity field is illustrated by the iso-surface of 10% of its maximal magnitude for  $v_{tip}/v_{hub} = 4$ . Similarly to the rotor vorticity of the VATT, the regions of high vorticity, observed in Fig. 6.21 and Fig. 6.22 for lower ratios  $v_{tip}/v_{hub}$ , are separated by spaces where the rotor vorticity is smaller than 10% of  $\max|\omega_w|$ . The separation occurs for both the CFCTT and the CFATT.

The differences in the inner structure of the rotor vorticity field between the CFCTT and the CFATT configurations are presented in Fig. 6.23-Fig. 6.29, where the horizontal black line denotes the position of the seabed. The range of the values in Fig. 6.23-Fig. 6.29 is the same as in Fig. 6.9.

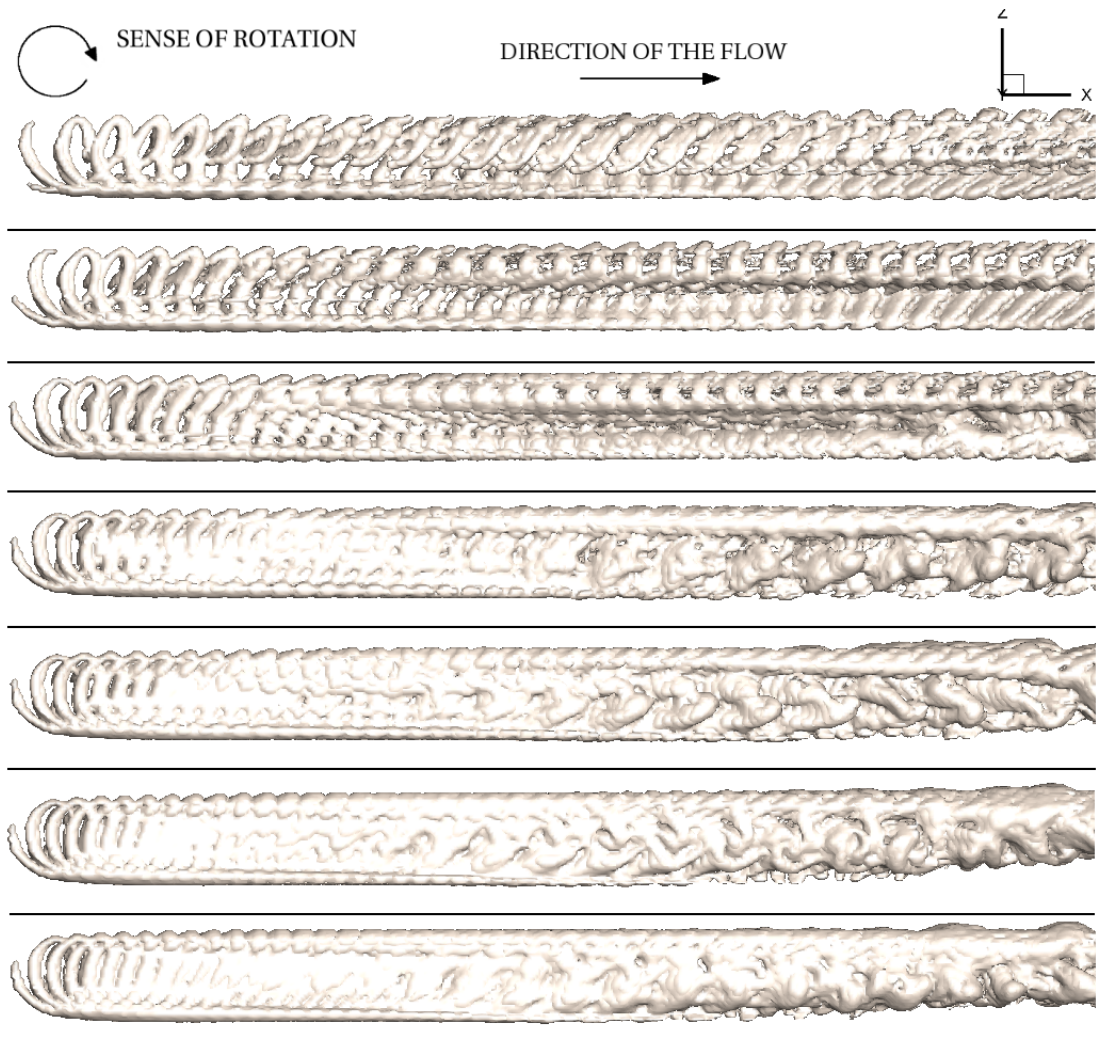


Figure 6.21: The rotor vorticity field down-stream of the CFCTT of the fully developed wake, from top to bottom:  $v_{tip}/v_{hub} = 4, 4.5, 5, 5.56, 6, 6.67, 7$ .

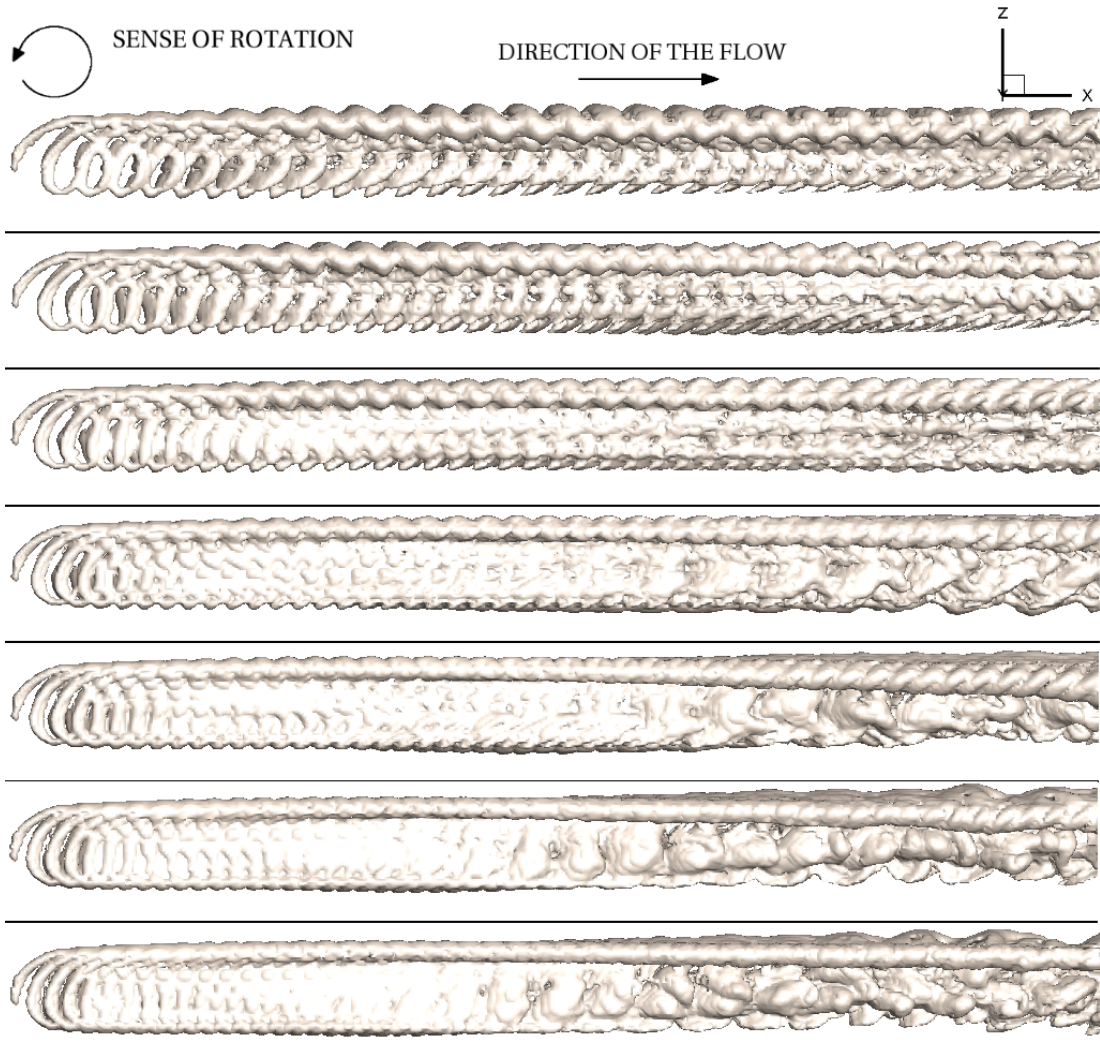


Figure 6.22: The rotor vorticity field down-stream of the CFATT of the fully developed wake, from top to bottom:  $v_{tip}/v_{hub} = 4, 4.5, 5, 5.56, 6, 6.67, 7$ .

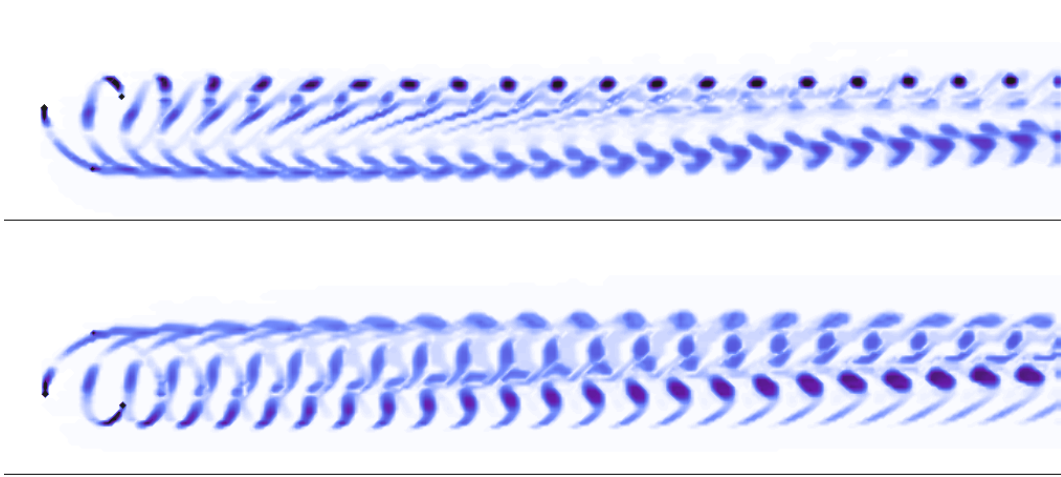


Figure 6.23: Y-slice of the rotor vorticity field of the fully developed wake, top: the CFCTT, bottom: the CFATT,  $v_{tip}/v_{hub} = 4$ .

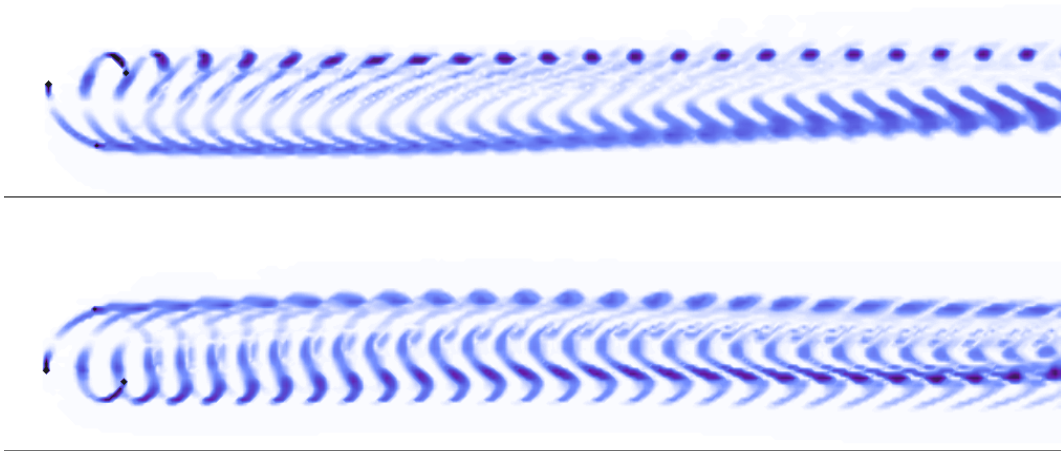


Figure 6.24: Y-slice of the rotor vorticity field of the fully developed wake, top: the CFCTT, bottom: the CFATT,  $v_{tip}/v_{hub} = 4.5$ .

The results indicate that the position of the strongest vortices, which are marked by the darkest colour in Fig. 6.23-Fig. 6.29, depends on the sense of rotation of the device. Down-stream of the CFCTT, the strongest vortices occur at a height of approximately  $z_{hub} + 0.33R$ , while down-stream of the CFATT, the strongest vortices are closer to the seabed, below the height of  $z_{hub}$ .

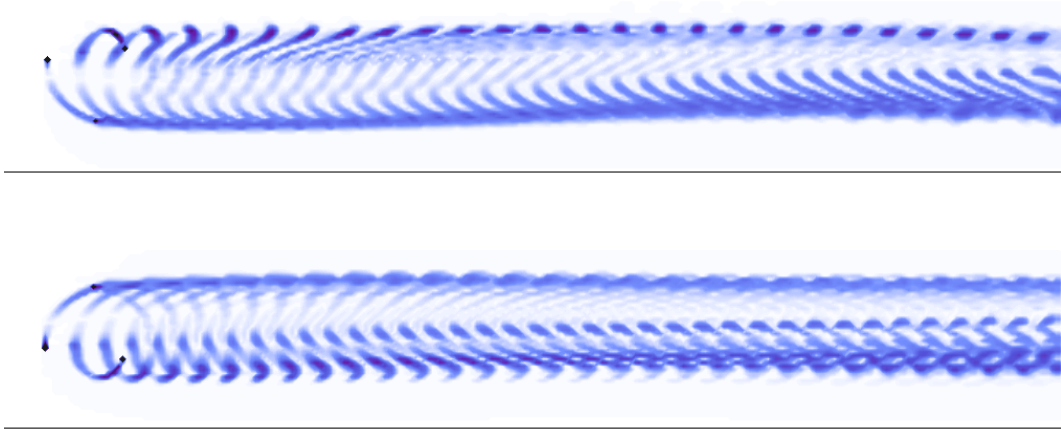


Figure 6.25: Y-slice of the rotor vorticity field of the fully developed wake, top: the CFCTT, bottom: the CFATT,  $v_{tip}/v_{hub} = 5$ .

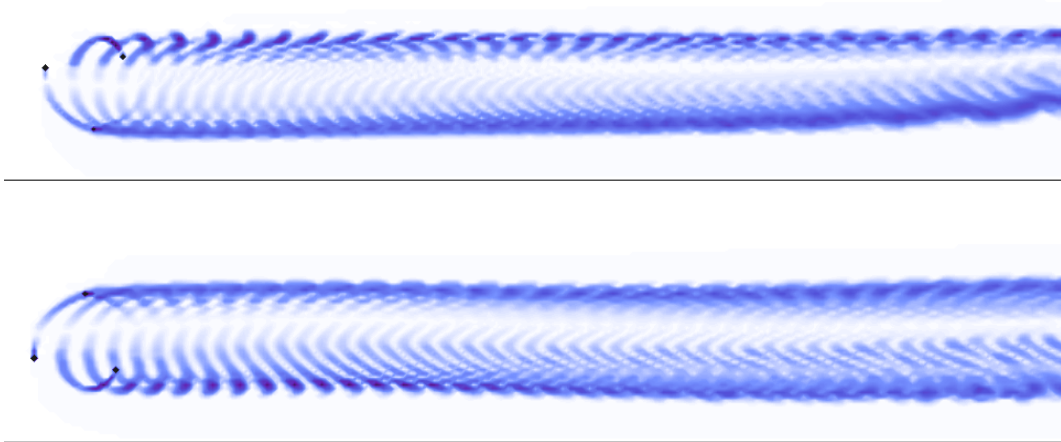


Figure 6.26: Y-slice of the rotor vorticity field of the fully developed wake, top: the CFCTT, bottom: the CFATT,  $v_{tip}/v_{hub} = 5.56$ .

As presented in chapter 5, the structure of the rotor vorticity down-stream of the HATT, namely the elevation of the rotor vorticity field by the boundary flow, resulted in a reduction of the influence of the HATT on the seabed. Motivated by the results for the HATT, the elevation of the rotor vorticity from the seabed for the two operating conditions of the CFATT is compared in Fig. 6.23-Fig. 6.29. The

influence of the flow down-stream of the devices on the seabed is qualitatively different for the CFCTT than for the CFATT. The differences between the two operating conditions of the CFCTT are illustrated by the planar section through the rotor vorticity field, perpendicular to the direction of the inflow, denoted as ‘x-slice’. The x-slices of the rotor vorticity for the two operating conditions are compared in Fig. 6.30 and Fig. 6.31.

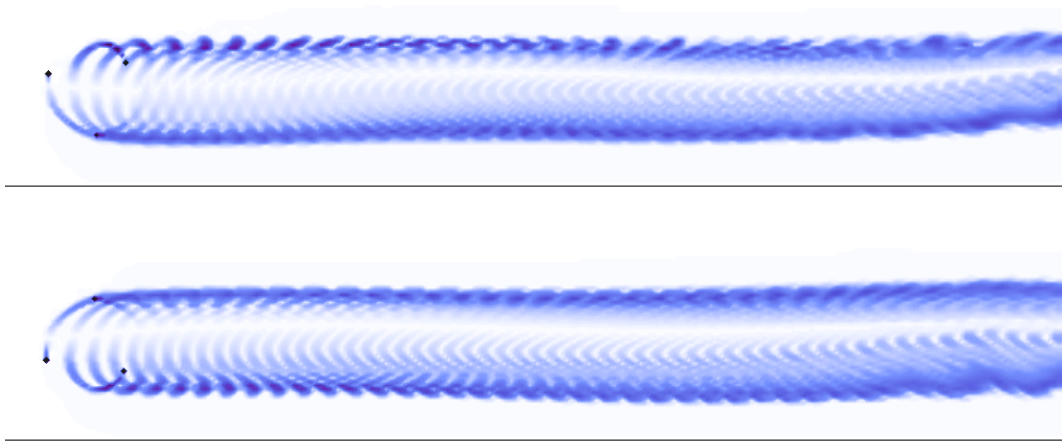


Figure 6.27: Y-slice of the rotor vorticity field of the fully developed wake, top: the CFCTT, bottom: the CFATT,  $v_{tip}/v_{hub} = 6$ .

The rotor vorticity approaches the seabed again after the initial elevation by the boundary flow for the CFCTT and the CFATT. The locations where the rotor vorticity is transported initially away from the seabed and where the flow further down-stream disturbs the seabed again depends on the inflow velocity.

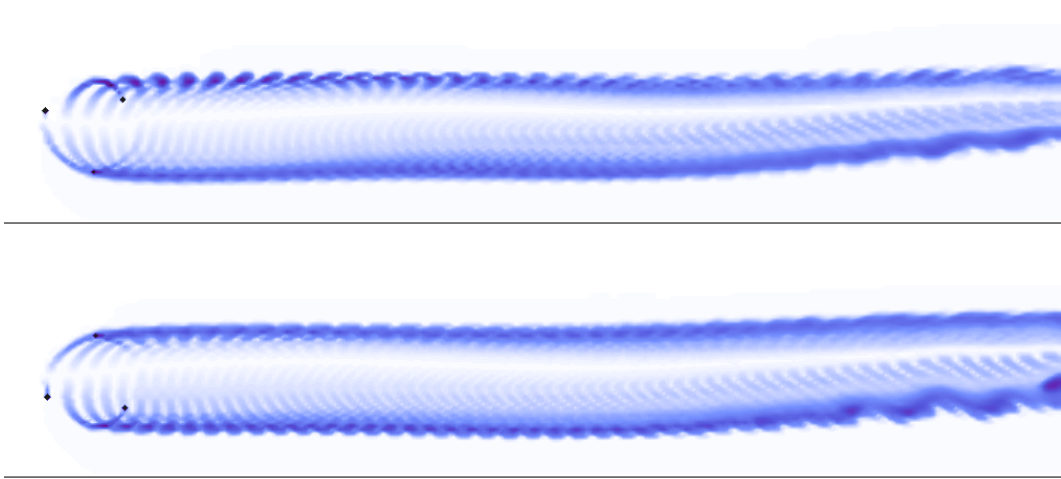


Figure 6.28: Y-slice of the rotor vorticity field of the fully developed wake, top: the CFCTT, bottom: the CFATT,  $v_{tip}/v_{hub} = 6.67$ .

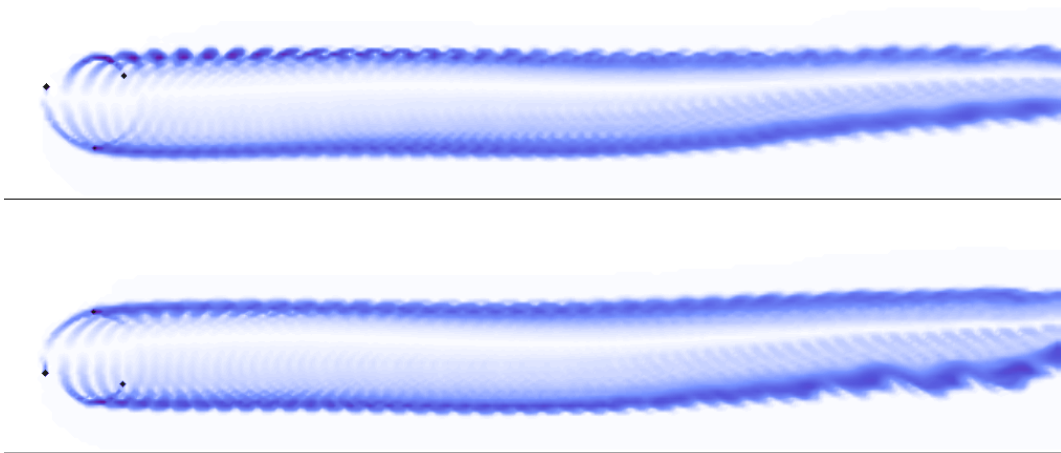


Figure 6.29: Y-slice of the rotor vorticity field of the fully developed wake, top: the CFCTT, bottom: the CFATT,  $v_{tip}/v_{hub} = 7$ .

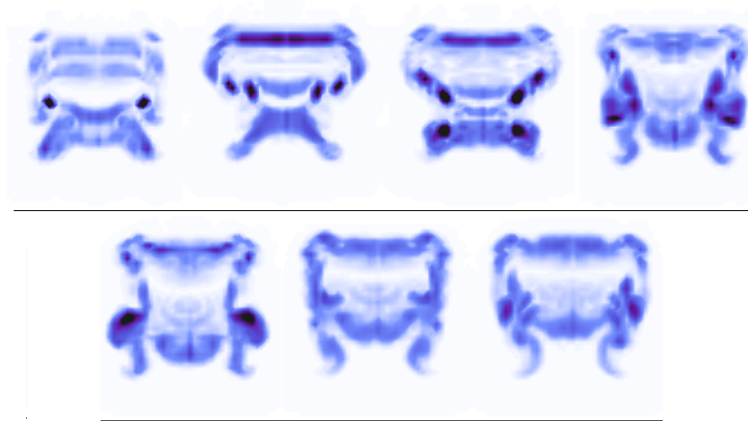


Figure 6.30: X-slice of the rotor vorticity field of the fully developed wake downstream of the CFCTT,  $x = 8.72R$ , from top-left to bottom-right:  $v_{tip}/v_{hub} = 4, 4.5, 5, 5.56, 6, 6.67, 7$ .

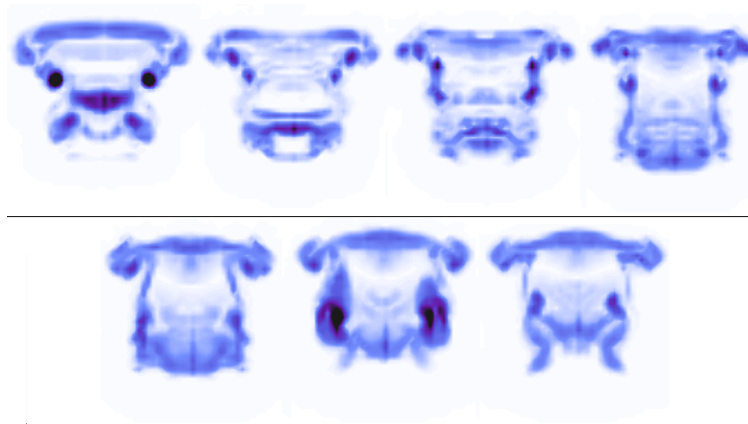


Figure 6.31: X-slice of the rotor vorticity field of the fully developed wake downstream of the CFATT,  $x = 8.72R$ , from top-left to bottom-right:  $v_{tip}/v_{hub} = 4, 4.5, 5, 5.56, 6, 6.67, 7$ .

All of the investigated inflow conditions result in the appearance of two lobes in Fig. 6.30, the shape of which varies with the inflow, time and distance from the rotor. The distance  $x = 8.72R$  is chosen to serve the analysis of the excess bed shear stress. The inner structure of the rotor vorticity field for the CFATT contains the lobes only for  $v_{tip}/v_{hub} = 7$  and those are observed further from the seabed (denoted by the black line in Fig. 6.31) than the lobes in the rotor vorticity down-stream of the CFCTT.

The tide induced wake vorticity,  $\omega^*$ , is illustrated by its ‘y-slice’ (the planar section perpendicular to the seabed and the rotor plane) in Fig. 6.32 for the CFCTT and in Fig. 6.33 for the CFATT. The maximum of  $|\omega^*|$ , observed for  $v_{tip}/v_{hub} = 4$ , is smaller than the maximum  $|\omega^*|$  for the VATT for both configurations of the CFCTT. The CFCTT induces higher values of  $|\omega^*|$  than the CFATT.

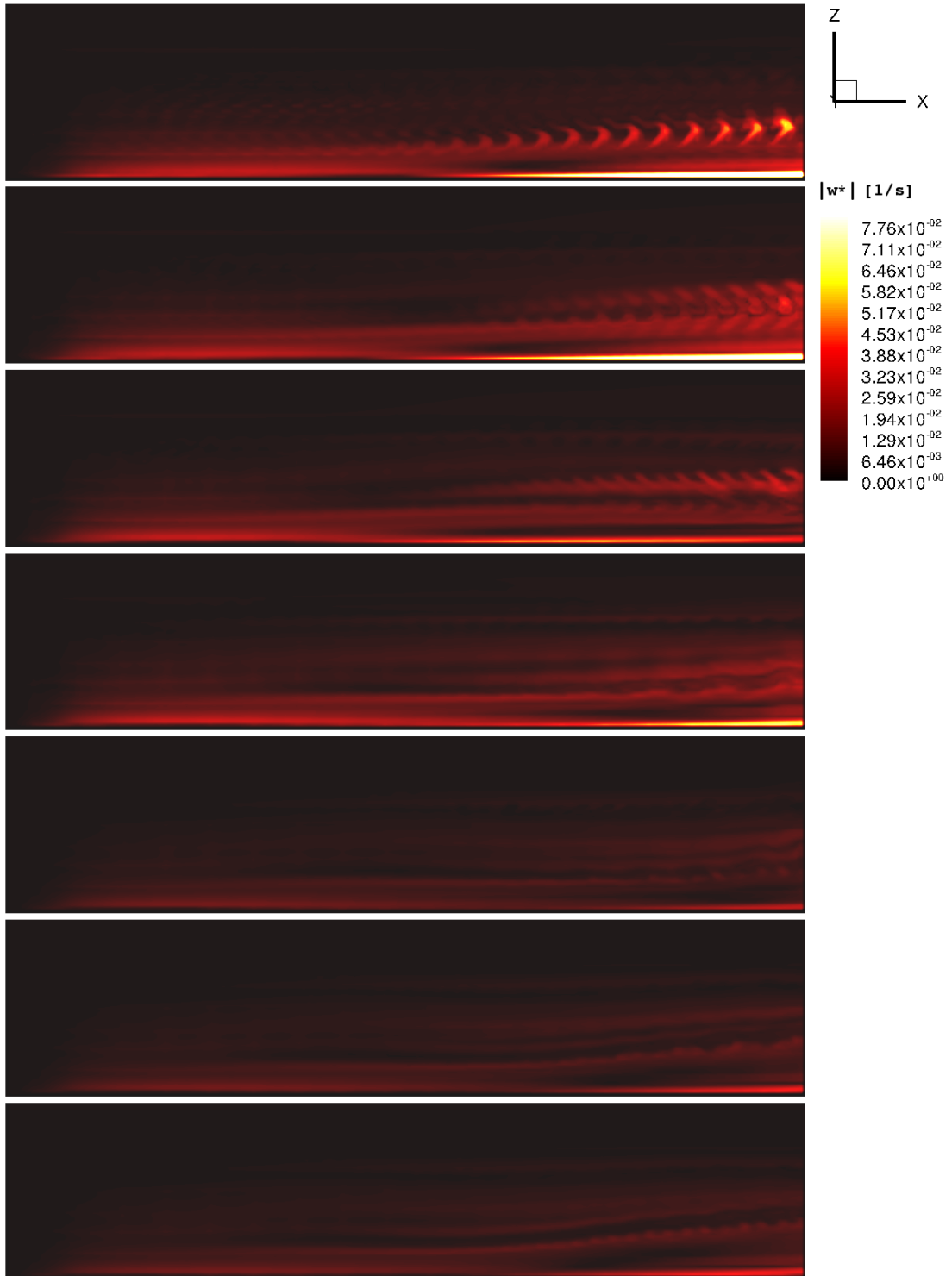


Figure 6.32: Y-slice of the tide induced wake vorticity field of the fully developed wake downstream of the CFCTT, from top to bottom:  $v_{tip}/v_{hub} = 4, 4.5, 5, 5.56, 6, 6.67, 7$ .

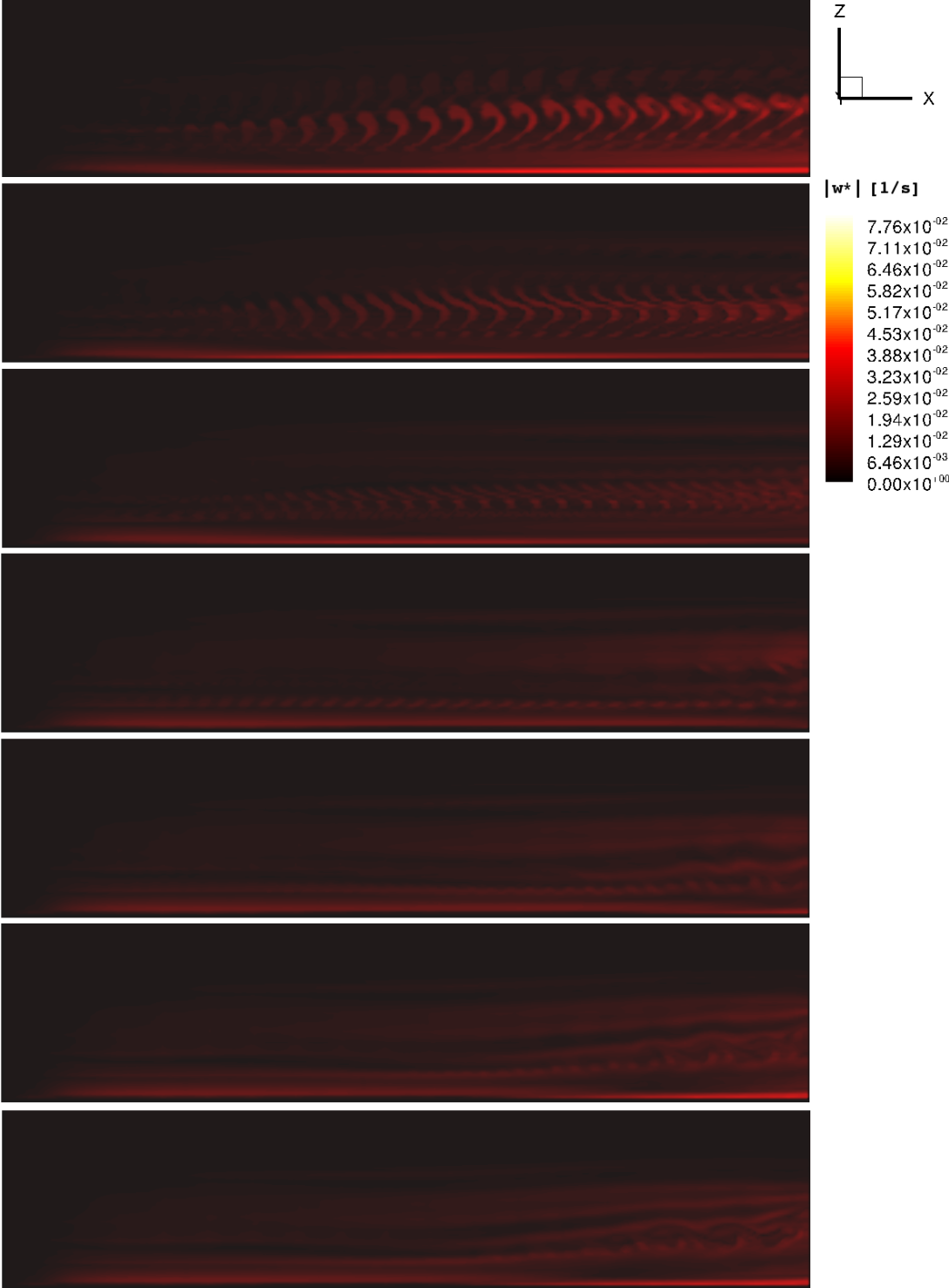


Figure 6.33: Y-slice of the tide induced wake vorticity field of the fully developed wake down-stream of the CFATT, from top to bottom:  $v_{tip}/v_{hub} = 4, 4.5, 5, 5.56, 6, 6.67, 7$ .

The tide induced wake vorticity represents less than 9% of the vorticity induced by the presence of the CFTT on the seabed,  $\omega_I$ . The ratio  $\max |\omega^*| / \max |\omega_w|$  increases with increasing inflow velocity. The composition of the induced vorticity field is illustrated in Fig. 6.34 for both operating conditions of the CFTT and the VATT.

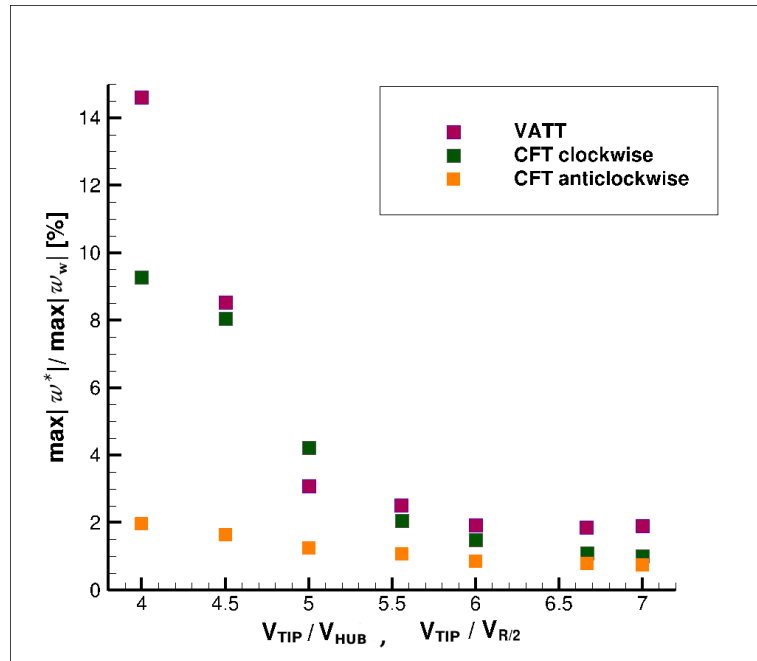


Figure 6.34: Composition of the induced vorticity field of the fully developed wake,  $\max |\omega^*|$  vs.  $\max |\omega_w|$ .

The presence of the CFTT on the seabed generates high near-bed velocity (via the induced vorticity) and, consequently, high excess bed shear stress (EXSS). In contrast with the HATT and the VATT, the region of positive EXSS within  $2R$  down-stream of the CFTT is not the most affected area of the seabed, since the CFTT induces the highest EXSS further from the rotor. Moreover, the structure of the EXSS for the CFTT is more complex than the EXSS observed for the HATT and the VATT, for which the seabed is most influenced by the ordered part of the induced vorticity field immediately down-stream of the devices. The EXSS

down-stream of the CFCTT for the investigated inflow conditions is presented in Fig. 6.35. The spatial distribution of the EXSS for the CFATT is displayed in Fig. 6.36.

The EXSS generated by the presence of the CFCTT in the boundary flow is influenced by the structure of the induced vorticity, composed of the rotor vorticity and the tide induced wake vorticity. Initially, the rotor vorticity,  $\omega_w$ , did not contain distinct lobe-shaped structures which are observable in Fig. 6.30. Once the tide induced wake vorticity,  $\omega^*$ , has reached its maximal values close to the seabed, the lobes of  $\omega_w$  start to develop. The lobes of  $\omega_w$  then generate the high EXSS in a number of spikes further down-stream of the CFCTT, which are most apparent for  $v_{tip}/v_{hub} \leq 5.56$  in Fig. 6.23-Fig. 6.25.

Further down-stream of the CFATT the rotor vorticity is encountered closer to the seabed than is the reach of the blades, which is noticeable especially for  $v_{tip}/v_{hub} = 5.56$  and 6 in Fig. 6.26 and Fig. 6.27. The location of the area of high EXSS corresponds to the region where the induced vorticity re-approaches the seabed, which is particularly apparent for  $v_{tip}/v_{hub} = 5.56$  in Fig. 6.26, and the maximum of the EXSS occurs in the area where the induced vorticity is closest to the seabed.

The EXSS averaged over the studied area of the seabed (AEXSS) is presented in Fig. 6.37 for the CFCTT and in Fig. 6.38 for the CFATT.

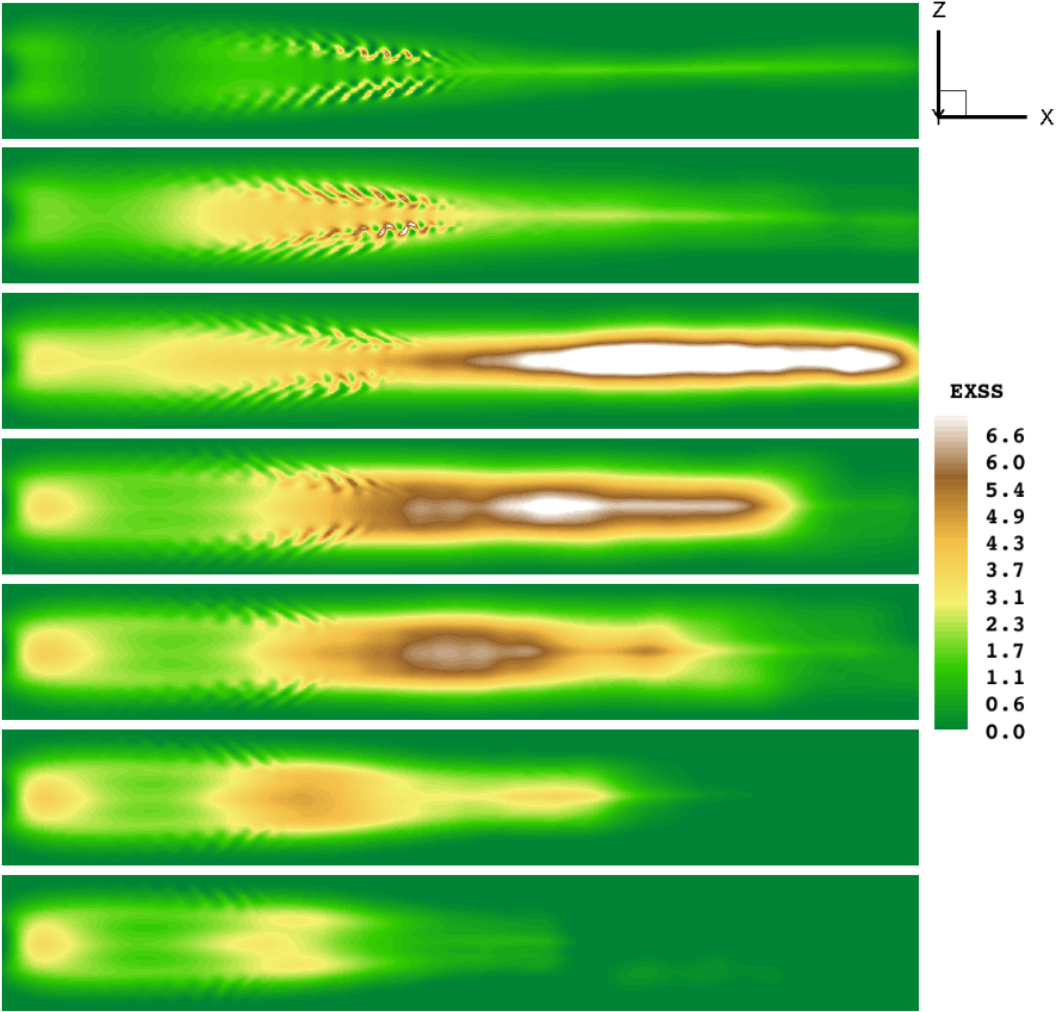


Figure 6.35: The excess bed shear stress induced by the CFCTT, from top to bottom:  $v_{tip}/v_{hub} = 4, 4.5, 5, 5.56, 6, 6.67, 7$ .

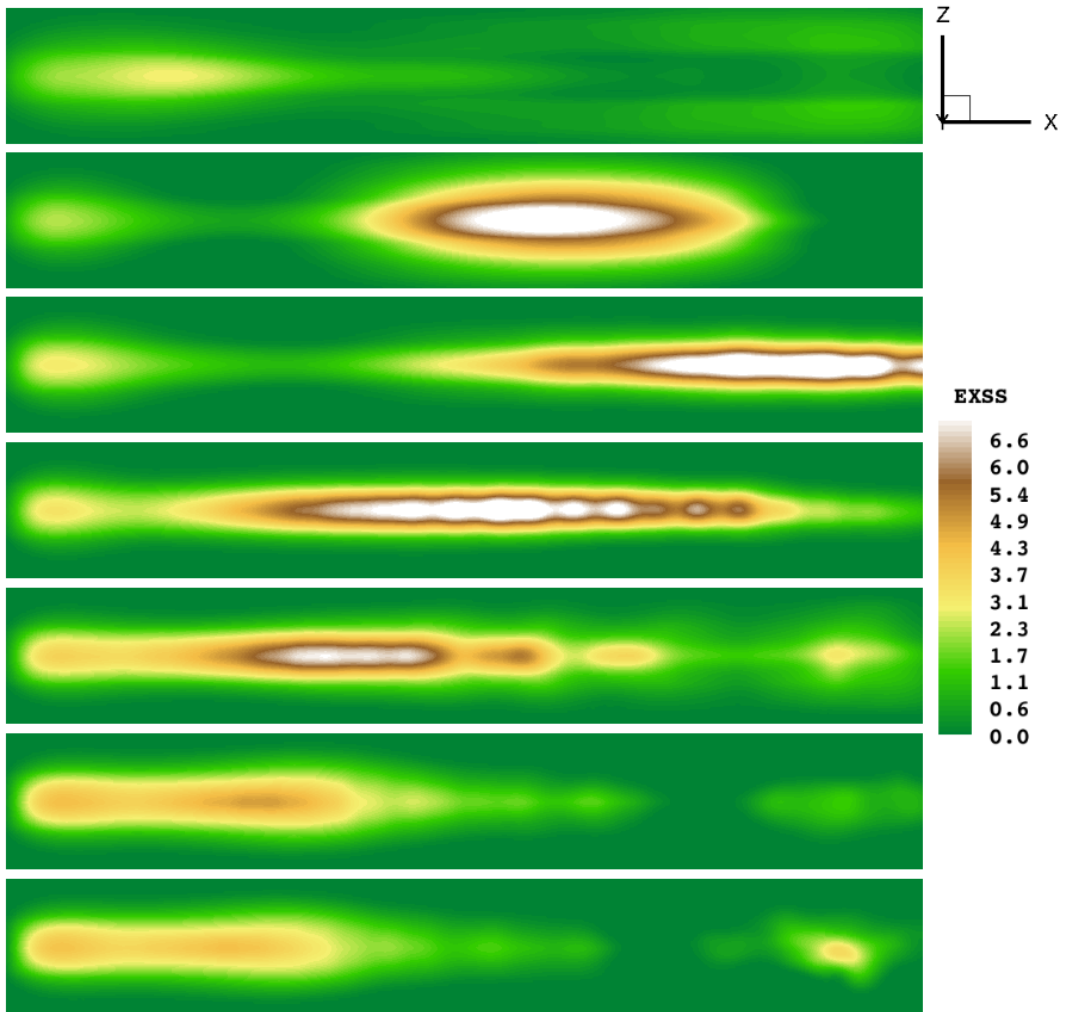


Figure 6.36: The excess bed shear stress induced by the CFATT, from top to bottom:  $v_{tip}/v_{hub} = 4, 4.5, 5, 5.56, 6, 6.67, 7$ .

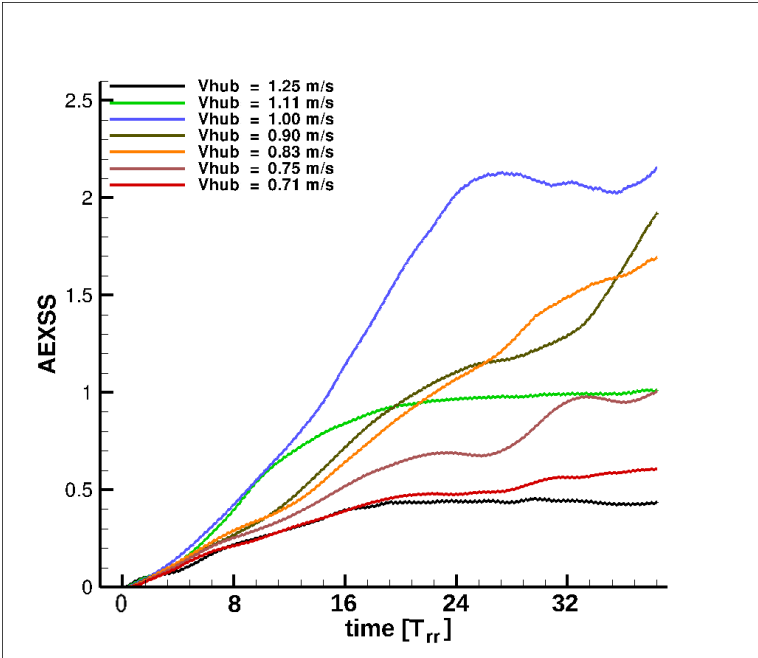


Figure 6.37: The AEXSS evolution for the CFCTT.

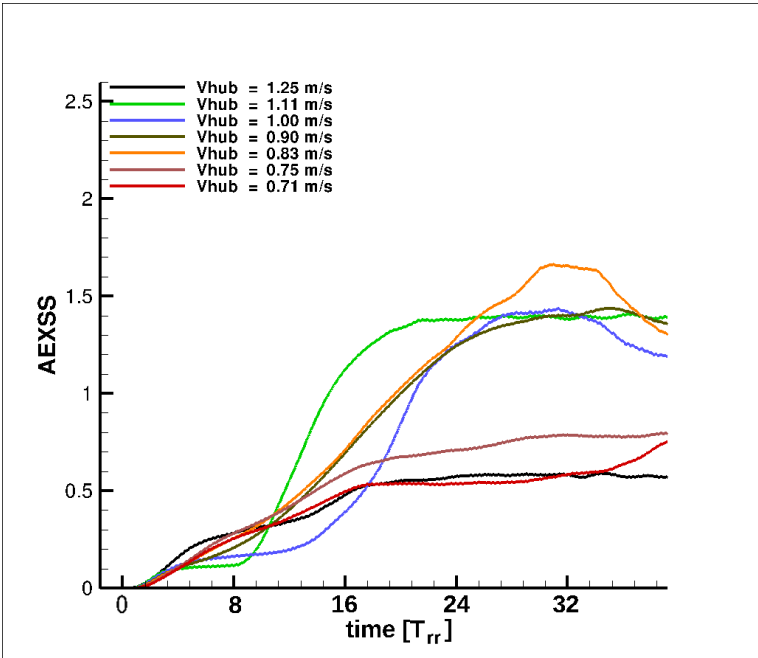


Figure 6.38: The AEXSS evolution for the CFATT.

The AEXSS down-stream of the CFCTT depends on the operating condition of the device. The AEXSS for the CFCTT indicates that the wake did not reach a stabilized state, which could characterise the behaviour of the flow, within the studied time interval. Indeed, not only is it the case that the AEXSS for the CFCTT did not stabilise, the AEXSS continues increasing with time.

The AEXSS for the CFATT, in contrast with the CFCTT, indicates that the impact of the device on the seabed can be characterised by the mean of the AEXSS over the time interval in which the AEXSS stabilised,  $[t_0, t_{END}]$ .

Although the AEXSS for the CFCTT continues increasing with time, the temporal mean of the AEXSS (MAEXSS) is used to compare the results for the CFCTT and the CFATT. The MAEXSS for the CFCTT, the CFATT and the VATT for the set of inflow conditions, listed in Table 6.3, is presented in Fig. 6.39. The increasing nature of the AEXSS for the CFCTT is demonstrated by the large error bars, which are calculated from the maximal change of the AEXSS over the interval  $[t_0, t_{END}]$ .

In contrast to the results obtained for the HATT, the MAEXSS for the CFCTT, the CFATT and the VATT do not exhibit a dependence on the inflow velocity which can be well approximated by a simple algebraic model. The MAEXSS for the CFCTT, the CFATT and the VATT did not exceed 2.5 over the studied time interval for any of the investigated inflow conditions. Furthermore, the influence of the VATT and the CFATT on the seabed stabilises over time. It needs to be emphasized, that this is not the case for the CFCTT.

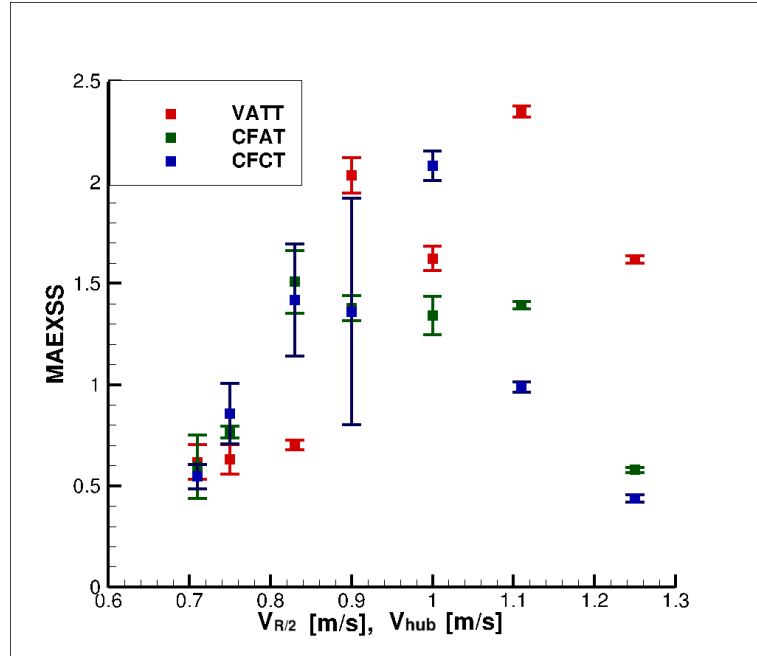


Figure 6.39: The temporal mean of the AEXSS for the VATT, the CFCTT and the CFATT.

The spatial extent of the impact needs to be taken into account in planning of array-installations of CFTTs. Unlike the HATT, which, according to the results presented in section 6.1, would cause sediment uplift in the confined area in the immediate vicinity of the device, the results presented here suggest that the CFTT would influence the motion of sediment further than  $5R$  down-stream of the rotor in both operating conditions. The location of the most affected area of the seabed depends on the inflow velocity. Since the set of the inflow velocities represent phases of the tidal cycle, as described in section 5.3, the flow down-stream of the CFTT may inflict shear stresses at a distance from the device which would vary during the tidal cycle.

## 6.3 Summary

The flow through the rotor of the vertical axis tidal turbine (VATT) and the cross-flow tidal turbine (CFTT) was predicted by the VTM equipped with the

model for the inflow in the form of a velocity profile. A sequence of velocity profiles was used as the inflow conditions for the VTM simulations, with the aim of uncovering the effect on the seabed during the tidal cycle caused by the VATT and CFATT in operation. The impact of these devices on the seabed is expressed by the excess bed shear stress (EXSS), which indicates the rate of uplift of sediment into suspension. The EXSS differs with the geometry of the TECD.

Both, the VATT and the CFATT cause an inclined vorticity structure to form down-stream of the rotor, the inclination of which is due to the vertical gradient of the inflow velocity. The gradient of the inflow promotes the elevation of the induced vorticity, effectively reducing the area of the seabed affected by the VATT. The tide induced wake vorticity influences the EXSS down-stream of the VATT, which represents up to 13% of the vorticity induced by the presence of the device on the seabed. The highest EXSS occurs immediately down-stream of the VATT, similar to the results for the horizontal axis configuration presented in chapter 5. The VATT configuration, however, invoked positive EXSS beyond  $2R$  from the rotor. The results indicate that the extent of the area affected by the VATT depends on the inflow velocity, with a longer extent for faster inflows. The mean averaged EXSS (MAEXSS) increases with the inflow velocity when  $v_{R/2} \leq 1$  for this device. Furthermore, faster inflow conditions result in lower values of the MAEXSS than for the inflow of  $v_{R/2} = 1$ .

The CFATT is considered in two operating conditions, clock-wise and anti-clock-wise rotation, defined in Fig. 6.14. Both, the clock-wise CFATT, referred to as the CFCTT, and the anti-clock-wise CFATT, referred to as the CFATTT, influence the seabed through the induced vorticity. The rotor vorticity together with the tide induced wake vorticity, which represents up to 9% of the induced vorticity for the CFCTT, generate high EXSS down-stream of the device. The CFATTT impacts the seabed over a narrower, elliptical region of high EXSS. The maximum of the EXSS averaged over the studied area of the seabed is smaller for the CFATTT than for the CFCTT. The far-reaching impact of the CFATT on the seabed contrasts sharply with the findings for the HATT and should be considered in any array deployment projects involving CFATTTs.

The configuration of TECDs affects significantly the nature of the impact of the flow down-stream of the devices on the seabed. The thorough study of the HATT, presented in chapter 5, indicates that the impact on the seabed is confined to an area close to the rotor. The results for the VATT suggest that the greatest influence is in the region surrounding of the device, however, the seabed further down-stream could also experience shear stresses induced by the presence of the VATT. Finally, the results for the CFCTT indicate that this device would, in relative terms, have the most variable impact of all the studied configurations of TECDs, with the greatest effect on the seabed in the area further from the rotor dependent on the inflow velocity.

The presented results uncover the variability of the impact of a TECD on the seabed with the configuration of the device.

# Chapter 7

## Conclusions and Future Work

The main purpose of the research presented in this dissertation was to explore the connection between a TECD and the Environment and the nature of the interactions within the TE system. The focus was on the physics of the small-scale three-dimensional phenomena in the flow through the rotor of a TECD with the aim of contributing to the understanding of the impact of TECDs on the seabed. The results show that the three-dimensional effects in the flow downstream of the rotor could indeed influence the marine environment over scales of a few centimetres.

Three types of TECDs were modelled by high-resolution three-dimensional computer simulations using the VTM, a state-of-the-art computer model. The visualisation of the flow through the rotor obtained from the VTM made the analysis of the three-dimensional phenomena occurring in the rotor wake possible. The first TECD is defined as a three-bladed, horizontal-axis device, and calibrated to represent a commonly used commercial design. The horizontal axis configuration of the TECD is referred to as the HATT in this chapter. The second TECD is also a three bladed device, defined as a vertical axis tidal turbine (VATT). The third TECD is technically the rotor of the VATT placed horizontally into the flow, referred to as a cross-flow tidal turbine (CFTT). The CFTT is considered in two operating regimes: rotating clock-wise (CFCTT) and anti-clock-wise (CFATT) around the axis, which is parallel to the seabed and perpendicular to the down-stream direction. The VATT and the CFTT represent alternatives to the horizontal axis configuration, which are considered for

---

commercial deployment.

The flow through the rotor of the HATT was initially investigated under the assumption that the inflow velocity is uniform, i.e. that the velocity of the tidal flow is a constant vector. The outcomes of this investigation, discussed in chapter 4, motivated the implementation of a more realistic model of the tidal flow into the VTM, which was then used to study the influence of the TECDs on the seabed. The more realistic inflow model comprises the inflow velocity in the form of a velocity profile and, since the assumption of the non-uniform inflow velocity implies the presence of a vorticity field in the absence of the rotor, the model includes the vorticity in the free-stream. The free-stream vorticity was simulated as time-invariant since the changes of tidal velocity over the time scales relevant to the wake development are negligible, according to available experimental data.

As opposed to the original version of the VTM, where the total vorticity field was spatially confined, the modified version of the VTM which includes the non-uniform inflow model needs to account for a boundless vorticity field. The modified VTM simulates the total vorticity in the flow, which comprises the free-stream vorticity and the vorticity induced by the presence of the rotor, the latter consisting of two components, the rotor vorticity and the tide induced wake vorticity. The first component originates at the blades of the rotor similarly to the vorticity field induced by the rotor under the uniform inflow condition. The second component represents the interaction between the tidal flow and the rotor, an interpretation which is based on the fact that the tide induced wake vorticity is zero in the uniform inflow case.

The modified VTM which incorporates the simulation of the two components of the induced vorticity uses a time-invariant grid geometry. The time-invariant grid replaced the adaptive grid, which was devised under the assumption that the inflow is uniform and that the total vorticity field is spatially confined. The new grid management reduced the length of the simulations below the time typically required by the original VTM to investigate the uniform inflow cases. The flow down-stream of each of the TECDs was simulated by the modified version of the VTM, in order to analyse the flow through the devices for a range of the inflow conditions and rotor parameters.

The relative difference between the shear stress, imposed by the flow on the seabed down-stream of the TECDs, and the critical bed shear stress, is called the excess bed shear stress (EXSS). The EXSS is used here as a measure of the changes in the sediment motion, caused by the presence of the TECDs, on the seabed. Furthermore, the spatial distribution of the instantaneous EXSS provides qualitative information about the effects of the TECDs on the seabed. The EXSS is needed to evaluate both the amount of sediment eroded from the seabed due to the presence of the TECDs and the concentration of the sediment suspended in the flow down-stream of the rotor. To express the overall impact of the TECDs on the seabed, the temporal mean of the excess bed shear stress averaged over the studied area of the seabed (MAEXSS), is employed.

The outcomes of the present research are presented in the following section.

## 7.1 Research Outcomes

The research questions listed in section 1.2, which defined the objectives of this dissertation, are addressed here for all three investigated configurations of the TECD.

### 7.1.1 What does the wake of a TECD look like?

The results of the VTM's simulations indicate that the flow down-stream of a TECD is governed by the vorticity field induced by the device and that the structure of the induced vorticity field depends on the inflow model. Two inflow models were used to simulate the flow down-stream of the HATT.

When the inflow velocity is assumed to be uniform, the vorticity originates at the blades of the HATT, hence it is called the rotor vorticity. This vorticity field contains filaments that form a helical structure immediately down-stream of the device, the strength of which depends on TSR. The results suggest that as the rotor vorticity is transported down-stream of the HATT by the flow the helical structure initially becomes deformed, and subsequently disintegrates fur-

ther down-stream at a distance which depends on TSR, leaving behind a cluster of fragments of the vorticity filaments.

When the inflow velocity is approximated by a velocity profile, the total vorticity present in the flow down-stream of a rotor consists of the free-stream vorticity and the induced vorticity, which is modelled as the superposition of the rotor vorticity and the tide induced wake vorticity. The rotor vorticity has a greater influence on the flow field down-stream of the HATT than the tide induced wake vorticity, for all investigated rotor configurations. The relationship of the two components of the induced vorticity fields is possible to quantify by the ratio of the maximal magnitude of the former to the maximal magnitude of the latter, which is more than fifty for the HATT, more than seven for the VATT and more than ten for the CFTT.

The structure of the rotor vorticity down-stream of the HATT exhibits similar features for both inflow models. In both cases, this vorticity field forms an ordered helical structure, composed of three tip vortex filaments, which disintegrates further down-stream of the HATT. The findings indicate a difference between the two cases, nevertheless. The vertical gradient of the inflow velocity is likely to cause the rotor vorticity to incline in comparison with the rotor vorticity of the uniform inflow case.

All of the investigated configurations of the TECD studied by the VTM result in the induced vorticity to be inclined due to the vertical gradient of the inflow velocity, with an initially ordered induced vorticity structure which disintegrates further down-stream of the rotor. Moreover, the results suggest that the induced vorticity further down-stream of the HATT as well as the VATT is transported away from the seabed by the boundary flow. Consequently, the HATT and the VATT configurations could have a limited influence on the seabed. The induced vorticity down-stream of the CFTT is also predicted to be transported away from the seabed in vicinity of the rotor, however, in contrast to the other two rotor configurations, the induced vorticity is likely to approach the seabed again further down-stream of the CFTT.

Since the inflow model in the form of a velocity profile is considered to be more realistic, only the data produced by the modified version of the VTM,

incorporating this feature, are used to assess the impact of the TECDs on the seabed.

### **7.1.2 How does the wake affect the flow velocity close to the seabed?**

The velocity of the flow at a height of 10 cm above the seabed (called the near-bed velocity) is likely to be influenced by the structure of the induced vorticity field. The results indicate that the near-bed velocity exceeds the free-stream velocity in the regions which are most influenced by the rotor vorticity. For the HATT configuration, the helical vortical structure immediately down-stream of the device is predicted to cause the high near-bed velocity to be confined within  $4R$  down-stream of the device. As a result, the shear stress on the seabed could exceed the threshold for sediment uplift in the vicinity of the HATT. The findings for the VATT suggests that the highest near-bed velocity occurs also in the vicinity of the rotor. In contrast to the findings for the HATT, the area further from the VATT is likely to be affected by the device as well. The modelling of the CFATT configuration yields data qualitatively different from the other two configurations. The near-bed velocity down-stream of the CFATT is predicted to reach a maximum further from the rotor for both investigated operating conditions (CFCTT and CFATT). The predicted location of the high near-bed velocity is correlated to the region where the rotor vorticity approaches the seabed again.

### **7.1.3 What effects do the devices have on the sediment?**

The EXSS down-stream of the TECDs is needed to determine the amount of sediment eroded from the seabed. The dependence of the EXSS on the speed of the tidal current was studied for all three configurations of the TECD.

The study concludes that both the HATT and the VATT are expected to generate the highest EXSS immediately down-stream of the rotor. The high EXSS down-stream of the HATT is likely to occur closer than  $4R$  to the device for all investigated inflow conditions. Furthermore, a positive EXSS could be

found beyond  $4R$  down-stream of the VATT. This indicates that the extent of the area affected by the VATT is larger for faster currents. The MAEXSS down-stream of the HATT consistently increases with increasing inflow velocity, while the MAEXSS obtained for the VATT only increases with the inflow velocity when  $v_{R/2} \leq 1$  m/s. Indeed, the results suggest that the currents faster than  $v_{R/2} = 0.9$  m/s can cause the MAEXSS to be lower than the value for  $v_{R/2} = 0.9$  m/s. The CFTT in both operating conditions, CFCTT and CFATT, is predicted to generate high EXSS further down-stream of the rotor (beyond  $4R$ ). The most apparent difference between the two operating conditions of the CFTT is the predicted geometry of the affected region of the seabed. The CFATT is likely to affect the seabed over a narrower region of high EXSS than the CFCTT. Down-stream of the CFATT, this region could be almost elliptical for  $v_{R/2} = 1.11$  m/s. The MAEXSS down-stream of the CFTT is, according to the VTM's predictions, comparable for both of the two operating conditions, however the MAEXSS for the CFCTT does not represent a stabilised state. More generally, the predicted far-reaching impact of the CFTT on the seabed contrasts sharply with the findings for the HATT.

Based on these results, the configuration of TECDs could significantly affect the nature of their impact on the marine environment. The expected impact of the HATT on the seabed is confined to an area close to the rotor. In the case of the VATT, the greatest influence is likely to be in the region surrounding the device, however the seabed further down-stream could also experience shear stresses generated by the VATT. The CFTT would have the most variable impact of all the configurations of TECDs, with the greatest effect on the seabed further from the rotor, at a distance which depends on the inflow velocity.

### **7.1.4 Can the change of these effects over time be approximated by an algebraic expression?**

The variation of the MAEXSS over the period of the tidal cycle can be derived from the predictions of the impact of the TECDs on the seabed for a number of

inflow conditions, since those inflow conditions can be interpreted as subsequent stages of the tidal cycle.

As mentioned earlier, the results suggest that the MAEXSS down-stream of the HATT increases with increasing inflow velocity. In the context of the tidal cycle this would signify that the erosion of the seabed down-stream of the HATT increases during incoming tide. The relationship between the predicted MAEXSS and the inflow velocity at the rotor hub and, consequently, the phase of the tidal cycle, can be approximated by the algebraic expression Eq. 5.10 for the HATT configuration.

### **7.1.5 Does the expression apply for all configurations of a TECD?**

The findings presented in this dissertation indicate that the effect on the seabed varies greatly with the configuration of the TECD. The VATT and CFTT configurations are likely to have qualitatively different impact on the seabed than the HATT. While the MAEXSS can be approximated by a monotonic function of the inflow velocity for the HATT configuration, this does not apply for the other two configurations of the TECD, according to VTM's predictions. Hence, the simple algebraic expression Eq. 5.10 is applicable only for the HATT configuration.

### **7.1.6 Which are the key factors influencing the effects of the devices on the seabed?**

The effect of the position of the HATT in the boundary layer on the EXSS is of particular interest. The results suggest that the distance between the HATT and the seabed influences the EXSS in two different ways. When the HATT is placed so that  $z_{hub} \geq 1.3R$ , the MAEXSS decreases with increasing distance from the seabed. The relationship between the position of the rotor and the MAEXSS predicted by the modified VTM is well approximated by the expression Eq. 5.14. When the hub of the HATT is closer than  $1.3R$  to the seabed, the large

gradient of the inflow velocity across the rotor area is likely to cause the rotor vorticity field to be transported away from the seabed within a shorter distance than in the cases when  $z_{hub} \geq 1.3R$ . The result for the minimum separation  $z_{hub} = 1.05R$  indicates that the area of the seabed affected by the HATT is located less than  $2R$  down-stream of the rotor. The formation of the ordered helical structure immediately down-stream of the HATT could be disrupted by the close proximity of the seabed. The predicted structure of the rotor vorticity is asymmetric as a result and the asymmetry of the ordered vortical structure causes further reduction of the impact of the HATT on the seabed. Indeed, the area of the high EXSS is likely to be smaller when the HATT is placed  $1.05R$  above the seabed in comparison with the positions of the rotor for which  $z_{hub} \leq 1.3R$ . The counter-intuitive conclusion is that the excess bed shear stress averaged over the investigated area of the seabed would decrease with  $z_{hub}$  for the HATT closer than  $1.3R$  to the seabed.

The instantaneous EXSS is used to evaluate the source of the sediment transported by the flow down-stream of the TECD. The motion of the sediment suspended in the flow, which depends on the sediment diffusivity and sediment size, is analysed for a range of the sediment parameters for the HATT configuration. The results indicate that the MAEXSS is smaller for larger sediment particles since the threshold for sediment uplift is higher for coarser sediment. The positive MAEXSS signifies that the seabed would be eroded as a result of the presence of the HATT for sand particles bigger than 0.25 mm and smaller than 0.75 mm. The highest concentration of the sediment is predicted to appear in the area below the ordered vortical structure observed in the rotor vorticity field for all of the investigated values of the sediment diffusivity. The distribution of the sediment in the flow down-stream of the HATT is considered to be realistic for sediment diffusivity between  $0.002 \text{ m}^2/\text{s}$  and  $0.01 \text{ m}^2/\text{s}$ . The conclusion of the parametric study is that the sediment transport model is sensitive to the choice of sediment diffusivity.

### **7.1.7 What could be the long term consequences of the presence of the TECDs on the seabed?**

Since the erosion down-stream of the HATT is predicted to increase as the tidal velocity increases, the amount of sediment leaving the seabed is likely to peak when the tidal velocity reaches a maximum. Under the assumption that the vector of the tidal velocity is directed normal to the rotor plane, the regions of the seabed likely to be eroded most are located on either side of the HATT, in an area proportional to the rotor radius. The high shear stresses in these two regions could damage the foundation of the device as well as the electrical cables used to connect the HATT to the shore. The results suggest that the erosion down-stream of the VATT is going to be greatest close to the device, however the seabed further from the device could be affected as well. The erosion down-stream of the CFTT is predicted to be greatest further from the device in comparison with the erosion near the other TECD configurations. The variable location of the highest erosion during the tidal cycle renders the CFTT the most unpredictable of the three configurations of the TECD in context of the long-term impact on the seabed.

To summarize, if the TECD is deployed in areas of the seabed covered by sand, the presence of a TECD on the seabed could lead to a displacement of large amounts of sand from the vicinity of the device further down-stream. This displacement could cause changes in the local seabed morphology over a period of years.

### **7.1.8 How could the marine environment change due to the presence of the TECD?**

The aforementioned possibility of a displacement of large amounts of sediment due to the presence of a TECD on the seabed and the potential change of the morphology of the seabed might influence the direction and speed of the tidal current. This hypothetical scenario would be detrimental to the initiative of extracting power from the tides as a part of the solution of the energy crisis,

since a change of the strength or direction of tidal currents could worsen the flow conditions previously suitable for power extraction.

If the devices were mounted onto the seabed with vegetation, the plants could be exposed to the high shear stresses in periodic intervals. The damage to the vegetation on the seabed might affect food-supply of marine fauna. Nevertheless, the degree of uncertainty of the findings due to awaiting experimental validation of the VTM's predictions renders any long-term predictions of the effects on marine flora and fauna speculative. As such the presented results need to be treated with caution and considered to provide essentially qualitative analysis of the near wake hydrodynamics.

## 7.2 Future Work

The modified Vorticity Transport Model could be extended to include surface effects (mentioned in chapter 5) in order to simulate the hydrodynamics of a TECD in shallow waters. The effect of surface waves on the flow down-stream of the TECD could be evaluated by implementing a free-surface model into the VTM. Furthermore, to fully capture all the physics of the wake of a TECD the VTM should be amended to include the diffusion effects discussed in section 2.4.7 and to include a full no-slip condition at the seabed, improving upon the approximation employed in the present study.

The predictions of the VTM presented in this dissertation are based on modelling of small-scale flow phenomena, with the assumption that the resolution of the grid is high enough to capture the most important flow features. These predictions could be improved if the effects of turbulence in the wake of a TECD on the sediment motion were simulated by an appropriate sub-grid turbulence model. An alternative to the VTM, which employs the vorticity confinement method has been considered a valid approach to implicit sub-grid turbulence modelling [89]. A.J. Chorin [39] connects the turbulence theory for incompressible flow and the vorticity field therein, identifying turbulence with a special case of statistical mechanics. Hence, Implicit Large Eddy Simulation (ILES) appears to be the most suitable choice for the VTM. The VTM's routines could be adapted to attain the

ILES quality, since the ILES condition often depends on the type of numerical scheme used to calculate advection. This approach requires thorough analysis of the TVD advection scheme (particularly the chosen wave amplifier functions) used in the VTM.

As mentioned earlier, the effect of the TECD on the seabed vegetation needs to be studied. A model of growth of marine plants could be devised, and calibrated to match the experiments of Nepf et al. [57], to assess the changes due to the presence of a TECD on the seabed. Outcomes of the proposed research would undoubtedly interest marine biologists who investigate the influence of man-made structures on the marine ecosystem.

The effect of the foundations of the TECD on the seabed could alter the flow down-stream of the device and change the location of the high bed shear stresses. When the combined environmental impact of the TECD and its foundations is known, the foundations could be designed to mitigate the effects of the TECD on the seabed. The design of the TECD should be optimized to have a minimal effect on the environment without compromising the power extraction capability. To predict the effect of a farm of TECDs on the marine environment, rotor-rotor interactions would need to be investigated in terms of high induced stresses on the seabed.

The applicability of the sediment model used within the modified VTM can be extended for a mixture of sediment types. A detailed small-scale model of motion of particulate matter should be devised and validated by experiments. Such a model could predict a realistic sediment diffusivity (mentioned in chapter 3) and settling velocity, which could then be used in the modified VTM.

The predictions of the impact of the TECDs on the marine environment presented in this dissertation need to be understood in an appropriate context. The investigation was focused on small-scale fluid phenomena changing over a period of seconds. An interface between the hydrodynamic and sediment modelling over the scales of the TECDs and large-scale oceanographic and sediment transport models is required to determine if the presence of the TECDs on the seabed causes changes of the morphology of the seabed and consequently the tidal currents.

To conclude, the VTM's simulations predict the evolution of the small-scale phenomena in the wake of a TECD which have not been investigated previously.

## 7.2 Future Work

---

The qualitative results presented in this dissertation suggest that more attention should be drawn to the small-scale hydrodynamics of the rotor wake. Notwithstanding the valuable predictions presented herein, for the VTM to be employed for further studies of the physics of the flow around TECs, a number of significant improvements to the model would be required, as previously identified.

# Appendix A

## Simulation Parameters

	Cell size	Time step	Grid size
Notation	$\Delta x/R$	$\Delta t$ [s]	$V_\Omega$
Value	0.040	0.035	$20R \times 4R \times (z_{hub} + 2R)$

Table A: Parameters of the simulations

## Appendix B

### Typical run times

	Run time of $T_{rr}$ <sup>‡</sup>
Uniform inflow simulations by the original VTM	73.6 h
Variable inflow simulations by the modified VTM	28.5 h

Table B: Comparison between the typical run times needed for completion of one rotor revolution

<sup>‡</sup>Run times vary with the settings of the output of the simulations.

# References

- [1] A. J. Line. *Computational Modelling of Helicopter High-Frequency Dynamics*. PhD thesis, Imperial College London, Department of Aeronautics, 2004. viii, 21, 22, 28, 30, 31, 32, 33, 35, 36, 37, 38, 46, 47
- [2] T. Smith J. H. Strickland and K. Sun. A vortex model of the darrieus turbine: an analytical and experimental study., 1981. Sandia, SAND81-7017. ix, 52
- [3] F. Scheurich. *Modelling the Aerodynamics of Vertical-Axis Wind Turbines*. PhD thesis, University of Glasgow, School of Engineering, 2011. ix, 21, 23, 52, 147, 159
- [4] M. Ramasamy T.E. Lee, J.G. Leishman. Fluid dynamics of interacting blade tip vortices with a ground plane. *64th Annual Forum of the American Helicopter Society*, April 2008. ix, 52, 53
- [5] C. Phillips. *Computational Study of Rotorcraft Aerodynamics in Ground Effect and Brownout*. PhD thesis, University of Glasgow, Department of Aerospace Engineering, 2010. ix, 21, 40, 47, 52, 53
- [6] WWF and the Office for Metropolitan Architecture. The energy report: 100% renewable energy by 2050, 2011. Editor in Chief: Stephan Singer. 1, 4
- [7] C. de Fraiture Lundqvist, J. and D. Molden. From field to fork curbing losses and wastage in the food chain, 2008. Stockholm International Water Institute (SIWI) Policy Brief. 1

## REFERENCES

---

- [8] ABP Marine Environmental Research Ltd. for The Met Office. Atlas of uk marine renewable energy resources, 2008. Proudman Oceanographic Laboratory. 1
- [9] A. S. Bahaj. Marine current energy conversion: the dawn of a new era in electricity production. *Phil. Trans. R. Soc.*, 371(A), 2013. 2, 3
- [10] Black and Veatch Consulting Ltd for Carbon Trust. Phase ii uk tidal stream energy resource assessment, 2005. Technical report no. 107799/D/2200/03, London, UK. 2
- [11] The European Wind Energy Association. Wind in power: European statistics 2012, 2013. Data source: EWEA, wind energy data and ocean energy data. 2, 3
- [12] G.P. Harrison A.S. Iyer, S.J. Couch and A.R. Wallace. Variability and phasing of tidal current energy around the united kingdom. *Renewable Energy Journal*, 51(1):343–357, 2013. 3, 4
- [13] B. L. Van Der Waerden. The heliocentric system in greek, persian and hindu astronomy. *Annals of the New York Academy of Sciences*, 500:525–545, 1987. 3
- [14] M.J. Dadswell and R.A. Rulifson. Macrotidal estuaries: a region of collision between migratory marine animals and tidal power development. *Biological Journal of the Linnean Society*, 51(12):93–113, 1994. 5
- [15] Alden Research Laboratory Inc. for Electric Power Research Institute. Evaluation of fish injury and mortality associated with hydrokinetic turbines, 2011. Technical report. 5
- [16] Scottish Association for Marine Science. Annual report 2009-2010. 5
- [17] J-S. Lopez-Gutierrez C. Matutano, V. Negro and M. D.Esteban. Scour prediction and scour protections in offshore wind farms. *Renewable Energy Journal*, 57(1):358–365, 2013. 5, 19

## REFERENCES

---

- [18] P. Troch L. De Vos, J. De Rouck and P. Frigaard. Empirical design of scour protections around monopile foundations: Part 1: Static approach. *Ocean Engineering*, 58(6):540–553, 2011. 5
- [19] R. Falconer R. Ahmadian and B. Bockelmann-Evans. Far-field modelling of the hydro-environmental impact of tidal stream turbines. *Renewable Energy*, 38(1):107–116, 2012. 6, 8
- [20] R. Ahmadian and R. Falconer. Assessment of array shape of tidal stream turbines on hydro-environmental impacts and power output. *Renewable Energy*, 44(1):318–327, 2012. 6
- [21] S.J. Couch S. P. Neill, E.J. Litt and A.G. Davies. The impact of tidal stream turbines on large-scale sediment dynamics. *Renewable Energy*, 34(12):2803–2812, 2009. 6, 8
- [22] J.R Jordan S. P. Neill and S.J. Couch. Impact of tidal energy converter (tec) arrays on the dynamics of headland sand banks. *Renewable Energy*, 37(1):387–397, 2012. 6, 58, 62
- [23] D. R. Plew and C. L. Stevens. Numerical modelling of the effect of turbines on currents in a tidal channel tory channel, new zealand. *Renewable Energy*, 57(1):269–282, 2013. 6
- [24] T.Wang Z. Yang and A. E. Copping. Modeling tidal stream energy extraction and its effects on transport processes in a tidal channel and bay system using a three-dimensional coastal ocean model. *Renewable Energy*, 50(1):605–613, 2013. 6
- [25] P. E. Robins. Influence of tidal-stream energy extraction on sediment dynamics. *EWTEC2013 conference proceedings*, 2013. 6
- [26] M. C. Easton and D. K. Woolf. The influence of non-linear turbine dynamics on the environmental stress of tidal stream arrays. *EWTEC2013 conference proceedings*, 2013. 6, 58, 59

## REFERENCES

---

- [27] Y. Li M. J. Churchfield and P. J. Moriarty. A large-eddy simulation study of wake propagation and power production in an array of tidal-current turbines. *Proceedings of European Wave and Tidal Energy Conference*, 2011. 6
- [28] L.E. Myers and A. S. Bahaj. An experimental investigation simulating flow effects in first generation marine current energy converter arrays. *IET Renewable Power Generation*, 6(4):613–627, 2010. 7
- [29] c C. Amos J. De Ronde A. Bolle, Z.B. Wang. The influence of changes in tidal asymmetry on residual sediment transport in the western scheldt. *Continental Shelf Research*, 30(8):871–882, 2010. 12
- [30] Andritz Hydro Hammerfest. [www.hammerfeststrom.com](http://www.hammerfeststrom.com), 2013. 12
- [31] OpenHydro Group. [www.openhydro.com](http://www.openhydro.com), 2013. 12
- [32] Scotrenewables Tidal Power. [www.scotrenewables.com](http://www.scotrenewables.com), 2013. 12
- [33] Nova Innovation. [www.novainnovation.co.uk](http://www.novainnovation.co.uk), 2013. 12
- [34] MCT. [www.marineturbines.com](http://www.marineturbines.com), 2013. 12
- [35] RWE. [www.rwe.com/web/cms/en/1113816/rwe-innogy/about-rwe-innogy/rwe-npower-renewables](http://www.rwe.com/web/cms/en/1113816/rwe-innogy/about-rwe-innogy/rwe-npower-renewables), 2013. 12
- [36] Meygen. [www.meygen.com](http://www.meygen.com), 2013. 12
- [37] Scottishpower Renewables. [www.scottishpowerrenewables.com](http://www.scottishpowerrenewables.com), 2013. 12
- [38] T. M. Fletcher and R. Brown. Simulation of wind turbine wake interaction using the vorticity transport models. *Wind Energy*, 13(7):587–602, 2010. 21
- [39] A. J. Chorin. *Vorticity and Turbulence*. Springer-Verlag, 1997. 26, 192
- [40] L. Rosenhead. The spread of vorticity in the wake behind a cylinder. *Proceedings of the Royal Society of London, Series A*, 127:590–612, 1930. 27
- [41] D.W. Moore. Finite amplitude waves on aircraft trailing vortices. *Aeronautical Quarterly*, 23:307–314, 1972. 27

## REFERENCES

---

- [42] E. F. Toro. A weighted average flux method for hyperbolic conservation laws. *Proceedings of the Royal Society of London, Series A: Mathematical and Physical Sciences*, 423(1865):401–418, 1989. 29
- [43] E. F. Toro. Some aspects of shock capturing methods for gas dynamics. *College of Aeronautics Report, Cranfield Institute of Technology*, (9112), 1991. 30, 31
- [44] A. Harten. High resolution schemes for hyperbolic conservation laws. *Journal of Computational Physics*, 49(3):357–393, 1983. 31
- [45] G. Strang. On the construction and comparison of finite difference schemes. *SIAM Journal of Numerical Analysis*, 5(3):995–1011, 1968. 31
- [46] L. Greengard and V. Rokhlin. A fast algorithm for particle simulations. *Journal of Computational Physics*, 73(2):325–348, 1987. 34
- [47] R. Krasny and K. Lindsay. A particle method and adaptive treecode for vortex sheet motion in three-dimensional flow. *Journal of Computational Physics*, 127(2):879–907, 2001. 35
- [48] G. Arfken. *Mathematical Methods for Physicists 3rd edition*. Academic Press, Orlando, FL, 1985. 42
- [49] D.M. O’Doherty C.E. Morris A. Mason-Jones and T. O’Doherty. Influence of a velocity profile & support structure on tidal stream turbine performance. *Renewable Energy*, 52(2):23–30, 2013. 45, 57, 99
- [50] M. Richmond J. Thomson, B. Polagye and V. Durges. Quantifying turbulence for tidal power applications. *OCEANS2010 Conference Proceedings*, page , 2010. 51, 154
- [51] D. Kim T.M. Fletcher, R.E. Brown and O.J. Kwon. Predicting wind turbine blade loads using vorticity transport and rans methodologies. *EWEC2009 conference proceedings*, 2009. 53

## REFERENCES

---

- [52] D.-J. R. Walstra L.C. van Rijn and M. van Ormondt. Unified view of sediment transport by currents and waves iv: Application of morphodynamic model. *Journal of Hydraulic Engineering*, 133(7):776–793, 2007. 57
- [53] J.P. Gore M.J. Zimberg, S.H. Frankel and Y.R. Sivathanu. A study of coupled turbulent mixing, soot chemistry, and radiation effects using the linear eddy model. *Combustion and Flame*, 113(3):454–469, 1998. 57
- [54] A.G. Stevenson. Metal concentrations in marine sediments around scotland:a baseline for environmental studies. *Continental Shelf Research*, 21:879–897, 2001. 58
- [55] L.C. van Rijn. Unified view of sediment transport by currents and waves i: initiation of motion, bed roughness, and bed-load transport. *Journal of Hydraulic Engineering*, 133(6):649–667, 2007. 59, 60, 61, 62, 64
- [56] N. Cheng S. Duan and L. Xie. A new statistical model for threshold friction velocity of sand particle motion. *Catena*, 104:32–38, 2013. 59
- [57] H.M. Nepf. Flow and transport in regions with aquatic vegetation. *Annual Review of Fluid Mechanics*, 44(1):123–142, 2012. 59, 193
- [58] R. C. Hildale J. Huang and B. P. Greimann. *Erosion and Sedimentation Manual, Chapter 4: Cohesive Sediment Transport*. U.S. Department of the Interior, Bureau of Reclamation, Sedimentation and River Hydraulics Group, Denver, Colorado, 2006. 60, 63
- [59] D. Paphitis. Sediment movement under unidirectional flows: an assessment of empirical threshold curves. *Coastal Engineering*, 43:227–245, 2001. 60
- [60] F. Hjulstrom. *Study of the Morphological Activity of Rivers as Illustrated by the River Fyris*. Geological Institute of Upsala, Upsala, Sweden, 1935. 60
- [61] A. Shields. Application of similarity principles and turbulence research to bedload movement (english translation of the original german manuscript). *Hydrodynamics Laboratory, California Institute of Technology*, (167), 1936. 60

## REFERENCES

---

- [62] D.L. Inman. Sorting of sediments in the light of fluid mechanics. *Journal of Sedimentary Research*, 19:51–70, 1949. 60
- [63] A. Sundborg. The river klararven, a study of fluvial processes. *Geografiska Annaler*, 38(3):127–316, 1956. 60
- [64] I.N. Mc Cave M.C. Miller and P.D. Komar. Threshold of sediment motion under unidirectional current. *Sedimentology*, 24(4):507–527, 2007. 60, 62
- [65] P.D. Komar and Z. Li. Pivoting analyses of the selective entrainment of sediments by shape and size with application to gravel threshold. *Sedimentology*, 33:425–436, 1986. 60
- [66] A.J. Grass. Initial instability of fine bed sand. *Journal of the Hydraulics Division*, 96(3):619–632, 1970. 61
- [67] A.J. Grass. Structural features of turbulent flow over smooth and rough boundaries. *Journal of Fluid Mechanics*, 50(2):233–255, 1971. 61
- [68] A.A. Kalinske. Movement of sediment as bed-load in rivers. *Transactions, American Geophysical Union*, 28(4):615–620, 1947. 61
- [69] S. Sarkar S. Dey and L. Solari. Near-bed turbulence characteristics at the entrainment threshold of sediment beds. *Journal of Hydraulic Engineering*, 137(9):945–958, 2011. 61
- [70] Y. Bai J. Ma, D.Xu and J.J.R. Williams. Probability model for gravel sediment entrainment in turbulent flows. *Journal of Hydro-environment Research*, 2013. 61, 63
- [71] A.F. Blumberg and G.L. Mellor. A description of a three-dimensional coastal ocean circulation model. *Three-Dimensional Coastal Ocean Models, Coastal Estuarine Sciences*, 4:1–16, 1987. 61, 62, 67
- [72] L.C. van Rijn. *Principles of sediment transport in rivers, estuaries and coastal seas*. Aqua Publications, Amsterdam, The Netherlands, 1993. 62

## REFERENCES

---

- [73] J. S. Ribberink. Bed-load transport for steady flows and unsteady oscillatory flows. *Coastal Engineering*, 34:59–82, 1998. 62, 63, 64
- [74] Y-G. Wang M-T. Zhang D-S. Jeng C. Zhang, J-H. Zheng and J-S. Zhang. A process-based model for sediment transport under various wave and current conditions. *International Journal of Sediment Research*, 326(4):498–512, 2011. 62, 67
- [75] J.D Keller-K. McClure P.Gilmore D.A. Wachspress, G.R. Whitehouse and M. Dorsett. Physics based modeling of helicopter brownout for piloted simulation. *Interservice/industry Training, Simulation, and Education Conference*, 2008. 63
- [76] W.R. Parker-R.B. Krone A.J. Mehta, E.J. Hayter and A.M. Teeter. Cohesive sediment transport part i: Process description. *Journal of Hydraulic Engineering*, 115(8):1076–1093, 1989. 64
- [77] L.C. van Rijn. Unified view of sediment transport by currents and waves ii:suspended transport. *Journal of Hydraulic Engineering*, 133(6):668–689, 2007. 64
- [78] L.C. van Rijn. Sediment transport, part i: Bed load transport. *Journal of Hydraulic Engineering*, 110(10):1431–1456, 1984. 64, 65, 90
- [79] N.S. Cheng. A simplified settling velocity formula for sediment particle. *Journal of Hydraulic Engineering*, 123(2):149–152, 1997. 66
- [80] L.C. van Rijn. Sediment transport, part ii: Suspended load transport. *Journal of Hydraulic Engineering*, 110(11):1613–1641, 1984. 66
- [81] U. Zanke. *Berechnung der Sinkgeschwindigkeiten von Sedimenten*. Reihe Mitteilungen des Franzius-Instituts für Wasserbau und Küsteningenieurwesen der TU Hannover, Technical University, Hannover, West Deutschland, 1977. 66
- [82] J. A. Zyserman and J. Fredsoe. Data analysis of bed concentration of suspended sediment. *Journal of Hydraulic Engineering*, 120(9):1021–1042, 1994. 66

## REFERENCES

---

- [83] H.Rouse. Experiments on the mechanics of sediment suspension. *Proceedings of the Fifth International Congress of Applied Mechanics, Cambridge*, pages 550–554, 1938. 66
- [84] L. E. Holmedal and D. Myrhaug. Boundary layer flow and net sediment transport beneath asymmetrical waves. *Continental Shelf Research*, 26(2): 252–268, 2006. 67
- [85] Aquatic Renewable Energy Technologies. Case study - hammerfest strom, 2008. Technical report. 72
- [86] C.F. Fleming S.C. McIntosh and R.H.J. Willden. The inuence of vertical velocity shear on tidal turbine performance and wake recovery. *Oxford Tidal Energy Workshop*, March 2012. 90
- [87] S.C. McIntosh. Personal communication. 2nd April 2012. 90
- [88] T. Stallard A. Olczak and P. Stansby. The influence of waves on tidal stream turbine wake recovery. *EWTEC2013 conference proceedings*, 2013. 91
- [89] Margolin L.G. Grinstein, F. F. and W.J. Rider. *Implicit Large Eddy Simulation*. Cambridge University Press, 2007. 192